Modelling of Reactive Transport in Porous Media using Continuous Time Random Walks

Rodolfo Oliveira

A thesis submitted to the Department of Earth Science and Engineering, Imperial College London, in partial fulfilment of the requirements for the degree of Doctor of Philosophy.

Imperial College London
Department of Earth Science and Engineering

August, 2021

Statement of Originality

I declare that this thesis is entirely my own work under the supervision of Dr. Branko Bijeljic and Prof. Martin J. Blunt. The work was performed in the Department of Earth Science and Engineering at Imperial College London. All published and unpublished materials used in the thesis have been given full acknowledgement. This work has not been previously submitted, in whole or in part, to any other academic institution for a degree, diploma, or any other qualification.

Rodolfo Oliveira

Copyright Notice

Modelling of Reactive Transport in Porous Media using Continuous Time Random Walks by **Rodolfo Oliveira** is licensed under **CC BY-NC-ND 4.0**[1]. The summary of, and not a substitute for, the license follows below. Under this license, you are free to:

Share – copy and redistribute the material in any medium or format

Adapt – remix, transform, and build upon the material for any purpose, even commercially.

The licensor cannot revoke these freedoms as long as you follow the license terms:

Attribution – You must give appropriate credit, provide a link to the license, and indicate if changes were made. You may do so in any reasonable manner, but not in any way that suggests the licensor endorses you or your use.

Share Alike – If you remix, transform, or build upon the material, you must distribute your contributions under the same license as the original.

No additional restrictions – You may not apply legal terms or technological measures that legally restrict others from doing anything the license permits.



[1]For the complete legal text of Attribution-NonCommercial-NoDerivatives 4.0 International (CC BY-NC-ND 4.0) please visit https://creativecommons.org/licenses/by-nc-nd/4.0/legalcode.

Acknowledgements

I would like to express my sincerest gratitude for my supervisors Prof. Martin Blunt and Dr. Branko Bijeljic for their dedication, guidance and support over the years of my study. I will always be in debt for this opportunity. I would like to give a special thanks to Adam Colbourne, Andrew J. Sederman, Mick D.Mantle, Lynn F.Gladden and the Magnetic Resonance Research Centre (MRRC) at the University of Cambridge for the invaluable contribution of the NMR experimental datasets and the hosted visits. I would also like to acknowledge Schlumberger Research for partially funding my work, and Imperial College Research Computing Service for the support and usage of its facilities. And to my early stage examiner, Prof. Stephen Neethling, and viva examiners, Prof. Velisa Vesovic and Dr. Daniel W. Meyer, your insightful feedback and interest have been of great assistance in the preparation of this work.

I would like to thank all my friends that made my time in Imperial College London enjoyable and whose contributions both at a personal and technical level were fundamental for this achievement. Thomas de Oliveira, Matthew Kirby, Lukas Mosser, Michael Steventon, Mosayeb Shams, Ali Raeini, Hannah Menke, João Paulo Pereira, Kamaljit Singh, Hossam Osman, Felipe Huerta, Geraldo Fiorini, Christiano Borges, Orlando Neto, Ricardo Colombo, and Aline Walter, your company and advices will never be forgotten.

Last but not least I would like to thank my parents Maria Beatriz and Lideir for their care and support even when far from one another, and my beloved wife Mayara for her patience, special care, and the subtracted hours of our living.

To Mayara.

Abstract

Reactive transport in porous media is commonly encountered in chemical engineering (*e.g.* packed beds), contaminant hydrology, reactive flow in batteries and fuel cells, and nuclear waste disposal. Some of those applications are centred in carbonate rocks, which hold over 60 % of hydrocarbon reserves and are considered as potential sinks for carbon storage in aquifers and reservoirs.

We start with the description of the Continuous Time Random Walk (CTRW) particle transport model which is validated against experimental results in the literature. We then show that our model is capable of reproducing Fickian and non-Fickian transport signatures by carefully choosing a combination of the characteristic advective and diffusive times t_1 and t_2, and the transport heterogeneity parameter β. The combination of parameters showed the ability to model sub- and super-diffusive systems. Furthermore the model also captures hydrodynamic dispersion over 6 orders of magnitude, and the model sensitivity to the β parameter demonstrates how it can be used to represent samples with different physical heterogeneity.

Having the transport component of our model defined, we proceed and extend it to a reactive transport model by including a first-order kinetics model to account for chemical reaction. Our model is validated with a dataset for a Ketton carbonate rock sample undergoing dissolution on injection of an acid, monitored using Nuclear Magnetic Resonance (NMR). The experimental data includes the 3D porosity distribution at the beginning and end of the experiment, 1D porosity profiles along the direction of flow during dissolution, as well as the molecular fluid displacement probability distributions (propagators). We also demonstrate that heterogeneity in the flow field leads to an effective reaction rate, limited by transport of reactants, that is almost three orders of magnitude lower than measured under batch reaction conditions. This study establishes a workflow to calibrate and validate the CTRW reactive transport model with NMR experiments.

After validating the transport and reactive model, we systematically demonstrate the impact of physical heterogeneity on transport and reactive flow signatures. We study this by creating three porous media of increasing heterogeneity,

subjected to three advective dominated transport regimes each, and examine the emergent effective reaction rates. The different Pe numbers were capable of reproducing the appearance of two distinct dissolution patterns – a compact or face dissolution pattern and a channelized dissolution pattern. The distribution of propagators of each sample showed the imprint of heterogeneity on its asymmetrical shape, as well as the contrast between slow and fast regions that increased with the dissolution process. Later we extended the models to examine the impact of β in the average porosity evolution and effective reaction rates. The change in concentration is slower with a decrease of β which is in line with the behaviour of transport only descriptions.

Finally, we study the impact of coupled flow and chemical heterogeneity on effective reaction rates. We start by modelling a multi-species fluid/fluid reactive system with the injection of sodium carbonate Na_2CO_3 and calcium chloride $CaCl_2$ solutions through different halves of a porous domain and observe the production of sodium chloride NaCl and calcium carbonate $CaCO_3$. The increase of heterogeneity leads to an increase in the production of NaCl and $CaCO_3$ by increasing the mixing of the injected solutions. Then we use the same heterogeneous reactive transport solver to model porous media consisting mostly of calcite with dolomite near the fast flowing channels. The dependence of the effective reaction rates of the different minerals is related to their distance from fast-flowing channels. These results are supported by the results found in the literature where the pore-scale pattern of dissolution was measured on chemically heterogeneous samples.

We conclude our work suggesting additional work and experimental acquisitions to improve the predictability of our model, the addition of adsorption, precipitation and bio-chemical alterations of the porous media and a multi-scale integration using direct simulations at under-resolved scales.

Related Work

Peer-Reviewed Publications

Oliveira, R., Bijeljic, B., Blunt, M.J., Colbourne, A., Sederman, A.J., Mantle, M.D., Gladden, L.F. (2021). A continuous time random walk method to predict dissolution in porous media based on validation of experimental NMR data. *Advances in Water Resources*, 149. https://doi.org/10.1016/j.advwatres.2021.103847

Oliveira, R., Blunt, M.J., Bijeljic, B. (2021). Impact of Physical Heterogeneity, Transport Conditions on Effective Reaction Rates. *manuscript submitted to Transport in Porous Media.*

Oliveira, R., Blunt, M.J., Bijeljic, B. (2021). The Impact of the Coupled Physical and Chemical Heterogeneity on the Effective Reaction Rates in Porous Media (*manuscript in preparation*)

Presentations and Posters

Oliveira, R., Blunt, M.J., Bijeljic, B. (2021). Impact of Physical Heterogeneity on Effective Reaction Rates. *abstract accepted – InterPore 2021* (*oral*)

Oliveira, R., Bijeljic, B., Blunt, M.J., Colbourne, A, Sederman, A.J., Mantle, M.D., Gladden, L.F. (2018). Transport, Reactive Flow Modelling Using A Particle Tracking Method Based on Continuous Time Random Walks. *Computational Methods in Water Resources XXII*, 396. http://cmwrconference.org/2018/proceedings/ (*oral*)

Sederman, A.J., Colbourne, A., Mantle, M.D., Gladden, L.F., **Oliveira, R.**, Bijeljic, B., Blunt, M.J. (2017). Monitoring carbonate dissolution using spatially resolved under-sampled NMR propagators, MRI. *American Geophysical Union, Fall Meeting*, H12A-04. https://ui.adsabs.harvard.edu/abs/2017AGUFM.H12A..04S (*oral*)

Oliveira, R., Muljadi, B.P., Bijeljic, B., Blunt, M.J., Colbourne, A., Sederman, A.J., Mantle, M.D., Gladden, L.F. (2017). Modelling, Upscaling of Transport in Carbonates During Dissolution: Validation, Calibration with NMR Experiments. *UKCCSRC Spring Biannual Meeting* (*poster*).

Oliveira, R., Bijeljic, B., Blunt, M.J., Colbourne, A, Sederman, A.J., Mantle, M.D., Gladden, L.F. (2017). Transport, Reactive Flow Modelling Using A Particle Tracking Method Based on Continuous Time Random Walks. *American Geophysical Union, Fall Meeting*, H13A-1350. http://ui.adsabs.harvard.edu/abs/2017AGUFM.H13A1350O (*poster*)

Contents

Statement of Originality i

Copyright Notice ii

Acknowledgements iii

Abstract v

Related Work vii

List of Figures xii

List of Tables xxix

1 Introduction 1
- 1.1 Reactive Transport in Porous Media . . . 1
- 1.2 Carbonate Rocks . . . 2
- 1.3 Scales of heterogeneity in porous media . . . 3
- 1.4 Objectives . . . 9
- 1.5 Thesis outline . . . 9

2 Literature Review 11
- 2.1 Transport in Porous Media . . . 11
  - 2.1.1 Anomalous Transport . . . 17
- 2.2 Reactive Transport in Porous Media . . . 17
- 2.3 Impact of Heterogeneity on Reactive Transport . . . 22
- 2.4 Numerical Modelling Methods . . . 27
- 2.5 Continuous Time Random Walks . . . 31
- 2.6 Summary and Motivation . . . 36

3 Modelling Transport in Porous Media using Continuous Time Random Walks 38
- 3.1 Model Description . . . 39

3.1.1 Lattice Flow Model . . . 39
3.1.2 Particle Transport Model . . . 43
3.2 Transport Validation . . . 51
3.2.1 Effect of the Number of Particles . . . 51
3.2.2 Asymptotic Time Behaviour . . . 53
3.2.3 Hydrodynamic Dispersion . . . 54
3.3 Transport in Representative Elementary Volumes as Sample Domains . . . 57
3.4 Conclusions . . . 63

4 Predicting Dissolution in Porous Media using CTRW and Validation with NMR Data 65
4.1 Description of the Reactive Transport Model . . . 66
4.2 Reactive Transport Algorithm . . . 70
4.3 NMR Experimental Data Description . . . 72
4.4 Results . . . 74
4.4.1 Porosity Profiles . . . 74
4.4.2 MRI Acquisition . . . 75
4.4.3 NMR Propagator Measurements . . . 75
4.5 Ketton Carbonate Model . . . 80
4.5.1 Initial Model Calibration . . . 80
4.5.2 Calcite Dissolution Modelling . . . 82
4.5.3 Porosity evolution . . . 84
4.5.4 Average dissolution rate . . . 87
4.5.5 Particle propagators . . . 88
4.6 Discussion . . . 90
4.7 Conclusions . . . 91

5 Impact of Initial Physical Heterogeneity on Effective Reaction Rates 92
5.1 Description of the CTRW Reactive Transport Model . . . 93
5.2 Signatures of Physical heterogeneity . . . 94
5.2.1 Description of the Porous Media . . . 94
5.2.2 Signatures of Flow Heterogeneity . . . 98
5.2.3 Signatures of Transport Heterogeneity . . . 99
5.3 Impact of Physical Heterogeneity on Reactive Flow . . . 104
5.3.1 Visualization of Dissolution and Porosity Evolution . . . 104
5.3.2 Effect of Physical Heterogeneity on Reaction Rates . . . 107
5.3.3 Transit-time Distributions and Particle Propagators . . . 109
5.4 Discussion . . . 114

5.5 Conclusions 115

6 Coupled Flow and Chemical Heterogeneities — The Impact of Chemical Spatial Distribution on Effective Reaction Rate 117
6.1 Description of the Geochemical Solver 118
6.2 Fluid-Fluid Reactive System 118
6.2.1 Description of the Fluid-Fluid CTRW Reactive Transport Model 119
6.2.2 Mixing Induced by Physical Heterogeneity 124
6.3 Fluid-Solid Reactive System 130
6.3.1 Description of the Fluid-Solid CTRW Reactive Transport Model 130
6.3.2 Dissolution of Mineral Heterogeneous Systems 133
6.4 Discussion 141
6.5 Conclusions 141

7 Conclusions and Future Work 143
7.1 Conclusions 143
7.2 Suggestions for Future work 145
7.2.1 Reactive Transport Modelling 145
7.2.2 Multi-scale Modelling 146

Bibliography 149

Appendix A CTRW Solutions Using Numerical Laplace Inversion 176
A.1 Centre of Mass Velocity and Dispersion Coefficients 176
A.2 Resident Concentration 177
A.3 Numerical Laplace Transform Inversion 177

Appendix B Procedure to Generate Heterogeneous Domains 180

Appendix C Evolution of the Dissolution Patterns 182

Appendix D Procedure to Calculate Histograms of Proximities 189

Appendix E Permissions for Reuse of Copyrighted Materials 191

List of Figures

1.1 Geographical distribution of carbonate reserves. From Schlumberger (2007a), using data from IEA (2006), Schlumberger (2007b), and BP (2008). Copyright © 2007 Schlumberger. All rights reserved. 1

1.2 Conceptual representations of different scales of investigation. Each illustration is an idealized representation of the pore, core and field scales. The pore-scale relates to the measurements capable of distinguishing the distribution of pores and grains. The core-scale relates to the measurements capable of distinguishing textural information of ensemble porous material. The field-scale relates to facies and information from distribution of well and field data. Modified from Oliveira (2014). 4

1.3 Different scales of measurements for permeability estimation as a function of a characteristic length. Each method of measurement is capable of estimating permeability of samples and describing it in terms of different classes. Adapted from Nordahl and Ringrose (2008), Ringrose et al. (2008), and Ringrose and Bentley (2015). 5

1.4 (a) Injected dye tracer in homogenous sand pack under constant flow (Levy and Berkowitz, 2003), and (b) horizontal contours of maximum concentration in an heterogeneous aquifer (Adams and Gelhar, 1992). Each example shows the occurrence of non-Fickian transport at a different observation scale – with 3 orders of magnitude difference in size. The experiment of Levy and Berkowitz (2003) shows that even at a fully saturated and uniform medium, the dye is distorted away from a symmetrical shape and differently for each injection point. The field scale example of Adams and Gelhar (1992) shows the tracer plume distortion happening with observation wells spaced in a distance smaller than the expected hydraulic conductivity block sizes. 8

2.1 Solution for the one-dimensional form of the Advective-Dispersion Equation (ADE) as defined in equation (2.7) for different parametrizations $\eta = D/vx$ (Ogata and Banks, 1961). The value of η is inversely proportional to Pe, so lower η values represent highly advective regimes and higher η values represent dispersive dominated regimes. 14

2.2 Comparison of equation (2.8) and the experimental data present in Orlob and Radhakrishna (1958) for tracer breakthrough in a bead pack and a sandpack. 14

2.3 Longitudinal dispersion coefficient versus Péclet number. Numerical results for a synthetic sandpack, sandstone and carbonate from Bijeljic et al. (2004) and experimental measurements from Pfannkuch (1963), Seymour and Callaghan (1997), Kandhai et al. (2002), Khrapitchev and Callaghan (2003) and Stöhr (2003). Copyright © 2004 by the American Geophysical Union. All rights reserved. 16

2.4 Relationship between the injection rate Q and the required number of pore volumes to breakthrough the sample PV_{BT} for hydrochloric acid and acetic acid. The optimum injection rate is given at the minimum PV_{BT}. Despite modelled to have the same acid capacity, HAc outperformed HCl for those given conditions. From Fredd and Fogler (1998). Copyright © 1998 American Institute of Chemical Engineers. All rights reserved. 20

2.5 Neutron raiographs of different limestone dissolution patterns using a $0.25\,\mathrm{mol\,dm^{-3}}$ EDTA and pH 4 from Fredd and Fogler (1998). The experiments showed the increasing channel branching in wormholes with the decreasing Damköhler numbers. Copyright © 1998 American Institute of Chemical Engineers. All rights reserved. 21

2.6 $Pe - Da$ diagram showing the boundaries between different dissolution regimes. The diagram highlights the Pe-dependence when transitioning from the regimes of compact dissolution, conical wormholes and dominant wormholes, and the Da dependence when transitioning from the regimes of uniform dissolution, ramified wormholes and dominant wormholes. Extracted from Golfier et al. (2002). Copyright © 2002 Cambridge University Press. All rights reserved. 21

2.7 The results for molecular displacements obtained by NMR showing the (a) molecular propagators and (b) normalized displacement variance. There is a significant amount of stagnant zones, showed by $\zeta/\langle\zeta_0\rangle = 0$. The displacement variance increased with the sample heterogeneity and no sample has achieved the asymptotic, or Fickian, transport behaviour. From Scheven et al. (2005a). Copyright © 2005 American Institute of Physics. All rights reserved. 23

2.8 The evolution of (a) molecular displacement distributions and the (b) normalized Probability Density Function (PDF) of velocities for Mt Gambier and Estallaides limestones. The advection-dominated regions, at $|\mathbf{u}|/u_{av} \gg 1$, contributes to the fast mobile tails seen in the molecular propagators distribution at $\zeta/\langle\zeta_0\rangle \gg 1$. The diffusion-only regions, at $|\mathbf{u}|/u_{av} \ll 1$, are responsible for the stagnant regions seen in the molecular propagators at $\zeta/\langle\zeta_0\rangle = 0$. From Bijeljic et al. (2013a). Copyright © 2013 American Geophysical Union. All rights reserved. 24

2.9 Effective reaction rates for calcite and dolomite related to the (a) full volume, (b) fast-flowing channels and (c) slow regions. The effective reaction rate significantly decreases after the channel is formed (dashed line). From Al-Khulaifi et al. (2019). Copyright © 2019 The Authors. All rights reserved. 26

2.10 Different representations of fluids accordingly to the Eulerian discretisation (a) and the Lagrangian discretisation (b). 27

2.11 Particle single hop illustrating the change from (x_0, t_0) by random increments in space and time (ξ, τ) described by equation (2.17) and defined by Montroll and Weiss (1965). 31

2.12 Illustration of a random walk figure 2.12a with a constant step distance and duration and a continuous time random walk figure 2.12b also with a constant step distance but with a random duration between steps. 32

2.13 First passage time distribution for $0 < \beta < 1$ from Berkowitz et al. (2000) using the power-law function equation (2.22). Copyright © 2000 by the American Geophysical Union. All rights reserved. 33

2.14 The particle trajectory in space and velocity as illustrated in figure 2.12, and using equation (2.24) defined by a near homogeneous system characterized with $\beta = 1.8$. The domain used to illustrate the trajectories is described in chapter 3. The large velocities ($\sim 10^3$) are responsible for the particles early arrival and are manifested in the particle breakthrough curves (BTCs). . . . 35

2.15 Comparison for the BTC of a Berea sandstone core using the ADE (dashed line) and CTRW (continuous line) model fit . The experimental data is obtained from Scheidegger (1959) and the best fit results from Cortis and Berkowitz (2004). The quantity j is the normalized flux-averaged concentration. The CTRW model uses the truncated power-law model equation (2.24) and $\beta = 1.59$. Copyright © 2004 Soil Science Society of America. All rights reserved. 36

3.1 Domain idealization and lattice topology with scalar fields (porosity and permeability) used to define the nodes and links within the domain Ω and boundaries Γ. The topology is represented by nodes interconnected by links. Each node of the lattice has the properties defined from a given scalar field. The lattice corresponds to the underlying discrete domain. The pressure P_0 and P_1 is specified in the nodes at Γ_0 and Γ_1 and will be later used to solve the pressure inside the domain Ω. 40

3.2 Lattice representation and the correspondent incidence matrix. The rows correspond to the links and columns to the nodes. Node 4 is highlighted as an example to show that it is connected by links 3 and 7. Similarly link 7 is highlighted to show that it connects node 4 and 5. 42

3.3 Link and node types in the lattice, each representing an element inside the domain, at the face, edge and corner of the enclosed lattice. The other elements are obtained by applying a rotation to these and are not displayed here for simplicity. 42

3.4 General lattice consisting of nodes interconnected by links. This depicts a particle transition from a node i to a node j through a link k with prescribed velocity v_{ij}, probability of displacement p_{ij} and transit time distribution ψ_{ij}. 43

3.5 The effect of t_1, t_2 and β on the shape of the transit-time distribution ψ. The values for t_1 and t_2 are obtained from the flow field and transport parameters, and the value of β is fitted to experimental data. ψ distribution is nearly constant for $t \ll t_1$, has a constant slope of $t^{-1-\beta}$ for $t_1 < t < t_2$ and asymptotically goes for zero for $t \gg t_2$. 45
3.6 Calculated ψ function and its integral for $t_1 = 1.0\,\mathrm{s}$, $t_2 = 1.0 \times 10^4\,\mathrm{s}$ and $\beta = 1.5$. The shaded intervals highlight the regions where $t \ll t_1$ with ψ is nearly constant, $t_1 < t < t_2$ with $\psi \propto t^{-1-\beta}$, and where $t \gg t_2$ with ψ asymptotically going to zero. The integral of the ψ function has a constant slope for $t \ll t_1$ with most of its weight coming from the rest of the t-axis. 46
3.7 Analytical and integrated ψ functions (solid lines) and the reconstructed function from sampled values of the ψ integral (circles). The function was constructed using $t_1 = 1.0\,\mathrm{s}$, $t_2 = 1.0 \times 10^4\,\mathrm{s}$ and $\beta = 1.5$. The reconstructed function is able to recover the overall shape of the analytical ψ function for a wide range of values. 46
3.8 A 2D graph constructed from the concept described in figure 3.4 and with the main flow direction aligned with $+x$-axis and $v = 0$ perpendicular to this direction. The results of the probability of displacement in such a scenario and under different Pe numbers are shown in figure 3.9. 48
3.9 Probability of transitioning p_{ij} and the cumulative of it P_{ij} for $Pe = 1$ and $Pe = 10$. For $Pe = 1$, the probability of travelling in any direction is nearly the same, with a higher chance of going towards the flow (east) and smaller chance against the flow (west). When Pe increases by an order of magnitude, the probability is predominantly driven by the flow direction. 48
3.10 Particle trajectories for different Pe numbers. At low Pe numbers, the velocity field has little influence on the particle displacement, with most of the effect originating from diffusion. As Pe increases the advective forces become predominant and the mean particle trajectory aligns more with the mean flow direction, to the point that dispersion perpendicular to the flow is nearly absent. 49
3.11 Comparison between the particle trajectories at the fixed recorded time Δt and the actual sampled times $\Delta\tau$. Given the stochastic nature of the problem, the seed was fixed in order to sample the same random numbers for both cases. 50

3.12 Several different particle trajectories represented by a different colour for $Pe = 10$. The particles move towards $+x$-axis, following the main flow direction, but still experience dispersion as seen from the trajectory projected in the $y - z$ plane. 51
3.13 Effect of the number of particles N_p on the normalized mean particle velocity and normalized mean longitudinal particle dispersion for $Pe = 100$. This case was constructed with a uniform porosity of $\phi = 0.3$, $K = 1 \times 10^{-12}\,\mathrm{m}^2$ and $\beta = 1.8$. As the number of particles increases, the high-frequency noise reduces, and the behaviour at early times is better resolved. However the overall trend and evolution is captured in all cases. 52
3.14 Effect of the number of particles in the time-step taken per Δt iteration and relative error in the normalized dispersion ϵ_D and normalized velocity ϵ_v. The time taken per iteration scales linearly with the number of particles for $N_p \gtrapprox 10^3$. The error decreases faster with the increase of particles. 53
3.15 Asymptotic time behaviour for the longitudinal dispersion coefficient and the mean velocity for $\beta = 0.25$, 0.75 and 1.5 and $\tau_2 = 10^3$, 10^4, 10^5 and 10^6. For the interval $1 \ll \tau \ll \tau_2$ and transport characterized by $0 < \beta < 1$, the longitudinal dispersion $D_L \propto \tau^{2\beta-1}$ and for $1 < \beta < 2$, $D_L \propto \tau^{2-\beta}$ (Dentz et al., 2004; Berkowitz et al., 2006). 55
3.16 Asymptotic longitudinal dispersion coefficient for $\beta = 0.25$, 0.75 and 1.50. The increase of the β values represent the increase of heterogeneity, from highly heterogeneous sample ($\beta = 0.25$) to mildly heterogeneous sample ($\beta = 1.5$). The experimentally measured points for unconsolidated beadpacks and sandpakcs taken from the literature (Pfannkuch, 1963; Seymour and Callaghan, 1997; Kandhai et al., 2002; Khrapitchev and Callaghan, 2003; Stöhr, 2003), and are left indistinguishable from each other for simplicity, but were differentiated in figure 2.3 of chapter 2. . . . 56
3.17 Conceptual picture illustrating the representation of two different materials and its mapping into nodes. This concept depicts porous grains within a porous matrix, however it can represent the presence of any other feature (*e.g.* channels). 57

3.18 Examples of marine ooids and open fractures, common in limestones. The ooids are spherical structures of different porosity that can be in a porous matrix or surrounded by a micrite cement. The highlighted rectangle has a side of 100 µm. Open fractures act as the main conduct for flow and transport in a porous matrix. The letters uA and A stands for unaltered and altered fractures. 58
3.19 Geometry for the (a) spherical inclusion and (b) infinite channel. Despite using 2D illustrations, both domains extend in L in the direction perpendicular to the figure. Each subdomain Ω is defined by its porosity and permeability, with porosity $\phi_0 = 0.3$ and $\phi_1 = 0.015$ and permeability $K_0 = 2 \times 10^{-12}\,\mathrm{m}^2$ and $K_1 = 5 \times 10^{-15}\,\mathrm{m}^2$. 59
3.20 Snapshot of particle positions for different Pe at $t/t_1 = 0.5$. Lower Pe are characterized by a smeared out plume when compared to higher Pe numbers. The porosity and permeability contrast between the subdomains properties traps the particles in the spherical inclusions. 60
3.21 Particle propagators at $t/t_1 = 0.5$ for different Pe in the (a) sphere and (b) channel domains. The propagator distribution is calculated from the distribution of the particle displacement ζ normalized by the mean particle displacement $\langle\zeta\rangle_0$. 61
3.22 Normalized mean particle velocity $v_x/\langle v_x\rangle$ along the main flow direction for the (a) sphere and (b) channel domains and $Pe = 10, 100$ and 1000. The time is normalized by the mean advective time so that for times larger than $t/t_1 \gg 1$ the normalized particles mean velocity approaches asymptotically $v_x/\langle v_x\rangle \to 1$. It is evident that this behaviour is already observed for $t/t_1 > 10^{-2}$. . 62
3.23 Normalized longitudinal particle dispersion D_l/D_m for the (a) sphere and (b) channel domains and $Pe = 10, 100$ and 1000. Longitudinal dispersion increases with time, characteristic of the super-diffusive transport regime, observed when $t/t_1 > 10^{-2}$. . . 62

4.1 Simplified illustration of an ensemble of particles (a) and the detailed representation of a single particle (b) transiting and reacting through a lattice (c-d). The increase of blue depicts an increase of the aqueous calcium concentration. A particle transits in the lattice with variable transit-time $\Delta\tau$ and displacement Δx. After each transition, the number of moles of aqueous calcium in a particle increases by Δn, as a consequence of the reaction within the node of origin, which in turn has its porosity increased by $\Delta\phi$. 66

4.2 Particle equilibrium and trajectory in a 2D lattice. The lattice has fixed values of $t_1 = 0.03\,\mathrm{s}$, $t_2 = 3.0\,\mathrm{s}$ and $\beta = 1.6$ and the particle reacts with it using $k_r = 0.2\,\mathrm{s}^{-1}$. The particle step goes from ⓪ to ②, where from ⓪ to ① the particle reacts with the node of origin and from ① to ② it moves from the node of origin to the target node. 68

4.3 Comparison between the analytical solution of the moles of aqueous calcium defined in equation (4.3) and the simulated results using equation (4.4) and equation (3.12) for (a) two particles and for (b) the mean of 100 000 particles. The model uses $k_r = 0.2\,\mathrm{s}^{-1}$, $t_1 = 0.03\,\mathrm{s}$, $t_2 = 3.0\,\mathrm{s}$ and $\beta = 1.6$. The change in the number of moles of aqueous calcium associated with each particle is proportional to the particle transit-time at the end of each transition. 68

4.4 (a) Porosity profile evolution from the beginning to the end of the dissolution experiment. (b) The region where the sample is located is highlighted from approximately 0 m to 0.072 m. The porosity profiles are coloured accordingly to the acquisition time, from the beginning of the experiment to the end at $1.254 \times 10^4\,\mathrm{s}$. The highest porosity alteration can be seen in the first 0.015 m of the sample, reducing sharply and is nearly absent after 0.055 m. 74

4.5 Evolution of porosity difference from the beginning to the end of the dissolution experiment. The region where the sample is located between 0.00 m and 0.072 m. The porosity profiles are coloured accordingly to the acquisition time, from the beginning of the experiment to the end at $1.254 \times 10^4\,\mathrm{s}$. 75

4.6 Porosity field for the carbonate sample at the beginning (a) and at the end (b) of the dissolution experiment. The porosity is normalized using the 1D porosity profiles. The channel formed is visualised in the second image by applying an opacity filter for $\phi < 0.3$. 76

4.7 Photograph of the carbonate sample at the end of the dissolution experiment. 76
4.8 Top: NMR propagators at the entry (a) and exit (b) of the sample during the dissolution experiment. Bottom: the difference between the propagators at the beginning and the end of the experiment. Most of the alterations are present at the entry face of the sample. The exit face is left nearly intact, preserving the original distribution from the beginning of the experiment. 77
4.9 Complete distribution of propagators during the dissolution experiment colour-coded by the length of the sample. The measurements were taken across the length of the sample $l = 0.072\,\mathrm{m}$ using an observation time $\Delta = 0.25\,\mathrm{s}$. 78
4.10 Propagators distribution during the dissolution experiment stacked by its length and colour-coded by the amplitude of the distribution. 79
4.11 Initial porosity and permeability distribution. The porosity-permeability correlation factors $a = 2.2 \times 10^{-8}\,\mathrm{m}^2$ and $b = 6.2$ are defined in equation (3.3) and based on the Ketton limestone experiments Honari et al. (2015). 80
4.12 Initial porosity field and calculated pressure. The porosity is constructed from the Magnetic Resonance Imaging (MRI) acquisition. The calculated pressure reflects the initial heterogeneity of the sample modelled after the MRI-derived porosity. 81
4.13 Particle propagator distribution for different values of β. The best fit was obtained with $\beta = 0.9$. 83
4.14 Porosity profiles and axis inset with a zoomed-in detail along the flow direction for different numbers of injected particles per time step, at the beginning and at $t = 1 \times 10^3\,\mathrm{s}$. We used $N_{\mathrm{particles}} = 1000$ for a time step $\Delta t = 10\,\mathrm{s}$ as the optimum number of particles injected by observing that the porosity profile did not change if more particles were injected. 84
4.15 Porosity profiles and axis inset with a zoomed-in detail along the flow direction for different porosity change precisions at the end of the simulation. We choose the value of $\Delta\phi = 1 \times 10^{-4}$ as the optimum total porosity change to update the pressure field. Reducing this value increases the amount of times that the pressure is updated, but showed no influence in the porosity evolution. . . 85

4.16 Profiles for the simulated porosity and relative porosity difference compared to the experimentally-measured NMR porosity profiles. Figure (a) shows the initial porosity profile, figure (b) and (c) the porosity and porosity difference at $t = 6.0 \times 10^3$ s, and figure (d) and (e) at the end of the experiment, $t = 1.2 \times 10^3$ s. 86
4.17 Porosity field in the experiment (a) and simulation (b) at 1.2×10^4 s, the end of the dissolution experiment. Only values of $\phi \geq 0.3$ are shown. Once the channel breaks through, it becomes the dominant source of transport. 87
4.18 Experimental and simulated estimated effective dissolution rate. The simulated effective dissolution rate is nearly 780 times smaller than the batch reaction rate while the experimental effective dissolution rate is nearly 680 times smaller than the batch calcite dissolution rate, $r = 8.1 \times 10^{-4}\,\mathrm{mol\,m^{-2}\,s^{-1}}$ (Peng et al., 2015).The error bars reflect uncertainty in the experimental measurements. 88
4.19 Particle distribution injected at the core inlet compared against the molecular propagators at (a) 0 s and (b) 1.2×10^4 s. These times represent the dissolution experiment at the beginning and the end. 89
4.20 Particle mean velocity evolution. The graphs show the mean velocity v for the domain at the beginning ($t = 0$ s) and at the end ($t = 1.2 \times 10^4$ s) of the simulation. As $v \propto t^{\beta-1}$ we estimate the values of β at the beginning and end of the simulation as $\beta_{\text{initial}} = 0.49$ and $\beta_{\text{final}} = 0.64$. 89
4.21 The evolution in the $\psi(t)$ function for all available links in the domain at the beginning ($t = 0.0$ s) and end ($t = 1.2 \times 10^4$ s) of the simulation. The shades of colours shows the overlapping the ψ functions distributions and the continuous lines the ψ functions using the minimum, average and maximum values t_1 in the links. 90

5.1 Simplified illustration of (a) an ensemble of particles and (b) the detailed representation of a single particle (b) before and (c) after transiting and reacting through a lattice. The change in colour depicts an increase of the aqueous calcium concentration. A particle transits in the lattice with variable transit-time $\Delta\tau$ and displacement Δx, obtained from a locally defined transit-time distribution ψ_{ij} and displacement probability p_{ij}. After each transition, the number of moles of aqueous calcium in a particle increases by Δn, as a consequence of the reaction within the node of origin, which in turn has its porosity increased by $\Delta\phi$. Modified from Oliveira et al. (2021). 94

5.2 Different radius for the solid spheres used to generate the initial porosity fields of sample Het. 1, 2 and 3. The porosity in the regions where the spheres are located is set to zero. The spheres are uniformly distributed in the domain and allowed to overlap. The mean radius for (a) Het. 1 is $\langle r_1\rangle = 1.5 \times 10^{-3}$ m, for (b) Het. 2 $\langle r_2\rangle = 3.0 \times 10^{-3}$ m and for (c) Het. 3 $\langle r_3\rangle = 4.5 \times 10^{-3}$ m, and the standard deviation for radius is $\sigma_{r1} = \sigma_{r2} = \sigma_{r3} = 0.2$. 96

5.3 Initial non-zero porosity distribution for Het. 1, 2 and 3. The mean porosity value for Het. 1 is $\langle\phi_1\rangle = 0.29$, for Het. 2 is $\langle\phi_2\rangle = 0.25$ and for Het. 3 is $\langle\phi_3\rangle = 0.17$. The more homogeneous sample Het. 1 has a larger peak at $\phi = 0.3$, whereas the other samples are characterized by the tail of the distribution towards lower values of porosity. 97

5.4 Initial permeability distribution for Het. 1, 2 and 3. The porosity-permeability correlation factors are defined in equation (5.2) and listed in table 5.1. The mean permeability value for Het. 1 is $\langle K_1\rangle = 1.69$ D, for Het. 2 is $\langle K_2\rangle = 3.15 \times 10^2$ mD and for Het. 3 is $\langle K_3\rangle = 4.50$ mD. The heterogeneity of the samples extends the tail in the permeability distribution to lower-end values. . . . 97

5.5 Initial porosity fields (a) to (c) and the corresponding calculated pressure fields for (d) to (f) respectively for Het. 1, 2 and 3. The porosity field is constructed using zero porosity inclusions in a background porosity field of $\langle\phi\rangle = 0.3$ as showed in figure 5.2. The calculated pressure reflects the initial heterogeneity of the sample, gradually increasing the local pressure differences from Het. 1 to 3. 98

5.6 Normalized velocity distribution for the different samples. The shape of the normalized velocity distribution shows a sharp peak at $v_x/\langle v_x \rangle = 1$ with a narrow velocity distribution for Het. 1. In contrast, Het. 2 and 3 have a much wider distribution with a smeared-out tail towards lower velocity values. The inset shows the same distributions but without the log-log transformation. . 99

5.7 Normalized particle breakthrough (continuous lines) and the ADE best-fit using equation (2.8) (dashed lines) for each individual heterogeneity and $Pe = 0.0542$, 0.542 and 5.42. As the sample heterogeneity increases, the particle breakthrough departs from the ADE equation (2.8) model, and this effect increases as the Péclet number increases. 100

5.8 Initial particle propagators for Het. 1, 2 and 3 at $t/t_1 = 0.5$ and $t/t_1 = 1.0$, and Péclet numbers of $Pe = 0.0542$ (a) and (b), $Pe = 0.542$ (c) and (d) and $Pe = 5.42$ (e) and (f). As Pe increases, the contrast between the faster and the slower moving particles increases, showing a peak at $\zeta/\langle\zeta\rangle = 0$. The cut-off at the higher end of the Het. 3 is due to the particles exiting the domain, and making them unavailable for the calculation. 101

5.9 Longitudinal dispersion coefficient versus Péclet number. Numerical results for Het. 1, 2 and 3 and experimental measurements on beadpacks and sandpacks from Bijeljic et al. (2004) using the sources of Pfannkuch (1963), Seymour and Callaghan (1997), Kandhai et al. (2002), Khrapitchev and Callaghan (2003) and Stöhr (2003). 103

5.10 Dissolution-induced porosity of the different samples at $t/t_1 = 1$ for Het. 1 using $\beta = 1.8$, Het. 2 using $\beta = 1.2$ and Het. 3 $\beta = 0.6$, and Péclet numbers of $Pe = 0.0542$, and at $t/t_1 = 10$ for $Pe = 0.542$ and 5.42. Below each row characterised with the same Pe number the results for $\beta = 1.8$ for the same Pe are presented for comparison. The model transport heterogeneity parameter β intensifies the emerging dissolution pattern; the dissolved channels are formed earlier and reach further when compared to $\beta = 1.8$. . 106

5.11 Porosity profiles along the flow direction ($x-$axis) for Het. 1, 2 and 3, and Péclet numbers of (a) $Pe = 0.0542$, (b) $Pe = 0.542$ and (c) $Pe = 5.42$. At low Pe number the dissolution occurs mostly at the inlet, characteristic of a compact dissolution front. For $t/t_1 \ll 1$ porosity increases proportionally to time but the change in porosity reduces and reduction becomes smaller for $t/t_1 \gg 1$. 107

5.12 Histogram of porosity distributions for Het. 1, 2 and 3 with Pe = 0.0542, 0.542 and 5.42 at different normalized advective times t/t_1. Dissolution is fastest in regions of high porosity, as these regions naturally focus flow and the transport of fresh reactants. Lower porosity regions have little to no influence at higher Pe; only when diffusion is significant can such regions experience noticeable dissolution. 108

5.13 Detail of the histogram of porosity distributions for Het. 1 at different normalized advective times t/t_1. The peak in $\phi = 0.3$ is nearly identical for $t/t_1 = 0.5$ and 1.0. We only show the case of Het. 1 and $Pe = 0.0542$ however the same happens for the other cases illustrated in figure 5.12. 108

5.14 Normalized effective reaction rate plotted against $1/\sqrt{t}$ for Het. 1, Het. 2 and Het. 3 respectively and β = 1.8, 1.2 and 0.6, at Pe = 0.0542, 0.542 and 5.42. The effective reaction rate is normalized with the batch reaction rate of calcite (table 5.1). The black solid line is the 1:1 trend, highlighting the power-law scaling of $r_{\text{eff}} \sim t^{-a}$ with $a = 0.5$. The power-law scaling factors a for each sample and Pe is shown in table 5.3. 110

5.15 (Top row) Local ψ functions before ($t/t_1 = 0$) and after (t/t_1 = 10) dissolution defined at the links located near the inlet at $\mathbf{x}_1$ = (0.5, 3.7, 3.0) $\times 10^{-3}$ m and (Bottom row) local ψ functions at $t/t_1 = 10$ at $\mathbf{x}_1$ and near the outlet at $\mathbf{x}_2$ = (12.0, 0.8, 3.0) $\times 10^{-3}$ m, for Het. 1, 2 and 3 at $Pe = 0.0542$ and 5.42. 111

5.16 Particle propagators for Het. 1 with $\beta = 1.8$, Het. 2 with $\beta = 1.2$ and Het. 3 with $\beta = 0.6$ at $t/t_1 = 0.5$ and $t/t_1 = 1.0$, and Péclet numbers of Pe = 0.542. The results are compared against the initial particle propagators from figure 5.8 (dashed lines). 113

5.17 Normalized velocity distributions for the different samples. The lower velocity values contribute to the slow and diffusive only transitions. The high velocity values contribute to the advective dominated transitions, responsible for the highly mobile tails and the formation of dissolution channels. 114

6.1 Domain geometry and the particle representation with the reinjection condition. The domain is filled with $CaCl_2$ in the top half and with Na_2CO_3 in the bottom half, which flow in the positive $x-$direction. To conserve mass, all the produced particles when transitioning beyond the domain $x > L$, are reinjected at $x = 0$. 120

6.2 Conceptual representation of the fluid-fluid reactive system. Particles might contain any distribution of species, but for simplicity this diagram shows particles containing only theoretical species A or B, that produces species C. (a) We start with a distribution of particles with theoretical aqueous species A and B at a given node. (b) At checkpoint times Δt, each node behaves as a batch reactor, mixing and reacting all available species in it. (c) The resulting species C are then distributed among the particles contained in the node. (d) The model proceeds with the particles transitions, when particles either leave with the produced species or arrive with other species. 122

6.3 Initial porosity fields for (a) Het. 1 and (b) Het. 3. The porosity field is constructed using zero-porosity inclusions in the background porosity field of $\langle\phi\rangle = 0.3$ as shown in figure 5.2 and discussed in chapter 5. 123

6.4 Averaged species concentration at the nodes of the lattice of Het. 1 for Ca^{2+}, Na^{+}, NaCl and $CaOH^{+}$ in $z-$direction for Pe = 10 and 100 at $t/t_1 = 1$. Flow is from left to right with the injection of Na_2CO_3 solution at the top and of $CaCl_2$ solution at the bottom. 127

6.5 Averaged species concentration at the nodes of the lattice of Het. 3 for Ca^{2+}, Na^{+}, NaCl and $CaOH^{+}$ in $z-$direction for Pe = 10 and 100 at $t/t_1 = 1$. Flow is from left to right with the injection of Na_2CO_3 solution at the top and of $CaCl_2$ solution at the bottom. 128

6.6 Average concentration of NaCl along the flow direction for Péclet number of (a) Pe = 10 and (b) 100 at $t/t_1 = 1$. As the system becomes more advective, mixing becomes less efficient and the production of NaCl is reduced. 129

6.7 Change in the concentration of NaCl for Péclet number of Pe = 10 and 100 over (a) normalized time and the (b) departure from equilibrium concentration. At early times the increase in the change in concentration is constant but then sharply reduces. The increase in the change in concentration is weakly dependent on the concentration when far from equilibrium. 129

6.8 Conceptual representation of the fluid-solid reactive system. Particles might contain any distribution of species, but for simplicity this diagram shows particles containing only theoretical mineral species A and aqueous species B, that produces species C. (a) We start with a distribution of particles with theoretical aqueous species B and nodes with solid species A. (b) At checkpoint times Δt, each node behaves as a batch reactor, mixing and reacting all available species in it. (c) The total porosity in the node is then updated to reflect the dissolved species from the solid phase of the nodes to the aqueous species, and the resulting species in the aqueous phase are then distributed among the particles contained in the node. (d) The model proceeds with the particles transitions, when particles either leave with the produced species or arrive with other species. 132

6.9 Molar concentrations of calcite and dolomite averaged perpendicular to the flow in 3D lattice network having physical heterogeneity Het. 3. The concentration of calcite and dolomite was randomly distributed over the domain following a 3:1 and 1:3 ratio. 134

6.10 Dissolution induced fluid-solid surfaces for both cases with the ratio of the distribution of calcite to dolomite of (a) 3:1 and (b) 1:3. The dissolution front in the case with the higher concentration of calcite reaches further, since for the case (b), dolomite acts as a shield to the reactive front. 135

6.11 Porosity, calcite and dolomite mean volumetric fraction along the flow direction at the initial state (dashed line) and the final state (continuous line), for both cases with the ratio of the distribution of calcite to dolomite of (a) 3:1 and (b) 1:3. For both cases the majority of the sample inlet is dissolved, but more effectively in the case with the higher calcite content. 136

6.12 Effective reaction rates related to the total mineral volume of the sample, the fast flowing channels and slow regions, for both cases with the ratio of the distribution of calcite to dolomite of (a) to (c) 3:1 and (d) to (f) 1:3. At late times, in the case of calcite to dolomite ratio 1:3 the reaction rate of dolomite in fast flowing channels is higher than that of calcite due to dolomite shielding calcite from the reactant supply. 138

6.13 Histograms showing the initial and the final proximity to the fast flowing channels and to slow regions, for both cases with the ratio of the distribution of calcite to dolomite of (a) to (d) 3:1 and (e) to (h) 1:3. 140

7.1 Idealized graph upscale from pore-scale to core-scale. The motivation behind this approach is to model a core-scale domain as if it is composed of several different pore-scale models, each being enough to describe the length-scale of a link in the core-scale. The naming of pore and core-scale is simply to relate to the problems described herein; the same idea can be implemented from any fine to coarser models. 146
7.2 Upscaling concept from a given original scale to two upscaling steps up. At each face Γ of the subdomain Ω we can observe the breakthrough of particles and characterize it accordingly. 147
7.3 Different ψ fits using a truncated power-law function for ψ and a composite ADE combining two different distributions. There is a high degree of error at larger times and the model fails to perform as well as expected, when using a single ψ function. Using of a composite ψ intends for better adjustment of the transit-time distribution, specially for the particles arriving at late times. . . 148

A.1 Comparison between (a) the numerical Laplace Transform Inversion algorithms of Gaver (1966) and Stehfest (1970) and Hoog et al. (1982) and the analytical solution of the function $f(t) = e^t$ (b) and the error between the analytical solution and the numerical methods. 179

B.1 Illustration of the procedure to create the samples Het. 1, 2 and 3. We start with (a) a 3D image with background porosity, (b) sample the radius and centres of several solid spheres, (c) use it to remove porosity from the background porosity image, (d) the original lattice with nodes centres coincident with the 3D image cell centres, (e) the highlighted nodes that will be modified, and finally (d) the lattice with the porosity of the nodes mapped from the 3D image with the removed porosity. 181

C.1 Porosity dissolution of Het. 1, 2 and 3 with $\beta = 1.8$ at $t/t_1 = 1$ to 10 and Péclet number $Pe = 20$. 183
C.2 Porosity dissolution of Het. 1, 2 and 3 with $\beta = 1.8$ at $t/t_1 = 1$ to 10 and Péclet number $Pe = 200$. 184
C.3 Porosity dissolution of Het. 1, 2 and 3 with $\beta = 1.8$ at $t/t_1 = 1$ to 10 and Péclet number $Pe = 2000$. 185

C.4 Comparison of the porosity dissolution of Het. 2 with $\beta = 1.8$ and 1.2 and Het. 3 with $\beta = 1.8$ and 0.6 at $t/t_1 = 1$ to 10 and Péclet number $Pe = 20$. We omit the results of Het. 1 because there are no differences in the transport parameter β. 186
C.5 Comparison of the porosity dissolution of Het. 2 with $\beta = 1.8$ and 1.2 and Het. 3 with $\beta = 1.8$ and 0.6 at $t/t_1 = 1$ to 10 and Péclet number $Pe = 200$. We omit the results of Het. 1 because there are no differences in the transport parameter β. 187
C.6 Comparison of the porosity dissolution of Het. 2 with $\beta = 1.8$ and 1.2 and Het. 3 with $\beta = 1.8$ and 0.6 at $t/t_1 = 1$ to 10 and Péclet number $Pe = 2000$. We omit the results of Het. 1 because there are no differences in the transport parameter β. 188

D.1 Probability density function and cumulative distribution function of the velocity. The vertical line shows the cut-off at 0.75 of the CDF, and all velocities above this value are selected to locate the fast flow channels. 190

List of Tables

1.1 Comparison of sandstones and carbonate reservoir characteristics. Modified from Choquette and Pray (1970) and Ahr (2008). 3

2.1 Longitudinal dispersion regimes from Bijeljic et al. (2004) and Sahimi (2011). With the exception of the transition regime, that does not present a direct relation with Péclet number (Pe) and the restricted diffusion regime that is simply controlled by the porous media tortuosity, each regime can be defined in terms of the Pe number. 16

3.1 Domain properties and parameters used for the domain consisting of spherical inclusion and infinite channel. The properties of each subdomain are different but are kept constant within the subdomains. 59

4.1 Model properties and dissolution parameters. 70
4.2 Ketton carbonate sample properties and dissolution experiment parameters. 73
4.3 Parameters used and the KS-test between the particle propagators and the experimental propagators for different fitted values of β. The value of $\beta = 0.9$ scored the highest KS-test and was selected for subsequent simulations. 82
4.4 Comparison between the geometries of the experimental acquisition and simulated model of the channel formed by dissolution. . 85

5.1 Initial sample properties. All samples are built using the same background porosity and permeability correlation factors, while the main difference is in the size of the distributed solid spheres, where the porosity is set to zero. 95
5.2 Mean initial and final porosity and permeability for the Het. 1, 2 and 3 and $Pe = 0.0542$, 0.542 and 5.42. 105

5.3 Power-law scaling for the effective reaction rate for $Pe = 0.0542$, 0.542 and 5.42 and for samples Het. 1, 2 and 3. The power-law scaling t^{-a} with $a > 0.5$ is a result of the persistence of incomplete mixing. 110

6.1 Initial sample properties. All samples are built using the same background porosity and permeability correlation factors. The molecular diffusion coefficient is considered to be the same for all species. 123

6.2 Composition of the injected fluids at $T = 25\,°C$ and $P = 1\,MPa$. The composition of the injected particles is divided between two halves: the top consisting of Na_2CO_3 solution and the bottom consisting of a $CaCl_2$ solution. At the initial states, there are no particles sharing both a $CaCl_2$ and Na_2CO_3 concentration, and like so no produced species resulting of its reaction: NaCl(aq), $CaCO_3$(aq) and $CaHCO_3{}^+$, are present at $t = 0\,s$. The solution has pH = 10.49 in the top half and pH = 6.43 in the bottom half. 124

6.3 Average molar concentrations of the injected species at the initial state, for the species at an ideal fully-mixed system, and for the advective systems with characteristic Péclet number of Pe = 10 and 100 at $t/t_1 = 1$. The system shows how the advective dynamics contributes to the incomplete mixing of the species, reducing the expected conversion of $CaCl_2$ and Na_2CO_3 into NaCl(aq), $CaCO_3$(aq) and $Ca(HCO_3)^+$. 125

6.4 Composition of the injected fluid ($T = 25\,°C$, $p = 1\,MPa$) at the inlet $x = 0\,m$. 134

6.5 Power-law scaling a (t^{-a}) for the effective reaction rate related to the total mineral volume of the sample, the fast flowing channels and slow regions, for both cases with the ratio of the distribution of calcite to dolomite of 3:1 and 1:3 137

A.1 First 18 coefficients shown with 12 digits precision. The columns runs faster than the rows, such that the elements in the table read as $a_i = a_{\mathrm{row,col}}$, *e.g.* the first and second elements are $a_1 = a_{1,1} = 4.9 \times 10^{-5}$ and $a_2 = a_{1,2} = -6.0 \times 10^{-1}$. 178

A.2 Comparison between the numerical Laplace Transform Inversion using the algorithms developed by Stehfest (1970) and Hoog et al. (1982) for $f(t) = e^t$ and $1 \geq t \leq 10$, ϵ represents the error between the analytical function and the numerical Laplace Transform Inversion algorithms. 179

List of Tables

E.1 List of the used references, the published media and the copyright holders. 191

CHAPTER 1

Introduction

1.1 Reactive Transport in Porous Media

Carbonate rocks hold over 60 % of hydrocarbon reserves (IEA, 2006; Schlumberger, 2007b; BP, 2008) and are considered as potential sinks for carbon storage in aquifers and reservoirs (Bachu, 2003; Metz et al., 2010). Figure 1.1 illustrates the geographical distribution of carbonate reserves.



Figure 1.1: Geographical distribution of carbonate reserves. From Schlumberger (2007a), using data from IEA (2006), Schlumberger (2007b), and BP (2008). Copyright © 2007 Schlumberger. All rights reserved.

Furthermore, reactive transport in porous media is commonly encountered in chemical engineering (*e.g.* packed beds), contaminant hydrology (MacQuarrie and Sudicky, 1990), reactive flow in batteries and fuel cells (Gayon Lombardo et al., 2019), nuclear waste disposal (Kenney et al., 2017), oil recovery (Egbe et al., 2021), carbon storage (Metz et al., 2010), and chemical reactor engineering (Fogler, 1987). In some applications, such as well stimulation by acidization is required, while in others, such as in dissolution-induced compromised well

integrity, reaction is detrimental.

Common to all these applications is that effective reaction rates may depend strongly not only on the nature of the chemical reactants but also on the porous media structure and composition which makes design of reactive processes complex.

Fluid/solid reaction rates depend on the size and the connectivity of the pores, which are associated with flow and transport heterogeneity. In this work we will call this physical heterogeneity. Moreover, the effective reaction rates may depend on the chemical composition of the solid matrix which we will call chemical heterogeneity. Despite its relevance and importance, the impact of physical heterogeneity on reactive transport in porous media is not fully understood. Furthermore, it is well known that reaction rates are scale dependent in geological porous media it is common to have orders of magnitude differences fom pore to field scales (White and Brantley, 2003).

While some recent experimental work has tried to systematically characterize the impact of physical and/or chemical heterogeneity at the pore-scale (Al-Khulaifi et al., 2017; Al-Khulaifi et al., 2018; Al-Khulaifi et al., 2019), more work is needed to address these important phenomena at the continuum scale. In this thesis a new model based on Continuous Time Random Walk (CTRW) has been developed to provide reactive transport predictions in complex porous media having a range of physical and/or chemical heterogeneity.

We selected carbonate rocks to examine in this thesis since they are important for many applications, listed above, where reaction plays a significant role. In principle, the model developed and the concepts applied in this thesis can be applied to any porous media of interest.

1.2 Carbonate Rocks

Carbonate rocks have unique attributes that distinguish them from siliciclastics and therefore require different methods of study (Choquette and Pray, 1970). They are formed within the depositional basin by biological, chemical, and/or detrital processes. Such rocks have a complex pore-scale structure (Blunt et al., 2013; Wildenschild and Sheppard, 2013), with geometrical and chemical features that differ significantly from sandstones (Choquette and Pray, 1970); for instance, the permeability of limestone formations can extend over several orders of magnitude (Clerke, 2009) and have a significant amount of interconnected micro- and macro-porosity (Lin et al., 2016). They largely consist of skeletal remains and other biological constituents that include fecal pellets, lime mud, and microbial mediated cements (Folk, 1959). The most common way to classify carbonate rocks is based on their texture formed by their components and their

Table 1.1: Comparison of sandstones and carbonate reservoir characteristics. Modified from Choquette and Pray (1970) and Ahr (2008).

Characteristics	Sandstones	Carbonates
Primary porosity variance	Low	High
Type of primary porosity	Almost exclusively inter-particle	Inter-particle, intra-particle, inter-crystalline, moldic, vuggy, cavernous, fenestral, or "constructed void"
Type of ultimate porosity	Almost exclusively primary inter-particle	Highly variable owing to different origins or pore types
Typical pore size	Diameter and throat sizes related to depositional texture	Diameter and throat size may not be related to depositional texture
Typical pore shape	Varies with particle shape	From strongly related to totally unrelated to particle shape
Uniformity of pore size and shape distribution	Relatively uniform in homogeneous sand bodies	Fairly uniform to extremely heterogeneous

distributions (Folk, 1959; Dunham, 1962).

Table 1.1 summarizes the differences between sandstones and carbonates. The depositional environment and diagenetic history of such reservoirs also brings the presence of clay minerals (Tosca and Wright, 2015). The environment and diagenesis dictates the pore structure of a carbonate rock, where rock constituents could be sustained by a clay matrix (Terra et al., 2010) or, by dissolution, the same clay could lead to the creation of secondary porosity (Wright and Barnett, 2015). Naturally the complex relations of porosity and permeability ultimately controls the petrophysical characteristics of carbonate reservoirs (*e.g.* Rezende and Pope, 2015).

1.3 Scales of heterogeneity in porous media

In this thesis we will exclusively study carbonate rock consisting of calcite and/or dolomite. However, the model and concepts can be applied to other sedimentary rock.

When studying rocks one common practice is to break it into unit volumes to summarize measurements and observations. Those units are called representative elementary volumes and are extremely useful when defining heterogeneity. Figure 1.2 illustrates different scales of investigation and the elements that can be identified at any individual scale. Each illustration is an idealized representation of the pore, core and field scales. The pore-scale relates to the measurements capable of distinguishing the distribution of pores and grains for mm size samples. The core-scale relates to the measurements made with rock

samples at the cm scale, sufficiently accurate to distinguish textural information of ensemble porous material. The field-scale relates to the distribution of facies and information from well and field data at the km scale.

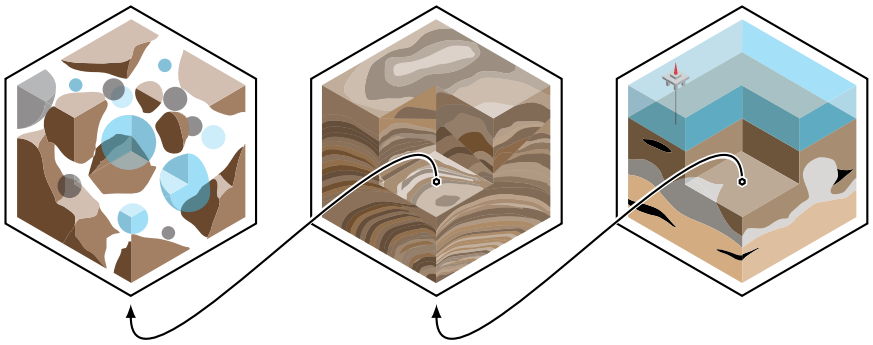


Figure 1.2: Conceptual representations of different scales of investigation. Each illustration is an idealized representation of the pore, core and field scales. The pore-scale relates to the measurements capable of distinguishing the distribution of pores and grains. The core-scale relates to the measurements capable of distinguishing textural information of ensemble porous material. The field-scale relates to facies and information from distribution of well and field data. Modified from Oliveira (2014).

As an example, permeability can be measured at the core-scale using Routine Core Analysis (RCA) or estimated from several techniques such as well logs and well-testing at intermediate scales spanning from the core-scale to field-scale (Boyd et al., 2015). Each of these techniques measures different physical phenomena and estimate permeability at a particular scale of observation. Figure 1.3 illustrates this and how the definition of classes is tied to each individual scale.

By imposing a pressure gradient in a core sample it is possible to estimate permeability using Darcy's Law (Klinkenberg, 1941). Core samples are generally restricted by the amount of available material and integrity of the same, yet they are still considered the ground truth and often used to calibrate other measurements. Nuclear Magnetic Resonance (NMR) logs uses the pore-signal relaxation times to construct pore-size distributions and estimate the permeability (Timur, 1969; Kenyon et al., 1988; Ahmed et al., 1991; Kenyon, 1997). Such measurements are limited to the vicinity of the well and are only capable of characterizing layers of a given formation at a time. Well-test analyses the rate and pressure data during periods of draw-down and build-up to estimate permeability and reservoir pressures (Gringarten, 2012). X-ray tomography measurements on the mm-size rock samples are capable of precisely characterizing the distribution of fluids and minerals controlling residual saturations and

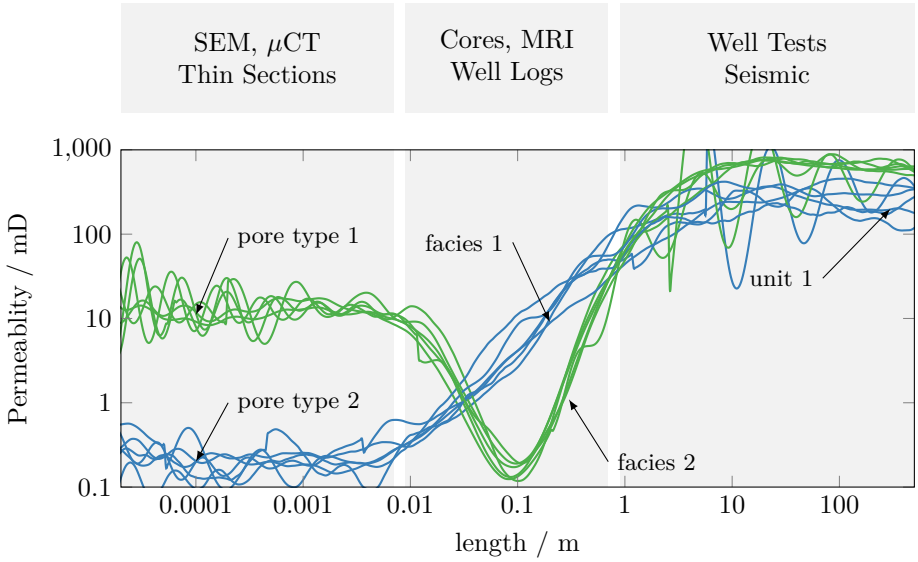


Figure 1.3: Different scales of measurements for permeability estimation as a function of a characteristic length. Each method of measurement is capable of estimating permeability of samples and describing it in terms of different classes. Adapted from Nordahl and Ringrose (2008), Ringrose et al. (2008), and Ringrose and Bentley (2015).

contact-angles (Andrew et al., 2014; Scanziani et al., 2017), but lack features at the field-scale, such as fractures or faults that are orders of magnitude larger and can dominate flow and transport (Warren and Root, 1963; Szymczak and Ladd, 2012; Kuchuk and Biryukov, 2015).

The ability to summarize rock properties in terms of their average behaviour or classes of homogeneous materials, such as pore-types and reservoir facies, allows for simpler but at times less accurate models. This approach however assumes that non-resolved heterogeneities might not play a significant role on the behaviour predicted by these models.

To develop a model for reactive transport in porous media, an accurate description of flow, transport and chemical reaction is needed. We will now briefly demonstrate that even for transport only, the complexity in porous media structure at different scales requires the use of sophisticated models, such as the CTRW model employed in this work.

Flow at the pore-scale can be modelled using the incompressible Navier-Stokes equations,

$$\frac{\partial \mathbf{v}}{\partial t} + (\mathbf{v} \cdot \nabla)\,\mathbf{v} - \frac{\mu}{\rho}\nabla^2 \mathbf{v} = -\mu \nabla P + \mathbf{f}_b \tag{1.1}$$

where $\mathbf{v}$ is the velocity of the fluid, μ is the viscosity and ρ the density of the

fluid, P is the imposed pressure, and $\mathbf{f}_b$ are the imposed body forces *e.g.* gravity and magnetic forces. The transport of different species at the pore-scale is then modelled by the Reaction-Advection-Diffusion equations,

$$\frac{\partial c}{\partial t} + \mathbf{v} \cdot \nabla c - D\nabla^2 c = R, \tag{1.2}$$

where c is the species concentration, D is the molecular diffusion coefficient and R is the sink or source term related to the reaction of the species. A negative value of, $R < 0$, models the consumption of species in the domain, and a positive value of, $R > 0$, models the production of species in the domain.

At the next larger scale, termed continuum or Darcy scale flow is modelled by using (Bear, 1972; Vafai, 2015) Darcy's Law (Darcy, 1856),

$$\mathbf{q} = -\frac{K}{\mu}\nabla P, \tag{1.3}$$

shown here ignoring gravity, where q is the flux, μ is the viscosity of the fluid, K the permeability of the porous media, and ∇P is the pressure gradient imposed in the domain. When accompanied by higher order terms ($\sim \nabla^2\mathbf{v}$), equation (1.3) is called as Brinkman equation (Brinkman, 1949). The flux q relates to the area available for flow A and volumetric flow Q in the relation A with $q = Q/A$, such that equation (1.3) can also be written as

$$\mathbf{Q} = -\frac{KA}{\mu}\nabla P. \tag{1.4}$$

The transport of species at the continuum scale is then described by the Advective-Dispersion Reaction Equation (ADRE)

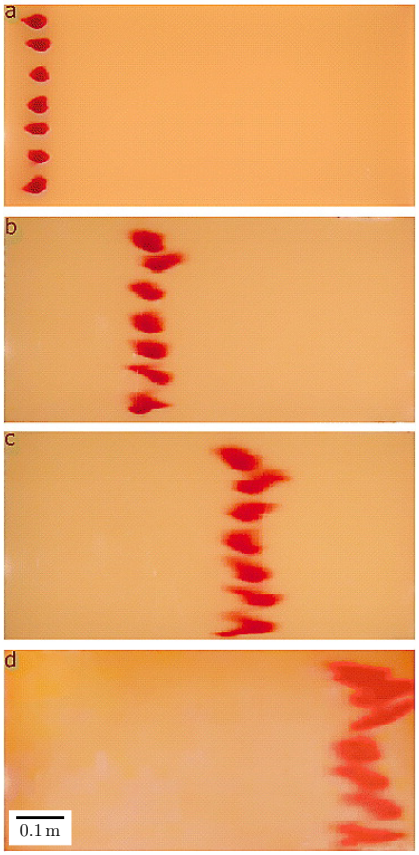
$$\phi\frac{\partial c}{\partial t} + \mathbf{q} \cdot \nabla c - \mathbf{D}\nabla^2 c = R, \tag{1.5}$$

where ϕ is the porosity of the medium, and $\mathbf{D}$ is the dispersion coefficient tensor. The resemblance of the transport equations equation (1.2) and equation (1.5) are immediate, but equation (1.5) often fails to capture the transport behaviour expected of porous media.

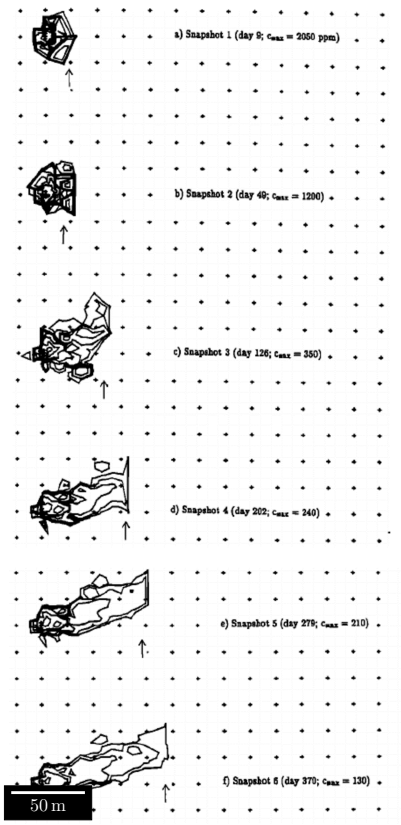
That solutions to equation (1.5) often fail to predict transport adequately has been observed by many authors (Adams and Gelhar, 1992; Raje and Kapoor, 2000; Gramling et al., 2002; Levy and Berkowitz, 2003; Wilson et al., 2004; Berkowitz and Scher, 2009; Dentz et al., 2011; Bijeljic et al., 2011; Berkowitz et al., 2016; De Anna et al., 2014). This is nicely illustrated in figure 1.4 (Adams and Gelhar, 1992; Levy and Berkowitz, 2003), that shows the evolution of a tracer at (a) the laboratory scale in a homogeneous sand pack and at (b) the

field scale in a heterogeneous aquifer. The sandpack of Levy and Berkowitz (2003) was constructed with a controlled grain size and assumed to be uniform, yet the solute breakthrough curve (BTC) and the shape of the plume cannot be modelled using equation (1.5) alone in an equivalent homogeneous domain. Adams and Gelhar (1992) on the other hand, showed that neither at a much larger scale and using averaged grid blocks, the highly distorted BTC for the tracer could not be properly modelled. The inability of Advective-Dispersion Equation (ADE) to model the BTCs can be attributed to non-resolved heterogeneities over different scales.

Averaging techniques aim to incorporate the underlying variability of different fine scale features, *i.e.* volume averaging methods (Quintard and Whitaker, 1994; Whitaker, 1999) were used to account for effective material properties. The usual assumption is that there exists a size L much larger than the size of the under-resolved features l, such that $L \gg l$ is large enough to capture the macroscopic transport behaviour. This assumption is not limited to spatial length-scale alone, but applicable to time-scale as well. The CTRW modelling framework offers a practical approach to this problem (Dentz et al., 2004; Berkowitz et al., 2006) and is the basis of the current work.



(a) Homogenous sandpack (Levy and Berkowitz, 2003). Copyright © 2003 Elsevier Science B.V. All rights reserved.



(b) Heterogeneous aquifer (Adams and Gelhar, 1992). Copyright © 1992 American Geophysical Union. All rights reserved.

Figure 1.4: (a) Injected dye tracer in homogenous sand pack under constant flow (Levy and Berkowitz, 2003), and (b) horizontal contours of maximum concentration in an heterogeneous aquifer (Adams and Gelhar, 1992). Each example shows the occurrence of non-Fickian transport at a different observation scale – with 3 orders of magnitude difference in size. The experiment of Levy and Berkowitz (2003) shows that even at a fully saturated and uniform medium, the dye is distorted away from a symmetrical shape and differently for each injection point. The field scale example of Adams and Gelhar (1992) shows the tracer plume distortion happening with observation wells spaced in a distance smaller than the expected hydraulic conductivity block sizes.

1.4 Objectives

As discussed in section 1.1 the main research questions which have hitherto not been systematically addressed and which will be studied in this thesis are:

i Can we accurately predict reactive transport in porous media at the continuum scale using probabilistic models?

ii How the dissolution-induced pore-scale heterogeneities affect the overall reactive transport behaviour at the continuum scale?

iii What is the impact of physical heterogeneity on effective reaction rates at the continuum scale?

iv What is the impact of coupled physical and chemical heterogeneity on reactive transport in porous media at the continuum scale?

The main objectives are:

1. To develop a novel CTRW based reactive transport model for simulating reactive transport at the continuum scale. Development of the CTRW model is presented in chapters 3 and 4.

2. To validate CTRW reactive transport model against NMR dissolution experiment. The validation is presented in chapter 4.

3. To apply the newly developed CTRW model to systematically study the impact of physical (that is, flow and transport) heterogeneity on effective reaction rates at the continuum scale. The results are presented in chapter 5.

4. To apply the CTRW model to examine the coupled impact of physical and chemical (or mineralogical) heterogeneity on effective reaction rates at their continuum scale. This work is shown in chapter 6.

1.5 Thesis outline

In this chapter we motivated the work on reactive transport in porous media performed in this thesis along with the research questions to be addressed and the main objectives. Chapter 2 will present a literature review, with a focus on reactive transport in porous media, and will describe commonly employed numerical methods used to solve single and multiphase flow and transport problems in groundwater and contaminant hydrology applications. We then pay particular attention to the CTRW framework and its use in the literature further

motivating development of our reactive transport model to address the unresolved problems discussed in chapter 1. Chapter 3 presents the transport model using the CTRW framework by means of discrete particle transitions on a fixed regular lattice. Chapter 4 extends the transport model to account for reaction and presents model validation using NMR experimental data. Chapter 5 tests the predictive capability of the newly developed CTRW reactive transport model to evaluate the impact of physical heterogeneity on the effective reaction rates. In chapter 6 the coupled impact of physical and chemical heterogeneity on the effective reaction rates is examined in detail. Conclusions on the ability of the model to accurately predict reactive transport in porous media in a systematic way are drawn in chapter 7. In the same chapter future work is proposed and discussed.

CHAPTER 2

Literature Review

This chapter starts with the description of the fundamental equations for solute transport in porous media, detailing the variables used and common solutions for concentration plumes and showing the dispersion regimes as a function of dimensionless numbers describing transport conditions. Next, it details previous studies on modelling of reactive transport in porous media, including reaction mechanisms and dissolution patterns in limestones and dolomites. Finally, the available numerical methods that have been used in the past decades to study reactive transport in porous media are reviewed, with a particular focus on highlighting the fundamentals of Continuous Time Random Walk (CTRW). This chapter ends with a summary on the advantages and disadvantages offered by different modelling approaches and the reasons for selection of the CTRW framework for the model developed in this thesis.

2.1 Transport in Porous Media

Mass transport is commonly modelled using Fick's laws (Fick, 1855), that was inspired by the work of Fourier (1822) on diffusion of heat in a conducting body and by Ohm (1827) on the transport of electricity on a conductor, which respectively originated to what is known today as the Fourier and Ohm laws. Fick's first law of diffusion states that the molar flux is proportional to the concentration gradient,

$$\mathbf{J} = -D\nabla c, \tag{2.1}$$

where $\mathbf{J}$ is the molar flux, D the diffusion coefficient and c the concentration.

Fick's second law of diffusion predicts how the concentration changes with

time and is simply an expression of conservation of mass,

$$\frac{\partial c}{\partial t} - D\nabla^2 c = 0. \tag{2.2}$$

Using the continuity equation for an incompressible fluid, $\nabla \cdot \mathbf{v} = 0$, and equation (2.1), we obtain the Advection Diffusion Equation (ADE):

$$\frac{\partial c}{\partial t} + \mathbf{v} \cdot \nabla c - D\nabla^2 c = 0. \tag{2.3}$$

When moving in a microscopic domain, individual particles manifest hydrodynamic dispersion. This results from (a) external forces acting on the liquid, (b) the microscopic geometry of the pore system, (c) molecular diffusion caused by concentration gradients, (d) variations in liquid properties, (e) changes of the tracer's concentration due to chemical or physical processes in the liquid phase, and (f) interactions between liquid and solid phases (Bear, 1972).

Reactive transport is often summarized using dimensionless numbers based on characteristic times. Among those we highlight two of the most common the Péclet (Pe) and Damköhler (Da) numbers, and often the Péclet-Damköhler number. Those numbers use a combination of the following characteristic times

$$\tau_{\text{adv}} = \frac{L}{v} \tag{2.4a}$$

$$\tau_{\text{diff}} = \frac{L^2}{D} \tag{2.4b}$$

$$\tau_{\text{reac}} = \frac{Ln}{r} \tag{2.4c}$$

where L is the characteristic length of the system, v is the characteristic velocity, D is the characteristic diffusion coefficient, r is the characteristic reaction rate and n the characteristic molar density of the system. Using the definitions in equation (2.4), we can further define the Péclet and Damköhler numbers as

$$Pe = \frac{\tau_{\text{diff}}}{\tau_{\text{adv}}} = \frac{Lv}{D} \tag{2.5a}$$

$$Da = \frac{\tau_{\text{adv}}}{\tau_{\text{reac}}} = \frac{r}{vn} \tag{2.5b}$$

$$PeDa = \frac{\tau_{\text{diff}}}{\tau_{\text{reac}}} = \frac{Lr}{Dn} \tag{2.5c}$$

Equation (2.5a) compares the ratio of the time that a certain volume of solute takes to travel a distance L by diffusion τ_{diff} to the time to travel the same length by advection τ_{adv}. For $Pe \ll 1$, diffusion dominates and the solute diffuses faster than it advects through the domain, and for $Pe \gg 1$, the behaviour

is opposite, advection dominates and the solute travels faster than it diffuses. Equation (2.5b) compares the ratio of the time a certain volume of solute takes to react in an ideal batch reactor τ_{reac} to the time to travel by advection τ_{adv}. For $Da \ll 1$ the time τ_{reac} that a given amount of solute takes to react is higher than the time for it to move for another region τ_{adv}, and for $Da \gg 1$ the reactions are assumed to be in equilibrium before the solute is displaced from its original site. Equation (2.5c) has a similar meaning to Equation (2.5b) but comparing the characteristic reaction time τ_{reac} to characteristic diffusion time τ_{diff}, instead of the characteristic advective time.

Equation (2.3) was solved analytically by Ogata and Banks (1961) for an unbounded one dimensional medium and a a fluid with concentration $c = 0$, subjected to an instantaneous point injection with concentration $c = c_0$ at $x = 0$. This forms the following boundary conditions,

$$c(0,t) = c_0;\ t \geq 0, \tag{2.6a}$$

$$c(x,0) = 0;\ x \geq 0, \tag{2.6b}$$

$$c(\infty,t) = 0;\ t \geq 0, \tag{2.6c}$$

leading to the following analytical solution

$$\frac{c}{c_0} = \frac{1}{2}\operatorname{erfc}\left(\frac{1-\xi}{2\sqrt{\xi\eta}}\right) + \frac{1}{2}\exp\left(\frac{1}{\eta}\right)\operatorname{erfc}\left(\frac{1+\xi}{2\sqrt{\xi\eta}}\right) \tag{2.7}$$

where $\xi = vt/x$ and $\eta = D/vx$ are dimensionless parameters, and erfc is the complementary error function. The value of η is inversely proportional to the Pe number, so lower η values represent highly advective regimes and higher η values represent dispersive dominated regimes. Figure 2.1 shows the behaviour of this equation using the previously defined dimensionless terms. As η becomes small, the concentration distribution becomes symmetric around $\xi = 1$, and for larger values of η the second term in equation (2.7) becomes significant and the concentration is asymmetrical. This means that the symmetry in the concentration distribution is more prominent for larger values of D or short distances.

Despite asymmetry, when the system achieves steady-state, or when t is sufficiently large ($t \to +\infty$), equation (2.7) asymptotically becomes symmetrical and it is simplified to

$$\frac{c}{c_0} = \frac{1}{2}\operatorname{erfc}\left(\frac{1-\xi}{2\sqrt{\xi\eta}}\right). \tag{2.8}$$

At this limit, Orlob and Radhakrishna (1958) showed the validity of equation (2.8) using transport experiments in a beadpack and a sandpack, as shown in figure 2.2.

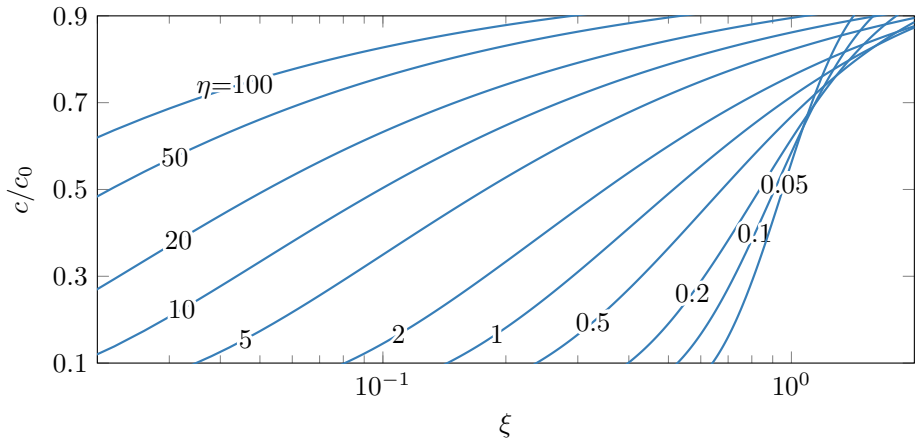


Figure 2.1: Solution for the one-dimensional form of the Advective-Dispersion Equation (ADE) as defined in equation (2.7) for different parametrizations $\eta = D/vx$ (Ogata and Banks, 1961). The value of η is inversely proportional to Pe, so lower η values represent highly advective regimes and higher η values represent dispersive dominated regimes.

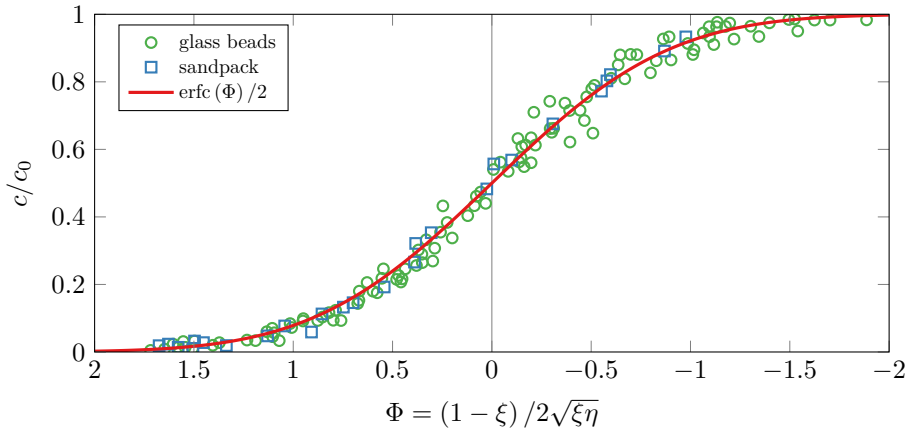


Figure 2.2: Comparison of equation (2.8) and the experimental data present in Orlob and Radhakrishna (1958) for tracer breakthrough in a bead pack and a sandpack.

Other processes, such as electrochemical migration and diffusion in concentrated solutions, where Fick's laws is not strictly applicable are not part of this study and are not going to be listed here but are properly presented in Steefel and Maher (2009).

The longitudinal dispersion coefficient D_L is obtained from the variance of the distance travelled by the solute (Bijeljic et al., 2004)

$$D_L = \frac{1}{2}\frac{d\sigma_L^2}{dt}, \tag{2.9}$$

where σ_L^2 is the variance of the particle displacements along the longitudinal direction. The asymptotic value of the longitudinal dispersion coefficient is obtained when the change in the longitudinal variance is nearly constant.

Aris (1956) showed that the dispersion coefficient for a tube of any shape is given by

$$\frac{D_L}{D_m} = 1 + \delta_s \left(\frac{l_s V_m}{D_m}\right)^2 \tag{2.10}$$

where l_s is the characteristic length scale of the tube and δ_s is the shape factor based on the cross section of the tube.

The behaviour of the longitudinal dispersion coefficient is fit by the empirical relation (Bijeljic et al., 2004),

$$\frac{D_L}{D_m} = \frac{1}{F\phi} + \alpha Pe + \beta Pe^{\delta} + \gamma Pe^2, \tag{2.11}$$

The first term is related to low Pe numbers, and dependent only on the formation resistivity factor F and porosity ϕ, the second represents mechanical dispersion, the third accounts for dispersion due to diffusion form the boundary layers, and the fourth accounts for hold-up dispersion. Equation (2.11) is similarly defined for transverse dispersion (Bear, 1972; Bijeljic and Blunt, 2007; Boon et al., 2016).

There are four dispersion regimes for laminar flow (Bijeljic et al., 2004; Sahimi, 2011): 1. Restricted diffusion; 2. Transition; 3. Power-law; 4. Mechanical dispersion. With the exception of the transition regime, $0.3 < Pe < 5$, that does not present a direct relation with Péclet number (Pe) and the restricted diffusion regime, $Pe \ll 1$, that is simply controlled by the porous media tortuosity, each regime can be defined in terms of Pe shown in table 2.1. Transversal dispersion regimes are similarly defined and were studied by Bijeljic and Blunt (2007), Delgado (2007), and Boon et al. (2016).

Table 2.1: Longitudinal dispersion regimes from Bijeljic et al. (2004) and Sahimi (2011). With the exception of the transition regime, that does not present a direct relation with Pe and the restricted diffusion regime that is simply controlled by the porous media tortuosity, each regime can be defined in terms of the Pe number.

	Dispersion Regime	Pe	Model
1	Restricted diffusion	$\mathrm{Pe} \ll 1$	$D_L/D_m = 1/F\phi$
2	Transition	$0.3 < \mathrm{Pe} < 5$	—
3	Power-law	$5 < \mathrm{Pe} < 300$	$D_L/D_m = \beta\,\mathrm{Pe}^{\delta}$
4	Mechanical dispersion	$\mathrm{Pe} > 300$	$D_L/D_m = \alpha\,\mathrm{Pe}$

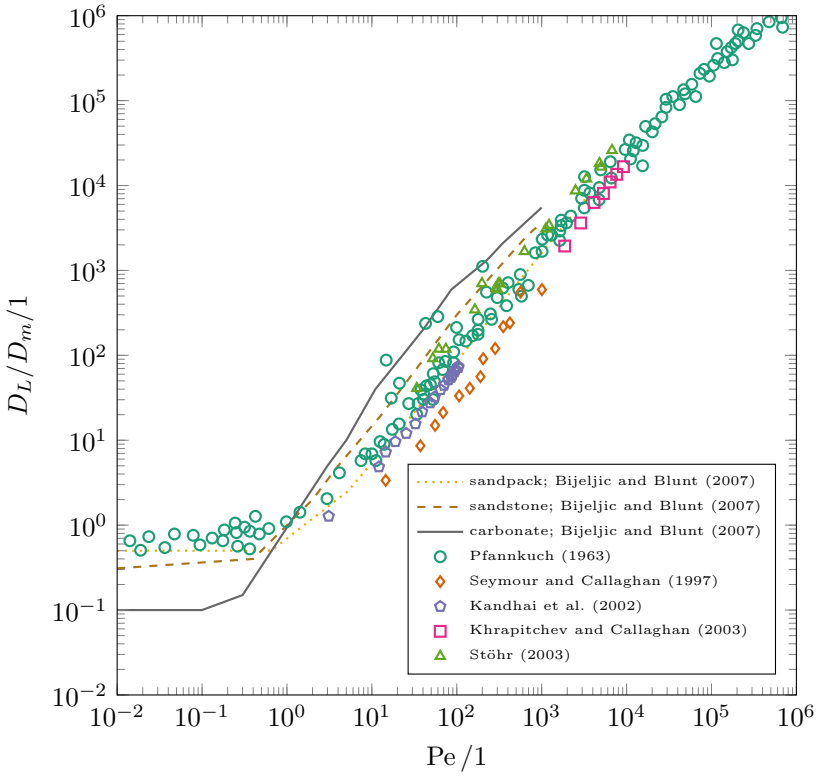


Figure 2.3: Longitudinal dispersion coefficient versus Péclet number. Numerical results for a synthetic sandpack, sandstone and carbonate from Bijeljic et al. (2004) and experimental measurements from Pfannkuch (1963), Seymour and Callaghan (1997), Kandhai et al. (2002), Khrapitchev and Callaghan (2003) and Stöhr (2003). Copyright © 2004 by the American Geophysical Union. All rights reserved.

2.1.1 Anomalous Transport

Despite the success of models of dispersion based on the ADE, there are several examples of anomalous, or non-Fickian, transport in laboratory experiments and field-scale tracer studies. This is interpreted as the inability of capturing experimental observations with solutions using averaged macroscopic parameters, deviating from analytical solutions, such equation (2.8) (Bear, 1972). Generally the interplay between mixing and spreading mechanisms at different scales leads to anomalous transport (Silliman and Simpson, 1987), characterized by the non-linear growth of particle variance in time.

Silliman et al. (1987) investigated the mechanisms that causes anisotropy in the longitudinal dispersion coefficient using two sand boxes with controlled conductivity and sodium chloride as a tracer. The authors suggested that the mechanisms are strongly linked to the hydraulic anisotropy tensor. Levy and Berkowitz (2003) observed subtle, but measurable differences in breakthrough curves (BTCs) between what was observed and analytical solutions of the one-dimensional ADE even in a homogeneous sandpack. The curves were then successfully fitted using the CTRW formulations, which will be presented mathematically later, and the authors reinforced the idea that there are no completely homogeneous formations. Sidle et al. (1998) presented a tracer breakthrough data of a fractured till in Funen, Denmark. The hydraulic properties of the fractured layers were unknown, making it difficult to quantify the tracer transport using traditional tools. Motivated by this and by the observed BTCs, Kosakowski et al. (2001) employed the CTRW framework to overcome such problems. They showed that CTRW model was able to capture the non-Fickian behaviour, and performed better than a conceptual discrete fracture model.

2.2 Reactive Transport in Porous Media

If we now consider the simple reactions that simultaneously take place with transport, we can examine the equilibrium and kinetics of the desired system. Williams et al. (1970) generalized the reactions of an acid with calcium carbonates as

$$2\,H^+ + CaCO_3 \rightleftharpoons CO_2 + Ca^{2+} + H_2O \tag{2.12}$$

They showed a procedure to measure reaction rates as well as the solution for an arbitrary kinetic model based on Duhamel's theory. The authors noted that most measurements had involved static experiments, in which a cube of limestone was in contact with an unstirred acid. Due to this, such experiments were mass transfer-limited and indicated first-order reaction regardless of the true order of the surface reaction processes.

Nierode and Williams (1971) used the observations of Williams et al. (1970) to determine the kinetic model of the reaction of hydrochloric acid and limestones. They designed their experiment in such a way that they could accurately measure the reaction rate at the surface of the rock and that their measurement was independent of mass transfer rate. The results were then used to support design of acid and acid-fracturing treatments.

The dissolution rates of limestones and dolomites differ significantly. The dissolution process in limestones is mass-transfer limited when $T > 0\,^{\circ}\mathrm{C}$ (Lund et al., 1973) and for dolomites reaction-limited when $T < 50\,^{\circ}\mathrm{C}$ (Lund et al., 1975). The reaction stoichiometry for limestones and dolomites are respectively given by:

$$\mathrm{CaCO_3} + 2\,\mathrm{H^+} \rightleftharpoons \mathrm{CO_2} + \mathrm{H_2O} + \mathrm{Ca^{2+}} \tag{2.13a}$$

$$\mathrm{CaMg[CO_3]_2} + 4\,\mathrm{H^+} \rightleftharpoons 2\,\mathrm{CO_2} + 2\,\mathrm{H_2O} + \mathrm{Ca^{2+}} + \mathrm{Mg^{2+}} \tag{2.13b}$$

Plummer et al. (1978) studied the dissolution of calcite in a CO_2-water system at different temperatures and pressures. Their results indicated three simultaneous mechanisms of reaction,

$$\mathrm{H^+} + \mathrm{CaCO_3} \rightleftharpoons \mathrm{Ca^{2+}} + \mathrm{HCO_3^-} \tag{2.14a}$$

$$\mathrm{H_2CO_3} + \mathrm{CaCO_3} \rightleftharpoons \mathrm{Ca^{2+}} + 2\,\mathrm{HCO_3^-} \tag{2.14b}$$

$$\mathrm{H_2O} + \mathrm{CaCO_3} \rightleftharpoons \mathrm{Ca^{2+}} + \mathrm{HCO_3^-} + \mathrm{OH^-} \tag{2.14c}$$

The authors observed that for fixed temperature and CO_2 partial pressure, the reaction rate is described by

$$r = k_1\alpha_{\mathrm{H^+}} + k_2\alpha_{\mathrm{H_2CO_3}} + k_3\alpha_{\mathrm{H_2O}} - k_4\alpha_{\mathrm{Ca^{2+}}}\alpha_{\mathrm{HCO_3^-}}, \tag{2.15}$$

where k_i are the first order rate constants and α_i the bulk fluid values for the activities of the species. Like the study of Berner and Morse (1974), the authors found it convenient to separate the system in three different regimes:

1. independent of $P_{\mathrm{CO_2}}$, depending only on pH;
2. function of $P_{\mathrm{CO_2}}$ and the pH;
3. calcium precipitation starts affecting the system.

Their study used a more thorough investigation and confirmed the initial observations of Berner and Morse (1974).

Busenberg and Plummer (1982) studied the dissolution of dolomite samples at different $P_{\mathrm{CO_2}}$, temperatures and pH from $0-10$. The results showed that the

dissolution is independent of the stirring rates and followed the chemical heterogeneous reactions of Plummer et al. (1978) in equation (2.15). The authors recognized two stages of dissolution: one brief non-stoichiometric dissolution, and a stoichiometric dissolution controlled by three parallel reactions, two of which with half order with respect to H^+ and H_2CO_3, and a constant rate in the absence of the same. The order of the studies was later contested by Chou et al. (1989), that also found a fractional order but of value 0.75.

Compton et al. (1989) conducted an experiment to study the dissolution of calcite with high mass transport under the influence of three strong acids, all with pH < 4. The authors demonstrated that under these circumstances the system can be properly modelled by a first-order heterogeneous reaction,

$$r = k_1 \alpha_{H^+}. \tag{2.16}$$

Peng et al. (2015) carefully studied the dissolution of calcite in HCl and CO_2-water systems to avoid mass-transfer limitations and keep it far from equilibrium. The authors measured reaction rates over a range of pressures, temperatures and pH. Later in Peng et al. (2016), the authors measured the rates of dissolution for Ketton and North-Sea chalk under reservoir conditions. We will use these results in our modelling studies later.

Hoefner and Fogler (1988) visualized the channel formation in limestones and dolomites samples by casting a metallic alloy in the opened spaces. They showed the rates of channel formation and growth as a factor of the fluid velocity and reaction rates, in both the experiments and a simplified pore-network model. Later Daccord et al. (1993) took the observations further in order to model the dissolution patterns named as wormholing phenomena. The authors described the flow properties of the wormhole in terms of its equivalent size, and studied the influence of flow rates and the acid capacity. They recognized that more parameters are needed in order to completely describe the system. Bazin (2001) developed a laboratory method for measurement of matrix-fracture systems under dissolution, and evaluated the impact of a more complete set of parameters in the emerged dissolution patterns. Under similar conditions, Swoboda-Colberg and Drever (1993) observed the effective reaction rates with two orders of magnitude differences between the lab and field study. Our model will also be able to identify different dissolution regimes and quantify the difference between effective and batch reaction rates.

Fredd and Fogler (1998) showed the influence of wormhole formation on transport properties, including the dependence of Damköhler number. The experimental system was composed of HCl core-flooding under several flow conditions, for two different acids, and constructed Pore Volumes to Breakthrough

(PV_{BT}) graph, in figure 2.4. Figure 2.5 shows the increase in channel branching of the wormholes with the decrease of the Damköhler number. The figure also highlights the amount of PV_{BT} needed to achieve each pattern.

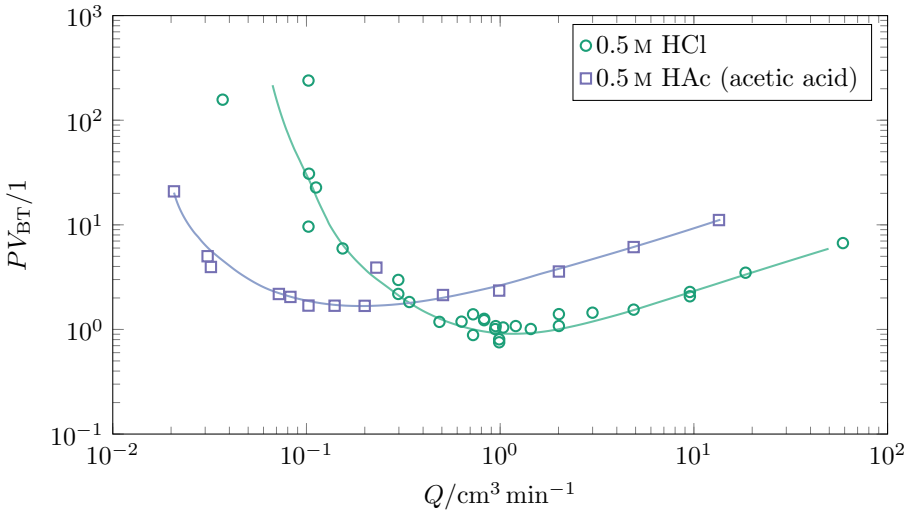


Figure 2.4: Relationship between the injection rate Q and the required number of pore volumes to breakthrough the sample PV_{BT} for hydrochloric acid and acetic acid. The optimum injection rate is given at the minimum PV_{BT}. Despite modelled to have the same acid capacity, HAc outperformed HCl for those given conditions. From Fredd and Fogler (1998). Copyright © 1998 American Institute of Chemical Engineers. All rights reserved.

Golfier et al. (2002) tested the ability of Darcy-scale models to describe dissolution regimes, in particular to wormhole formation, and extended the diagram presented by Fredd and Fogler (1998) using a combination of and $Pe - Da$, as in figure 2.6. This diagram indicates the expected dissolution patterns for a sample under flow and transport of an acidic solution. We show later that our model can successfully predict the compact dissolution pattern and a preferentially channelized pattern.

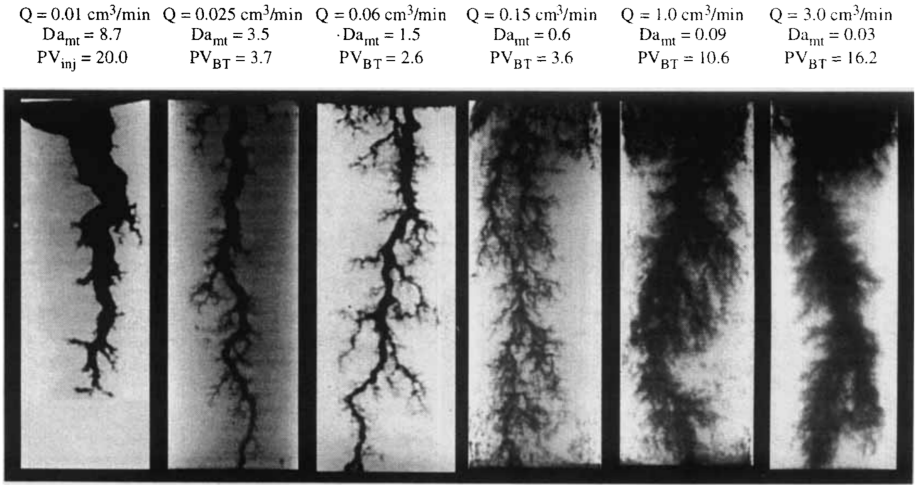


Figure 2.5: Neutron raiographs of different limestone dissolution patterns using a 0.25 mol dm^{-3} EDTA and pH 4 from Fredd and Fogler (1998). The experiments showed the increasing channel branching in wormholes with the decreasing Damköhler numbers. Copyright © 1998 American Institute of Chemical Engineers. All rights reserved.

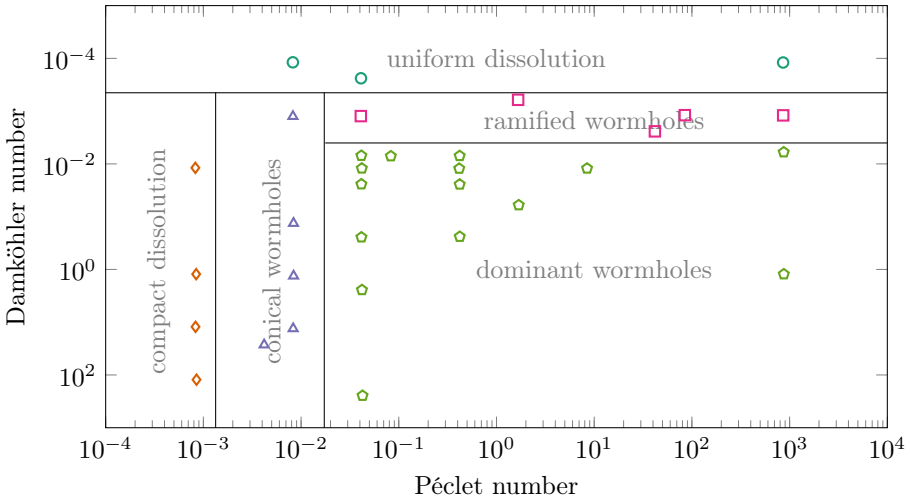


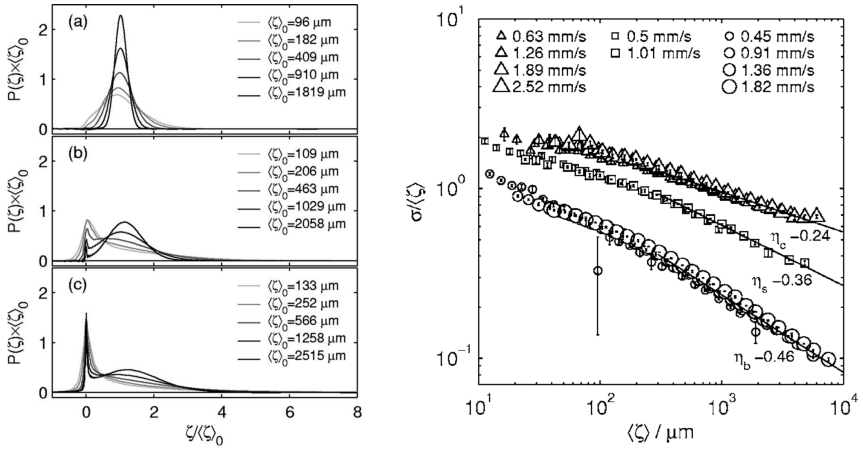
Figure 2.6: $Pe - Da$ diagram showing the boundaries between different dissolution regimes. The diagram highlights the Pe-dependence when transitioning from the regimes of compact dissolution, conical wormholes and dominant wormholes, and the Da dependence when transitioning from the regimes of uniform dissolution, ramified wormholes and dominant wormholes. Extracted from Golfier et al. (2002). Copyright © 2002 Cambridge University Press. All rights reserved.

2.3 Impact of Heterogeneity on Reactive Transport

The physical heterogeneity of porous media impacts flow fields and the solute transport and distribution throughout the medium. The recognition of a wide span in the porosity distributions and hence physical heterogeneities often motivates the improvement of numerical models to properly model transport in porous media (Pereira Nunes et al., 2015; Bultreys et al., 2015; Weishaupt et al., 2019; Ferreira et al., 2020). We will show that it is possible to model unresolved physical heterogeneity with the usage of a Truncated Power-Law (TPL) model and the fitted transport heterogeneity parameter β. Molecular displacements, or flow propagators, measured by Nuclear Magnetic Resonance (NMR) define the motion of molecules in a given domain (Callaghan, 1993; Seymour and Callaghan, 1997) and are reliable measurements for non-Fickian dispersion in porous media (Scheven et al., 2005a). We will compare our model predictions with NMR measurements in this thesis.

Inspired by the results of Seymour et al. (2004) with NMR molecular displacements, Scheven et al. (2005a) studied the NMR molecular displacements as an indicator of heterogeneity in three samples: a beadpack, a sandstone and a carbonate, to study porous materials from a low to a high level of heterogeneity. They subjected each of those samples to different flow conditions ($Pe \in [20, 80]$) and used different observation times to estimate the pre-asymptotic transport behaviour of the solute in those samples. Figure 2.7 shows the NMR molecular displacements and the variance of the displacement. The molecular propagators show a degree of asymmetry at early times, even for the beadpack which is regarded as a homogenous medium. For the sandstones and carbonates, there is a significant and persistent stagnant zone – that is particles that do not move. The authors showed that asymptotic, or Fickian, transport behaviour was not met for any of the samples. They also observed that the displacement variance increases with the pore-space heterogeneity.

The complex arrangement of pores and grains subject solute transport to a wide range of velocities; this is larger in carbonate samples compared to sandstones and bead packs in most cases (Blunt et al., 2013; Bijeljic et al., 2013a; Bijeljic et al., 2013b). To explain the asymmetrical shape of the molecular propagators of carbonates, Bijeljic et al. (2013b) studied six carbonate samples. They showed that due to the highly complex connectivity of carbonates, there is a significant contrast between flow regions in a sample. Figure 2.8 shows the (a) molecular distribution of two of the carbonate samples and breaks down the (b) Probability Density Function (PDF) of the normalized velocity into differ-

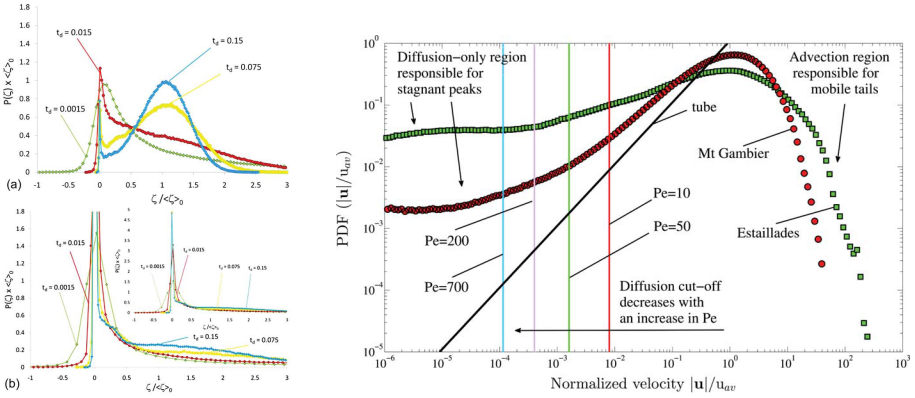


(a) Molecular propagators normalized by the mean displacement $\zeta/\langle\zeta_0\rangle$ for (a) a beadpack, (b) a sandstone, and (c) a carbonate sample.

(b) Displacements variance $\sigma/\langle\zeta\rangle$ vs mean displacement $\langle\zeta\rangle$, for a beadpack (circles), sandstone (squares) and carbonate (triangles).

Figure 2.7: The results for molecular displacements obtained by NMR showing the (a) molecular propagators and (b) normalized displacement variance. There is a significant amount of stagnant zones, showed by $\zeta/\langle\zeta_0\rangle = 0$. The displacement variance increased with the sample heterogeneity and no sample has achieved the asymptotic, or Fickian, transport behaviour. From Scheven et al. (2005a). Copyright © 2005 American Institute of Physics. All rights reserved.

entiate physical phenomena contributing to each segment of the distribution. The advection-dominated regions, for $|\mathbf{u}|/u_{av} \gg 1$, contributes to the fast mobile tails seen in the molecular propagators at $\zeta/\langle\zeta_0\rangle \gg 1$. The diffusion-only regions, for $|\mathbf{u}|/u_{av} \ll 1$, are responsible for the stagnant regions seen in the molecular propagators at $\zeta/\langle\zeta_0\rangle = 0$. The higher velocity probability of Estaillades when compared to Mt. Gambier, for the diffusion-only regions is also reflected by the larger stagnant region in the molecular propagator.



(a) Evolution of the molecular displacement $P(\zeta)$ (a) Mt Gambier and (b) Estallaides.

(b) Advection and diffusion contributions to the normalized velocity distribution of Mt Gambier and Estaillades limestones.

Figure 2.8: The evolution of (a) molecular displacement distributions and the (b) normalized PDF of velocities for Mt Gambier and Estallaides limestones. The advection-dominated regions, at $|\mathbf{u}|/u_{av} \gg 1$, contributes to the fast mobile tails seen in the molecular propagators distribution at $\zeta/\langle\zeta_0\rangle \gg 1$. The diffusion-only regions, at $|\mathbf{u}|/u_{av} \ll 1$, are responsible for the stagnant regions seen in the molecular propagators at $\zeta/\langle\zeta_0\rangle = 0$. From Bijeljic et al. (2013a). Copyright © 2013 American Geophysical Union. All rights reserved.

Measuring molecular propagators can be time-consuming for dynamic systems, so under-sampling methods have been developed to accelerate the acquisitions – such as non-uniform sampling (Scheven et al., 2005b; Mitchell et al., 2008) and compressed sensing (Paulsen et al., 2011). Colbourne et al. (2016) developed a technique that significantly speeds up the recordings which enabled observation of the temporal evolution of the flow propagators during a dissolution experiment. This enabled the study of the impact of dissolution processes in the stagnant regions of a limestone by Muljadi et al. (2018). The authors also observed the change of the fitted transport heterogeneity parameter β as a proxy of the porous media heterogeneity change by dissolution. We will use this dataset in the work presented in this thesis.

Chemical heterogeneity and the effects it has on species transport, are dif-

ficult to isolate from the impacts of the physical heterogeneity in the initial pore structure. There exists a time-dependent effect such that at early-times physical heterogeneity can increase solute spreading but not mixing (Kitanidis, 1994; Dentz et al., 2011), and also a spatial-dependent effect which when observing larger scales shows a reduction of the effective reaction rate (Li et al., 2008). Noiriel et al. (2009) studied the changes in the surface area of limestone induced by dissolution, and showed that even for a pure calcite sample, the arrangement of calcite in micrite grains and sparite cements significantly controlled the surface area evolution of the samples. Black et al. (2015) showed the high uncertainty in the kinetic model parameters that leads to reaction rates spanning over several orders of magnitude. Smith et al. (2013) investigated the response to partial pressures of a CO_2-saturated brine and the initial pore structure and ratios of calcite to dolomite. Salehikhoo and Li (2015) constructed composites of different porous materials to study the dissolution of chemically heterogeneous rock samples in a controlled and systematical way. The authors conducted a series of experiments with different distributions of magnesite at different flow rates, and observed that its spatial distribution has negligible effects on the reaction rates at low velocities but that the effect was significant at higher velocities.

By using a Micro Computed Tomography (μCT) and Scanning Electron Microscope (SEM) several researchers have studied pore-scale processes during dissolution. The results of Menke et al. (2018) and Al-Khulaifi et al. (2018) showed that channel formation and evolution are strongly influenced by the initial pore structure heterogeneity and flow rate, while Singh et al. (2018) showed how intra-granular porosity can affect the dissolution patterns by increasing the pore connectivity of the sample. They showed that in heterogeneous media, rather than there being a uniform dissolution regime at low Da, see figure 2.6, preferential dissolution channels form. We will show the same phenomenon in our simulations. Al-Khulaifi et al. (2019) conducted a series of experiments with different initial flow velocities and chemical heterogeneity, but using a carbonate sample consisting of dolomite and calcite in a 8 : 1 ratio. The authors quantified the impact of physical and chemical heterogeneity using the mineral reactants proximity to the fast flow channels. Figure 2.9 shows the effective reaction rates for calcite and dolomite related to the fast and slow flow regions. The authors observed that the effective reaction rate significantly decreases after the channel is formed, when calcite became shielded by dolomite. The reaction rate decrease for calcite was higher than for dolomite and when near fast-flowing channels the reaction rate of dolomite was even higher than of calcite. This is attributed to the mineral distribution and chemical heterogeneities of the samples. We will study this system later when we assess the effect of chemical heterogeneity.

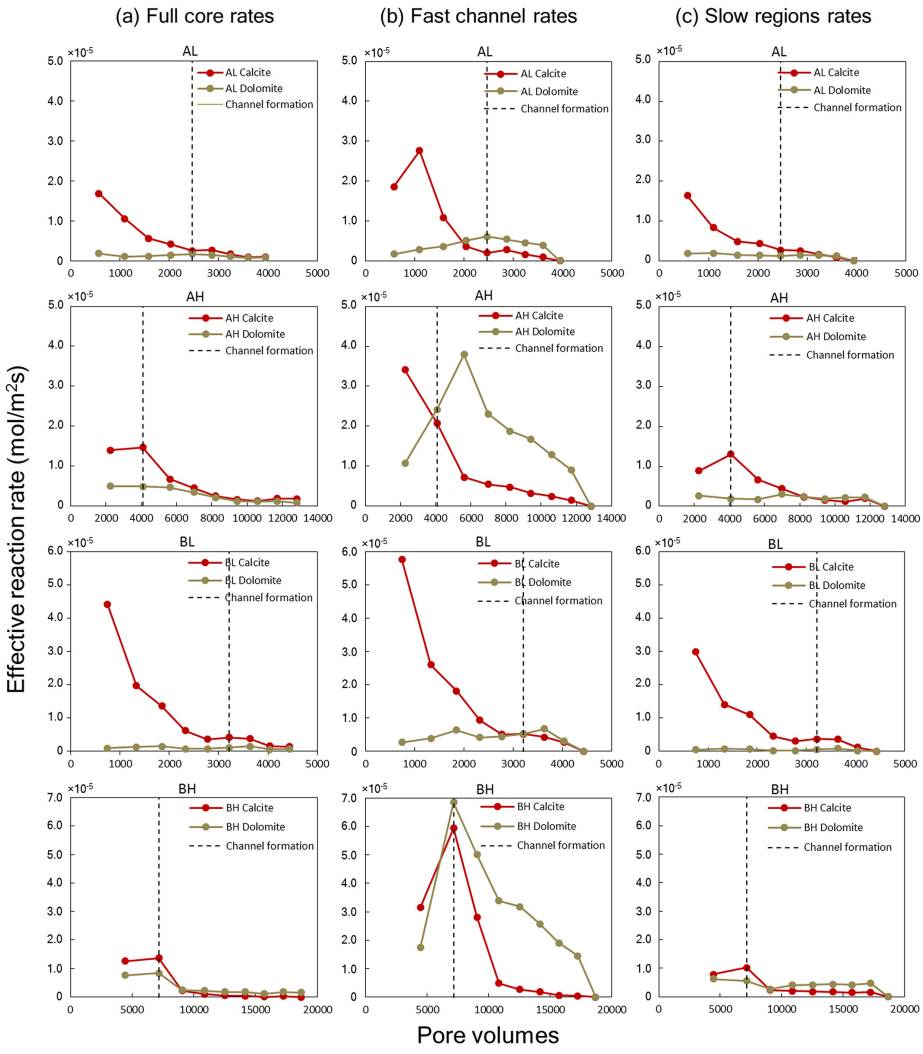


Figure 2.9: Effective reaction rates for calcite and dolomite related to the (a) full volume, (b) fast-flowing channels and (c) slow regions. The effective reaction rate significantly decreases after the channel is formed (dashed line). From Al-Khulaifi et al. (2019). Copyright © 2019 The Authors. All rights reserved.

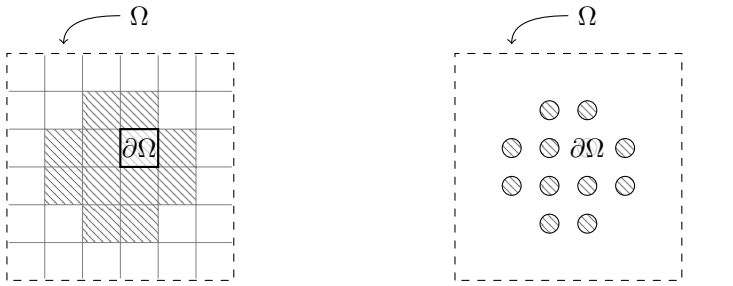
Oliveira et al. (2020) modelled multi-species reactive transport in a carbonate presenting a combination of macro and micro-porosity to highlight the contribution of the advection-dominated and diffusion-limited transport components in the effective rates of formation and consumption of chemical species. The combined impact of physical and chemical heterogeneity shows the persistence of pre-asymptotic rates for some species while the rate of others were already behaving asymptotically to steady-state values.

2.4 Numerical Modelling Methods

There are several models used to quantify reactive transport in porous media. In this section we show the application of different numerical models to study porous media flow and transport.

Pore Network Modelling (PNM) is a simple yet powerful method that was introduced by Fatt (1956) and which has been widely used in multiphase flow and transport (Chatzis and Dullien, 1985; Fenwick and Blunt, 1998; Valvatne and Blunt, 2004; Raeini et al., 2018), non-Newtonian fluid flow (Sochi, 2010), and porous media dissolution (Zhao and Ioannidis, 2007; Raoof et al., 2013; Tansey and Balhoff, 2016). The method relies on reconstructing the pore-space topology as a graph of pores interconnected by throats. There are several methods to construct this graph, using a watershed segmentation (Gostick, 2017) or the commonly used maxima inscribed balls (Dong and Blunt, 2009). More recently Raeini et al. (2017) and Raeini et al. (2018) generalized PNM, enriching its capabilities to describe geometrical properties of the pore-space by using sub-elements with conductivities calculated from direct simulation.

Classic Eulerian mesh based methods discretize the domain in elements where transport equations can be solved using either an integral or differential approach.



(a) Eulerian representation (b) Lagrangian representation

Figure 2.10: Different representations of fluids accordingly to the Eulerian discretisation (a) and the Lagrangian discretisation (b).

The Finite Difference Method (FDM) is the traditional choice of reservoir simulator engines (Fanchi, 1986), discretizing Darcy equations along with pressure corrections to account for the presence of wells (Peaceman, 1978). The method uses regular stencils to represent the domain, making it easy to run in parallel and a straight-forward candidate for Graphic Processing Unit (GPU) implementations (Nickolls et al., 2008).

The Finite Volume Method (FVM) has been used to study flow, transport and reaction in explicit realizations of the pore space (Meakin and Tartakovsky, 2009; Molins et al., 2012; Liu and Mostaghimi, 2018). Oliveira et al. (2019) has developed a multi-species reactive transport model using the advection-diffusion equation coupled with a homogeneous chemical equilibrium model and studied fluid/fluid reaction in a carbonate rock. FVM is another choice for the engine of reservoir simulators (Rasmussen et al., 2019).

The Finite Element Method (FEM) is capable of better representing complex geometrical structures when compared to FVM or FDM. This is advantageous when modelling pore-scale domains created from tomography image acquisitions (Akanji and Matthai, 2010), or fluvial channels within a reservoir (Gomes et al., 2017). At the pore-scale Fourar et al. (2004) evaluated high Reynolds flow of a Newtonian fluid to evaluate inertial effects and the Reynolds critical point from which Darcy's law is no longer valid and Forcheimer's equation becomes necessary. At the reservoir scale, Jackson et al. (2015) successfully combined the method with FVM in a dynamically adaptive framework to precisely capture the saturation-shock in a multi-phase flow reservoir model.

The Lattice Boltzmann Method (LBM) uses the movement of an ensemble of particles to reproduce the Navier-Stokes equation. It was used by Boek and Venturoli (2010) to model fluid flow in a two-dimensional Berea sandstone micro-model and to calculate the dispersion of tracer particles, which was later validated by a particle image velocimetry experiment. The authors also used the method to estimate the permeability of sub-samples extracted from a Bentheimer sandstone and showed the measurement dependency on the sample size. Grader et al. (2010) used LBM to estimate water-oil relative permeabilities from computed tomography models of rock samples from Abu Dhabi. They conducted blind tests and showed the ability of the model to represent the saturation evolution of experimental core-floods.

Smoothed Particle Hydrodynamics (SPH) is a meshless method that models fluid flows in a Lagrangian framework by discretizing the fluids as particles. Those particles are used as interpolation points to solve governing partial differential equations. The method was originally developed to simulate astrophysical flows (Lucy, 1977) and was later extended by many authors to study a vast class of problems in continuum solid and fluid mechanics. There are publications us-

ing SPH to model problems from magnetohydrodynamics (Price, 2012) to unstable immiscible flows (Bandara et al., 2013). However care should be taken to properly understand the model limitations and avoid unphysical results. The tensile instability is an example of an unphysical result on the presence of density contrasts between fluids that creates an artificial gap at the interfaces and can be avoided by properly selecting the model formulation (Agertz et al., 2007). Monaghan (2005) presents an overview of different formulations and lists the main advantages of the method that makes it preferable over grid based methods. Tartakovsky et al. (2015) had described several applications for SPH in multiphase flow and reactive transport in porous media. The authors showed several of the typically adopted formulations for single-phase, multiphase flow, reactive transport, microbial growth and mineral precipitation, as well as their applications.

Stochastic processes are another commonly used method of choice to model transport and reactive flow in porous media. The theory and practical challenges to model stochastic subsurface systems and have it implemented by practitioners inspired a debate documented by Rajaram (2016). The invited authors discussed problems and their views for such systems and generally share a similar message regarding the scale of investigation and adoption of the right model of study. Fogg and Zhang (2016) discusses the impact of geological texture on the permeability variability and highlights the characterization bias towards higher permeable materials when estimating permeability. Sanchez-Vila and Fernàndez-Garcia (2016) pointed out the difficulties to model reactive transport systems in an efficient and reliable way, considering the hypothesis such as complete mixing at the given scale.

The Random Walk (RW) method is a Lagrangian approach to track particles subjected to a velocity field and a random displacement to emulate dispersion. Salamon et al. (2006) studied the advantages and limitations of the different implementations of the RW method in heterogeneous media with both low and high velocity contrast. The dispersion coefficient was estimated using RW by Sahimi et al. (1983) and Salles et al. (1993) for different regular networks. The authors also covered a range of different Pe numbers and observed the Gaussian behaviour of the convective particles at longer times. Le Borgne et al. (2010) observed that moderate and strong permeability heterogeneity caused non-Fickian mixing during early times, which gets attenuated at longer times. The RW method is often coupled to an underlying mesh with averaged values of velocities and chemical components computed in it, which can be interpreted as if each cell is completely mixed on its level. The accuracy in calculating the concentration fields is limited by the amount of particles, so that smooth concentration distributions become hard to be constructed when not in presence of

large number of particles Herrera et al. (2009).

Developed by Gillespie (1976), the Stochastic Simulation Algorithm (SSA) is an exact method to model the time evolution of a chemical system. The method is similar to the RW, but instead of having particles transiting in space we have a chemical system transiting through chemical states (Gillespie, 1977). The method models each and every individual reaction event without considering approximated time increments. In order to overcome this, the τ-leaping approximation was developed by Gillespie (2001) to simulate larger times covering several reaction events, given that they satisfy the leap condition. The authors also introduced another equivalent strategy, the k_α-method that instead of leaping over time, it would leap over a number of reaction events. The method was later extended by Rathinam et al. (2003) to model stiff systems in an implicit formulation and presented a speed gain in relation to the conventional τ-leaping method.

The CTRW concept was proposed by Montroll and Weiss (1965) as a generalization of the RW method in a regular lattice, where walks would occur to the nearest-neighbouring sites with randomly distributed times. This is the framework that we will use in this thesis for modelling reactive transport. This inspired the development of a generalized transport theory in disordered systems by Scher and Lax (1973a). The method was then used to study impurity conduction in semi-conductors (Scher and Lax, 1973b), followed by the experimental observations and models of Montroll and Scher (1973), Scher and Montroll (1975), Tiedje (1984), and Bos and Burland (1987). Later Berkowitz and Scher (1997) and Berkowitz et al. (2000) applied the CTRW formalism to model anomalous transport in random fracture networks and in heterogeneous porous media. The CTRW method was also used to develop an upscaling methodology to integrate pore, core and field scales by employing different transit-time functions derived from smaller scales by Rhodes et al. (2008). Edery et al. (2010) used CTRW to describe particle transport of a bimolecular reaction system, in which particle of type A reacted with a particle of type B to form a particle of type C, whenever their distance was smaller than an interaction radius. The method was also recently proposed as a tool to model chemical reactions by Ben-Zvi et al. (2018) and Ben-Zvi et al. (2019) by discretising the spatial concentration using the FEM framework. The method is not limited to transport only: Aquino and Dentz (2017) used CTRW to derive a generalised chemical master equation that allows general waiting-times between reactions and hence model incomplete mixing in chemical reactions.

The majority of the previous models employ a particular formulation of the Advection-Dispersion Equation, and by doing so fail to represent the scale dependency of geological materials, even for homogeneous systems (Steefel et

al., 2015). The CTRW provides an efficient and practical framework to study reactive transport at a continuum scale. It uses a parametrization that accommodates under-resolved geological features, that often leads to non-Fickian behaviour. With the right choice of parameters, CTRW is capable of recovering the model described by the Advection-Dispersion Equation. This has motivated use to develop a CTRW based model for reactive transport. In the next we show the basic equations and usage of the CTRW framework for transport in porous media.

2.5 Continuous Time Random Walks

This section introduces the fundamentals of our model, that will be further detailed for transport only in chapter 3 and extended to account for reactive transport in chapter 4.

In general terms, CTRW models transport of solute particles by random increments in space and time (Montroll and Weiss, 1965),

$$\mathbf{x}^{n+1} = \mathbf{x}^n + \xi^n, \tag{2.17a}$$

$$t^{n+1} = t^n + \tau^n, \tag{2.17b}$$

where $\mathbf{x}$ denotes the particle location, ξ the particle spatial increment, t the particle time, τ the temporal increment, and the superscripts n denotes the current step and $n+1$ the next step. Within particle transitions, during time τ^n, the particle velocity v^n is constant and defined by $v^n = \xi^n/\tau^n$. This characteristic, that differs the RW from CTRW model is illustrated in figure 2.12.

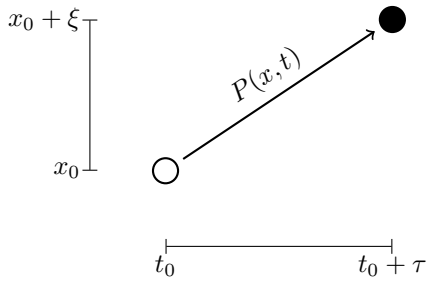
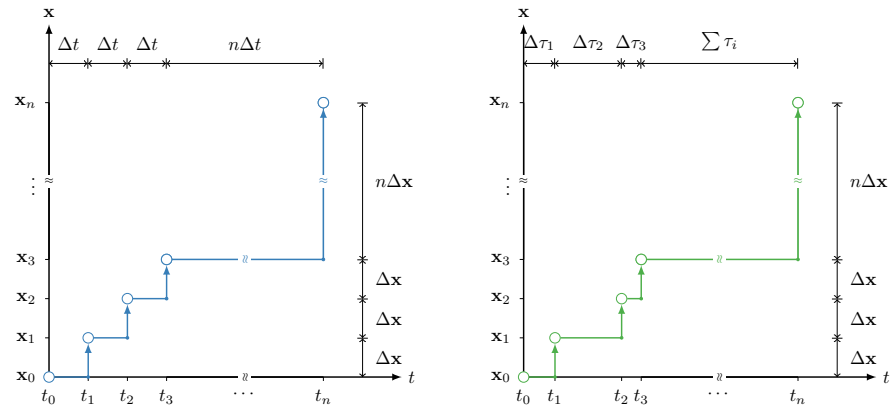


Figure 2.11: Particle single hop illustrating the change from (x_0, t_0) by random increments in space and time (ξ, τ) described by equation (2.17) and defined by Montroll and Weiss (1965).

The probability P of a particle arriving at a given position $\mathbf{x}$ after n steps



(a) Random Walk (b) Continuous Time Random Walk

Figure 2.12: Illustration of a random walk figure 2.12a with a constant step distance and duration and a continuous time random walk figure 2.12b also with a constant step distance but with a random duration between steps.

is given by the recurrent relation

$$P^{n+1}(\mathbf{x}) = \sum_{\mathbf{x}'} p(\mathbf{x}', \mathbf{x}) P^n(\mathbf{x}'), \tag{2.18}$$

where $p(\mathbf{x}, \mathbf{x}')$ is the probability of a particle that started at $\mathbf{x}$ to move to $\mathbf{x}'$. The probability of arrival at $\mathbf{x}$ per unit time is defined in Scher and Lax (1973a) as

$$R(\mathbf{x}, t) = \sum_{\mathbf{x}'} \int_0^t \psi(\mathbf{x}' - \mathbf{x}, t - t') R(\mathbf{x}', t) \, \mathrm{d}t. \tag{2.19}$$

The formal ensemble average of the Master Equation (ME) presented in Oppenheim et al. (1977) and Shlesinger (2003) is demonstrated in Klafter and Silbey (1980), and leads to the Generalized Master Equation (GME)

$$\begin{aligned} \frac{\partial}{\partial t} P(\mathbf{x}, t) = &- \sum_{\mathbf{x}'} \int_0^t \psi(\mathbf{x}' - \mathbf{x}, t - t') P(\mathbf{x}, t') \, \mathrm{d}t' \\ &+ \sum_{\mathbf{x}'} \int_0^t \psi(\mathbf{x} - \mathbf{x}', t - t') P(\mathbf{x}', t') \, \mathrm{d}t' \end{aligned} \tag{2.20}$$

where $P(\mathbf{x}, t)$ is the probability of a particle being at $\mathbf{x}$ at time t, and $\psi(\mathbf{x}, t)$ is the memory function given by the joint space and time transition probability density functions. The memory function term is often described as $M(\mathbf{x}, t)$ by Dentz et al. (2004) and Berkowitz et al. (2006). The probability $P(\mathbf{x}, t)$ described in equation (2.20) is equal to the probability of a particle leaving $\mathbf{x}$ towards $\mathbf{x}'$ minus the probability of a particle to remain at $\mathbf{x}$. The type of

transport described by equation (2.20) makes no distinction between advective, diffusive or dispersive means of transport, but bundles them together.

Kenkre et al. (1973) and Shlesinger (1974) demonstrated that the GME, equation (2.20), is equivalent to the CTRW, equation (2.19).

Our focus now lies on the decoupled transition distributions for space and time (Dentz and Berkowitz, 2003),

$$\psi(\mathbf{x}, t) = p(\mathbf{x})\,\psi(t) \tag{2.21}$$

where $p(\mathbf{x})$ is the transition probability density function and $\psi(t)$ is the transit time probability density function. The CTRW theory is valid for a wide range of cases, and with the right selection of the ψ function, it is possible to reproduce the macroscopic transport behaviour of complex media (Berkowitz et al., 2001).

The choice of an exponential decay function, $\psi(t) \sim e^{-\lambda t}$, reproduces the conventional Gaussian spreading of Fickian transport (Scher and Montroll, 1975; Margolin and Berkowitz, 2000). Scher and Montroll (1975) and Berkowitz and Scher (1997) proposed a power-law $\psi(t)$ function that with the right choice of its β parameter, is capable of characterizing both Fickian and non-Fickian transport using a relation

$$\psi(t) \sim t^{-1-\beta}, \tag{2.22}$$

with the exponent $\beta > 0$. Figure 2.13 shows the example of First-Passage Time Distributions (FPTD) and different choices of β using the relation in equation (2.22). The results were calculated using the asymptotic results present in (Berkowitz et al., 2000).

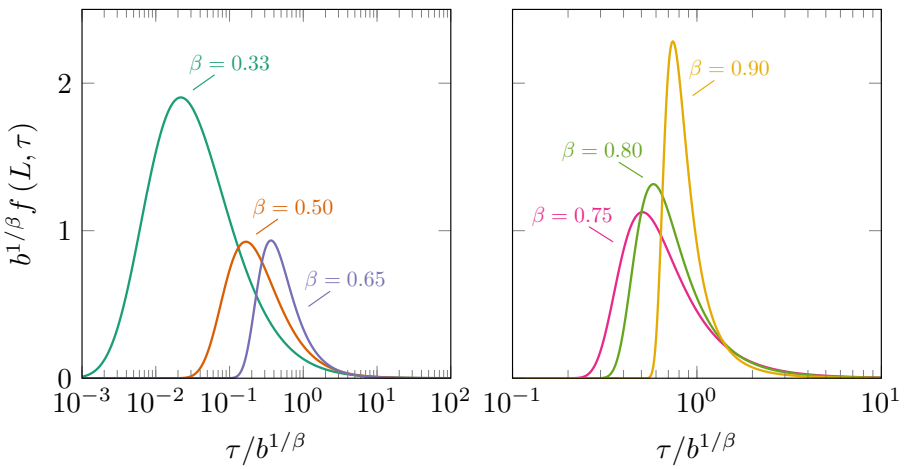


Figure 2.13: First passage time distribution for $0 < \beta < 1$ from Berkowitz et al. (2000) using the power-law function equation (2.22). Copyright © 2000 by the American Geophysical Union. All rights reserved.

Natural systems are often modelled using a truncated power-law function, such that there is a time scale cut-off to account for when the system behaves as if it is homogeneous (Berkowitz et al., 2006). Equation (2.22) is then characterized by two time scales, t_1 that represents the mean transition time and t_2 that corresponds to the time to encounter the largest heterogeneities (Dentz et al., 2004).

The definition of the characteristic times t_1 and t_2 is respectively associated to the mean flow velocity and molecular diffusion (Bijeljic and Blunt, 2006) such that

$$t_1 = \frac{l}{v}, \tag{2.23a}$$

$$t_2 = \frac{l^2}{D_m}, \tag{2.23b}$$

where l is the domain length, v the mean flow velocity and D_m the molecular diffusion coefficient. With this, equation (2.22) becomes

$$\psi(t) = \left[t_1 \left(\frac{t_2}{t_1} \right)^{\beta} e^{\frac{t_1}{t_2}} \Gamma\left(-\beta, \frac{t_1}{t_2} \right) \right]^{-1} e^{-t/t_2} (1 + t/t_1)^{-1-\beta}, \tag{2.24}$$

where $\Gamma(a, z)$ is the incomplete Gamma function $\Gamma(a, z) = \int_z^{\infty} t^{a-1} e^{-t} \mathrm{d}t$, also defined as upper incomplete Gamma function (Abramovitz and Stegun, 1974).

Equation (2.24) is empirical yet successfully reproduces non-Fickian transport signatures at different time scales (Dentz et al., 2004; Berkowitz et al., 2006; Bijeljic and Blunt, 2006; Berkowitz and Scher, 2009; Edery et al., 2015).

Figure 2.14 illustrates the particle trajectory in space and the velocity variation in time, as conceptually described in figure 2.12, and using equation (2.24) defined by a near homogeneous system characterized with $\beta = 1.8$. The complete model and details of the domain used to illustrate these trajectories are described in chapter 3, section 3.1. The large velocities ($\sim 10^3$) are note frequent but are responsible for the particles early arrival and are manifested in the particle BTCs.

Transport behaviour is anomalous for $0 < \beta < 2$ and $t_1 \gg t \gg t_2$ but asymptotically becomes Fickian with $t \gg t_2$ (Dentz et al., 2004); for $\beta > 2$ it already becomes Fickian for $t \gg t_1$. The parameter β defines three different regimes (Berkowitz et al., 2001):

1. For $\beta > 2$, the mean position scales with t, the standard deviation with $t^{1/2}$ and $\sigma_{\mathbf{x}}/\langle \mathbf{x} \rangle \sim t^{-1/2}$;

2. For $1 < \beta < 2$, the solute moves with the mean fluid velocity, the standard deviation increases as $t^{(3-\beta)/2}$ and $\sigma_{\mathbf{x}}/\langle \mathbf{x} \rangle \sim t^{(1-\beta)/2}$;

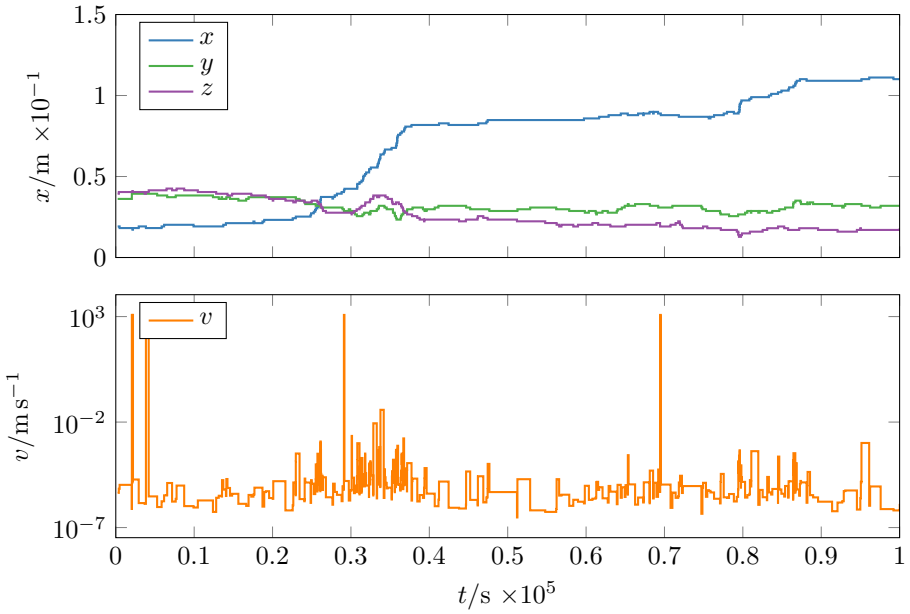


Figure 2.14: The particle trajectory in space and velocity as illustrated in figure 2.12, and using equation (2.24) defined by a near homogeneous system characterized with $\beta = 1.8$. The domain used to illustrate the trajectories is described in chapter 3. The large velocities ($\sim 10^3$) are responsible for the particles early arrival and are manifested in the particle BTCs.

3. For $0 < \beta < 1$, both the mean and standard deviation scales similarly, $\langle \mathbf{x} \rangle \sim \sigma_{\mathbf{x}} \sim t^{\beta}$ and $\sigma_{\mathbf{x}} / \langle \mathbf{x} \rangle \sim$ constant.

The value of β is related to the heterogeneity of the system, with relatively homogeneous materials such as sandpacks and sandstones obtaining $\beta = 1.8$ Bijeljic and Blunt (2006), and heterogeneous carbonates obtaining $\beta = 0.7$ (Bijeljic et al., 2011). Figure 2.15 shows the comparison of the ADE and CTRW models made by Cortis and Berkowitz (2004) using experimental data from Scheidegger (1959).

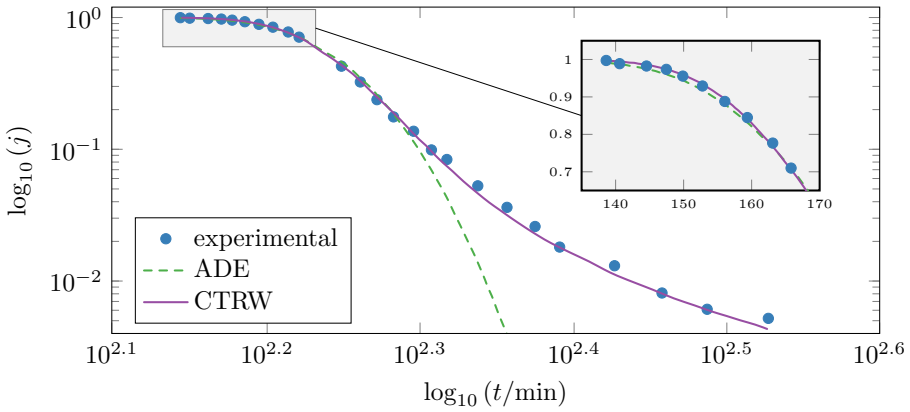


Figure 2.15: Comparison for the BTC of a Berea sandstone core using the ADE (dashed line) and CTRW (continuous line) model fit . The experimental data is obtained from Scheidegger (1959) and the best fit results from Cortis and Berkowitz (2004). The quantity j is the normalized flux-averaged concentration. The CTRW model uses the truncated power-law model equation (2.24) and $\beta = 1.59$. Copyright © 2004 Soil Science Society of America. All rights reserved.

Figure 2.15 highlights that Berea sandstones, usually taken as homogenous, can present non-Fickian transport signatures (Levy and Berkowitz, 2003). The usage of the CTRW model better represents the complete BTC when compared to the ADE model, that despite matching the center of mass of the solute, it fails to capture the behaviour at early and late times.

2.6 Summary and Motivation

In this chapter we presented the literature review of reactive transport in porous media in sections 2.1 and 2.2. Next we presented the physical and chemical heterogeneity impact in reactive transport in section 2.3. In section 2.4 we showed the commonly employed numerical models, and then the main features of the CTRW model that support our work in section 2.5.

We showed that there are several approaches to model reactive transport, and that at the continuum scale, there is a complex interaction between physical and chemical heterogeneity that significantly impacts effective reaction rates. We also showed that the CTRW framework provides an appropriate alternative to account for both Fickian and non-Fickian transport behaviour. This motivated us to develop a novel CTRW based reactive transport model for simulating reactive transport at the continuum scale.

CHAPTER 3

Modelling Transport in Porous Media using Continuous Time Random Walks

This chapter describes the Continuous Time Random Walk (CTRW) framework and how it is employed to describe transport of particles on a lattice. Solute transport is modelled coupling flow calculated on a lattice (termed the Lattice Flow Model) and particle transport which includes advection and diffusion (which we term the Particle Transport Model).

Traditional models make use of the Advective-Dispersion Equation (ADE) to simulate solute transport in porous media (Bear, 1972) with the inclusion of an additional term to account for reactive processes,

$$\frac{\partial(\phi c)}{\partial t} = -\nabla \cdot (\phi \mathbf{v} c) + \nabla \cdot \nabla (\phi \mathbf{D} c) + R, \tag{3.1}$$

where c is the solute concentration, $\mathbf{v}$ is the Darcy velocity, $\mathbf{D}$ is the dispersion coefficient and R is the reaction term, that either behaves as a sink or a source, according to the process of interest.

Instead of having the solute concentration modelled as a continuous field variable, we describe it using a Lagrangian framework with particles distributed on a lattice (Bijeljic and Blunt, 2006; Le Borgne and Gouze, 2008; Kang et al., 2011; Pereira Nunes et al., 2016a; Pereira Nunes et al., 2016b).

The chapter starts with the model description, showing the flow modelling that provides the parameters describing the particles transit-time distributions and probability of spatial transitions on the lattice consisting of nodes and links. The observed macroscopic transport parameters are then shown for idealized domains, reconstructing the sub-diffusive and super-diffusive behaviour described in the literature, and finally the model usage in simplified geometries is presented to show its capability to account for underlying transport physics. The transport components described in this chapter are used in the same way to model reactive flow in chapters 4 to 6.

3.1 Model Description

The solute transport model consists of two main components: (a) the Lattice Flow Model and (b) the Particle Transport Model. The lattice flow model is used to calculate the pressure gradients and mean velocities so that the particle transport model can then have defined particle probability distributions for spatial transitions and transit-times throughout the domain representing the porous medium.

3.1.1 Lattice Flow Model

Our domain is defined as Ω with boundary Γ and is discretized in a cubic connected lattice. The lattice is an abstraction of a regular grid, where nodes represent the grid cells and the links the faces between such cells. Scalar fields assigned to grid cells are mapped to the nodes and links of our lattice, as in figure 3.1a.

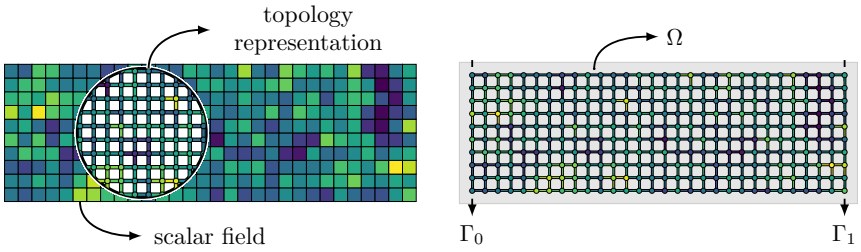
Despite being depicted as a two-dimensional field, the scalar fields adopted herein are three-dimensional and emerge from a three-dimensional image acquisition where each voxel, or grid cell, has defined values, *e.g.* porosity and permeability. Therefore it is only natural to consider the values at the grid cells to be coincident with the values at the nodes of our model, requiring us to interpolate them to the links. For additive properties like the porosity, we calculate the value at the links using the arithmetic mean of the values in the connected nodes,

$$\phi_k = \frac{\phi_i + \phi_j}{2}, \tag{3.2}$$

where ϕ is the porosity and k is the index of the link connecting nodes i and i.

In the absence of a more sophisticated metric, the permeability can be calculated using a power-law correlation with the porosity,

$$K_k = a\phi_k^b, \tag{3.3}$$



(a) domain idealization (b) lattice topology

Figure 3.1: Domain idealization and lattice topology with scalar fields (porosity and permeability) used to define the nodes and links within the domain Ω and boundaries Γ. The topology is represented by nodes interconnected by links. Each node of the lattice has the properties defined from a given scalar field. The lattice corresponds to the underlying discrete domain. The pressure P_0 and P_1 is specified in the nodes at Γ_0 and Γ_1 and will be later used to solve the pressure inside the domain Ω.

where K is the permeability and a and b are adjustment parameters. The permeability follows the definition of the porosity. If the initial porosity of the link is $\phi_k = 1$, the permeability of the link is defined as $K_k = a$. If the porosity of the link is zero, the permeability is also defined as zero, and the link is unavailable for flow and transport of any particles. For computational reasons, the smallest represented porosity value is $\phi = 1 \times 10^{-12}$, and the permeability is defined using the appropriate correlation factors. Section 3.1.2 discusses the particle flow implications of having link velocities approximately equal to zero. Such power-law correlations between porosity and permeability are widely used, to model the evolution of permeability in dissolution experiments (Menke et al., 2015; Honari et al., 2015). Other relations for porosity and permeability such as Kozeny-Carman (KC) correlation can also be employed (Kozeny, 1927; Carman, 1937).

We solve the pressure field in the lattice for a domain Ω with boundaries Γ, as represented in figure 3.1b, by ensuring the mass conservation at node i and all connected links k,

$$\sum_{\forall k \in i} Q_k = 0, \tag{3.4}$$

where Q is the volumetric flux at link k, connected by node i and j. The flux Q is defined within each link k by Darcy's law (Darcy, 1856),

$$Q = -\frac{KA}{\mu}\frac{\Delta P}{\Delta L} \tag{3.5}$$

where A is the cross-sectional area, μ the viscosity of the fluid, P the pressure and L the length of the link. At the boundaries Γ of the domain we impose

Dirichlet conditions,

$$P_k = P_{\Gamma_0}, \quad \forall k \in \Gamma_0, \tag{3.6a}$$

$$P_k = P_{\Gamma_1}, \quad \forall k \in \Gamma_1, \tag{3.6b}$$

where P_{Γ_0} and P_{Γ_1} are the specified pressures at the boundaries Γ_0 and Γ_1, that will later be used to define the pressure at the inlet and outlet of the domain.

The system of equations formed by equation (3.4) is written as

$$\mathbf{BQ} = 0, \tag{3.7}$$

where $\mathbf{B}$ is the lattice incidence matrix and $\mathbf{Q}$ is the flux vector. We then define the conductivity matrix as

$$C_{ij} = \frac{K_k A}{l\mu} \tag{3.8}$$

so that equation (3.5) becomes

$$\mathbf{Q} = \mathbf{CB}^T\mathbf{p}. \tag{3.9}$$

Finally by substituting equation (3.9) in equation (3.7), we obtain the system of equations defining our problem

$$\mathbf{BCB}^T\mathbf{p} = 0. \tag{3.10}$$

The incidence matrix B has shape $m \times n$, where m is the number of links and n the number of nodes in the lattice.

$$B_{m,n} = \begin{bmatrix} b_{1,1} & b_{1,2} & \cdots & b_{1,n} \\ b_{2,1} & b_{2,2} & \cdots & b_{2,n} \\ \vdots & \vdots & \ddots & \vdots \\ b_{m,1} & b_{m,2} & \cdots & b_{m,n} \end{bmatrix} \tag{3.11}$$

where $b_{k,i} = 1$ if the link k is connected to the node i, otherwise $b_{k,i} = 0$.

Figure 3.2 illustrates a generic lattice and its incidence matrix. The lattice is summarized in a 7×6 matrix with both node 4 and link 7 highlighted as an example. The sum of the elements in a column is equal to the node connectivity.

Our lattice consists of a cubic graph, with regularly spaced nodes. Each node is connected by 6 other nodes, with exception of the boundaries that will either be connected to 3, 4 or 5 other nodes as illustrated in figure 3.3.

The linear system of equations described in equation (3.10) results in a sparsely distributed matrix and it is solved using a Generalized Minimal Resid-

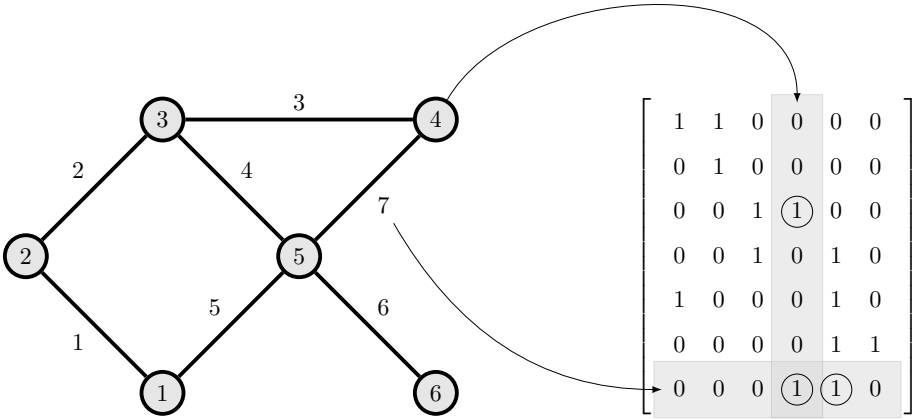
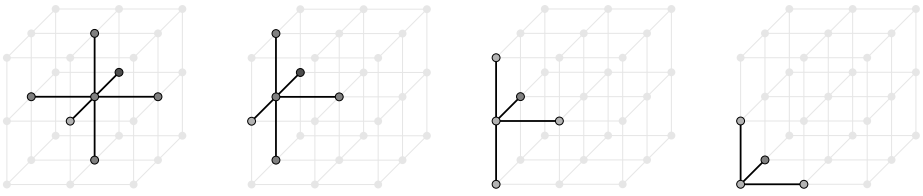


Figure 3.2: Lattice representation and the correspondent incidence matrix. The rows correspond to the links and columns to the nodes. Node 4 is highlighted as an example to show that it is connected by links 3 and 7. Similarly link 7 is highlighted to show that it connects node 4 and 5.



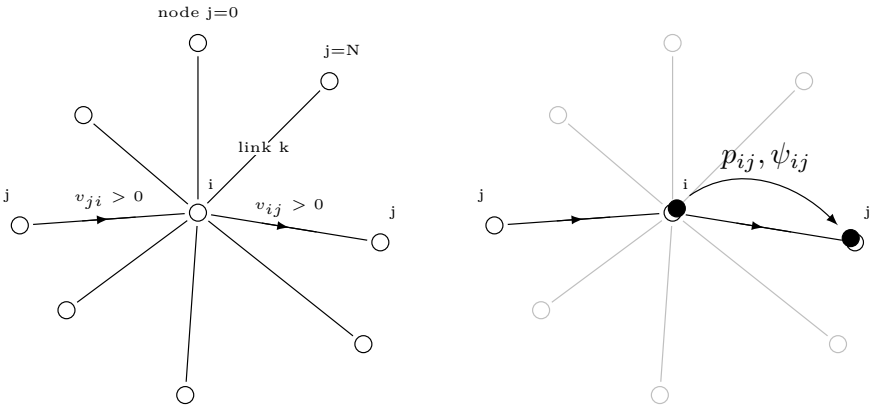
(a) inner (b) face (c) edge (d) corner

Figure 3.3: Link and node types in the lattice, each representing an element inside the domain, at the face, edge and corner of the enclosed lattice. The other elements are obtained by applying a rotation to these and are not displayed here for simplicity.

ual (GMRES) method (Saad and Schultz, 1986) implemented in the Portable, Extensible Toolkit for Scientific Computation (PETSc) framework (Abhyankar et al., 2018).

3.1.2 Particle Transport Model

We model solute transport as a series of particle transitions on a lattice. The transitions are governed by the decoupled probability distributions for the transit-time and displacement of the particles. Figure 3.4 shows an idealization of the lattice with a node i at the origin connected to nodes $j \in [0, 1, \ldots, N]$ through a link k. Each link has a calculated probability of displacement p_{ij} and probability of transit-time ψ_{ij} (figure 3.4b) using the underlying properties of the link.



(a) General lattice consisting of an arbitrary number of nodes and links

(b) Particle transition from node i to node j with probability p_{ij} and ψ_{ij}

Figure 3.4: General lattice consisting of nodes interconnected by links. This depicts a particle transition from a node i to a node j through a link k with prescribed velocity v_{ij}, probability of displacement p_{ij} and transit time distribution ψ_{ij}.

The transit-time distribution ψ_{ij} is represented by a Truncated Power-Law (TPL) distribution which, empirically, matches experimental results (Levy and Berkowitz, 2003) defined using two different characteristic time scales (Dentz et al., 2004; Bijeljic and Blunt, 2006) and an adjustable parameter

$$\psi(t) = Ae^{-t/t_2}(1 + t/t_1)^{-1-\beta}, \tag{3.12}$$

where t_1 is the advective transit time, t_2 is the diffusive cut-off time, β is a fitting parameter representing the heterogeneity of the medium and A is a normalization constant such that $\int_0^\infty \psi(t')dt' = 1$ meaning that ψ can be used as

a Probability Density Function (PDF).

The probability for a transition to occur in the interval $(t, t + dt]$ is $\psi(t)dt$ and the parameters in equation (3.12) are defined as

$$t_1 = \frac{l}{|v_{ij}|}, \tag{3.13a}$$

$$t_2 = \frac{l^2}{D_m}, \tag{3.13b}$$

where v_{ij} is the velocity in the link between nodes i and j, D_m is the molecular diffusion coefficient and l is the length of the link. In this work we assume that l and D_m are fixed.

Equation (3.12) is empirical yet successfully reproduces non-Fickian transport signatures at different time scales (Dentz et al., 2004; Berkowitz et al., 2006; Bijeljic and Blunt, 2006; Berkowitz and Scher, 2009; Edery et al., 2015). We do not fit the values of t_1 and t_2 in equation (3.13); these are directly calculated from the flow field and the transport parameters. The velocity used to calculate t_1 is $v_k = v_{ij}$, the velocity in the link k between nodes i and j. The value of β however is fitted to experimental measurements. The asymptotic analysis for the mean velocity v of a plume of solute in Dentz et al. (2004) showed that for values of $\beta < 1$, $v \propto t^{\beta-1}$ and for $1 < \beta < 2$, v is constant.

Figure 3.5 illustrates the shape of ψ for different t_1, t_2 and β parameters. When plotted using a $\log - \log$ transformation, ψ is nearly constant for $t \ll t_1$, has a constant slope of $t^{-1-\beta}$ for $t_1 < t < t_2$ and asymptotically goes for zero for $t \gg t_2$. The asymptotic analysis for the mean velocity v of a plume of solute in Dentz et al. (2004) showed that for values of $\beta < 1$, $v \propto t^{\beta-1}$ and for $1 < \beta < 2$, v is constant.

Before proceeding any further, we need to ensure that our sampling routines are reconstructing the ψ function properly. As a practical example, we analyse a simple case with $\psi(t, t_1, t_2, \beta) = \psi(t, 1.0, 10^4, 1.5)$. Figure 3.6 shows the analytical $\psi(t)$ function calculated from using theses parameters, with the regions $t < t_1$ and $t > t_2$ highlighted, and the exponential growth of the cumulative distribution $\int \psi(t)\mathrm{d}t$. We then randomly take 10^9 samples from the cumulative of the ψ function and attempt to reconstruct the ψ function. The reconstructed function is present in figure 3.7 and is able to recover the overall shape of the analytical ψ function over a wide range of t values. The reconstructed function deteriorates for low probability values of t, however those values have little contribution to the distribution and are a consequence of the narrow increment in the integral of the probability function $\int \psi \, dt$.

Lastly, the probability of transition from node i to node j is calculated from the asymptotic solution of the ADE. The solution is developed in Rhodes and

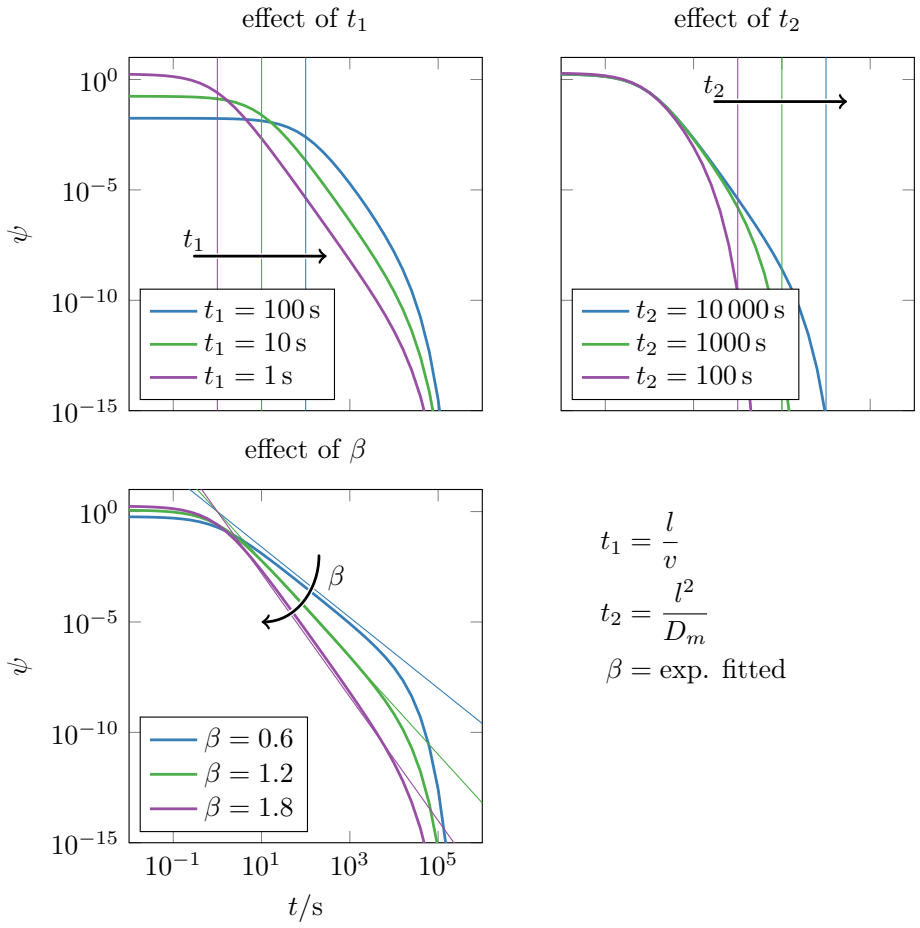


Figure 3.5: The effect of t_1, t_2 and β on the shape of the transit-time distribution ψ. The values for t_1 and t_2 are obtained from the flow field and transport parameters, and the value of β is fitted to experimental data. ψ distribution is nearly constant for $t \ll t_1$, has a constant slope of $t^{-1-\beta}$ for $t_1 < t < t_2$ and asymptotically goes for zero for $t \gg t_2$.

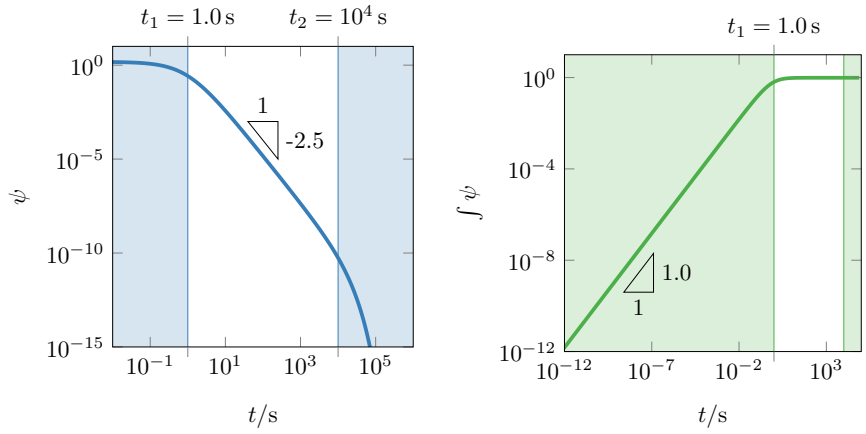


Figure 3.6: Calculated ψ function and its integral for $t_1 = 1.0\,\mathrm{s}$, $t_2 = 1.0 \times 10^4\,\mathrm{s}$ and $\beta = 1.5$. The shaded intervals highlight the regions where $t \ll t_1$ with ψ is nearly constant, $t_1 < t < t_2$ with $\psi \propto t^{-1-\beta}$, and where $t \gg t_2$ with ψ asymptotically going to zero. The integral of the ψ function has a constant slope for $t \ll t_1$ with most of its weight coming from the rest of the t-axis.

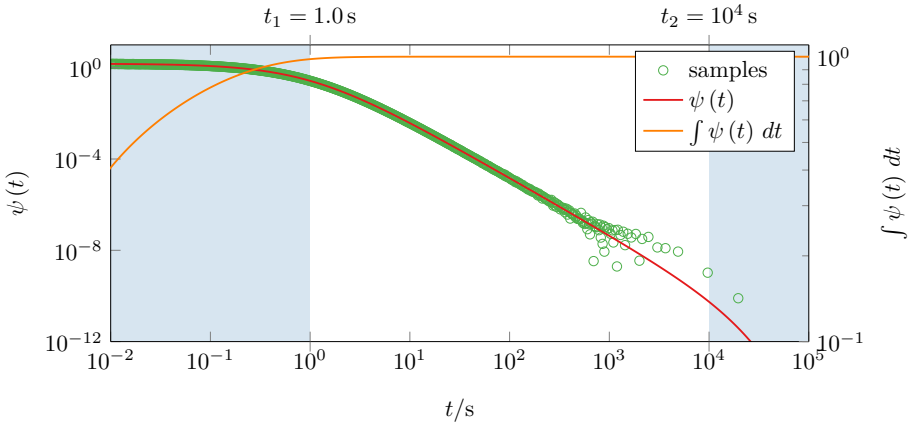


Figure 3.7: Analytical and integrated ψ functions (solid lines) and the reconstructed function from sampled values of the ψ integral (circles). The function was constructed using $t_1 = 1.0\,\mathrm{s}$, $t_2 = 1.0 \times 10^4\,\mathrm{s}$ and $\beta = 1.5$. The reconstructed function is able to recover the overall shape of the analytical ψ function for a wide range of values.

Blunt (2006) and generalized in Rhodes et al. (2008) as

$$p_{ij} = G\frac{Pe_{ij}}{1 - e^{-Pe_{ij}}}, \quad \forall v_{ij} > 0 \tag{3.14a}$$

$$p_{ij} = G\frac{Pe_{ij}}{e^{\,Pe_{ij}} - 1}, \quad \forall v_{ij} < 0 \tag{3.14b}$$

where Pe is the Péclet number, $Pe_{ij} = l|v_{ij}|/D_m$ is the locally defined Péclet number in the link connecting node i to node j, and G is a normalization factor such that $\sum_j p_{ij} = 1$. Simplifications of equation (3.14) are of great importance when implementing the numerical model and are detailed next.

There are cases in which equation (3.14) can become undefined and incur numerical errors. Such cases can be avoided with some algebraic manipulation. The two cases explained here are when the velocity asymptotically goes to zero or asymptotically goes to infinity.

Links where the velocity is approximately zero still contribute to the transport of particles. Transitions of such cases are interpreted as purely diffusive transitions. Using a Taylor series expansion at about $Pe \to 0$, *i.e.* $v \to 0$, reduces equation (3.14) to

$$\begin{aligned} p_{ij} &= G\frac{Pe_{ij}}{e^{Pe_{ij}} - 1} \\ &= G\frac{Pe_{ij}}{1 + Pe_{ij} + \mathcal{O}(Pe_{ij}^2) - 1}, \end{aligned} \tag{3.15}$$

which can be further simplified by ignoring higher order terms into

$$p_{ij} = G, \quad \forall v_{ij} = 0. \tag{3.16}$$

On the other hand, when $Pe \to \infty$, *i.e.* $v \to \infty$, equation (3.14) reduces to

$$p_{ij} = G\mathrm{Pe}_{ij}, \quad \forall v_{ij} > 0, \tag{3.17a}$$

$$p_{ij} = 0, \qquad \forall v_{ij} < 0. \tag{3.17b}$$

To illustrate the behaviour of equation (3.14) along with its simplifications, a 2D graph is created as shown in figure 3.8, where the main flow direction is aligned with $+x$-axis and $v = 0$ perpendicular to this direction. Figure 3.9 shows the effect of different Pe numbers on the probability of displacement of a particle on the 2D lattice in figure 3.8. For $Pe = 1$, the probability of travelling in any direction is nearly the same, with a higher chance of moving towards the flow (east) and smaller chance against the flow (west). When Pe increases by an order of magnitude, the probability is predominantly driven by the flow direction.

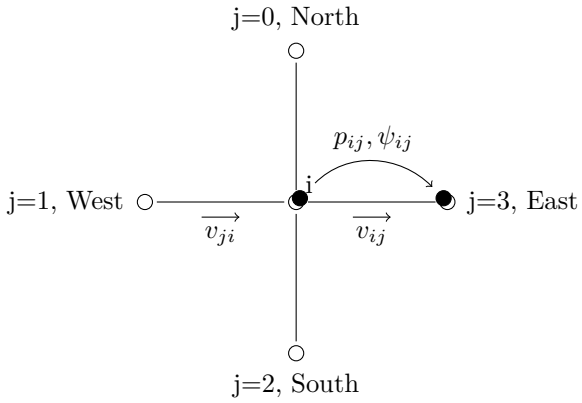


Figure 3.8: A 2D graph constructed from the concept described in figure 3.4 and with the main flow direction aligned with $+x$-axis and $v = 0$ perpendicular to this direction. The results of the probability of displacement in such a scenario and under different Pe numbers are shown in figure 3.9.

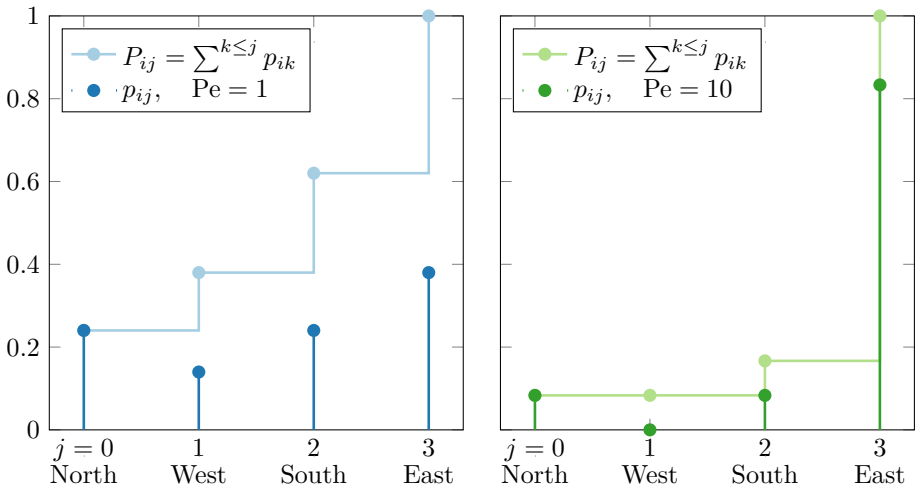


Figure 3.9: Probability of transitioning p_{ij} and the cumulative of it P_{ij} for $Pe = 1$ and $Pe = 10$. For $Pe = 1$, the probability of travelling in any direction is nearly the same, with a higher chance of going towards the flow (east) and smaller chance against the flow (west). When Pe increases by an order of magnitude, the probability is predominantly driven by the flow direction.

The trajectory for a single particle travelling on a 2D lattice with flow along the $+x$-axis direction is illustrated in figure 3.10. This illustrates a particle undergoing different flow dynamics, characterized by different Pe numbers. The particle is subjected to a velocity $v \neq 0$ in the $+x-$direction and $v = 0$ in every other direction. At low Pe numbers, the velocity field has little influence on the particle, with most of the effect stemming from diffusion. As Pe increases the advective forces become predominant and the mean particle trajectory aligns more with the mean flow direction, to the point that dispersion perpendicular to the flow is nearly absent.

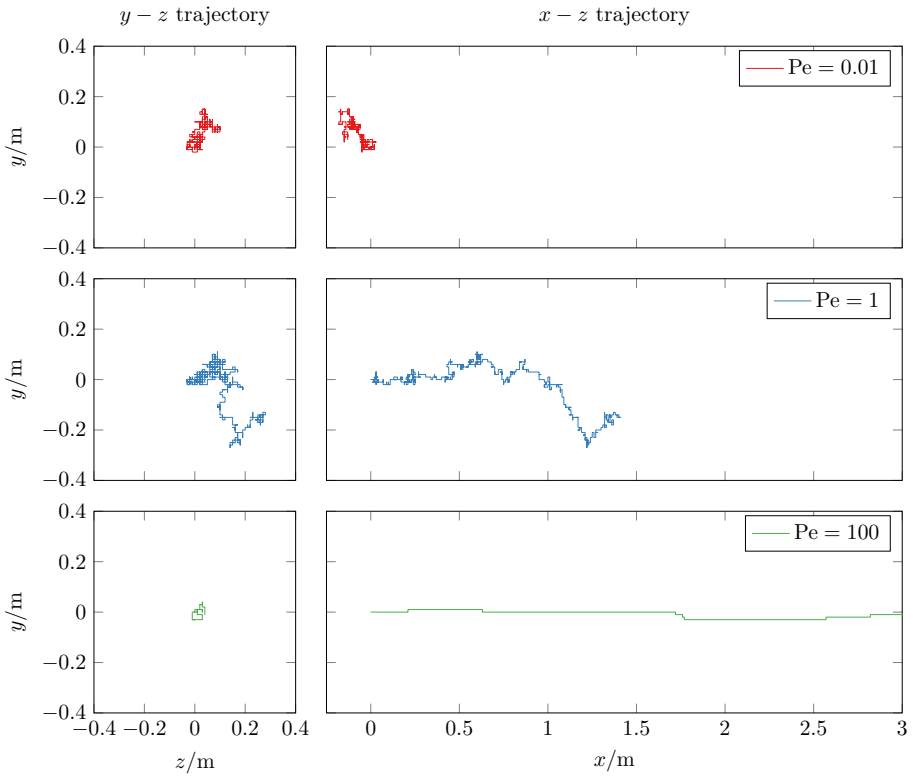


Figure 3.10: Particle trajectories for different Pe numbers. At low Pe numbers, the velocity field has little influence on the particle displacement, with most of the effect originating from diffusion. As Pe increases the advective forces become predominant and the mean particle trajectory aligns more with the mean flow direction, to the point that dispersion perpendicular to the flow is nearly absent.

In order to have a smaller number of output files and keep a common time axis for different particles, each particle is synchronized at the end of every time step Δt. The time steps Δt are fixed and independent of the particle

transit-times $\Delta\tau$,

$$\sum_{i=0} \Delta\tau_i \leq \Delta t, \quad \Delta\tau_i \sim \psi_{ij}\left(t_1, t_2, \beta\right). \tag{3.18}$$

If the sampled transit-time is smaller than the fixed time step, $\Delta\tau < \Delta t$, the particle transits to a new location and sample a new transit-time from equation (2.24). When the sampled transit-time is greater or equal to the fixed time step, $\Delta\tau \geq \Delta t$ we output the particle position, increment the current time and start the particle transitions again while the condition in equation (3.18) is still met.

Figure 3.11 shows the comparison between the particle trajectories at the fixed recorded time step Δt and the actual sampled times $\Delta\tau$, using the relation showed in equation (3.18). Given the stochastic nature of the problem, the seed was fixed in order to sample the same random numbers for both cases.

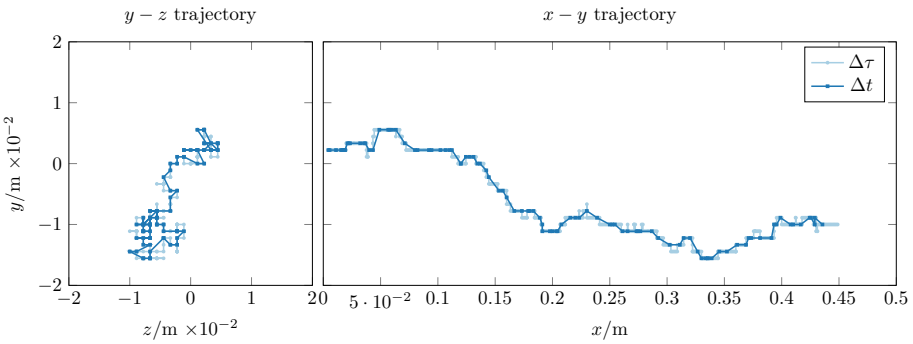


Figure 3.11: Comparison between the particle trajectories at the fixed recorded time Δt and the actual sampled times $\Delta\tau$. Given the stochastic nature of the problem, the seed was fixed in order to sample the same random numbers for both cases.

The injection of several different particles and its trajectories are illustrated in figure 3.12 for $Pe = 10$. The particles move towards $+x$-axis, following the main flow direction, but still show dispersion when the trajectories are projected in the $y - z$ plane.

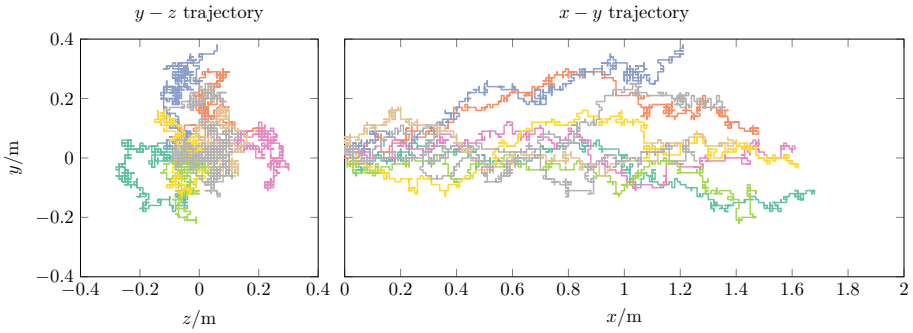


Figure 3.12: Several different particle trajectories represented by a different colour for $Pe = 10$. The particles move towards $+x$-axis, following the main flow direction, but still experience dispersion as seen from the trajectory projected in the $y - z$ plane.

3.2 Transport Validation

3.2.1 Effect of the Number of Particles

The high frequency noise displayed in the asymptotic behaviour of the mean particle velocity and dispersion, as seen in figures 3.15, 3.22 and 3.23, is reduced when increasing the number of particles. To support this statement figure 3.13 shows the result for a case with a uniform porosity of $\phi = 0.3$, $K = 1 \times 10^{-12}\,\mathrm{m}^2$, link size $l = 10^{-3}\,\mathrm{m}$, and $\beta = 1.8$, and a mildly advective regime with $Pe = 100$ resulting in characteristic transit time $t_1 = 10$ and diffusive cut-off time $t_2 = 10^3$. The figure shows the results using $N_p = 10^2$ to 10^6. These results are compared against the solutions for the average velocity and dispersion coefficient obtained from the numerical Laplace Transform Inversion as described in appendix A. As the number of particles increases, the high frequency noise reduces, and the transport behaviour at early times is more pronounced. Taking this effect in consideration, the number of particles is always kept as the minimum possible to still be able to obtain consistent results of the macroscopic transport parameters, or other quantities of interest.

The accuracy and simulation time of the proposed algorithm scales with the number of particles, simply put, the more particles are present in the domain, the more accurate and the longer are the simulations. To support this observation, figure 3.14 shows the effect of the number of particles in the time-step taken per Δt iteration and relative error in the normalized dispersion ϵ_D and normalized velocity ϵ_v. The time taken per iteration scales log-linearly with the number of particles for $N_p \gtrapprox 10^3$. The error for the velocity decreases faster with the increase of particles. The simulations used to benchmark the algorithm were

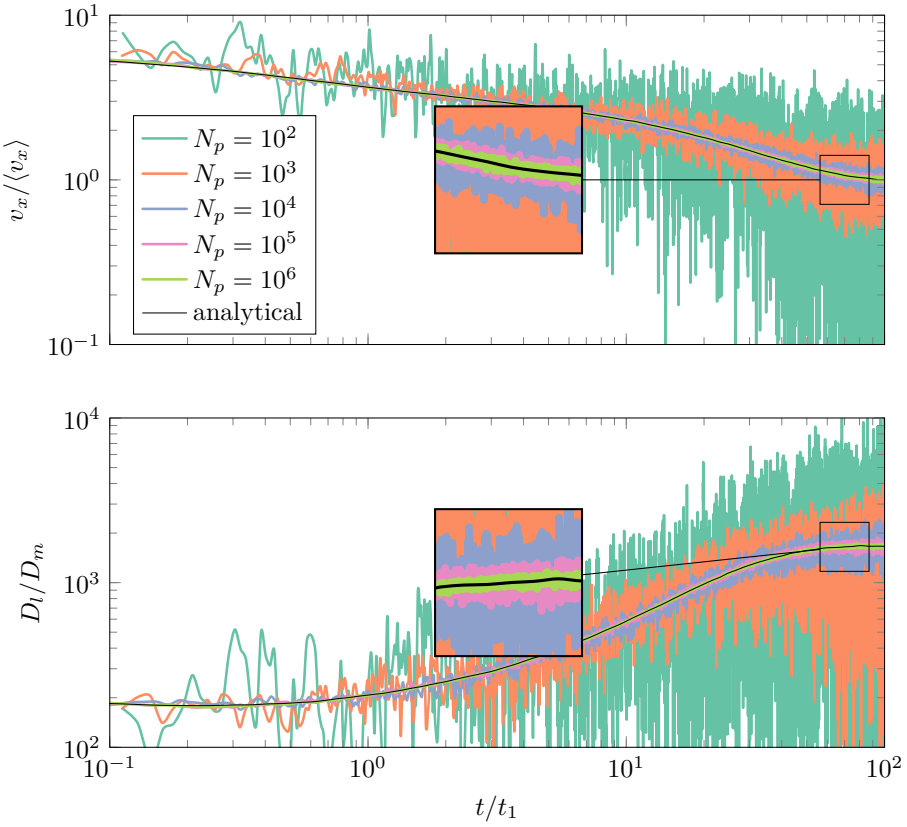


Figure 3.13: Effect of the number of particles N_p on the normalized mean particle velocity and normalized mean longitudinal particle dispersion for $Pe = 100$. This case was constructed with a uniform porosity of $\phi = 0.3$, $K = 1 \times 10^{-12}\,\mathrm{m}^2$ and $\beta = 1.8$. As the number of particles increases, the high-frequency noise reduces, and the behaviour at early times is better resolved. However the overall trend and evolution is captured in all cases.

obtained using an Intel™ Core™ i7-7700HQ processor [1].

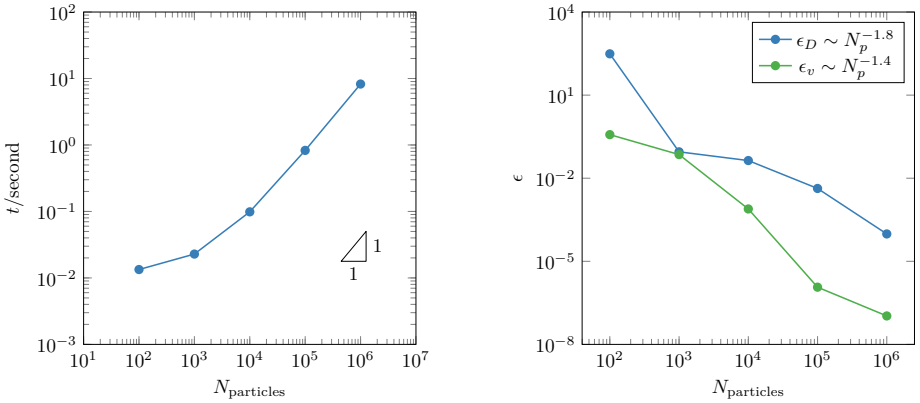


Figure 3.14: Effect of the number of particles in the time-step taken per Δt iteration and relative error in the normalized dispersion ϵ_D and normalized velocity ϵ_v. The time taken per iteration scales linearly with the number of particles for $N_p \gtrapprox 10^3$. The error decreases faster with the increase of particles.

3.2.2 Asymptotic Time Behaviour

The mean velocity and dispersion coefficients of solute plumes are key to identify transport time scales. The asymptotic behaviour will provide us means to understand if the current model is able to capture interesting transport signatures. The asymptotic analysis in Dentz et al. (2004) and Berkowitz et al. (2006) says that for the interval $1 \ll \tau \ll \tau_2$ and transport characterized by $0 < \beta < 1$, the longitudinal dispersion $D_L \propto \tau^{2\beta-1}$ and for $1 < \beta < 2$, $D_L \propto \tau^{2-\beta}$, where $\tau_2 = t_2/t_1$.

The model is validated by studying the mean velocity and longitudinal dispersion of a solute plume under three β values and several t_2 values. For convenience, the value of t_1 is kept fixed and only varied t_2. We inject $N = 10^4$ particles in the domain and observe their transport for over $t = 10^5$ s, which is equivalent to $\tau = 10^5$ if $t_1 = 1$ s. The results are consolidated in figure 3.15 and are compared against the average velocity and dispersion coefficient obtained from the numerical Laplace Transform Inversion and described in appendix A. The figures show the calculated values for the cases with different τ_2 in the symbols and the average values using solid lines.

For $\beta = 0.25$, the early behaviour of the mean velocity follows the scaling $v_m \propto \tau^{-0.75}$ and the longitudinal dispersion follows the scaling $D_L \propto \tau^{-0.5}$. For larger times, both mean velocity and longitudinal dispersion reaches a constant

[1] Intel™ Core™ i7-7700HQ – 2.8 GHz base frequency, up to 3.8 GHz with Intel™ Turbo Boost Technology, 6 MB cache, 4 cores

asymptotic value, decreasing for increasing τ_2. The time needed to reach the asymptotic value increases for increasing values of τ_2.

For $\beta = 0.75$, the early behaviour of the mean velocity follows the relationship $v_m \propto \tau^{-0.25}$ and the longitudinal dispersion follows the relationship $D_L \propto \tau^{0.5}$.

For $\beta = 1.5$, the mean velocity shows little impact in relation to τ_2 and quickly approaches a constant value. The longitudinal dispersion follows the scaling $D_L \propto \tau^{0.5}$.

The case of $\beta = 0.25$ represents sub-diffusive transport, when the dispersion decreases with time, and the case of $\beta = 0.75$ a super-diffusive transport, when the dispersion increases with time. Both cases were properly observed in the simulations, indicating the ability of the model to capture transport signatures at early times. Additionally all the cases are in agreement with the behaviour detailed in Dentz et al. (2004).

3.2.3 Hydrodynamic Dispersion

We calculate the longitudinal dispersion coefficient for 10^5 injected particles and $\beta = 0.25$, 0.75 and 1.50, the value of t_2 was kept constant and t_1 allowed to vary in order to obtain cases with different Pe numbers. Figure 3.16 shows the results compared against experimentally measured points from Pfannkuch (1963), Seymour and Callaghan (1997), Kandhai et al. (2002), Khrapitchev and Callaghan (2003), and Stöhr (2003) and are left indistinguishable for simplicity, but were differentiated in figure 2.3 of chapter 2. The model is able to capture the mean behaviour of the experiments for $\beta = 1.5$, but for the other values of β underestimates when $Pe \leq 1$ and overestimates when $Pe \geq 1$.

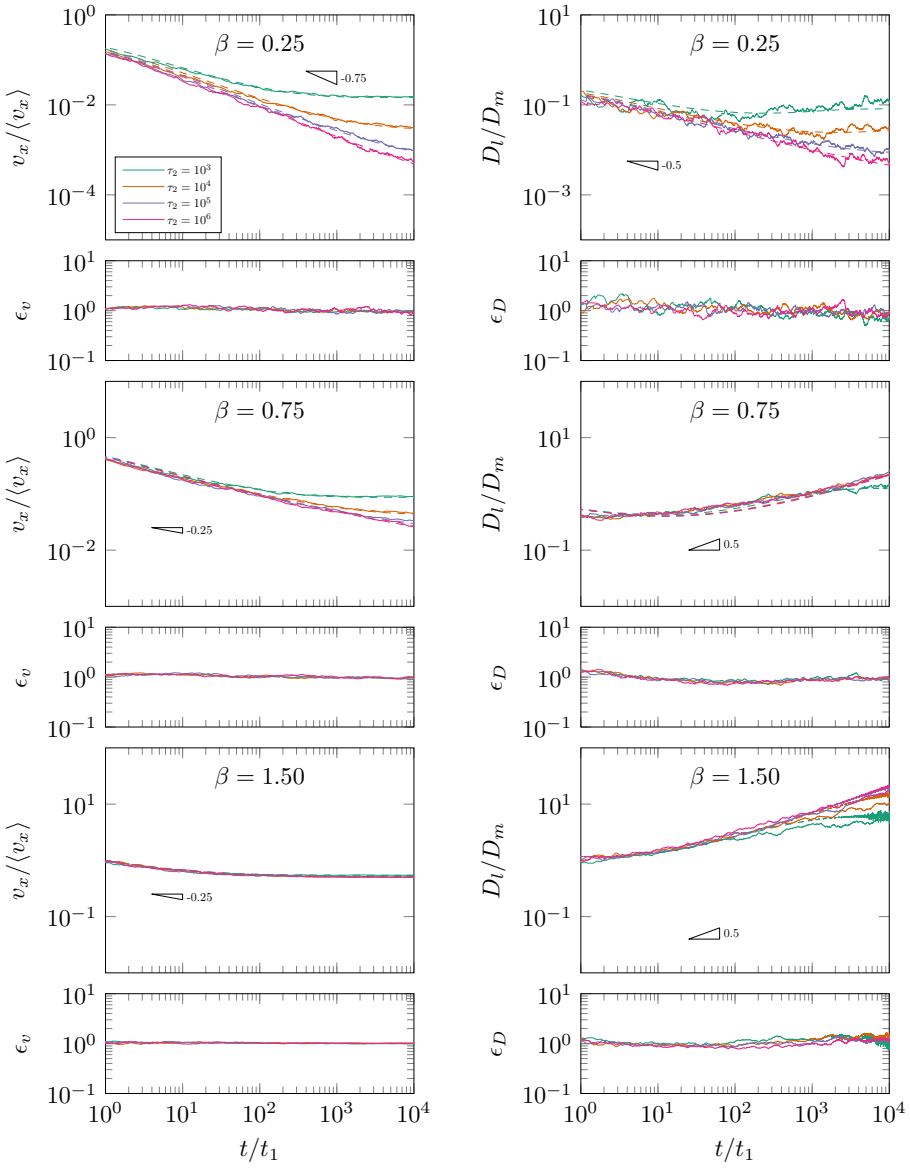


Figure 3.15: Asymptotic time behaviour for the longitudinal dispersion coefficient and the mean velocity for $\beta = 0.25$, 0.75 and 1.5 and $\tau_2 = 10^3$, 10^4, 10^5 and 10^6. For the interval $1 \ll \tau \ll \tau_2$ and transport characterized by $0 < \beta < 1$, the longitudinal dispersion $D_L \propto \tau^{2\beta-1}$ and for $1 < \beta < 2$, $D_L \propto \tau^{2-\beta}$ (Dentz et al., 2004; Berkowitz et al., 2006).

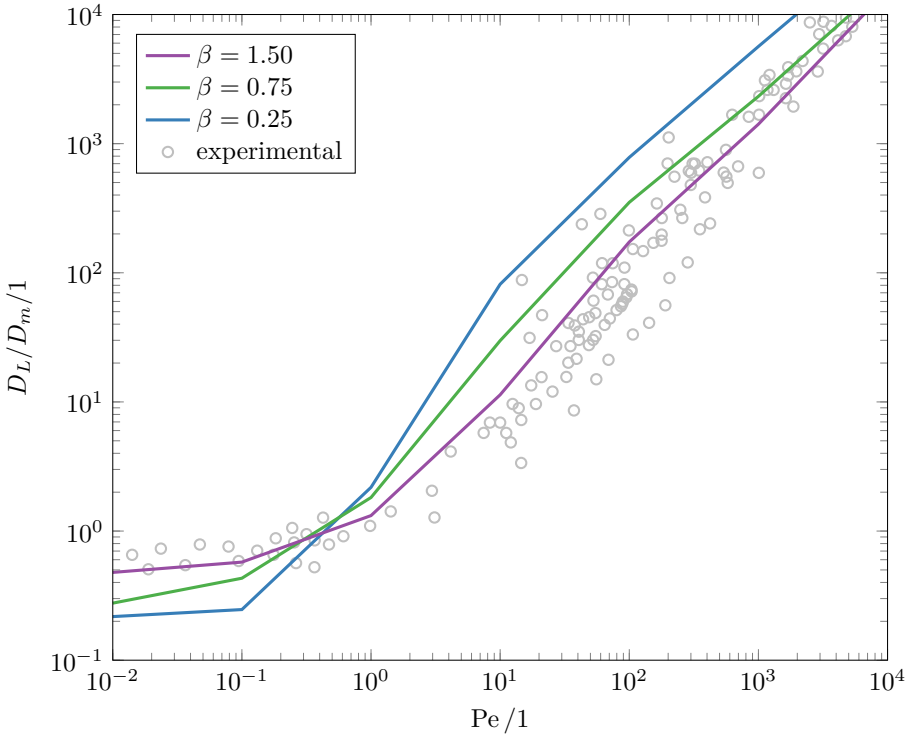


Figure 3.16: Asymptotic longitudinal dispersion coefficient for $\beta = 0.25$, 0.75 and 1.50. The increase of the β values represent the increase of heterogeneity, from highly heterogeneous sample ($\beta = 0.25$) to mildly heterogeneous sample ($\beta = 1.5$). The experimentally measured points for unconsolidated beadpacks and sandpakcs taken from the literature (Pfannkuch, 1963; Seymour and Callaghan, 1997; Kandhai et al., 2002; Khrapitchev and Callaghan, 2003; Stöhr, 2003), and are left indistinguishable from each other for simplicity, but were differentiated in figure 2.3 of chapter 2.

3.3 Transport in Representative Elementary Volumes as Sample Domains

Further to the initial examples and validation of the previous sections, this section shows the application of the method to two samples consisting of a Representative Elementary Volume (REV) with a high permeability channel and another with a spherical inclusion.

The REV samples are constructed such that each node has its property defined from the domain of interest. Figure 3.17 shows the conceptual illustration representing different materials and how they are mapped back to the nodes.

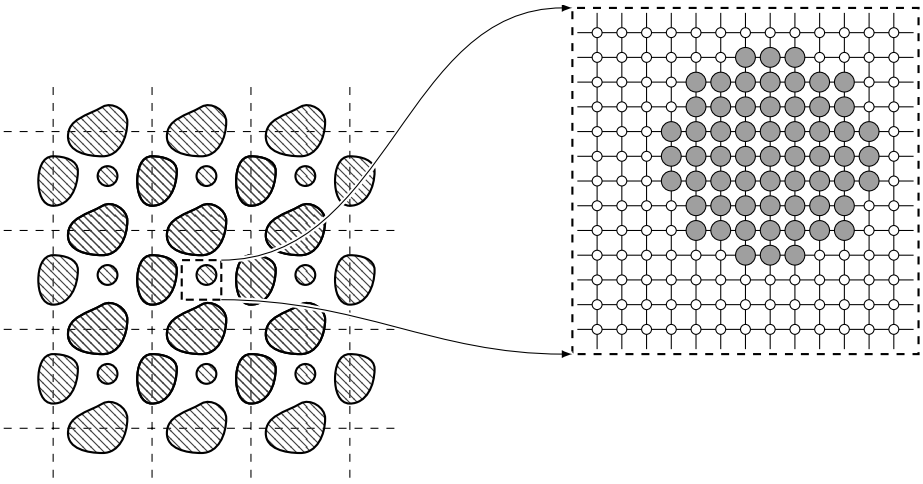
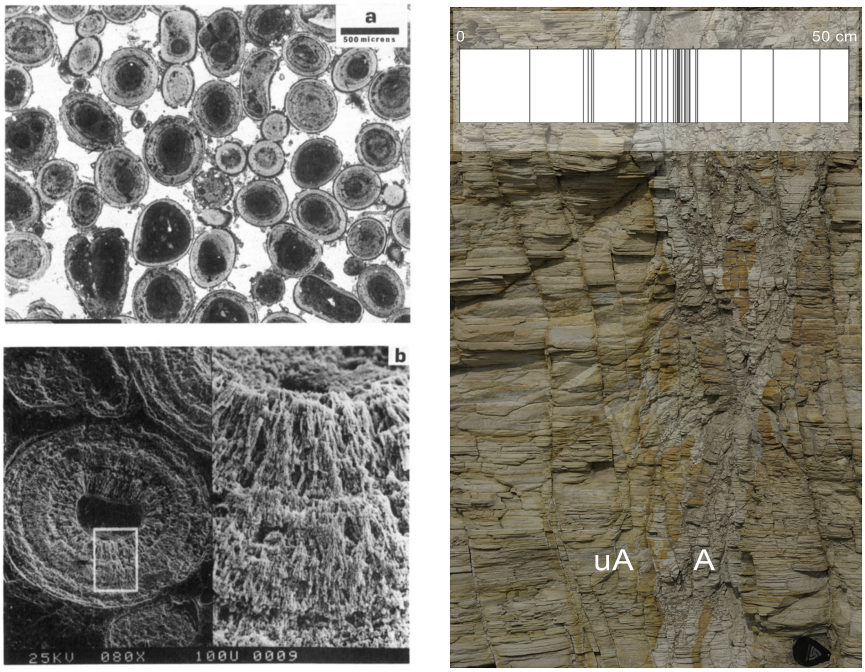


Figure 3.17: Conceptual picture illustrating the representation of two different materials and its mapping into nodes. This concept depicts porous grains within a porous matrix, however it can represent the presence of any other feature (*e.g.* channels).

The channel and spherical inclusion are constructed to resemble ooids and fractures (section 3.3), which are common fabric textures present in carbonate rocks. Ooids are spherical structures of different porosity that can be in a porous matrix or surrounded by a micrite cement (Kump and Hine, 1986). Open fractures act as the main conduct for flow and transport in a porous matrix and can span over several orders of magnitude (Laubach et al., 2018).

Section 3.3 shows the simplified geometry for the spherical inclusion and the infinite channel. Despite using 2D illustrations, both domains extend in L in the direction perpendicular to the figure plane. The spherical inclusion is centred in $(x_c, y_c) = (L/2, L/2)$ and has radius $r = L/2$. The channel is centred in the $y-$direction and has aperture $a = L/2$. Each subdomain Ω is defined by its porosity and permeability, with porosity $\phi_0 = 0.3$ and $\phi_1 = 0.015$ and

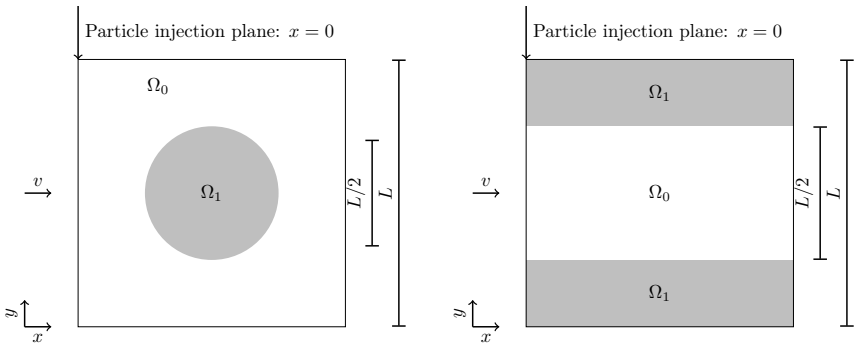


(a) Marine ooids (Kump and Hine, 1986)

(b) Open fractures (Laubach et al., 2018)

Figure 3.18: Examples of marine ooids and open fractures, common in limestones. The ooids are spherical structures of different porosity that can be in a porous matrix or surrounded by a micrite cement. The highlighted rectangle has a side of 100 µm. Open fractures act as the main conduct for flow and transport in a porous matrix. The letters uA and A stands for unaltered and altered fractures.

permeability $K_0 = 2 \times 10^{-12}\,\mathrm{m}^2$ and $K_1 = 5 \times 10^{-15}\,\mathrm{m}^2$. It is assumed that below the link resolution, the domain is nearly homogeneous with $\beta = 1.8$.



(a) Spherical inclusion (b) Infinite channel

Figure 3.19: Geometry for the (a) spherical inclusion and (b) infinite channel. Despite using 2D illustrations, both domains extend in L in the direction perpendicular to the figure. Each subdomain Ω is defined by its porosity and permeability, with porosity $\phi_0 = 0.3$ and $\phi_1 = 0.015$ and permeability $K_0 = 2 \times 10^{-12}\,\mathrm{m}^2$ and $K_1 = 5 \times 10^{-15}\,\mathrm{m}^2$.

Table 3.1 shows the parameters used to build the synthetic models. The domain is repeated $3\times$ in the $x-$direction to have larger number of nodes in the flow direction. Particles are injected in the origin of the $x-$axis and are subjected to symmetry condition at the boundaries of the domain.

Table 3.1: Domain properties and parameters used for the domain consisting of spherical inclusion and infinite channel. The properties of each subdomain are different but are kept constant within the subdomains.

Parameter	Symbol	Value	SI Unit
Porosity in Ω_0	$\phi_{\Omega 0}$	0.3	
Porosity in Ω_1	$\phi_{\Omega 1}$	0.015	
Permeability in Ω_0	$K_{\Omega 0}$	1.69×10^{-12}	m^2
Permeability in Ω_1	$K_{\Omega 1}$	1.69×10^{-12}	m^2
REV Length	L	0.1	m
Heterogeneity parameter	β	1.8	
Number of nodes in x	N_x	150	
Number of nodes in y and z	$N_{y,z}$	50	

Each case was studied under 3 different advective regimes, from low to high advective transport characterized by $Pe = 10, 100$ and 1000. A pressure gradient of $\Delta P = 1$ was imposed in each REV cell, and adjusted such that the $t_1 =$

$l/v = 1$, and $t_2 = Pe/t_1$ can then be estimated from the Pe numbers as $t_2 = 10$, 100 and 1000. The results for the particles displacement at $t/t_1 = 0.5$ are shown in figure 3.20. Lower Péclet numbers are characterized by a smeared out plume when compared to higher Péclet numbers. The porosity and permeability contrast between the subdomains traps the particles in the lower permeability and porosity regions. As no particles are initially inside the spherical inclusion at the initial state, the plume formed by the particles disperses more gradually. This is not possible to observe for the channel domain, where particles that start moving outside the channel struggle to leave the lower porosity regions.

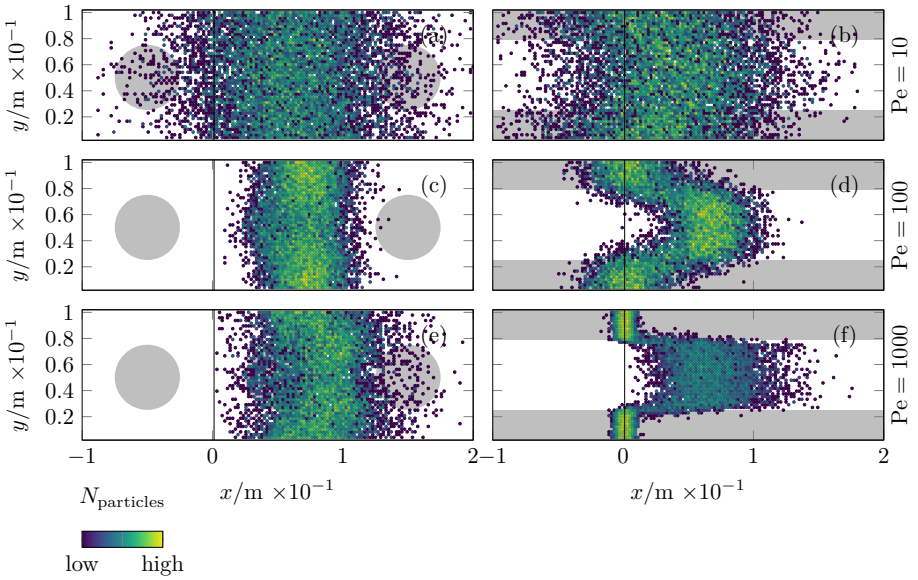


Figure 3.20: Snapshot of particle positions for different Pe at $t/t_1 = 0.5$. Lower Pe are characterized by a smeared out plume when compared to higher Pe numbers. The porosity and permeability contrast between the subdomains properties traps the particles in the spherical inclusions.

To highlight the plume formed by the particle transitions on the lattice, the particle propagator distribution is calculated and shown in figure 3.21 for both domains for the Pe numbers studied. The particle propagator distribution is normalized by the mean particle displacement, so that the particles having $\zeta/\langle\zeta\rangle_0 = 1$, represent exactly the mean displacement. The propagator distribution deviation from a single peak at $\zeta/\langle\zeta\rangle_0 = 1$ is expected to have a Gaussian shape if it were a solution of the ADE. Despite observing a near-Gaussian shape for the spherical inclusions in figure 3.21, the same behaviour is not seen for the channelized domain. The initial particle distribution at the lower porosity subdomain leave a strong imprint in the particle distribution, with a sharp stagnant

peak at $\zeta/\langle\zeta\rangle_0 = 0$ for highly advective regimes.

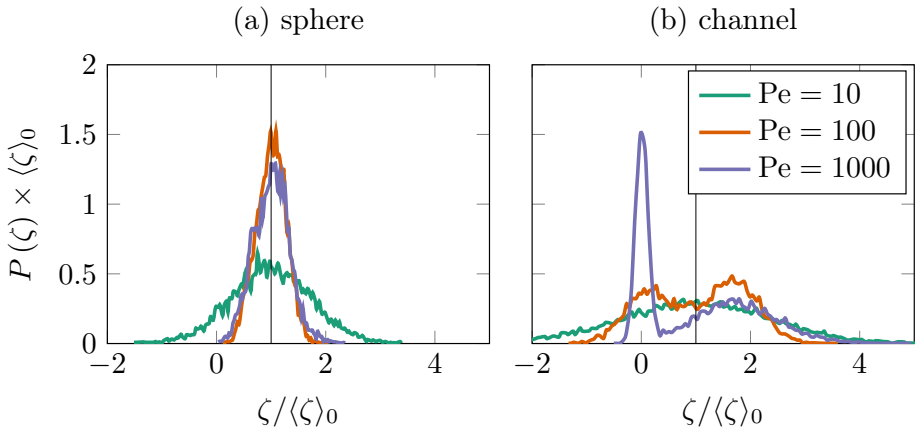


Figure 3.21: Particle propagators at $t/t_1 = 0.5$ for different Pe in the (a) sphere and (b) channel domains. The propagator distribution is calculated from the distribution of the particle displacement ζ normalized by the mean particle displacement $\langle\zeta\rangle_0$.

The normalized mean particle velocity is displayed in figure 3.22 and the normalized longitudinal particle dispersion in figure 3.23. The mean particle velocity v_x is calculated from the mean displacement of the plume of particles. The results are normalized by the transit time t_1, These results are also displayed for $Pe = 10, 100$ and 1000, showing little sensitivity to the mean velocity evolution, but this sensitivity is more evident in the evolution of the longitudinal dispersion. The mean velocity monotonically decreases for all cases, more prominently for $Pe = 1000$. This behaviour was previously highlighted in figure 3.15 and it is supported by the asymptotic analysis of the CTRW model in Dentz et al. (2004). Figure 3.15 shows that the higher τ_2, or the higher the Pe, longer it takes to achieves the asymptotic velocity using the CTRW framework.

It is observed that for $t/t_1 > 10^{-2}$ the normalized mean velocity is already $v_x/\langle v_x\rangle \to 1$, which is usually expected at later times when $t/t_1 \gg 1$. Longitudinal dispersion increases with time, characteristic of the super-diffusive transport regime, and similarly to the mean velocity this behaviour is also observed earlier, already at $t/t_1 > 10^{-2}$.

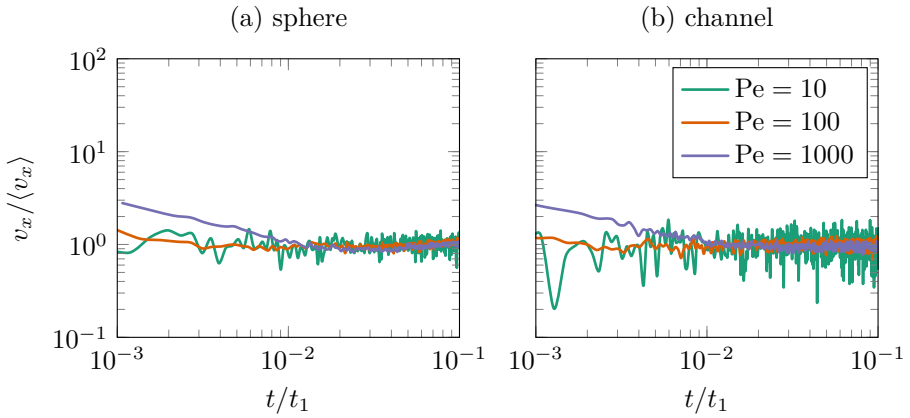


Figure 3.22: Normalized mean particle velocity $v_x/\langle v_x \rangle$ along the main flow direction for the (a) sphere and (b) channel domains and $Pe = 10, 100$ and 1000. The time is normalized by the mean advective time so that for times larger than $t/t_1 \gg 1$ the normalized particles mean velocity approaches asymptotically $v_x/\langle v_x \rangle \to 1$. It is evident that this behaviour is already observed for $t/t_1 > 10^{-2}$.

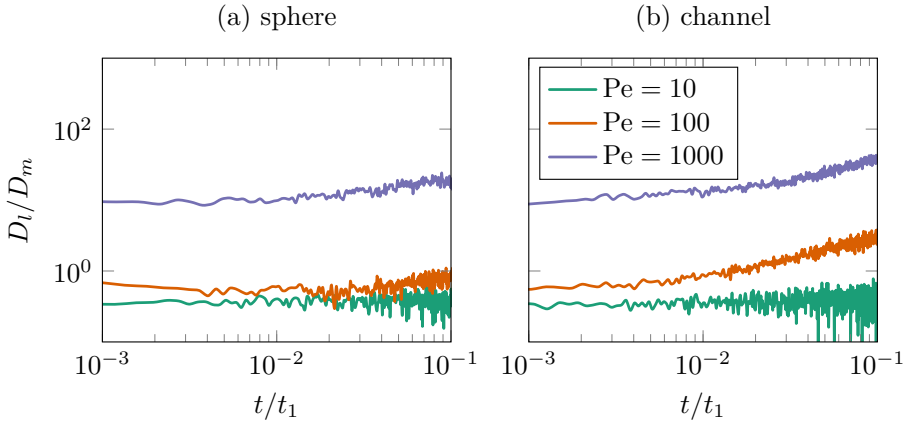


Figure 3.23: Normalized longitudinal particle dispersion D_l/D_m for the (a) sphere and (b) channel domains and $Pe = 10, 100$ and 1000. Longitudinal dispersion increases with time, characteristic of the super-diffusive transport regime, observed when $t/t_1 > 10^{-2}$.

3.4 Conclusions

This chapter described the CTRW particle transport model that is used in the work presented in this thesis. The first section shows the flow model on a lattice. This model is constructed honouring Darcy's law of flow in porous media, meaning that at the scale of interest, represented by the nodes and links, the flow rate behaves linearly with the pressure gradient (Whitaker, 1999). Transport in traditional models is represented by a diffusive Fick's law assuming that there is no sub-grid heterogeneity which is rarely the case (Adams and Gelhar, 1992; Scheven et al., 2005a), and even for controlled and homogeneous systems (Levy and Berkowitz, 2003), there is a heterogeneity below a scale l that cannot be accounted for with Advection Diffusion type models. It is important to note that transport in porous media is rarely Fickian.

As an alternative to account for these limitations the transport model is built using the CTRW framework. With the correct choice of transit-time distributions, CTRW accounts for unresolved heterogeneities below the scale l of the links and nodes, $l < L$, enriching the parameter space of the model (Berkowitz et al., 2006). The model is implemented using the TPL equation (3.12) to represent the transit-time function $\psi(t)$. This equation $\psi(t_1, t_2, \beta)$ is then described using two characteristic times, one advective and other diffusive, and the fitting parameter β is a proxy for the heterogeneity of the porous medium. Observations such as Fickian or non-Fickian transport signatures are possible to be captured by carefully choosing a combination of t_1, t_2 and β. Using the parameter β, it is possible to enrich the given homogenous characteristic of the model in which the links and nodes are assumed to represent and account for additional non-resolved heterogeneities.

The particle transport model is validated by studying asymptotic transport behaviour of a plume of particles. The model predictions are consistent with the results in the literature, examined for different values of the characteristic times t_1, t_2 and choices of the fitting parameter β. The combination of parameters showed the ability to model sub- and super-diffusive systems. Furthermore the model also captures the hydrodynamic dispersion over 6 orders of magnitude, and the model sensitivity to the β parameter demonstrates how it can be used to represent samples with different physical heterogeneity.

The model was then used to study idealized representations of fabric texture features that are often present in limestones. Despite simply using average parameters, the models are still able to show particle propagator distributions characterized by strong non-Gaussian imprints. This was even obtained with $\beta = 1.8$ that is associated with homogeneous materials, meaning that the transport signatures are mostly driven by the geometrical features that are much

coarser than the homogenous features assumed to be represented within links and nodes of the model. Although β can be used to represent under-resolved heterogeneity of the different materials, in this chapter it was kept constant and equal for all subdomains to allow for a simpler and direct comparison of the results. We will further explore the ability of β to represent porous media with different physical or flow and transport heterogeneity in chapter 5 of this thesis.

The CTRW-based model described in this chapter lays the foundation for the modelling work in the next three chapters; in which the model is first extended to include reactive flow (chapter 4) and later employed to study the impact of physical (chapter 5) and chemical heterogeneity (chapter 6) impact on the effective reaction rates in carbonate rocks.

CHAPTER 4

Predicting Dissolution in Porous Media using CTRW and Validation with NMR Data

In the previous chapter transport was modelled coupling flow calculated in a lattice and solute transport described in a Lagragean particle system. This chapter looks at how to incorporate single-species reactions in this model using a first-order kinetic model. This represents a novel development of Continuous Time Random Walk (CTRW) to describe reactive transport.

Our modelling approach is conceptually described as follows: a particle contains a number of moles of aqueous calcium. Particles are not created or destroyed; instead the number of moles associated with a particle changes over time. The aqueous calcium concentration is defined as the sum of the moles associated with each particle in a given volume. Solute transport is then modelled as particle transitions in a lattice, carrying the chemical components from site to site. Reactions are then accounted for as interactions between the chemical components in the particles and the chemical components in the lattice nodes, representing the solid.

Figure 4.1 illustrates the transport and reaction of a single particle and shows a given transition step. We describe the state of a particle p in terms of its position $\mathbf{x}$, number of moles of transported species (calcium in this paper) n and time t, or $p(\mathbf{x}, n, t)$. The particle transitions are controlled by the particle

displacement $\Delta\mathbf{x}$ and transit-time $\Delta\tau$, which are sampled from a Probability Density Function (PDF) that is derived from the flow and transport properties. Such properties are calculated from the pressure and flow field resolved in the lattice. At the end of every transition, the change of aqueous calcium moles associated with a particle Δn and the porosity $\Delta\phi$ in the node of origin is positive due to calcite dissolution at the node during the transit-time.

As the porosity increases, this modifies the underlying pore space, changing the flow field, and leading to the appearance of different dissolution patterns, *e.g.* channels. Those patterns are likely going to dominate the flow, focusing subsequent particle trajectories in such regions.

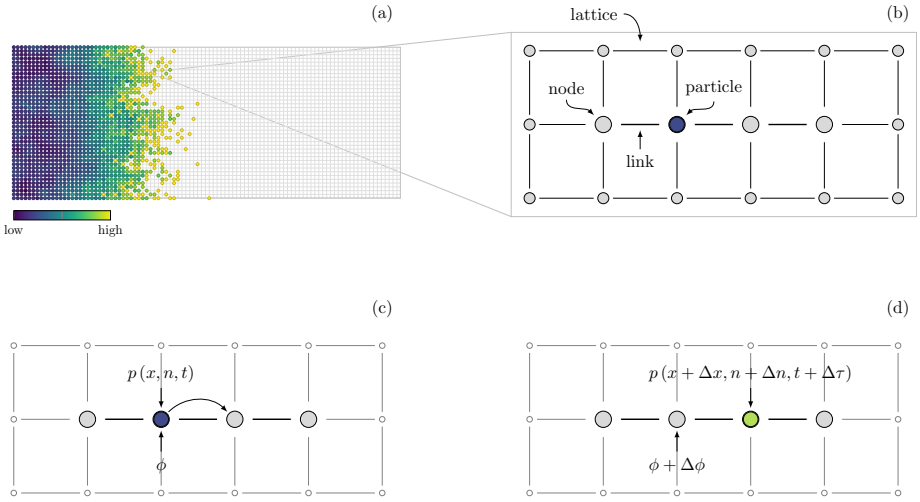


Figure 4.1: Simplified illustration of an ensemble of particles (a) and the detailed representation of a single particle (b) transiting and reacting through a lattice (c-d). The increase of blue depicts an increase of the aqueous calcium concentration. A particle transits in the lattice with variable transit-time $\Delta\tau$ and displacement Δx. After each transition, the number of moles of aqueous calcium in a particle increases by Δn, as a consequence of the reaction within the node of origin, which in turn has its porosity increased by $\Delta\phi$.

4.1 Description of the Reactive Transport Model

The main assumption in our reaction model is that dissolution is modelled with first-order kinetics in an ideal solution. We also do not allow the fluid to become over-saturated, so we do not allow precipitation. Finally, we will assume a constant specific surface area for reaction which does not change over time.

As described in Chapter 3, we discretize our domain as a lattice with proper-

ties defined in both nodes and links. This lattice represents a Ketton limestone, which is nearly entirely composed of calcite (Andrew et al., 2014). Thus we define the number of moles of calcium in each node which is equal to the number of moles of calcite:

$$n_{i\,\mathrm{Ca^{2+}}} = n_{i\,\mathrm{CaCO_3}} = (1-\phi_i)\,V\frac{\rho_{\mathrm{CaCO_3}}}{M_{\mathrm{CaCO_3}}}, \tag{4.1}$$

where $V = l^3$ is the effective volume of the node, ϕ_i the porosity of the node, ρ the density of calcite ($2.71 \times 10^3\,\mathrm{kg/m^3}$) and M the molar mass of calcite ($0.1\,\mathrm{kg/mol}$).

Dissolution occurs as particles containing acid, or H^+ rich particles, are injected in the domain and are allowed to react with the calcite rich nodes in the lattice.

This releases calcium from solid (in calcium carbonate) to the aqueous phase. We track the amount of calcium in the aqueous phase, following the approach of Pereira Nunes et al. (2016a) and Pereira Nunes et al. (2016b).

Dissolution is assumed to be first-order with the concentration of H^+, so that it be described with a first-order kinetic model where the number of moles of Ca^{2+} in a particle $n_{\mathrm{Ca^{2+}}}$, or simply n, is

$$\frac{dn}{dt} = k_r\,(n_{\mathrm{eq}} - n)\,, \tag{4.2}$$

where n_{eq} is the number of moles in a particle in the equilibrium, $n_{\mathrm{eq}} - n$ represents the departure from equilibrium and k_r is the reaction rate constant. Equation (4.2) can be solved analytically such that

$$n = n_{\mathrm{eq}}\left(1 - e^{-k_r t}\right). \tag{4.3}$$

In this chapter, and as we show later in section 4.4, we will employ this model to study the dissolution of calcite using a strong acid and under an advective regime, making the first-order simplification appropriate to this case.

The increase in moles of calcium associated with a particle is calculated in the node of origin at the end of each transition. The change of moles of aqueous calcium, Δn, is assumed to be proportional to the particle transit-time, such that equation (4.2) is approximated to:

$$\frac{dn}{dt} \approx \frac{\Delta n}{\Delta \tau} = k_r\,(n_{\mathrm{eq}} - n)\,, \tag{4.4}$$

with the particle transit-time chosen from the distribution defined in equation (3.12).

Figure 4.2 illustrates the conceptual description of this process coupling par-

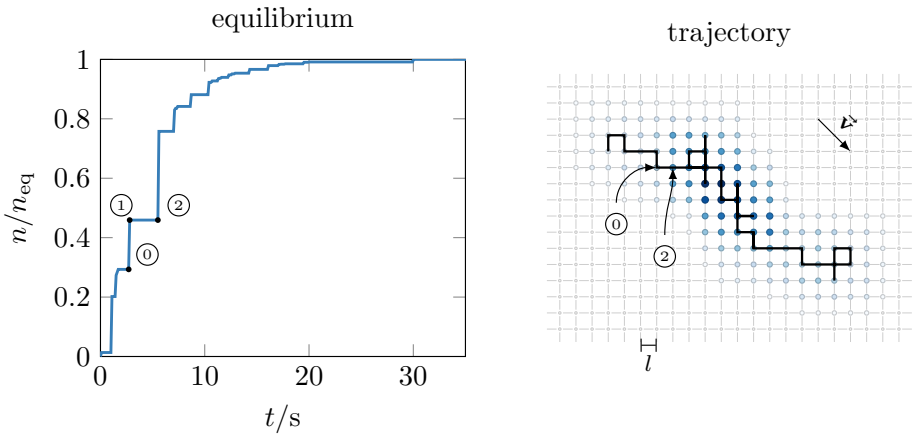


Figure 4.2: Particle equilibrium and trajectory in a 2D lattice. The lattice has fixed values of $t_1 = 0.03\,\mathrm{s}$, $t_2 = 3.0\,\mathrm{s}$ and $\beta = 1.6$ and the particle reacts with it using $k_r = 0.2\,\mathrm{s}^{-1}$. The particle step goes from ⓪ to ②, where from ⓪ to ① the particle reacts with the node of origin and from ① to ② it moves from the node of origin to the target node.

ticle transport and reaction in the lattice. Figure 4.3 shows the evolution of moles of Ca^{2+} for two different particles and the mean evolution for an ensemble of 100 000 particles as they transit and react in a homogeneous system. This system is represented by a constant characteristic times $t_1 = 0.03\,\mathrm{s}$, $t_2 = 3.0\,\mathrm{s}$ and $\beta = 1.6$, and the reaction rate constant is $k_r = 0.2\,\mathrm{s}^{-1}$. The Ca^{2+} evolution is compared against the analytical solution in equation (4.3).

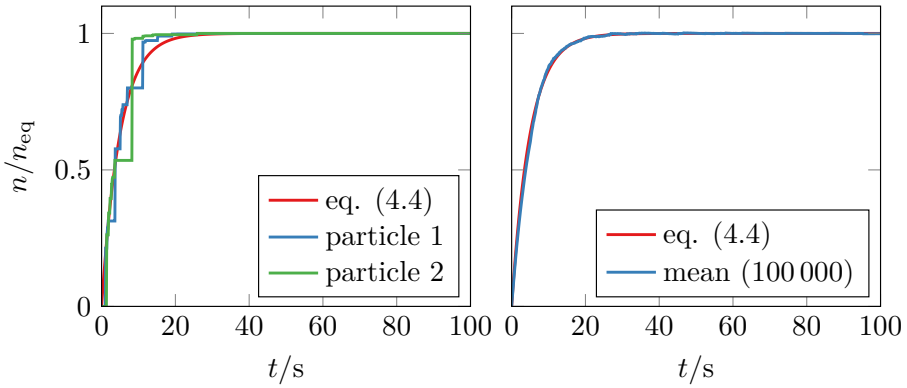


Figure 4.3: Comparison between the analytical solution of the moles of aqueous calcium defined in equation (4.3) and the simulated results using equation (4.4) and equation (3.12) for (a) two particles and for (b) the mean of 100 000 particles. The model uses $k_r = 0.2\,\mathrm{s}^{-1}$, $t_1 = 0.03\,\mathrm{s}$, $t_2 = 3.0\,\mathrm{s}$ and $\beta = 1.6$. The change in the number of moles of aqueous calcium associated with each particle is proportional to the particle transit-time at the end of each transition.

The increase of moles of dissolved calcium in the particle incurs a decrease of moles of calcite in the lattice nodes, such that after a transit-time $\Delta\tau$, the particle increases its moles by Δn and the node from which the particle originated its transition loses the same number of moles. As we assume that the solid domain is composed entirely of calcite, removing calcite from a node proportionally increases the porosity. We relate the increase of porosity ϕ_i with the amount of calcite n_i in the node after a particle transition,

$$\Delta\phi_i = \phi_i^{t+\Delta\tau} - \phi_i^t, \tag{4.5a}$$

$$\Delta n_i = n_i^{t+\Delta\tau} - n_i^t = k_r \Delta\tau (n_{eq} - n_i^t). \tag{4.5b}$$

From equation (4.5a) and equation (4.1) we relate the change of porosity ϕ_i with the change of calcite moles in the node and to the corresponding change in Ca^{2+} moles in the particle as

$$\Delta\phi_i = \Delta n_i \frac{M_{\mathrm{CaCO_3}}}{V_i \rho_{\mathrm{CaCO_3}}}. \tag{4.6}$$

To estimate the reaction rate constant k_r of the particles in a node, we relate it to the surface reaction rate r measured in laboratory experiments as

$$k_r = \frac{V \sigma_A}{n_{\mathrm{eq}}} r, \tag{4.7}$$

where $\sigma_A = A/V$ is the specific surface area of the node, which we assume is constant throughout the domain, and during the dissolution processes, and is defined as the area A over the volume V of the node. This is a strong assumption, but, as we show later, allows accurate predictions to be made. The batch reaction rate, r, was measured by Peng et al. (2015) to be $1.5 \times 10^{-3}\,\mathrm{mol\,m^{-2}\,s^{-1}}$ and is used to estimate $k_r = 6.28 \times 10^{-1}\,\mathrm{s^{-1}}$ where the other parameters used are given in table 4.1.

Table 4.1: Model properties and dissolution parameters.

Parameter	Symbol	Value	SI Units
Total simulation time	$t_{\max}$	1.25×10^{4}	s
Volumetric flux	Q	5.3×10^{-7}	$\mathrm{m^3\,s^{-1}}$
Mean velocity	v	3.06×10^{-3}	$\mathrm{m\,s^{-1}}$
Molecular diffusion coefficient of Ca^{2+} (Luquot and Gouze, 2009)	$D_{m_{Ca^{2+}}}$	2.2×10^{-9}	$\mathrm{m^2\,s^{-1}}$
Heterogeneity parameter	β	0.9	
Specific surf. area (Menke et al., 2015)	σ_A	8.0×10^{3}	$\mathrm{m^{-1}}$
Surf. reaction rate (Peng et al., 2015)	r_{calcite}	1.5×10^{-3}	$\mathrm{mol\,m^{-2}\,s^{-1}}$
Reaction rate constant	k_r	6.28×10^{-1}	$\mathrm{s^{-1}}$
Particle equilibrium	n_{eq}	8.3×10^{-10}	mol
Longitudinal model size	L_x	7.2×10^{-2}	m
Transversal model size	$L_{y,z}$	1.9×10^{-2}	m
Total number of links	N_{links}	1.89×10^{6}	
Total number of nodes	N_{nodes}	6.48×10^{5}	
Number of injected particles per Δt	$N_{\text{particles}}$	1.0×10^{3}	

4.2 Reactive Transport Algorithm

The algorithm describing the transport and reactive model consists of three solvers:

1. Flow solver – calculates the pressure gradient, and hence the local velocities, the initial transit-time and displacement probability functions (defined in chapter 3).

2. Transport solver – solves for the individual particle transitions within a time step (defined in chapter 3).

3. Reactive solver – calculates the calcite dissolution and porosity alterations proportional to the particle transit-time (defined in this chapter).

Each particle transits independently of one another; we require that after a number of transitions, we synchronize all particles at a common checkpoint with a time-step Δt. The synchronization is needed to have the particles stationary at a particular time so that the pressure field can be re-calculated by the flow solver while the time and displacement probabilities are updated. Particles are continuously injected in the domain, but for practical reasons and in order to conserve reactant influx in the model, we do it at every Δt checkpoint, such that the injected volume, $\mathrm{Vol} = Q\Delta t$, is consistent between the flow and transport solvers. The particles are only considered valid and kept in the simulation while $|n - n_{\text{eq}}| > \epsilon$, with ϵ being the computer's floating point precision. The particles are also removed from the simulation if they reach the exit boundary, $x > L_x$,

such that no back-diffusion is allowed at the outflow. This is to ensure the computational efficiency of the simulation.

The steps in the algorithm are listed below:

1. Create the lattice with an initial distribution of porosity ϕ and permeability K.
2. Solve the pressure field P in the lattice, calculate the local velocities v_{ij} and local Péclet numbers Pe_{ij} in the links.
3. Calculate the local probabilities of displacement p_{ij} (equation (3.14)) and the local transit-time distribution ψ_{ij} (equation (3.12)) in the links.
4. Inject the particles in the inlet using a flow-weighted injection rule.
5. Sample a displacement direction $\Delta\mathbf{x}$ from p_{ij} and transit-time $\Delta\tau$ from ψ_{ij} for each particle.
6. Move the particle from the node i to the node j, if $\sum \Delta\tau^m \leq \Delta t$, where m labels each particle transition. This is performed individually for each particle.
7. Increase the moles of aqueous calcium in the particle moles by Δn (equation (4.5b)) using the sampled transit-time $\Delta\tau$.
8. Dissolve the solids in the node of origin i and increase the porosity by $\Delta\phi_i$ (equation (4.6)).
9. Repeat steps 5 – 8 for all particles while $\sum \Delta\tau^m \leq \Delta t$. Each particle can undergo several transitions in one time step before the pressure field is updated.
10. Update the pressure field P if the mean porosity change is higher than a given threshold.
11. Repeat steps 2 – 10 until the end of the simulation.

The pressure field needs to be updated after the particles have changed the porosity in the nodes. At the end of each time step Δt, we calculate the domain mean porosity difference $\Delta\phi^m$ and the total porosity change since the last pressure update $\sum_{m=t}^{t+n} \Delta\phi^m$. If the total porosity change since the last pressure update is smaller than a given precision ϵ_ϕ we continue, otherwise the pressure field is re-calculated. The present study found that $\epsilon_\phi = 1 \times 10^{-4}$ was sufficient to keep the results consistent, in that more frequent recomputations of the flow field did not affect the results, as shown later in section 4.5.2.

4.3 NMR Experimental Data Description

Ketton limestone dissolution was characterized using Nuclear Magnetic Resonance (NMR) propagators and imaging techniques. These experiments were performed by collaborators at the Magnetic Resonance Research Centre (MRRC) at the University of Cambridge. Molecular propagators and 1D porosity profiles were continually acquired during the whole duration of the experiment, and a 3D porosity map was acquired at the beginning and at the end of the experiment. This data was used to calibrate the modelling method proposed in this study. All NMR measurements were done using a Bruker BioSpin AV spectrometer with a 2 T horizontal bore superconducting magnet (85 MHz ^{1}H frequency) and a 60 mm diameter birdcage radiofrequency (RF) coil.

The cylindrical Ketton sample had a length and diameter of 0.072 m and 0.038 m respectively, and was mainly composed of calcite (Andrew et al., 2014).

The whole experiment lasted for approximately 3.5 h and a total of 10 L of 0.01 mol L^{-1} HCl was injected through the sample: initially the sample was fully-saturated with distilled water. The measured flow rate was 8.3×10^{-7} m^3 s^{-1}, with a superficial velocity of 3.06×10^{-3} m s^{-1}.

The Péclet and Damköhler (Menke et al., 2016) numbers are defined as

$$\mathrm{Pe} = \frac{L\langle v\rangle}{D_m} \tag{4.8a}$$

$$\mathrm{Da} = \frac{\pi r}{\langle v\rangle n} \tag{4.8b}$$

and is calculated as $\mathrm{Pe} = 5.9 \times 10^2$ and $\mathrm{Da} = 7.7 \times 10^{-5}$. Table 4.2 contains a summary of the experimental parameters.

1D porosity profiles were acquired with a spin echo sequence with readout gradient. The measurements were optimised for minimum echo-time to avoid a relaxation or motion weighting of the overall signal in order to produce quantitative local porosity measurements. 256 complex data points were acquired with a spectral bandwidth of 400 kHz and an echo time of 0.96 ms. The field-of-view (FOV) was set to 112.8 mm giving a spatial resolution of the local porosity of 0.44 mm. Gravimetric measurements of average porosity were made for individual cores and the signal amplitude of the profiles scaled accordingly to provide quantitative porosity measurements. 3D images, using the RARE (Hennig et al., 1986) acquisition method, were acquired with $256 \times 128 \times 128$ voxels and an isotropic resolution of 391 µm; a recycle time of 1.5 s, echo time of 2.8 mm, and RARE-factor of 32 giving a total image time of 43 min 47 s. For both 1D and 3D images, hard pulses were used for both the 90° and 180° pulses and trapezoidal

Table 4.2: Ketton carbonate sample properties and dissolution experiment parameters.

Parameter	Symbol	Value	SI Units
Volume injected	$\mathrm{Vol}_{\mathrm{HCl}}$	1.0×10^{-2}	m^3
Concentration	c_{HCl}	1.0×10^{-2}	$\mathrm{mol\,L}^{-1}$
Total time	$t_{\max}$	1.25×10^{4}	s
Volumetric flux	Q	8.3×10^{-7}	$\mathrm{m}^3\,\mathrm{s}^{-1}$
Mean velocity	v	3.06×10^{-3}	$\mathrm{m\,s}^{-1}$
Mean initial porosity	$\bar{\phi}_0$	0.24	
Molecular diffusion coefficient	D_m	2.1×10^{-9}	$\mathrm{m}^2\,\mathrm{s}^{-1}$
Sample length	L	7.2×10^{-2}	m
Sample radius	R	1.9×10^{-2}	m
Péclet number	Pe	5.9×10^{2}	
Damköhler number	Da	7.7×10^{-5}	

gradients were used to minimise the echo-time.

The probability distribution of molecular displacements $P(\zeta)$, also known as a propagator, is obtained by observing water molecule displacements ζ during a given observation time Δ. Molecular propagator distributions are often normalized by the mean displacement ζ_0, indicating the transport heterogeneity when the distribution is far from $\zeta/\zeta_0 = 1$ and have asymmetrical shape (Scheven et al., 2005a). Under-sampled and spatially resolved propagator measurements were used to monitor the change in the distribution of fluid displacement as a function of position along X. Spatially Resolved Propagators (SRPs) were acquired using a modified alternating gradient pulse stimulated echo (AGPSTE) sequence (Cotts et al., 1989), where the acquisition is done in the presence of a readout gradient to obtain a spatially (x) resolved acquisition. The undersampling and reconstruction of the propagator was performed as previously described (Colbourne et al., 2016), with the individual reconstruction of q-space for each point in k-space. The spatially resolved dimension was acquired with the same parameters as the 1D profile experiments described above. The displacement encoding acquisition parameters were as follows: observation time, $\Delta = 250\,\mathrm{ms}$; number of acquired q-space points, 41; gradient pulse duration, $\delta = 2.5\,\mathrm{ms}$; and maximum applied magnetic field gradient strength, $g_{\max} = 10.5\,\mathrm{G\,cm}^{-1}$. The flow gradient was aligned with the superficial flow direction.

The 1D profiles and SRPs were acquired at 966 s intervals throughout the dissolution experiment whereas the 3D images were acquired before dissolution had started and at the end of the dissolution experiment after 10 L had flowed through the rock core.

4.4 Results

The section starts by presenting the NMR experimental results from Ketton limestone dissolution, detailing the 1D porosity profiles evolution, the 3D porosity images and finally the SRPs. Furthermore, we show the Ketton limestone model in section 4.5 and then in section 4.5.2 we describe the calcite dissolution model, detailing the results for the evolution of porosity, dissolution rate and particle propagators and comparing it with the experiment.

4.4.1 Porosity Profiles

NMR measures the intensity of magnetization at a given region, which is proportional to the number of protons subjected to NMR excitation (Chen et al., 1992). For a fully saturated rock sample, the amount of protons is directly related to the pore space of the sample, then NMR intensity is proportional to the porosity (Fordham et al., 1999).

The 1D porosity profiles were obtained at fixed intervals of 966 s, capturing not only the sample but the rock core holder entry and end effects, as illustrated in figure 4.4. The sample is located between the origin and approximately 0.072 m. The profiles show that the highest porosity alteration is in the first 0.015 m of the sample, then is sharply reduced, remaining nearly constant in the 0.035 m to 0.055 m interval, while the alteration in porosity is almost negligible near the outlet. The fluctuations in porosity reflect the natural heterogeneity of the rock.

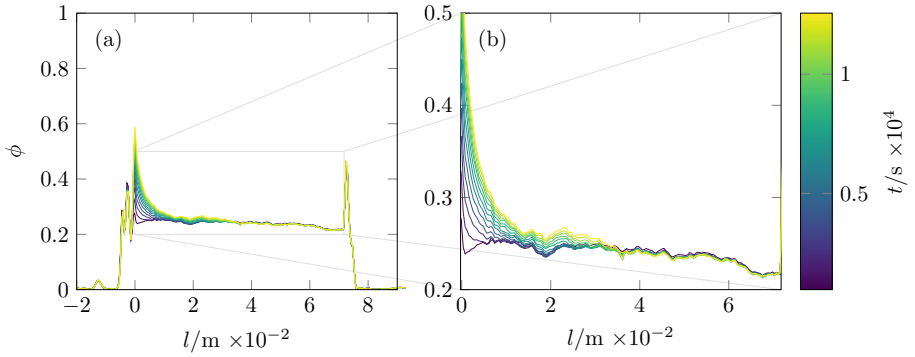


Figure 4.4: (a) Porosity profile evolution from the beginning to the end of the dissolution experiment. (b) The region where the sample is located is highlighted from approximately 0 m to 0.072 m. The porosity profiles are coloured accordingly to the acquisition time, from the beginning of the experiment to the end at 1.254×10^4 s. The highest porosity alteration can be seen in the first 0.015 m of the sample, reducing sharply and is nearly absent after 0.055 m.

This behaviour is better illustrated in figure 4.5, where we display the relative difference in the porosity as the dissolution experiment progresses; the change in porosity is limited to the first 0.05 m nearest the inlet.

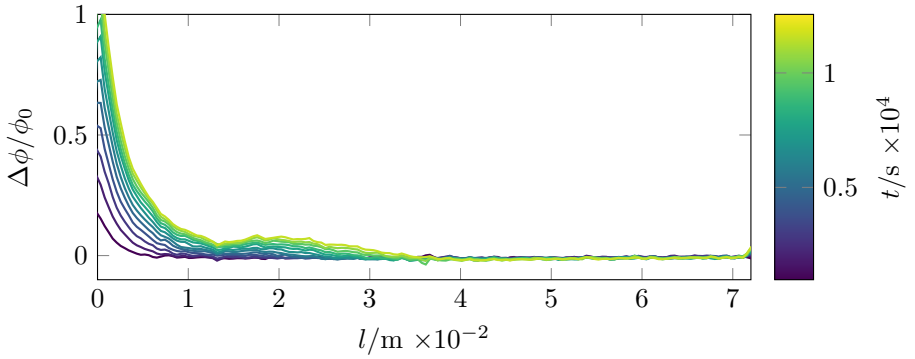


Figure 4.5: Evolution of porosity difference from the beginning to the end of the dissolution experiment. The region where the sample is located between 0.00 m and 0.072 m. The porosity profiles are coloured accordingly to the acquisition time, from the beginning of the experiment to the end at 1.254×10^4 s.

4.4.2 MRI Acquisition

Magnetic Resonance Imaging (MRI) acquisitions are obtained by making the frequency of magnetic field gradients spatially dependent; and the resolution of the image obtained is predominantly determined by signal strength and relaxation time Britton (2011).

The 3D magnetic resonance porosity measurements of the sample was only acquired at the beginning and end of the experiment. The total size of the image is 256 voxels in length, by 128 and 128 voxels in width and height, with the Region of Interest (ROI) defined by a cylinder with radius of 57 voxels and length of 180 voxels.

The 3D MRI porosity was normalized to match the 1D MRI porosity profiles, for consistency. Figure 4.6 shows the normalized MRI image at the beginning and end of the experiment. The flow channels formed are highlighted in the second image by applying an opacity filter for $\phi < 0.3$. Figure 4.7 shows a photograph of the carbonate sample at the end of the experiment.

4.4.3 NMR Propagator Measurements

The Pulsed Field Gradient Nuclear Magnetic Resonance (PFG-NMR) technique was used to continuously record the molecular probability of displacement $P(\zeta)$. The distribution $P(\zeta)$ is also known as a propagator, and is obtained by observ-

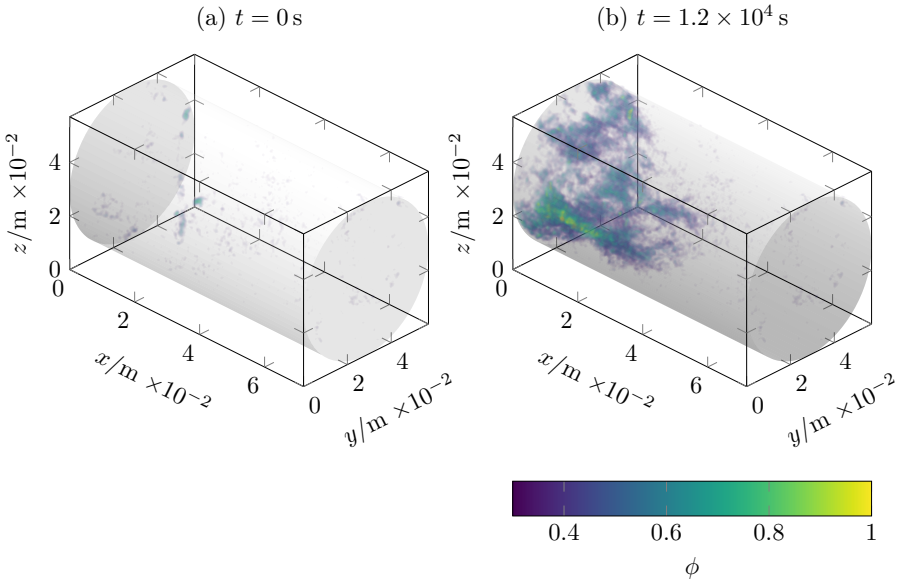


Figure 4.6: Porosity field for the carbonate sample at the beginning (a) and at the end (b) of the dissolution experiment. The porosity is normalized using the 1D porosity profiles. The channel formed is visualised in the second image by applying an opacity filter for $\phi < 0.3$.

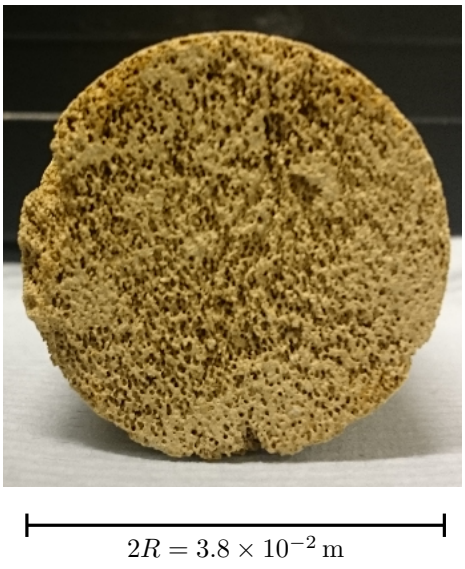


Figure 4.7: Photograph of the carbonate sample at the end of the dissolution experiment.

ing the displacements ζ of water molecules at a given observation time Δ. The acquisition makes use of the same technique present in Colbourne et al. (2016) to accelerate the NMR propagator measurements, allowing the dissolution dynamics to be captured. The propagators observation time was of $\Delta = 0.25\,\mathrm{s}$ separated by an interval of 16.1 min and each acquisition was longitudinally spaced by 0.005 m.

Figure 4.8 shows the propagators at the entry and exit of the sample during the whole duration of the dissolution experiment, and the difference between the first and last acquisitions. The entry of the sample underwent the most significant alterations, while the exit of the sample was left nearly intact which is consistent with the negligible change in porosity, consistent with the results shown in Figure 4.4. The complete description, with acquisitions at every 0.005 m of the sample, is displayed colour-coded by depth in figure 4.9 and colour-coded by amplitude in figure 4.10.

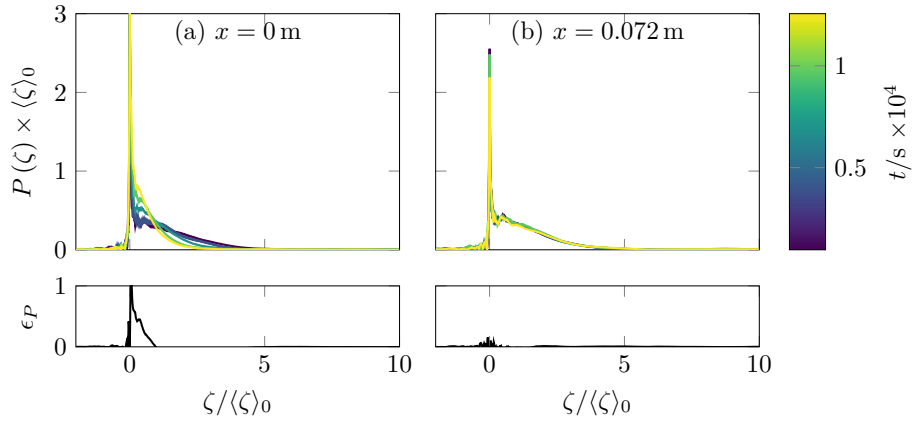


Figure 4.8: Top: NMR propagators at the entry (a) and exit (b) of the sample during the dissolution experiment. Bottom: the difference between the propagators at the beginning and the end of the experiment. Most of the alterations are present at the entry face of the sample. The exit face is left nearly intact, preserving the original distribution from the beginning of the experiment.

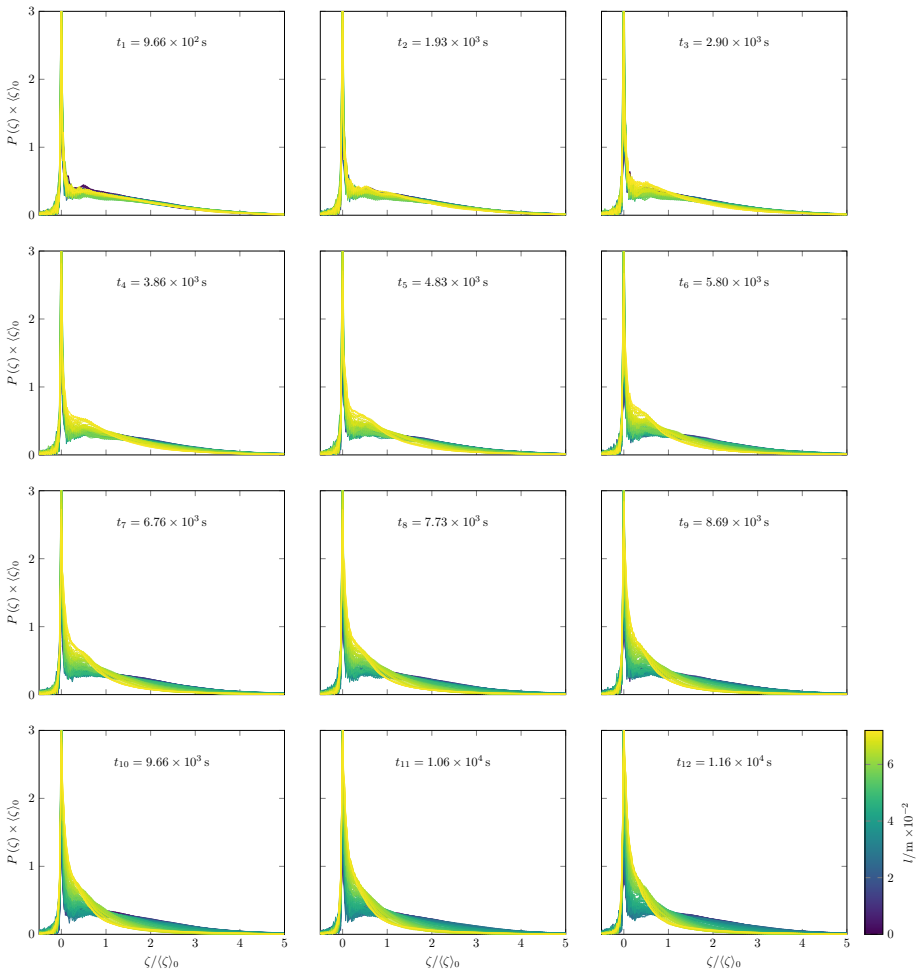


Figure 4.9: Complete distribution of propagators during the dissolution experiment colour-coded by the length of the sample. The measurements were taken across the length of the sample $l = 0.072\,\mathrm{m}$ using an observation time $\Delta = 0.25\,\mathrm{s}$.

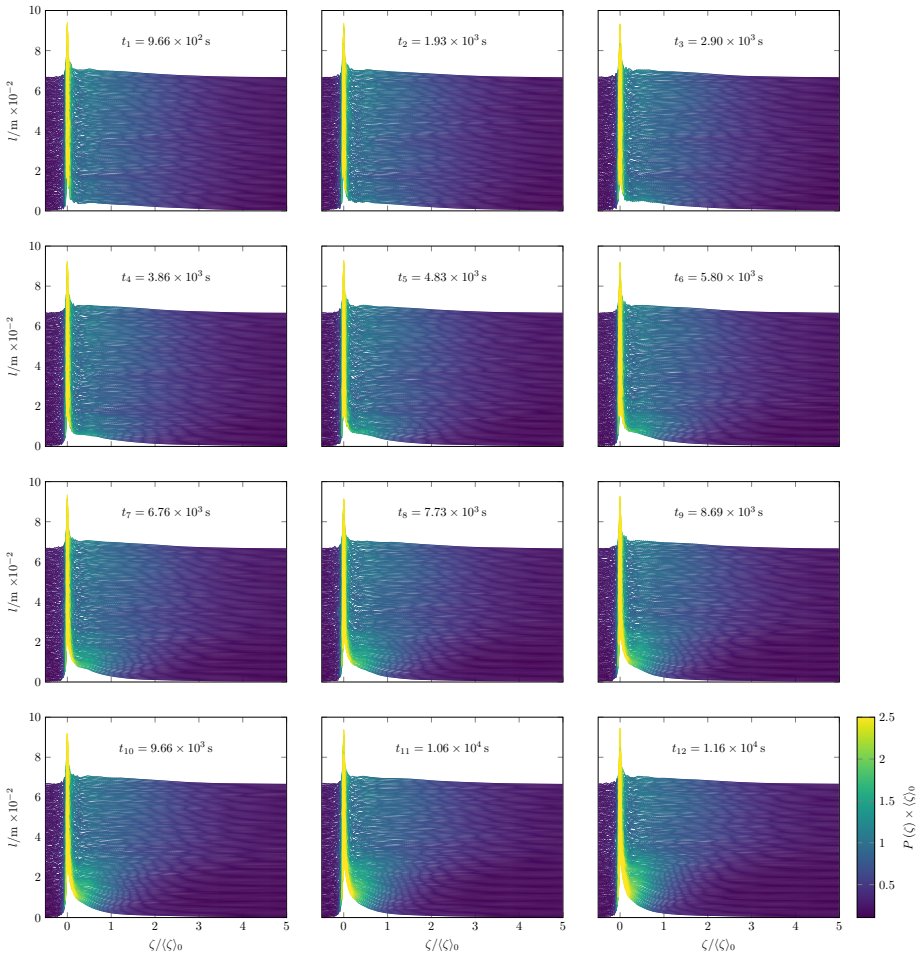


Figure 4.10: Propagators distribution during the dissolution experiment stacked by its length and colour-coded by the amplitude of the distribution.

4.5 Ketton Carbonate Model

The model for the Ketton carbonate sample dissolution described in the previous section, is divided into three main steps:

1. Creation of the initial porosity and permeability model;
2. Calibration of β using the experimentally measured propagators;
3. Development of the dissolution simulation.

The initial static model is calibrated using the available experimental data to ensure an approximation of the initial state of the sample. The results from the dissolution simulation, such as the porosity during dissolution and particle propagators, are then compared to the experimental measurements.

4.5.1 Initial Model Calibration

Our model is three-dimensional and the initial porosity ϕ_0 is constructed using the 3D MRI-derived porosity, described in the previous section. The initial permeability K_0 is then calculated using the power-law correlation of the porosity in equation (3.3). The coefficients in the correlation are based on the Ketton permeability measurements of Honari et al. (2015) with $a = 2.2 \times 10^{-8}\,\mathrm{m}^2$ and $b = 6.2$, and the resulting distributions are presented in figure 4.11.

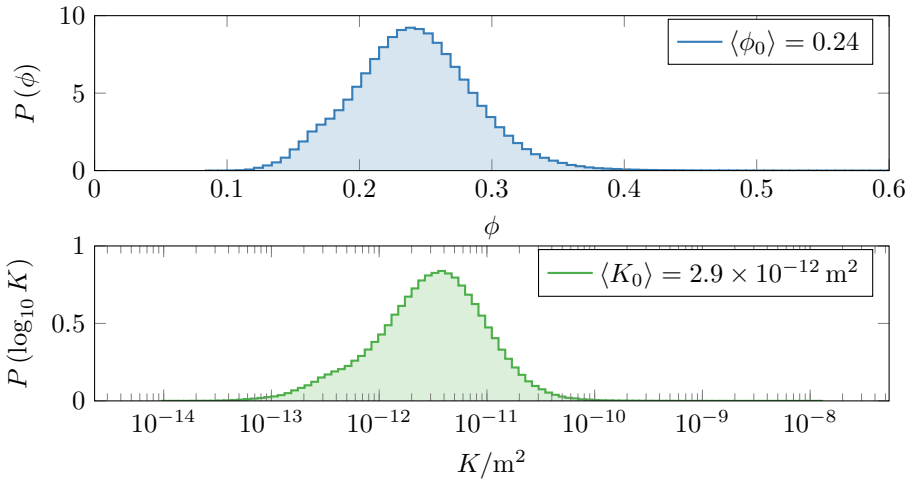
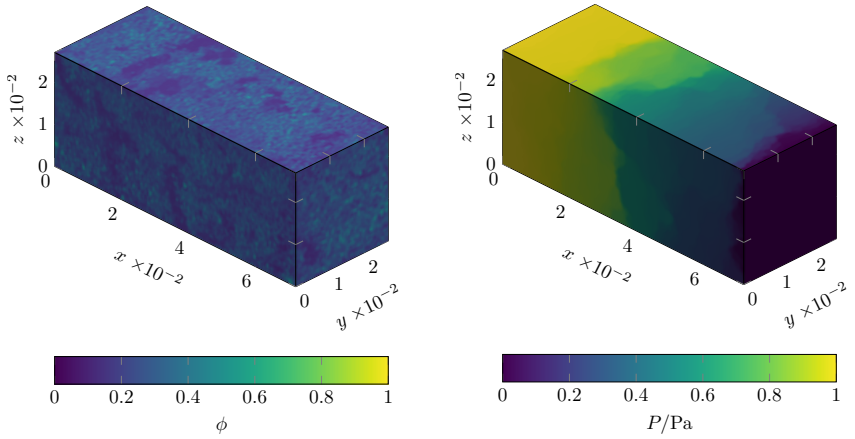


Figure 4.11: Initial porosity and permeability distribution. The porosity-permeability correlation factors $a = 2.2 \times 10^{-8}\,\mathrm{m}^2$ and $b = 6.2$ are defined in equation (3.3) and based on the Ketton limestone experiments Honari et al. (2015).

With the initial porosity and permeability distributions, we solve the pressure distribution by imposing a gradient of $\Delta P = 1\,\mathrm{Pa}$, and adjusting the resulting velocity field to the mean velocity of the experiment $\langle v \rangle = 3.06 \times 10^{-3}\,\mathrm{m\,s^{-1}}$. The initial porosity field and the calculated pressure are displayed in figure 4.12. The porosity distribution shows a heterogeneous sample, which directly reflects the MRI experimental data used to build the model.



(a) Porosity field (b) Pressure distribution

Figure 4.12: Initial porosity field and calculated pressure. The porosity is constructed from the MRI acquisition. The calculated pressure reflects the initial heterogeneity of the sample modelled after the MRI-derived porosity.

Having defined the initial porosity, permeability and flow field of the model, we can calculate the local ψ functions in each link. Our main assumption is that the characteristic times t_1 and t_2 of the ψ functions are defined from the flow field and transport parameters while the β parameter is set the same for all links. β accounts for pore-scale heterogeneity in the transport, below the scale of the underlying lattice, l: the effective value of β is related to the assumed lattice size l. We fix l and find β that provides an accurate representation of transport before dissolution. We will assume that β remains constant in both space and time during the dissolution process. The value of t_1 is calculated from the flow velocity in each link using equation (3.5). The value of t_2 is calculated from the molecular diffusion coefficient at 18 °C, $D_{m\,\mathrm{H_2O}} = 1.92 \times 10^{-9}\,\mathrm{m^2\,s^{-1}}$ (interpolated from the values in the Bruker Almanac, 2013) for the simulation of the propagators.

We fit β by evaluating the particle propagators from simulation and fitting them to the experimentally-measured propagators. This is obtained by injecting a pulse of particles, observing the particles for $\Delta = 0.25\,\mathrm{s}$ and measuring the difference between the experimental and modelled distribution of displacements.

We analyse the resulting particle propagator distribution from the simulation with the measured molecular propagator distribution and show the results in table 4.3. To compare the results, each model case was compared against the experimental distribution using the Kolmogorov-Smirnov (KS) test, for which the higher the $p-$value, the more similar are the distributions (Kolmogorov, 1933; Smirnov, 1939). The particle propagator distribution for the highest KS-test value of 0.22 is shown in figure 4.13. Lower values of β overestimate the number of slower particles ($\zeta/\langle\zeta\rangle_0 < 1$) and underestimate faster particles ($\zeta/\langle\zeta\rangle_0 > 1$). The value of $\beta = 0.9$ was selected for the simulations and used in the dissolution models presented next.

Table 4.3: Parameters used and the KS-test between the particle propagators and the experimental propagators for different fitted values of β. The value of $\beta = 0.9$ scored the highest KS-test and was selected for subsequent simulations.

Parameter	Symbol	Value	SI Units
Assumption			
Mean velocity	$\langle v \rangle$	3.06×10^{-3}	$\mathrm{m\,s^{-1}}$
Molecular diffusion coefficient of H_2O	D_m	2.2×10^{-9}	$\mathrm{m^2\,s^{-1}}$
Advective transit time	t_1	0.0261	s
Diffusive cut-off time	t_2	8.50	s
Fitting parameter	β	*KS-test*	
	0.5	0.0534	
	0.7	0.0589	
	0.9*	0.2237	
	1.1	0.0647	
	1.3	0.0103	
	1.5	0.0045	

* selected value.

4.5.2 Calcite Dissolution Modelling

HCl with a molar concentration of $0.01\,\mathrm{mol\,L^{-1}}$ is injected at a rate of $Q = 8.3 \times 10^{-7}\,\mathrm{m^3\,s^{-1}}$, see table 4.2, equivalent to injection of H^+ at $8.3 \times 10^{-6}\,\mathrm{mol\,s^{-1}}$. The value of t_2 is calculated from the molecular diffusion coefficient at 18 °C $D_{m\,Ca^{2+}} = 1.15 \times 10^{-9}\,\mathrm{m^2\,s^{-1}}$ (extrapolated from the values in Ribeiro et al., 2008) to account for the aqueous calcium in the particles. We choose the value of $N_{\text{particles}} = 1000$ for a time step $\Delta t = 10\,\mathrm{s}$; injecting more particles had no effect on the results. Figure 4.14 shows the porosity profiles after $1 \times 10^3\,\mathrm{s}$ for different numbers of injected particles, 10^2 and 10^3. Injecting 10^4 particles made no additional difference to the results and was omitted from the plot. The

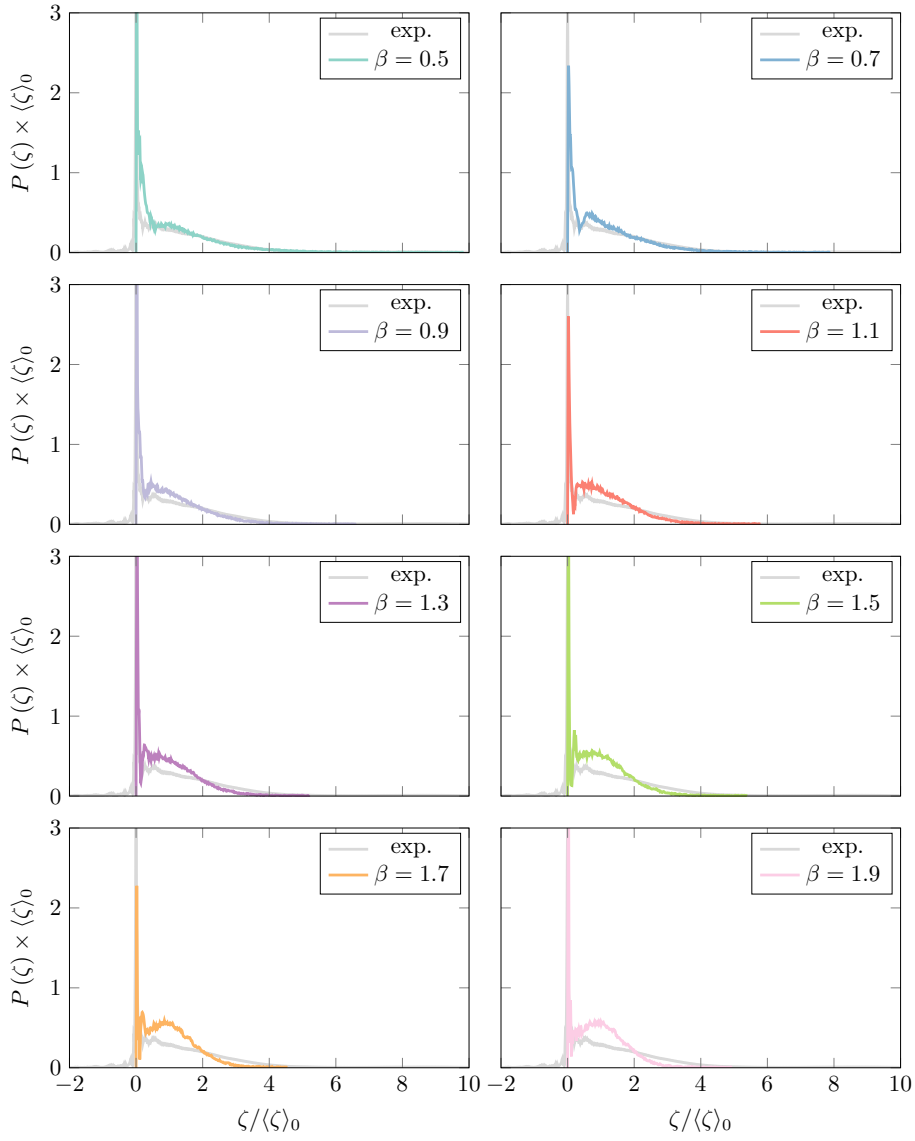


Figure 4.13: Particle propagator distribution for different values of β. The best fit was obtained with $\beta = 0.9$.

model is built using the parameters summarised in table 4.1.

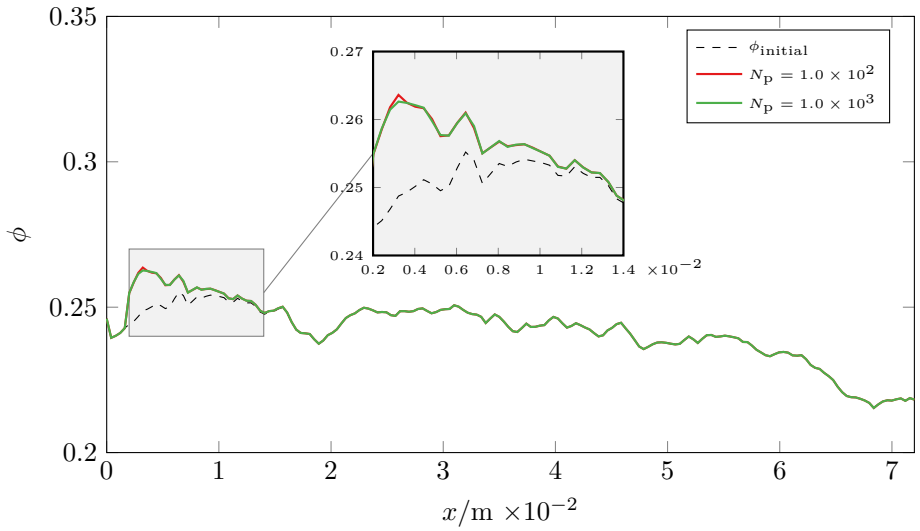


Figure 4.14: Porosity profiles and axis inset with a zoomed-in detail along the flow direction for different numbers of injected particles per time step, at the beginning and at $t = 1 \times 10^3$ s. We used $N_{\text{particles}} = 1000$ for a time step $\Delta t = 10$ s as the optimum number of particles injected by observing that the porosity profile did not change if more particles were injected.

The pressure field is recalculated whenever the total porosity increment $\Delta\phi > 1 \times 10^{-4}$. Reducing this value increases the amount of times that the pressure is updated, but this had no influence on the predicted changes in porosity. Figure 4.15 shows the porosity profiles for different numbers of pressure updates. The parameters used in these cases are the same as before.

4.5.3 Porosity evolution

The evolution of porosity obtained in the model is compared against the experimentally measured porosity profiles in figure 4.16 and the dissolution channels formed are shown in figure 4.17 and the geometries of the channels are described in table 4.4 from manual analysis of the images.. The first 0.002 m of the model is omitted as it is used as buffer layer to homogenize the flow at the inlet. The simulation reflects the experimental behaviour of the NMR porosity profiles, where most of the dissolution happens at the entry of the sample and is nearly absent after. There is a small discrepancy near the inlet with an underprediction of the porosity; overall though there is a good agreement between the model and the experiment.

In figure 4.17 from the simulation we observe the appearance of dissolution-formed channels, with a dominant channel formed near the inlet. The location of

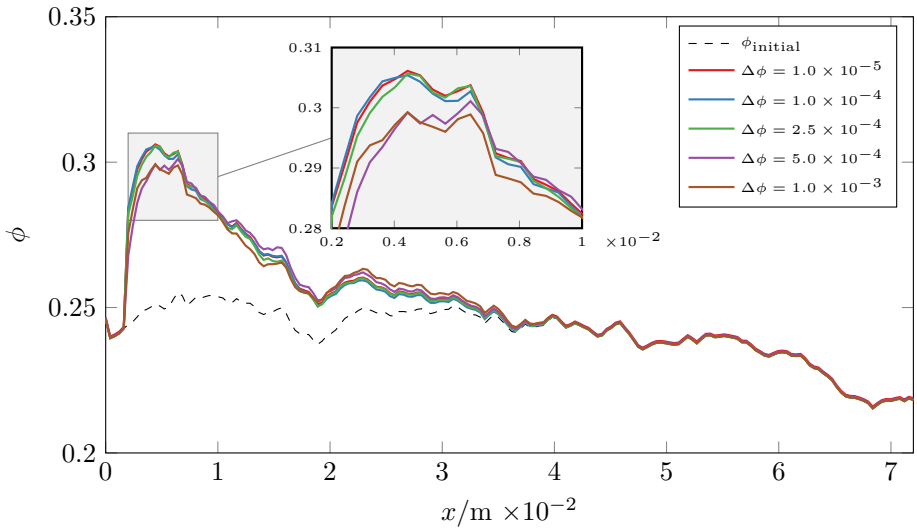


Figure 4.15: Porosity profiles and axis inset with a zoomed-in detail along the flow direction for different porosity change precisions at the end of the simulation. We choose the value of $\Delta\phi = 1 \times 10^{-4}$ as the optimum total porosity change to update the pressure field. Reducing this value increases the amount of times that the pressure is updated, but showed no influence in the porosity evolution.

the simulated channel is similar to the observed channel from the experimental image shown in figure 4.6. The appearance of the channel near the inlet reflects the higher initial porosity which focuses most of the flow at both the initial and later stage of the simulation, as the growth of the other channels formed is slower. Injecting a pulse of uniformly distributed particles at the face of the sample and registering their trajectories for $\Delta = 2\,\text{s}$, we observe that the channel near the inlet becomes the main medium of transport for the injected particles.

Table 4.4: Comparison between the geometries of the experimental acquisition and simulated model of the channel formed by dissolution.

Parameter	Symbol	Exp.	Sim.
Centre coordinate /m	y_c	2.35×10^{-3}	2.62×10^{-3}
	z_c	6.06×10^{-3}	4.67×10^{-3}
Total length /m	l_c	2.88×10^{-2}	2.52×10^{-2}
Mean radius /m	r_c	1.90×10^{-3}	1.28×10^{-3}

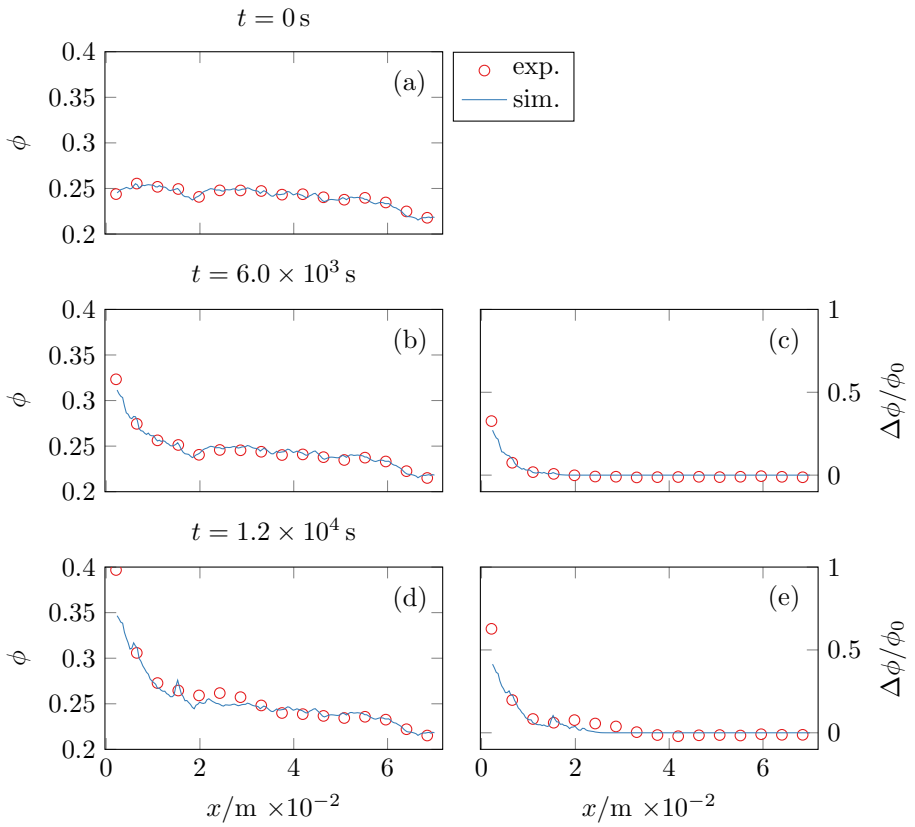


Figure 4.16: Profiles for the simulated porosity and relative porosity difference compared to the experimentally-measured NMR porosity profiles. Figure (a) shows the initial porosity profile, figure (b) and (c) the porosity and porosity difference at $t = 6.0 \times 10^3\,\mathrm{s}$, and figure (d) and (e) at the end of the experiment, $t = 1.2 \times 10^3\,\mathrm{s}$.

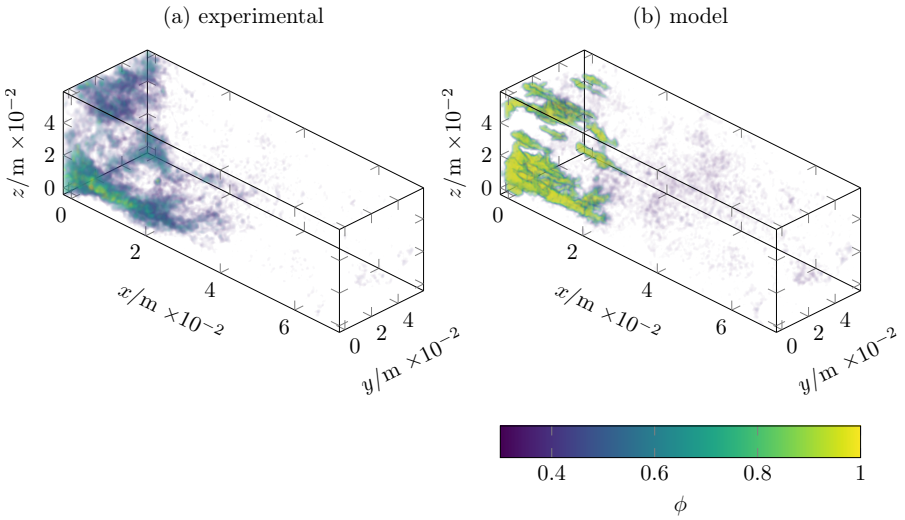


Figure 4.17: Porosity field in the experiment (a) and simulation (b) at 1.2×10^4 s, the end of the dissolution experiment. Only values of $\phi \geq 0.3$ are shown. Once the channel breaks through, it becomes the dominant source of transport.

4.5.4 Average dissolution rate

The average effective reaction rate can be defined as

$$r_{\mathrm{eff}} = \frac{\rho_{\mathrm{CaCO_3}}}{M_{\mathrm{CaCO_3}} S_A} \frac{\Delta\phi}{\Delta t}, \tag{4.9}$$

where $S_A = V_t \sigma_A$ is the sample surface area estimated from the total volume of the simulation domain V_t and specific surface area σ_A. $\Delta\phi$ is the difference in average porosity over a time Δt. In the experiments Δt is the time between measurements, while in the simulation it is the time-step between solutions of the velocity field. Figure 4.18 shows the experimental and predicted reaction rates over time: the effective reaction rate is approximately $r_{\mathrm{eff}}/r = 1.25 \times 10^{-3}$ for the simulations and $r_{\mathrm{eff}}/r = 1.47 \times 10^{-3}$ for the experiments averaged over the whole time of the process.

The uncertainty in the estimation of reaction rate comes mainly from the conversion of the NMR signal to porosity and calculating porosity changes. We estimate that the measured reaction rate is accurate to within approximately 20%.

These values differ by only 15 % showing that the simulations accurately capture the dissolution process. However r_{eff} is almost 3 orders of magnitude smaller than the bulk reaction rate r measured without transport limitations (Peng et al., 2015). The reason for this discrepancy is the highly heterogeneous,

channelled, flow pattern, which restricts dissolution to only a limited part of the whole rock.

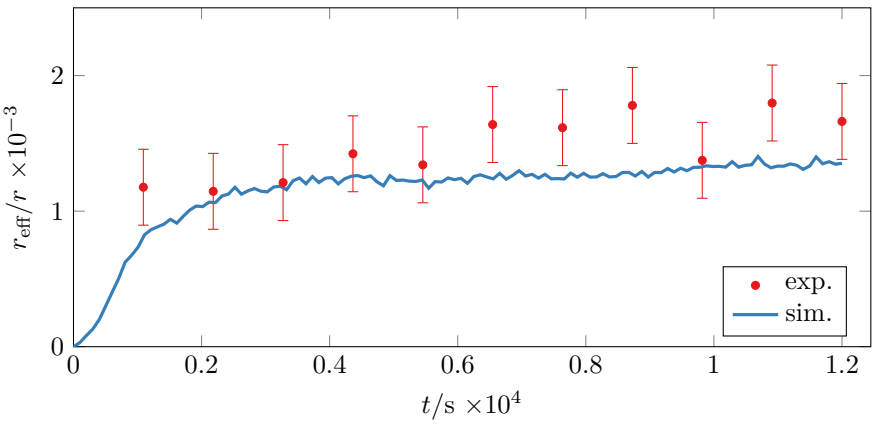


Figure 4.18: Experimental and simulated estimated effective dissolution rate. The simulated effective dissolution rate is nearly 780 times smaller than the batch reaction rate while the experimental effective dissolution rate is nearly 680 times smaller than the batch calcite dissolution rate, $r = 8.1 \times 10^{-4}\,\text{mol}\,\text{m}^{-2}\,\text{s}^{-1}$ (Peng et al., 2015).The error bars reflect uncertainty in the experimental measurements.

4.5.5 Particle propagators

The propagators or the probability of displacement provide a signature of particle transport. Using the same parameters as before but for non-reactive particles, we simulate a uniform injection at the entry and observe the particle displacements for $\Delta = 2.5 \times 10^{-1}$ s to reflect the same experimental conditions. The results are compared against the experimentally measured propagators and presented in figure 4.19.

When the mean particle velocity is plotted on a $\log - \log$ scale, as in figure 4.20, we observe that the mean velocity of the particles scales as $v \propto t^{\beta-1}$. This is consistent with the results in Dentz et al. (2004) for $\beta < 1$. Using this relation we estimate an initial average value of $\beta = 0.49$ and the final value of $\beta = 0.64$. The increase of β means that more particles are experiencing a more homogenous flow field within the dominant dissolved channel. Note that these are lower values than $\beta = 0.9$ in each link: here β is an average effective value that accounts for the heterogeneity on scales beyond a single link.

The increase in the probability of transitioning in faster links is seen in figure 4.21. The shades shows the overlapping ψ functions distributions and the continuous lines the ψ functions using the minimum, mean and maximum value

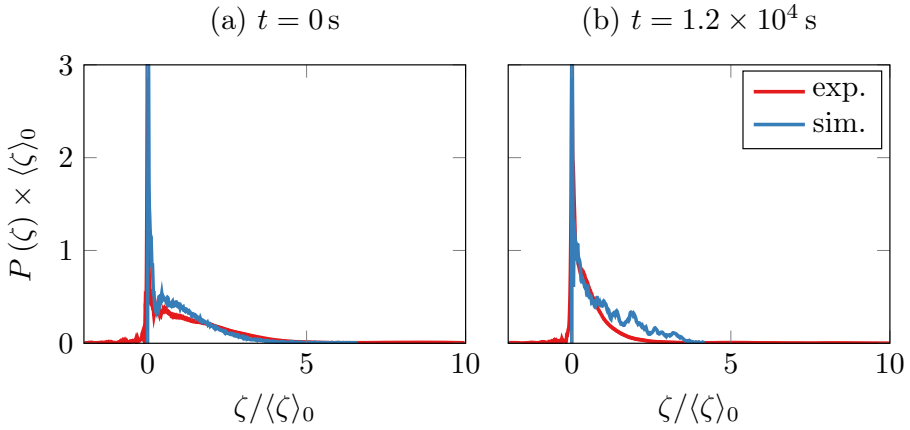


Figure 4.19: Particle distribution injected at the core inlet compared against the molecular propagators at (a) 0 s and (b) 1.2×10^4 s. These times represent the dissolution experiment at the beginning and the end.

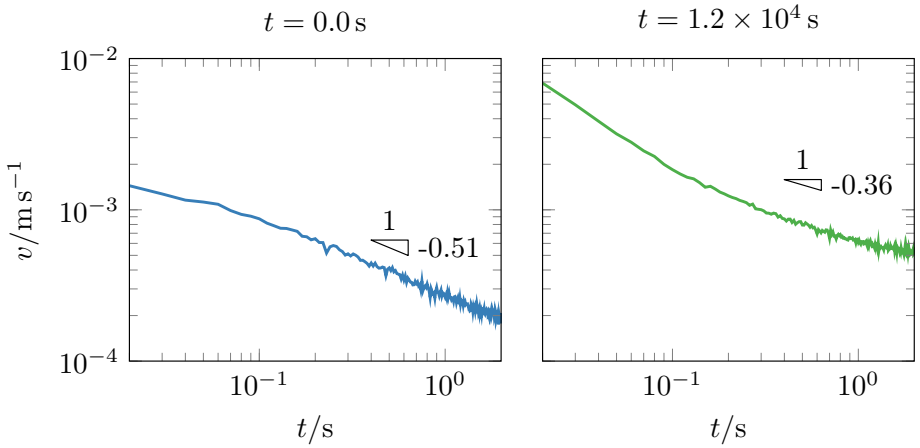


Figure 4.20: Particle mean velocity evolution. The graphs show the mean velocity v for the domain at the beginning ($t = 0\,\mathrm{s}$) and at the end ($t = 1.2 \times 10^4\,\mathrm{s}$) of the simulation. As $v \propto t^{\beta-1}$ we estimate the values of β at the beginning and end of the simulation as $\beta_{\mathrm{initial}} = 0.49$ and $\beta_{\mathrm{final}} = 0.64$.

t_1 in the links. As the dissolution processes increases the porosity it decrease the value of t_1 in the links. This increases the probability of transitions with short transit times, or transitions with higher velocity.

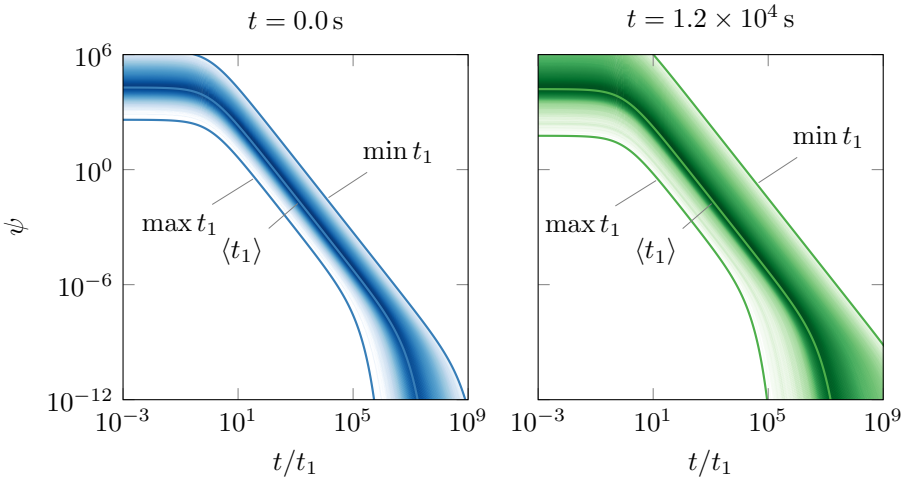


Figure 4.21: The evolution in the $\psi(t)$ function for all available links in the domain at the beginning ($t = 0.0\,\mathrm{s}$) and end ($t = 1.2 \times 10^4\,\mathrm{s}$) of the simulation. The shades of colours shows the overlapping the ψ functions distributions and the continuous lines the ψ functions using the minimum, average and maximum values t_1 in the links.

4.6 Discussion

The porosity field shows the formation of dissolution channels, qualitatively similar to the MRI-derived porosity, as seen in figure 4.17. The mean of the effective reaction rate is almost 3 orders of magnitude smaller than the batch reaction rate (Peng et al., 2015), but in good agreement with the estimated values from the NMR porosity profiles. Previous dissolution experiments at the pore scale showed effective reaction rates that are 10-20 times smaller than the batch reaction rate (Menke et al., 2015; Al-Khulaifi et al., 2017). Here, at a larger scale, transport limitations are even more important, indicating a significant amount of channelling, as evident in the porosity profiles.

Our use of β represents an under-resolved heterogeneity in individual links of the lattice, which is different to the approach of Muljadi et al. (2018) where β varied along slices of the domain, including several links at a time. Additionally, we use the initial porosity distribution of the MRI measurements to build our model, so that the emergent propagator distribution is not only dependent on the β parameter but also on the domain heterogeneity as well. The effective,

average value of β is lower than value in a link, since it encapsulates the emergent heterogeneity of the medium.

The initial heterogeneity focuses the flow in higher permeability zones, leading to more dissolution in these preferential pathways. This increases the permeability in these regions further, causing more flow focusing and dissolution. The end result is the emergence of a preferential flow channel that carries the vast majority of the flow where reaction is concentrated. The rest of the domain becomes largely stagnant with little flow and reaction - most of the available surface area for reaction does not have access to injected acid leading to a very low overall reaction rate.

4.7 Conclusions

We developed a CTRW model coupled with a first-order kinetics model to study the dissolution of a Ketton carbonate rock and compared it with experimental NMR measurements.

Our model requires the calibration of a single parameter β which characterizes transport heterogeneity to match the experimental propagator distribution. Having a calibrated initial state, we were able to predict the porosity evolution and the formation of dissolution channels similar to the experimentally-measured channels.

The model is able to qualitatively capture the observed dominant channel from the MRI measurement, and to estimate the effective reaction rate: we estimated an effective reaction rate that was, on average, 780 times lower than the bulk reaction rate without transport limitations; the experiments indicated a ratio of 680. The model is also able to quantitatively reproduce the NMR propagator distribution emerging from the Ketton limestone core sample. Finally, despite using a constant $\beta = 0.9$ value for all links in the model, we calculate emergent average β from the average velocity of the particles that takes different values both before and after dissolution. We observe that the evolution of the porosity field resulted in a higher emergent β than that before dissolution, because of the dissolution induced heterogeneity change as a result of the flow focusing into preferential channels.

Future work will extend the current model to incorporate multi-species mineral reaction and mineral heterogeneity as described in the chapters 5 and 6.

CHAPTER 5

Impact of Initial Physical Heterogeneity on Effective Reaction Rates

After validating the transport and reactive model in the previous chapters, we systematically demonstrate the impact of physical heterogeneity on transport and reactive flow signatures. We study this by creating three porous media of increasing heterogeneity, and examining the emergent effective reaction rates. The three samples are used to show different initial porosity and velocity distributions and are subjected to three advective dominated transport regimes characterized by Péclet numbers of $Pe = 0.0542$, 0.542 and 5.42. We will also compare our CTRW model results with solutions of the Advective-Dispersion Reaction Equation (ADRE).

This chapter will show how flow and transport heterogeneity affects the effective reaction rate. We will show that it is possible to model unresolved physical heterogeneity with a Truncated-Power-Law (TPL) transit time distribution model containing the transport heterogeneity parameter β (Dentz et al., 2004; Bijeljic and Blunt, 2006; Rhodes et al., 2009; Edery et al., 2014; Edery, 2021). We start with a description of the reactive transport model in section 5.1. Then we continue in section 5.2 with description of a physical heterogeneity of the three porous media selected for this study by quantifying of their initial flow and transport heterogeneity signatures. We then further investigate capabilities of our reactive transport CTRW framework to model dissolution. In section 5.3 we test this capability by assuming different initial flow fields emerging from

different transport heterogeneity.

5.1 Description of the CTRW Reactive Transport Model

At the macro-scale where Darcy's law is valid, the ADRE is described in equation (1.5) and showed in chapter 1 as

$$\phi \frac{\partial c}{\partial t} = -\nabla \cdot (\mathbf{v}c) + \nabla \cdot \phi \mathbf{D} \nabla c + R, \tag{5.1}$$

where ϕ is the porosity, c is the molar concentration of a given species, $\mathbf{v}$ is the Darcy velocity, $\mathbf{D}$ is the dispersion coefficient, and R is the reaction rate. The choice of R controls the reactions of the system, such that a value of $R = 0$ makes equation (5.1) applicable for an inert system, without dissolution or precipitation of any species, or a value of $R = k_r c$, as adopted in the present study, makes it appropriate to model first order kinetic reactions (Plummer et al., 1978; Gray et al., 2018; Oliveira et al., 2021).

The characteristic reaction time $t_r = 1/k_r$ is defined by the reaction rate constant k_r, and is much smaller than the advective transit-time t_1, or the characteristic transport time of all studied samples and conditions.

We use the model described in chapter 4 (Oliveira et al., 2021) and illustrated in figure 4.1. Instead of having the solute concentration modelled as a continuous field variable, we describe it using a Lagrangian framework with particles distributed on a lattice (Bijeljic and Blunt, 2006; Le Borgne and Gouze, 2008; Kang et al., 2011; Pereira Nunes et al., 2016a; Pereira Nunes et al., 2016b). Each particle contains a number of moles of aqueous calcium. Particles are not created or destroyed; instead the number of moles associated with a particle changes over time. The aqueous calcium concentration is defined as the sum of the moles associated with each particle in a given volume. Solute transport is then modelled as particle transitions in a lattice, carrying the chemical components from site to site. Reactions are then accounted for as interactions between the chemical components in the particles and the chemical components in the lattice nodes, representing the solid.

Next, we systematically demonstrate the impact of physical heterogeneity on transport and reactive flow signatures. We study this by creating three porous media of increasing heterogeneity, and examining the emergent effective reaction rates. The three samples are used to show different initial porosity and velocity distributions and are subjected to three advective dominated transport regimes characterized by Péclet numbers of $Pe = 0.0542$, 0.542 and 5.42. We will also

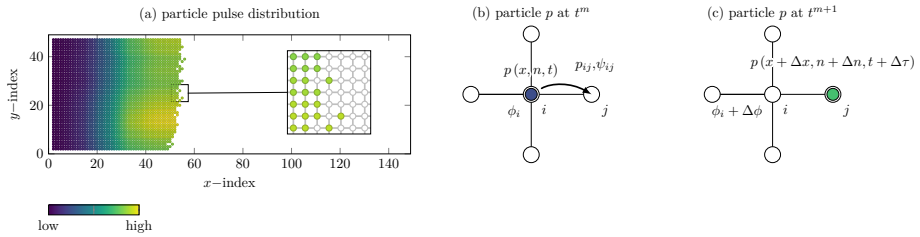


Figure 5.1: Simplified illustration of (a) an ensemble of particles and (b) the detailed representation of a single particle (b) before and (c) after transiting and reacting through a lattice. The change in colour depicts an increase of the aqueous calcium concentration. A particle transits in the lattice with variable transit-time $\Delta\tau$ and displacement Δx, obtained from a locally defined transit-time distribution ψ_{ij} and displacement probability p_{ij}. After each transition, the number of moles of aqueous calcium in a particle increases by Δn, as a consequence of the reaction within the node of origin, which in turn has its porosity increased by $\Delta\phi$. Modified from Oliveira et al. (2021).

compare our CTRW model results with the behaviour consistent with solutions of the ADRE.

5.2 Signatures of Physical heterogeneity

The samples studied are described in section 5.2.1. Next we evaluate the velocity distribution and particle propagators as proxies for the physical heterogeneity of the samples, similarly to what is described in Bijeljic et al. (2011) and Bijeljic et al. (2013a). Then in section section 5.2.2 we show the imprint of the regions available for flow on the velocity distributions. The signatures of transport heterogeneity are then shown in section 5.2.3, where we consider the shape of the particle propagators as an indication of the domain physical heterogeneity. The differences between stagnant and mobile particles are a direct consequence of the contrasts in the velocity distributions combined with the transport heterogeneity parameter β.

5.2.1 Description of the Porous Media

We build three samples with increasing heterogeneity: Het. 1, 2 and 3; see Appendix B for more details on the generation procedure. Each sample is built from a background 3D porosity field that is used to populate the properties of an underlying regular lattice, similarly to how the model for the Ketton limestone sample was constructed in chapter 4 (Oliveira et al., 2021). The cell centres of the 3D porosity field cells are coincident with the node centres of the lattice. The lattice has $N_x = 150$, $N_y = N_z = 50$ nodes along the x, y and z directions

and link size of $l = 10^{-3}$ m. Hence the total length of the sample is $L = 0.15$ m.

The 3D porosity field consists of a normally distributed porosity field with mean $\langle \phi_{\text{bg}} \rangle = 0.3$ and standard deviation $\sigma_{\phi\text{bg}} = 0.01$. This is called here the background porosity not to be confused with the samples' initial mean porosity. The heterogeneity is emulated by uniformly distributing solid spheres with $\phi_{\text{spheres}} = 0$. The spheres are allowed to overlap. The sphere radius for Het. 1, 2 and 3, is normally distributed with mean $\langle r_1 \rangle = 1.5 \times 10^{-3}$ m, $\langle r_2 \rangle = 3.0 \times 10^{-3}$ m and $\langle r_3 \rangle = 4.5 \times 10^{-3}$ m, the standard deviation $\sigma_{r1} = \sigma_{r2} = \sigma_{r3} = 0.2$ and the sphere centres are the same. Figure 5.2 shows the distribution and radius of the solid spheres for all samples and table 5.1 summarizes the parameters used.

Table 5.1: Initial sample properties. All samples are built using the same background porosity and permeability correlation factors, while the main difference is in the size of the distributed solid spheres, where the porosity is set to zero.

Parameter	S.I. Unit	Het. 1	Het. 2	Het. 3
$\langle \phi_{bg} \rangle$		0.30	0.30	0.30
$\sigma_{\phi\text{bg}}$		0.10	0.10	0.10
$\langle \phi \rangle$		0.29	0.25	0.17
$\langle K \rangle$	m^2	1.69×10^{-12}	3.15×10^{-13}	4.50×10^{-15}
a	m^2	1.00×10^{-8}	1.00×10^{-8}	1.00×10^{-8}
b		7.00	7.00	7.00
$\langle r \rangle$	m	1.50×10^{-3}	3.00×10^{-3}	4.50×10^{-3}
σ_r		0.20	0.20	0.20
β		1.80	1.20	0.60
ρ	$\text{m}^3\,\text{kg}^{-1}$	2.70×10^3	2.70×10^3	2.70×10^3
l	m	1.00×10^{-3}	1.00×10^{-3}	1.00×10^{-3}
$D_{m_{\text{Ca}^{2+}}}$	$\text{m}^2\,\text{s}^{-1}$	2.20×10^{-9}	2.20×10^{-9}	2.20×10^{-9}
σ_A	m^{-1}	8.00×10^3	8.00×10^3	8.00×10^3
r_{calcite}	$\text{mol}\,\text{m}^{-2}\,\text{s}^{-1}$	1.50×10^{-3}	1.50×10^{-3}	1.50×10^{-3}
k_r	s^{-1}	6.28×10^{-1}	6.28×10^{-1}	6.28×10^{-1}
n_{eq}	mol	8.30×10^{-10}	8.30×10^{-10}	8.30×10^{-10}

The presence of solid spheres of different radius reduces the mean porosity of each sample from $\langle \phi_{\text{bg}} \rangle = 0.3$ to $\phi_1 = 0.29$, $\phi_2 = 0.25$ and $\phi_3 = 0.17$, respectively for Het. 1, 2 and 3.

For Het. 1, the sphere radius and distribution makes the spheres very unlikely to overlap and the porosity of the sample is mostly driven by the background porosity such that for Het. 1 the mean porosity is $\phi = 0.29$. As the sphere radius increases, the domain of Het. 2 and Het. 3 becomes more irregular and the sample mean porosity is driven by the combination of the solid spherical

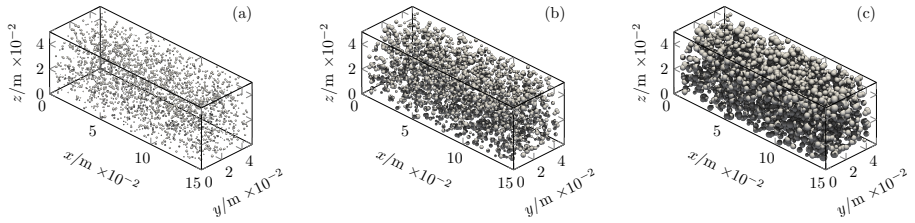


Figure 5.2: Different radius for the solid spheres used to generate the initial porosity fields of sample Het. 1, 2 and 3. The porosity in the regions where the spheres are located is set to zero. The spheres are uniformly distributed in the domain and allowed to overlap. The mean radius for (a) Het. 1 is $\langle r_1 \rangle = 1.5 \times 10^{-3}$ m, for (b) Het. 2 $\langle r_2 \rangle = 3.0 \times 10^{-3}$ m and for (c) Het. 3 $\langle r_3 \rangle = 4.5 \times 10^{-3}$ m, and the standard deviation for radius is $\sigma_{r1} = \sigma_{r2} = \sigma_{r3} = 0.2$.

inclusions and the background porosity. This significantly reduces the porosity and permeability when comparing Het. 1 to 2 and 3, as shown in table 5.1. As an analogy, Het. 1 is related to beadpacks, Het. 2 to a mildly homogeneous carbonate while Het. 3 to a highly heterogeneous carbonate. The heterogeneity of the samples lies on an observation scale that is larger than the link and node sizes, so we compare the choice of characteristic value of $\beta = 1.8$ for beadpacks, $\beta = 1.2$ for mildly homogeneous carbonates and $\beta = 0.6$ for highly heterogeneous carbonates, with a baseline of $\beta = 1.8$ for all three porous media in section 5.3. β is an empirical parameter that captures the heterogeneity of the medium at a scale below the scale of a link (at the pore scale) and which is not explicitly captured by the larger-scale heterogeneity in the model.

Similarly to the model described in chapters 3 and 4, the permeability at the link k is calculated using a power-law correlation with the porosity,

$$K = a\phi^b, \tag{5.2}$$

where a and b are fitting parameters defined in table 5.1. Such power-law correlations between porosity and permeability are widely used, to model the evolution of permeability in dissolution experiments (Menke et al., 2015; Menke, 2015; Honari et al., 2015). The initial porosity distribution is presented in figure 5.3 and the initial permeability distribution is presented in figure 5.4. The small porosity values ($\phi \ll 0.3$) occur when nodes are partially overlapping with the spheres and the porosity values are interpolated with the background porosity and the solid sphere porosity. The more heterogeneous the sample, the smaller are the peaks at the mean porosity $\langle \phi \rangle = 0.3$ and the larger is the number of porosity values at the lower end of the distributions.

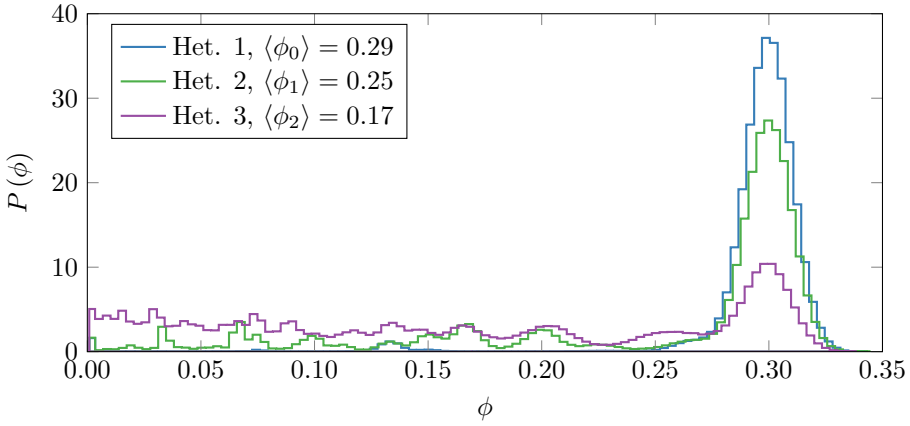


Figure 5.3: Initial non-zero porosity distribution for Het. 1, 2 and 3. The mean porosity value for Het. 1 is $\langle\phi_1\rangle = 0.29$, for Het. 2 is $\langle\phi_2\rangle = 0.25$ and for Het. 3 is $\langle\phi_3\rangle = 0.17$. The more homogeneous sample Het. 1 has a larger peak at $\phi = 0.3$, whereas the other samples are characterized by the tail of the distribution towards lower values of porosity.

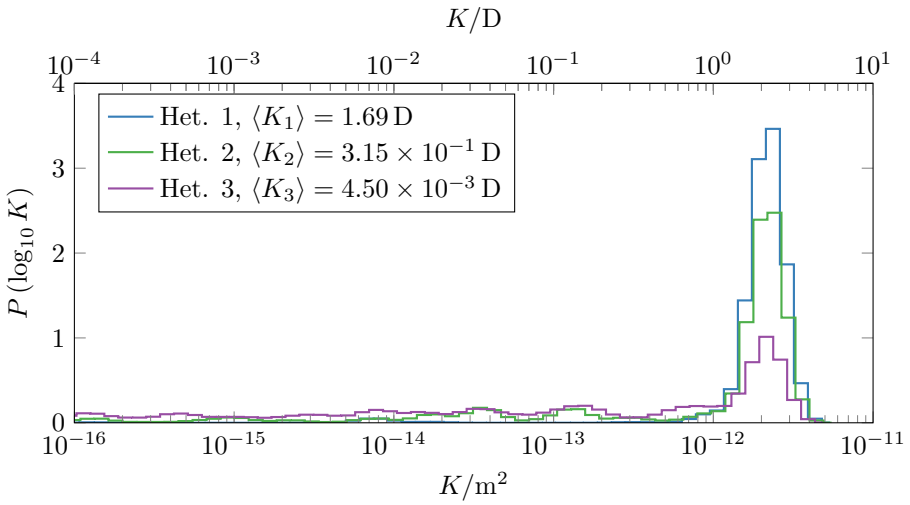


Figure 5.4: Initial permeability distribution for Het. 1, 2 and 3. The porosity-permeability correlation factors are defined in equation (5.2) and listed in table 5.1. The mean permeability value for Het. 1 is $\langle K_1\rangle = 1.69\,\mathrm{D}$, for Het. 2 is $\langle K_2\rangle = 3.15 \times 10^2\,\mathrm{mD}$ and for Het. 3 is $\langle K_3\rangle = 4.50\,\mathrm{mD}$. The heterogeneity of the samples extends the tail in the permeability distribution to lower-end values.

5.2.2 Signatures of Flow Heterogeneity

At the scale of individual links we assume that the heterogeneity of the system is characterized by $\beta = 1.8$, 1.2 and 0.6 respectively for Het. 1, 2 and 3, as presented in table 5.1. This hypothesis is further explored in section 5.3, where we consider different values of β in equation (3.12). To solve the velocity in the links, we impose a unit pressure gradient along the $x-$axis $\Delta P_x = 1$Pa and then scale the average velocity such that the Péclet number is equal to $Pe = 0.0542$, 0.542 and 5.42. These Péclet numbers represent three advection dominated transport regimes, from weakly to highly advection dominated.

The resulting pressure fields alongside the porosity fields are displayed side-by-side in figure 5.5. The lower porosity values significantly restrict the regions available for flow, focusing the transport only to the regions of higher porosity.

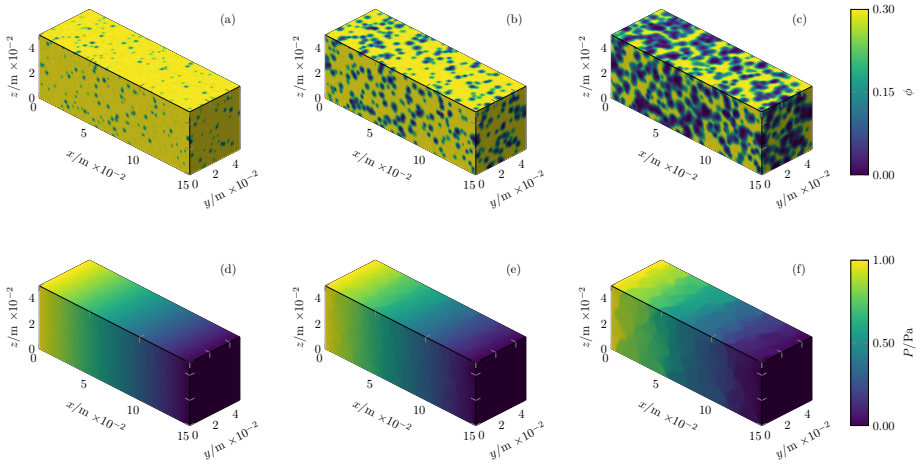


Figure 5.5: Initial porosity fields (a) to (c) and the corresponding calculated pressure fields for (d) to (f) respectively for Het. 1, 2 and 3. The porosity field is constructed using zero porosity inclusions in a background porosity field of $\langle\phi\rangle = 0.3$ as showed in figure 5.2. The calculated pressure reflects the initial heterogeneity of the sample, gradually increasing the local pressure differences from Het. 1 to 3.

From the pressure field, we calculate the normalized velocity distribution in the flow direction for each sample and plot it in figure 5.6. The shape of the normalized velocity distribution shows a sharp peak at $v_x/\langle v_x\rangle = 1$ with a narrow velocity distribution of only one order of magnitude of variation for Het. 1. This is markedly different than of Het. 2 and 3, that exhibit a much wider distribution than Het. 1 and a smeared-out tail towards lower velocity values. The velocity distribution for Het. 2 spans over nearly 10 orders of magnitude of variation in flow speed, experiencing very low velocities. The velocity distribution for Het. 3 variation is slightly wider than Het. 2, showing

higher probability contrast between the low and high velocities. At the high end of the distribution, the velocity in the links of Het. 3 can reach nearly 20 times the mean velocity. This is likely due to the regions available for flow that are restricted by the presence of the spherical solid inclusions with larger radius than of Het. 1 and 2. Additionally both Het. 2 and 3 show significant amounts of slower velocities, or near stagnant links, where solute transitions are mostly influenced by diffusion.

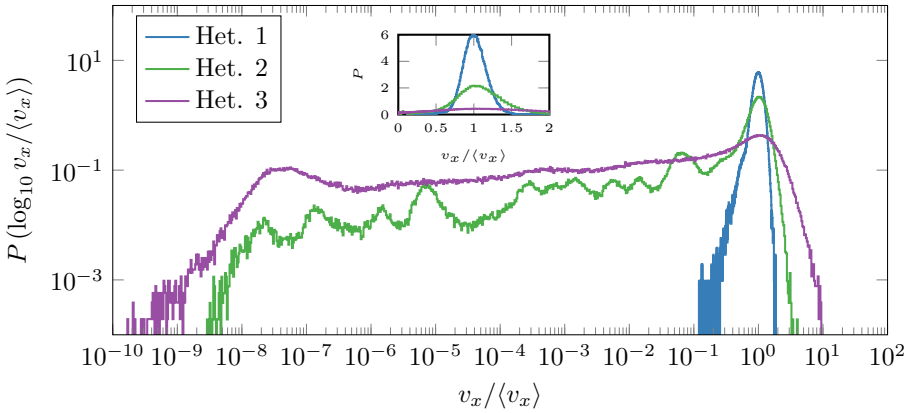


Figure 5.6: Normalized velocity distribution for the different samples. The shape of the normalized velocity distribution shows a sharp peak at $v_x/\langle v_x\rangle = 1$ with a narrow velocity distribution for Het. 1. In contrast, Het. 2 and 3 have a much wider distribution with a smeared-out tail towards lower velocity values. The inset shows the same distributions but without the log-log transformation.

5.2.3 Signatures of Transport Heterogeneity

The emergent particle breakthrough, used as a proxy for species production in the system, contains a strong signature of the domain's physical heterogeneity and fails to be modelled using an Advective-Dispersion Equation (ADE) model and the Gaussian behaviour from the solutions in equation (2.8), as illustrated in figure 5.7. The dispersion coefficient used in the ADE model was fitted to the observed particle breakthrough. As the sample heterogeneity increases, the particle breakthrough departs from the ADE model equation (2.8), and this effect increases as the Péclet number increases.

We calculate the probability of particle displacement, or particle propagators, $P(\zeta)$ by observing the particle displacements ζ over an observation time Δ and normalize it by the mean displacement $\langle\zeta\rangle_0$. Molecular displacements, or flow propagators, measured by Nuclear Magnetic Resonance (NMR) define the motion of molecules in a given domain (Callaghan, 1993; Seymour and Callaghan, 1997) and are reliable measurements for non-Fickian transport in

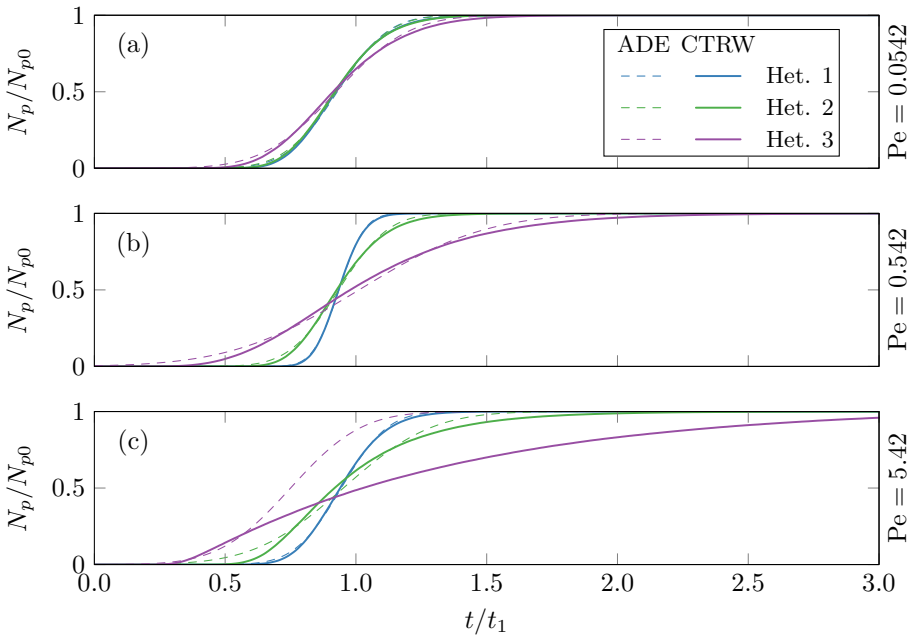


Figure 5.7: Normalized particle breakthrough (continuous lines) and the ADE best-fit using equation (2.8) (dashed lines) for each individual heterogeneity and $Pe = 0.0542$, 0.542 and 5.42. As the sample heterogeneity increases, the particle breakthrough departs from the ADE equation (2.8) model, and this effect increases as the Péclet number increases.

porous media (Scheven et al., 2005a; Scheven et al., 2005b). Particle propagators are calculated from the displacement of the particles and are analogues to molecular propagators. The calculated particle propagators in figure 5.8 are obtained by injecting 10^6 particles uniformly at $x = 0.02$ m, instead of at the inlet face to allow for back-diffusion through the inlet, and are tracked using observation times of $t/t_1 = 0.5$ and $t/t_1 = 1.0$. The observation times are normalized by the mean advective time to display the different samples in a consistent time frame, at late times when $t/t_1 \gg 1$ the particle propagator is expected to be fully developed to a Gaussian profile (Dentz et al., 2004; Berkowitz et al., 2006).

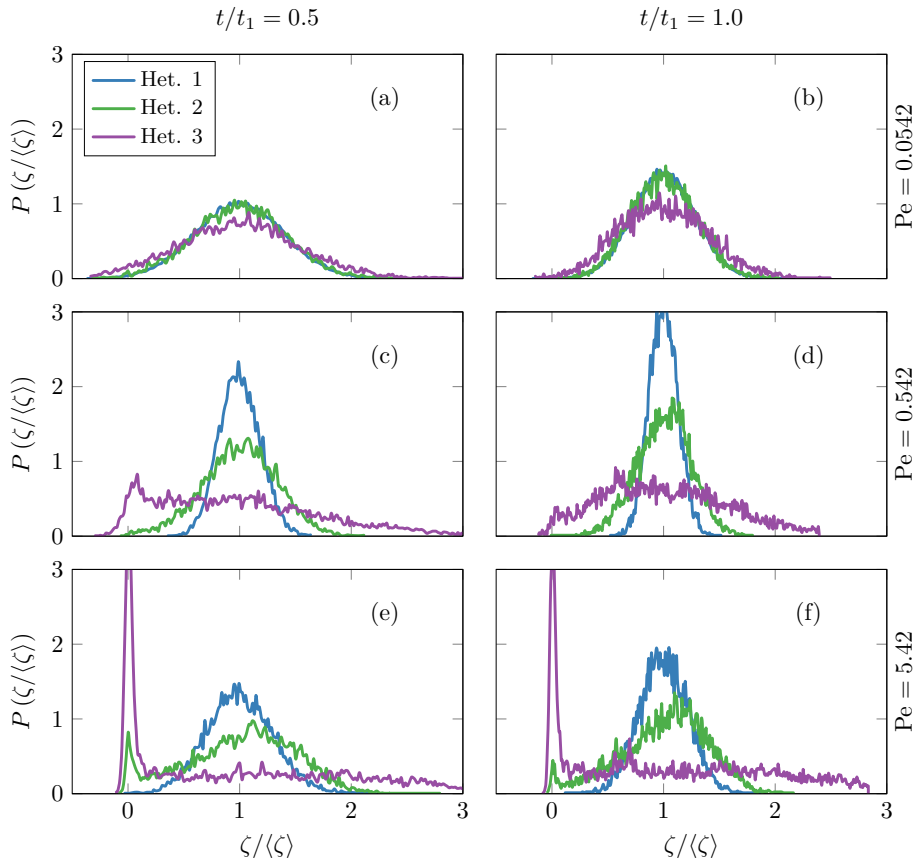


Figure 5.8: Initial particle propagators for Het. 1, 2 and 3 at $t/t_1 = 0.5$ and $t/t_1 = 1.0$, and Péclet numbers of $Pe = 0.0542$ (a) and (b), $Pe = 0.542$ (c) and (d) and $Pe = 5.42$ (e) and (f). As Pe increases, the contrast between the faster and the slower moving particles increases, showing a peak at $\zeta/\langle\zeta\rangle = 0$. The cut-off at the higher end of the Het. 3 is due to the particles exiting the domain, and making them unavailable for the calculation.

The porous media structure arising from the distribution of solid spherical inclusions significantly impacts the shape of the propagator distribution. The

profiles in most cases are far from the expected Gaussian profile that results from the solution of the transport equation using Fick's law, equation (5.1). For $Pe = 0.0542$, the propagator distributions for both samples Het. 1 and Het. 2 behave similarly, with little to no difference at early and late times. The propagator for Het. 3 is slightly asymmetrical at early times, showing higher probability of slow displacements ($\zeta/\langle\zeta\rangle < 1$) than for the other samples and takes longer to fully develop when compared to Het. 1 and 2. This is not the case for $Pe = 0.542$, that shows the signature of the pore space heterogeneity in all samples. Het. 1 shows little to no disturbance and is near Gaussian at both early and late times, Het. 2 seems to behave similarly but with a longer delay. However Het. 3, is highly asymmetrical with a high probability at $\zeta/\langle\zeta\rangle = 0$, showing a significant amount of stagnant particles at early observation times. This effect is still evident at later times when the profile fails to achieve the expected Gaussian shape. For $Pe = 5.42$, the observations are similar to those at $Pe = 0.542$, but with enhanced non-Gaussian behaviour. Both Het. 2 and 3 show the significant presence of stagnant particles, but Het. 2 is able to displace some particles towards the mean displacement $\langle\zeta\rangle$ as the probability in $\zeta/\langle\zeta\rangle = 0$ is smaller at later times. The particle propagator distribution for Het. 3 does not change significantly from early to late times.

Links showing characteristic advective times t_1 in the same order of the diffusive cut-off times t_2, or lower, are likely considered as of part of a stagnant region. Figure 5.6 shows that Het. 2 and 3 have velocities several orders of magnitude lower than the mean velocity. For $Pe = 0.0542$, diffusion is sufficiently rapid to allow particles in these slow-flow domains to be transported quickly to neighbouring links. However for $Pe = 0.542$ and 5.42, the differences in the velocity variation arising from the heterogeneity of the sample significantly increases the amount of stagnant particles.

Figure 5.9 shows the asymptotic normalized longitudinal dispersion coefficient D_L/D_m results for Het. 1, 2 and 3 versus Péclet number. The numerical results are compared against the experimental data presented in Bijeljic et al. (2004). The CTRW model reproduces the observed experimental measurements for beadpacks with $\beta = 1.8$ which describes fairly homogeneous media. For $Pe \ll 1$, D_L/D_m increases from Het. 3, 2 to 1 since the higher tortuosity in more heterogeneous media decreases the spread of solute by diffusion. However when advection is more dominant than diffusion, for $Pe \gg 1$, this behaviour is inverted, and D_L/D_m increases from most homogeneous Het. 1, to most heterogeneous Het. 3. This increase in physical heterogeneity is reflected in a decrease in β with values 1.8, 1.2 and 0.6 for Het. 1, 2 an 3 respectively.

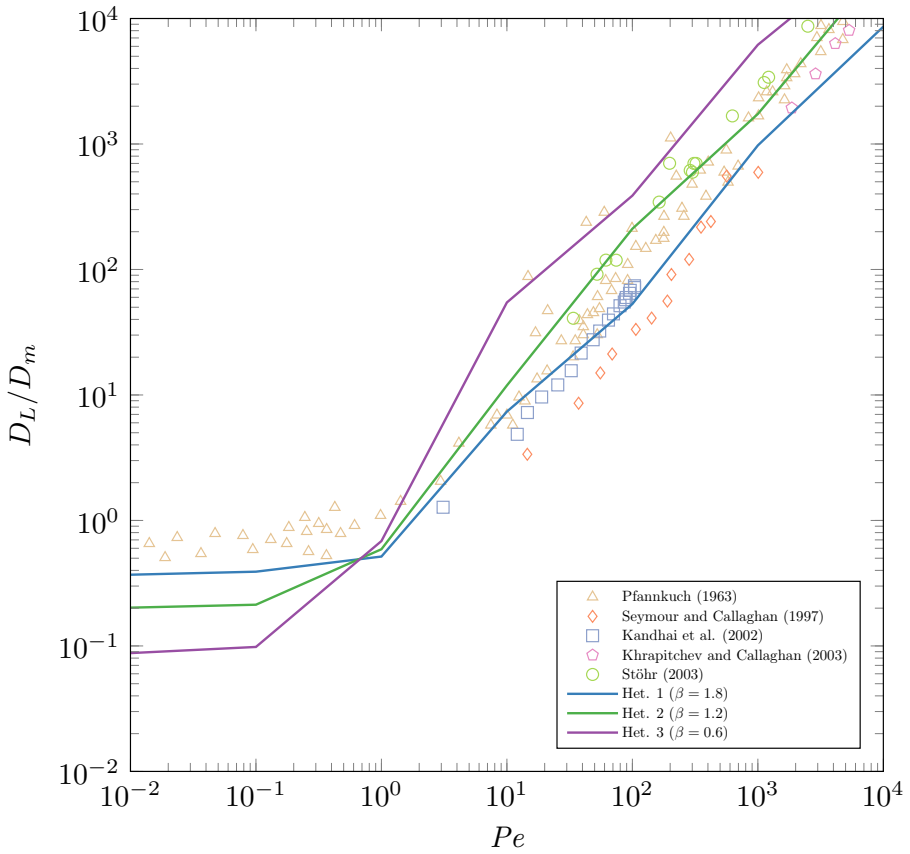


Figure 5.9: Longitudinal dispersion coefficient versus Péclet number. Numerical results for Het. 1, 2 and 3 and experimental measurements on beadpacks and sandpacks from Bijeljic et al. (2004) using the sources of Pfannkuch (1963), Seymour and Callaghan (1997), Kandhai et al. (2002), Khrapitchev and Callaghan (2003) and Stöhr (2003).

5.3 Impact of Physical Heterogeneity on Reactive Flow

We start in section 5.3.1 showing the dissolution patterns and the evolving porosity profiles. Next in section 5.3.2 we show the effects of the physical heterogeneity on the reaction rates. Finally in section 5.3.3 we show the impact of reactive flow on the evolution of the transit-time distributions ψ caused by the increase in porosity of the links and the post-dissolution particle propagators.

Each simulation runs for $t = 10^8$ s, 10^7 s and 10^6 s respectively for $Pe = 0.0542$, 0.542 and 5.42. This amounts to the injection of $V_{inj} = 7.3 \times 10^{-2}$ m^3 of acid, which is equivalent to injecting $PV = 6.74 \times 10^2$, 7.82×10^2, and 1.15×10^3 pore volumes respectively for Het. 1, 2 and 3. The characteristic reaction time $t_{\text{reac}} = 1/k_r = 1.59$ s, is 21 times smaller than the smallest characteristic advective time $t_1 = l/|v_{ij}| =$ of the fastest link in the lattice.

5.3.1 Visualization of Dissolution and Porosity Evolution

As mentioned previously we choose the $\beta = 1.8$, 1.2 and 0.6 for Het 1, 2 and 3 respectively to represent a beadpack or homogeneous consolidated media such as, a mildly homogeneous carbonate, and a highly heterogeneous carbonate (Bijeljic and Blunt, 2006; Bijeljic et al., 2011; Bijeljic et al., 2013a). However, we assume that all three solid structures can dissolve and at the same batch rate. The assumption is that lowering the β parameter respectively increases the domain heterogeneity at the scale of the nodes and links. Ideally we would estimate the local distribution of β from finer scales, such that each individual link would have a representative value, as described in Rhodes et al. (2008). However we keep the same assumption as in our previous work (Oliveira et al., 2021) and chapters; β is constant in time and space.

Figure 5.10 shows the emerging dissolution patterns for Het. 1 with $\beta = 1.8$, Het. 2 with $\beta = 1.2$ and Het. 3 with $\beta = 0.6$ for $Pe = 0.0542$, 0.542 and 5.42. After each row characterised with the same Pe number we also repeat the results for $\beta = 1.8$ for the same Pe for comparison. We show the snapshots of $t/t_1 = 1$ for $Pe = 0.0542$ and at $t/t_1 = 10$ for $Pe = 0.542$ and 5.42. For $Pe = 0.0542$ particle transport is more driven by diffusion and the majority of the dissolution happens at the inlet. The solid spherical inclusions play little role in restricting the available regions for dissolution for Het. 1, but have significant impact for Het. 2 and 3, for which the dissolution front reaches further into the sample. The dissolution pattern resembles compact or face dissolution for Het. 1, but has some channelling for Het. 2 and dominant channelling for Het. 3.

As Péclet number increases the particles are less likely to diffuse away from fast flowing channels, while experiencing shorter resident time in the nodes. Hence for $Pe = 0.542$ and 5.42 the dissolution forms a channelized pattern (Menke et al., 2015). The heterogeneity of the porous media do not allow a uniform dissolution, but leads to the formation of preferential channels. Table 5.2 shows the initial and final mean values for porosity and permeability of Het. 1, 2 and 3 and $Pe = 5.42$, 0.542 and 5.42.

It is evident that when the transport heterogeneity increases (β decreases), the emerging dissolution patterns change to more channelized behaviour. This indicates that a wider distribution of transit times promotes higher contrast for dissolution rates in the channels compared to the stagnant regions. This leads to a positive feedback, with the channels taking most of the flow and the injected reactant, exacerbating the contrast with the stagnant regions, and further enhancing dissolution in the channels. This impact is observed more prominently for Het. 3 and at higher Pe. The dissolved channels are formed earlier and reach further. Furthermore, this impact is more pronounced when the heterogeneity parameter β used in the model is decreased for Het. 2 and Het. 3 compared to when it is kept the same as $\beta = 1.8$.

Table 5.2: Mean initial and final porosity and permeability for the Het. 1, 2 and 3 and $Pe = 0.0542$, 0.542 and 5.42.

		ϕ		K/m^2	
Sample	Pe	initial	final	initial	final
Het. 1,	0.0542	0.29	0.65	1.69×10^{-12}	3.98×10^{-10}
$\beta = 1.8$	0.542	0.29	0.42	3.15×10^{-13}	2.29×10^{-11}
	5.42	0.29	0.33	4.50×10^{-15}	4.08×10^{-12}
Het. 2,	0.0542	0.25	0.59	1.69×10^{-12}	2.02×10^{-10}
$\beta = 1.8$	0.542	0.25	0.37	3.15×10^{-13}	9.45×10^{-12}
	5.42	0.25	0.29	4.50×10^{-15}	1.17×10^{-12}
Het. 2,	0.0542	0.25	0.60	1.69×10^{-12}	2.16×10^{-10}
$\beta = 1.2$	0.542	0.25	0.38	3.15×10^{-13}	1.06×10^{-11}
	5.42	0.25	0.30	4.50×10^{-15}	1.37×10^{-12}
Het. 3,	0.0542	0.17	0.46	1.69×10^{-12}	2.78×10^{-11}
$\beta = 1.8$	0.542	0.17	0.28	3.15×10^{-13}	9.18×10^{-13}
	5.42	0.17	0.20	4.50×10^{-15}	4.34×10^{-14}
Het. 3,	0.0542	0.17	0.42	1.69×10^{-12}	9.22×10^{-12}
$\beta = 0.6$	0.542	0.17	0.27	3.15×10^{-13}	3.18×10^{-13}
	5.42	0.17	0.21	4.50×10^{-15}	2.69×10^{-14}

The change in the mean porosity profiles along the flow direction are illus-

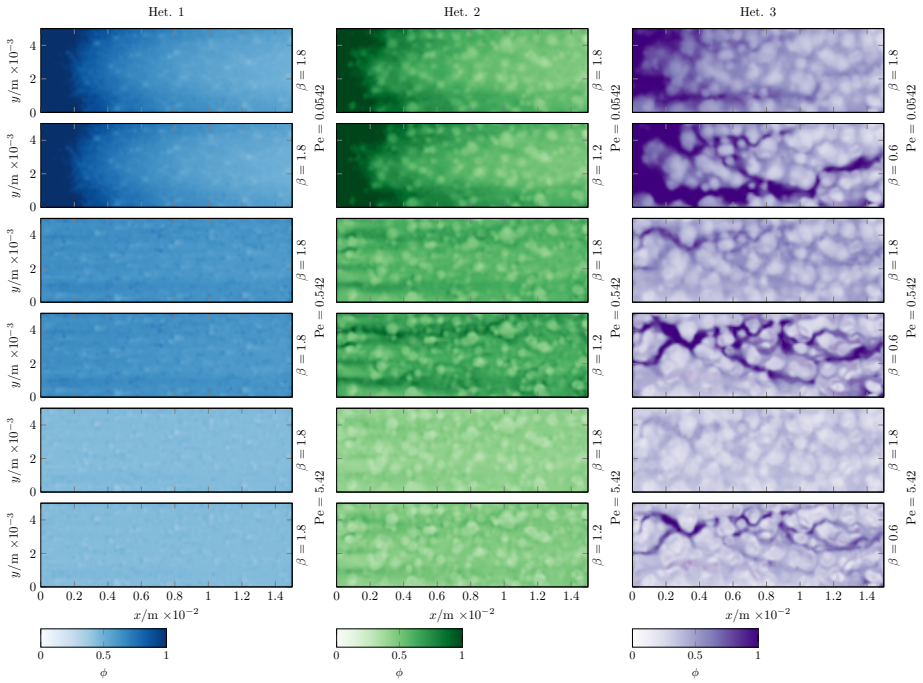


Figure 5.10: Dissolution-induced porosity of the different samples at $t/t_1 = 1$ for Het. 1 using $\beta = 1.8$, Het. 2 using $\beta = 1.2$ and Het. 3 $\beta = 0.6$, and Péclet numbers of $Pe = 0.0542$, and at $t/t_1 = 10$ for $Pe = 0.542$ and 5.42. Below each row characterised with the same Pe number the results for $\beta = 1.8$ for the same Pe are presented for comparison. The model transport heterogeneity parameter β intensifies the emerging dissolution pattern; the dissolved channels are formed earlier and reach further when compared to $\beta = 1.8$.

trated in figure 5.11 for Het. 1, 2 and 3 and $Pe = 0.0542$, 0.542 and 5.42. For a common normalized advective time t/t_1, the samples with highest porosity increase are the ones subjected to the smallest local Pe number, as the particles have a longer resident time in the nodes. The profiles highlight the differences between the different dissolution patterns; for low Pe number the dissolution follows a compact dissolution pattern mostly occurring at the inlet, and progressing with a lower rate further down the sample. For higher Pe numbers, the change in porosity in the inlet is not as significant. Furthermore, the impact of heterogeneity is observed, with the highest porosity change at the inlet for Het. 3.

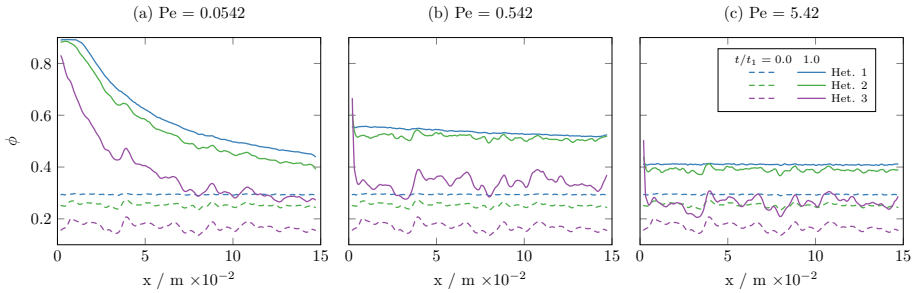


Figure 5.11: Porosity profiles along the flow direction ($x-$axis) for Het. 1, 2 and 3, and Péclet numbers of (a) $Pe = 0.0542$, (b) $Pe = 0.542$ and (c) $Pe = 5.42$. At low Pe number the dissolution occurs mostly at the inlet, characteristic of a compact dissolution front. For $t/t_1 \ll 1$ porosity increases proportionally to time but the change in porosity reduces and reduction becomes smaller for $t/t_1 \gg 1$.

Looking into the porosity distribution, figure 5.12 highlights the porosity intervals that were more effectively altered by dissolution. The regions of higher changes are in the vicinity of higher mean porosity, as these regions naturally focus flow and the transport of fresh reactants. Lower porosity regions have little to no influence at higher Pe; it is only when Pe is low and diffusion is significant that noticeable dissolution can be observed. The amount of porosity near $\phi = 0.3$ is nearly identical for $t/t_1 = 0.5$ and 1.0, and is illustrated in figure 5.13.

5.3.2 Effect of Physical Heterogeneity on Reaction Rates

Figure 5.14 shows the normalized effective reaction rate calculated for all Pe and samples, and compares it to the complete mixing reaction rate at late-time $r_{\text{eff}} \sim 1/\sqrt{t}$ (Dentz et al., 2011). This time scaling is predicted from solutions of the ADRE, 5.1, and assumes that the reactant undergoes diffusive mixing over a

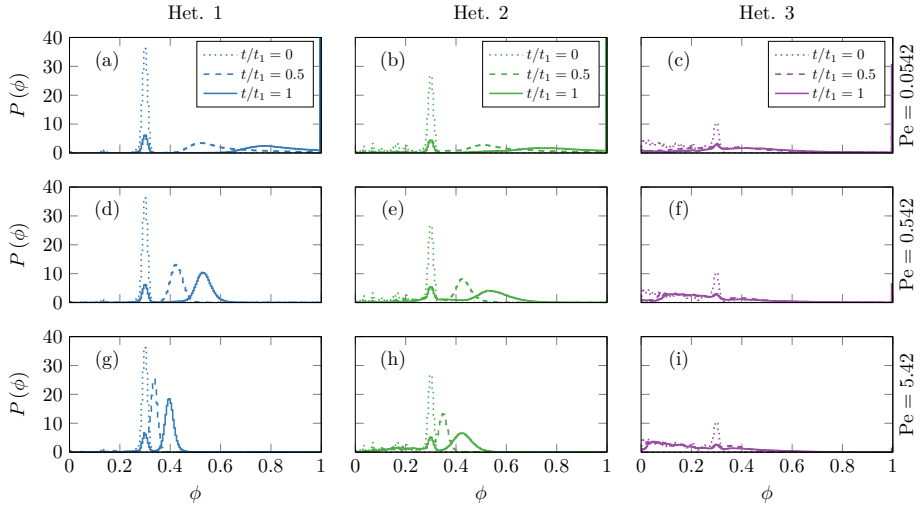


Figure 5.12: Histogram of porosity distributions for Het. 1, 2 and 3 with $Pe = 0.0542$, 0.542 and 5.42 at different normalized advective times t/t_1. Dissolution is fastest in regions of high porosity, as these regions naturally focus flow and the transport of fresh reactants. Lower porosity regions have little to no influence at higher Pe; only when diffusion is significant can such regions experience noticeable dissolution.

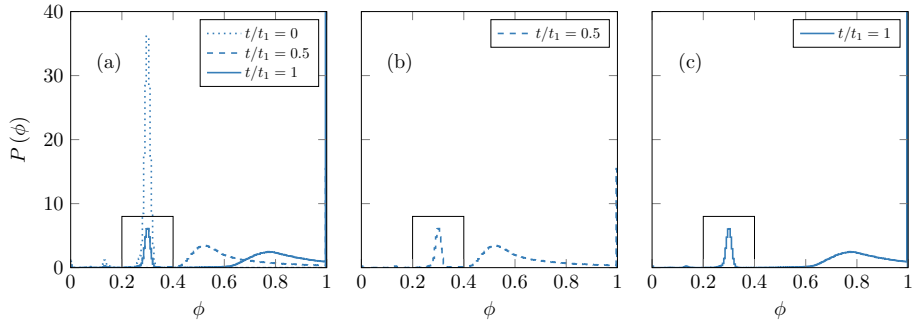


Figure 5.13: Detail of the histogram of porosity distributions for Het. 1 at different normalized advective times t/t_1. The peak in $\phi = 0.3$ is nearly identical for $t/t_1 = 0.5$ and 1.0. We only show the case of Het. 1 and $Pe = 0.0542$ however the same happens for the other cases illustrated in figure 5.12.

length that scales as $\sqrt{t}$. The effective reaction rate is normalized with the batch reaction rate of calcite measured in Peng et al. (2015). The effective reaction rate obtained by the CTRW model increases with time, achieves a maximum value, and then decreases towards but does not attain the complete mixing reaction rate given by the ADRE. At early times $t/t_1 \ll 1$, the CTRW model reaction rates are much smaller than would be predicted by a Fickian model. This is expected as the effective reaction rate given by the ADRE assumes that all reactants are perfectly mixed controlled by the asymptotic (and larger) value of the longitudinal dispersion coefficient D_l, whereas in fact the behaviour of D_L is preasymptotic and much lower than its asymptotic late-time value (Alhashmi et al., 2016). However, even at late times $t/t_1 \gg 1$, when D_L increases, the CTRW model effective reaction rates still deviate from the behaviour predicted assuming complete mixing for all Pe numbers studied, and with a different scaling for each porous medium.

At late times, the effective reaction rate scales as t^{-a} with $a > 0.5$ for all samples and Pe numbers, pointing out that r_{eff} is still far from the complete mixing reaction rate even at late-times when the effective reaction rate could be expected to scale with t^{-a} with $a = 0.5$ (Dentz et al., 2011). This is a result of the persistence of incomplete mixing. The late time power-law scaling for each individual sample and Pe number are presented in table 5.3. The scaling deviates further from the ideal value as Pe increases.

Effective reaction rates exhibit dependence on transport conditions. At early times, mixing taking place in the fast flow channels has stronger impact, hence reaction rates are higher for $Pe = 5.42$ compared to the lower Pe numbers. However, by late times diffusion has mixed the reactants in both fast channels and stagnant regions, resulting in the higher reaction rates for the lowest $Pe = 0.0542$. The impact of physical heterogeneity on the reaction rates at $Pe = 5.42$ is manifested as the highest maximum at early times for the most heterogeneous medium Het. 3. At both intermediate $Pe = 0.542$ and low $Pe = 0.0542$, diffusion leads to better mixing of reactants and results in the higher reaction rates for more homogeneous medium Het. 1.

5.3.3 Transit-time Distributions and Particle Propagators

Figure 5.15 shows the locally defined transit-time distribution ψ for Het. 1, 2 and 3 at $Pe = 0.0542$ and 5.42, at two times, $t/t_1 = 0$ s and $t/t_1 = 10$ s at the location near the inlet at $\mathbf{x}_1 = (0.5, 3.7, 3.0) \times 10^{-3}$ m and near the outlet at $\mathbf{x}_2 = (12.0, 0.8, 3.0) \times 10^{-3}$ m. The local ψ functions are calculated using equation (3.12), t_1 is calculated from the velocity at the link, t_2 is calculated

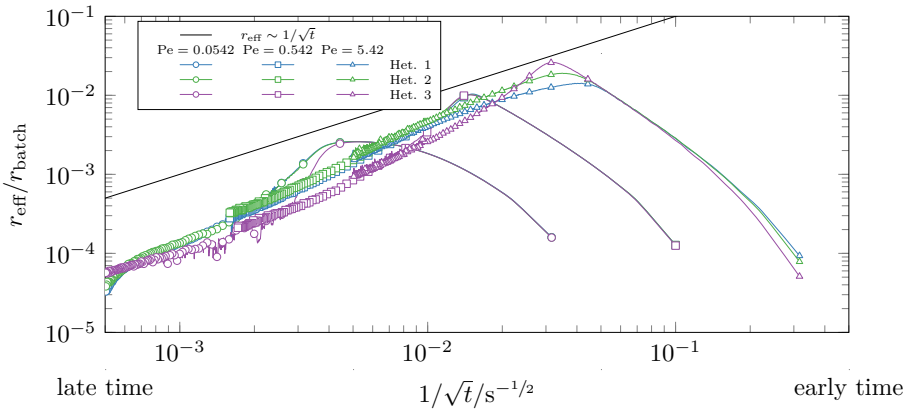


Figure 5.14: Normalized effective reaction rate plotted against $1/\sqrt{t}$ for Het. 1, Het. 2 and Het. 3 respectively and $\beta = 1.8$, 1.2 and 0.6, at $Pe = 0.0542$, 0.542 and 5.42. The effective reaction rate is normalized with the batch reaction rate of calcite (table 5.1). The black solid line is the 1:1 trend, highlighting the power-law scaling of $r_{\text{eff}} \sim t^{-a}$ with $a = 0.5$. The power-law scaling factors a for each sample and Pe is shown in table 5.3.

Table 5.3: Power-law scaling for the effective reaction rate for $Pe = 0.0542$, 0.542 and 5.42 and for samples Het. 1, 2 and 3. The power-law scaling t^{-a} with $a > 0.5$ is a result of the persistence of incomplete mixing.

	Het. 1		Het. 2		Het. 3	
Pe	$\langle r_{\text{eff}} \rangle$	$\sigma_{r_{\text{eff}}}$	$\langle r_{\text{eff}} \rangle$	$\sigma_{r_{\text{eff}}}$	$\langle r_{\text{eff}} \rangle$	$\sigma_{r_{\text{eff}}}$
0.0542	0.68	0.04	0.61	0.04	0.57	0.04
0.542	0.67	0.04	0.69	0.04	0.68	0.03
5.42	0.70	0.03	0.75	0.03	0.76	0.02

from the defined molecular diffusion coefficient, and using $\beta = 1.8$, 1.2 and 0.6 respectively for Het. 1, 2 and 3. When comparing the initial state $t/t_1 = 0$ to the final state $t/t_1 = 10$, the probability of shorter transitions increases for Het. 1 at both Pe numbers, more effectively for lower $Pe = 0.0542$ but is still significant for $Pe = 5.42$. The behaviour of the ψ function of Het. 2 is similar. However, Het. 3 experiences the same increase in ψ at both $Pe = 0.0542$ and 5.42. At lower Pe numbers, the links at the inlet dissolve entirely, but at higher Pe numbers only Het. 3 develops a channel developing through that particular location, such that the links there undergo the highest increase in velocity. When comparing the changes in the links near the inlet and near the outlet at the end of the dissolution simulation, Het. 1 shows little differences for $Pe = 0.0542$, and no differences for $Pe = 5.42$. This reflects the uniformity in which the porous media is dissolved at low Pe number and the lack of preferential formed channels at higher Pe number. Het. 2 shows a similar trend, but with slightly bigger difference for $Pe = 5.42$. However Het. 3 shows a different behaviour: there is no change at the inlet irrespectively of the Pe number, while at the outlet the probability at higher Pe number shows the emergent dissolved channel not as significant as in the $Pe = 0.0542$.

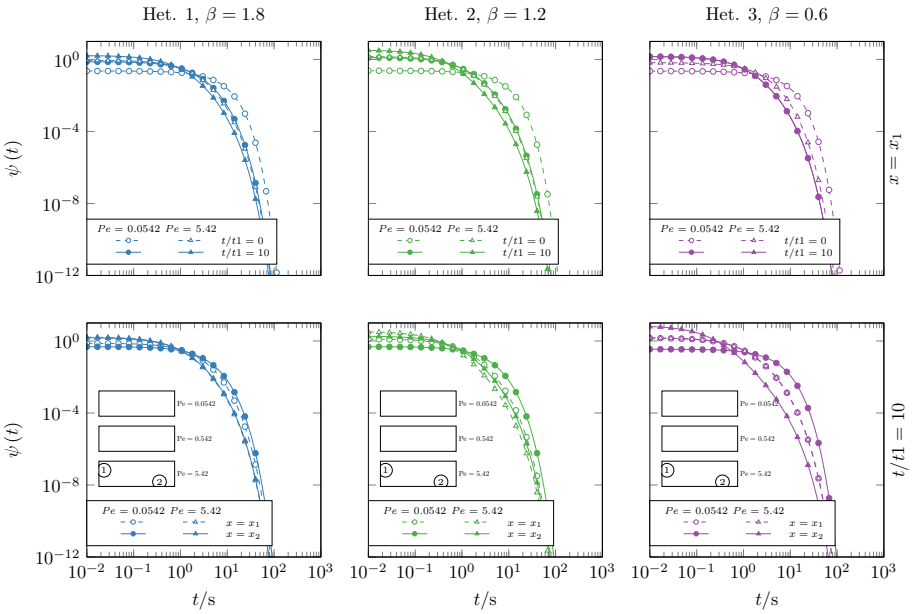


Figure 5.15: (Top row) Local ψ functions before ($t/t_1 = 0$) and after ($t/t_1 = 10$) dissolution defined at the links located near the inlet at $\mathbf{x}_1 = (0.5, 3.7, 3.0)$ $\times 10^{-3}$ m and (Bottom row) local ψ functions at $t/t_1 = 10$ at $\mathbf{x}_1$ and near the outlet at $\mathbf{x}_2 = (12.0, 0.8, 3.0)$ $\times 10^{-3}$ m, for Het. 1, 2 and 3 at $Pe = 0.0542$ and 5.42.

Figure 5.16 shows the propagators at $t/t_1 = 0.5$ and 1.0, after dissolution processes takes place, compared against the propagators of the initial porosity of figure 5.8. The dissolution process significantly alters the initial particle propagator and increases the contrast between slow and fast flow regions in all samples. At lower Pe number, the particle propagators are no longer able to recover a Gaussian-like distribution even at late times. The sharp cut-off in the high end of the propagator distribution is due to the fact that the particles exited the domain at the observation window t/t_1. At $Pe = 0.542$ the distribution is marked by a strong stagnant peak and is asymmetrical for all samples. Het. 1 is the only sample that starts to recover a Gaussian-like shape at late times, but still far from the initially observed distribution. For $Pe = 5.42$, the distribution mostly reflects the stagnant peak. Overall, the analysis of post-dissolution propagators indicates that dissolution results in heterogeneity signatures with a markedly higher degree of non-Fickian transport.

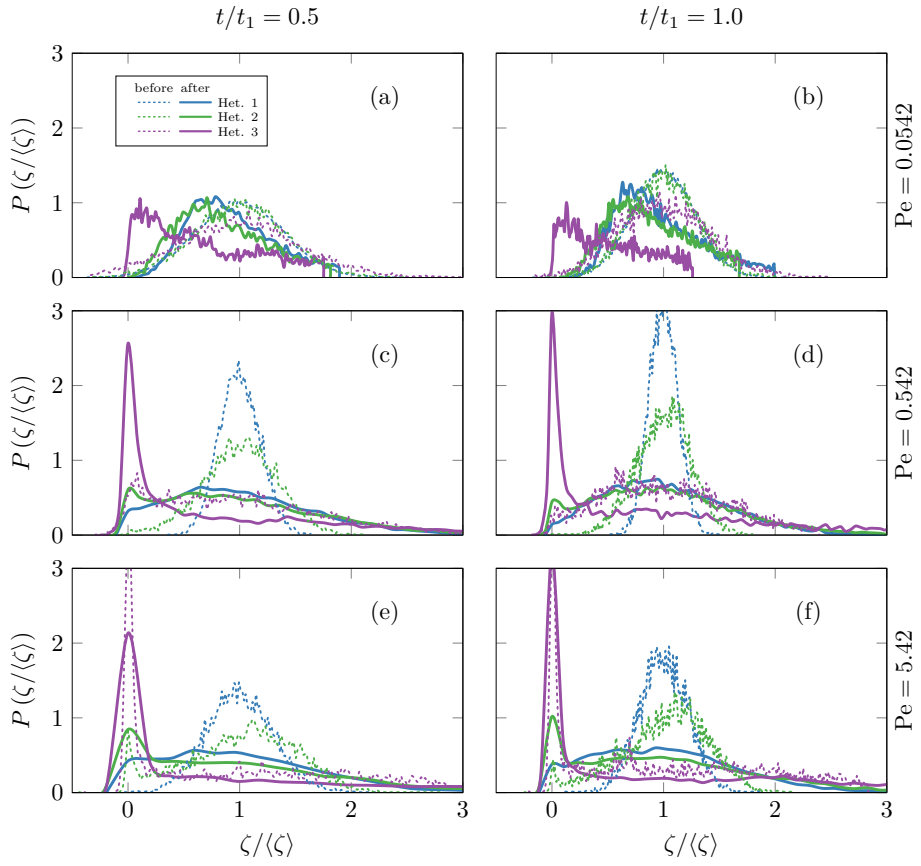


Figure 5.16: Particle propagators for Het. 1 with $\beta = 1.8$, Het. 2 with $\beta = 1.2$ and Het. 3 with $\beta = 0.6$ at $t/t_1 = 0.5$ and $t/t_1 = 1.0$, and Péclet numbers of $Pe = 0.542$. The results are compared against the initial particle propagators from figure 5.8 (dashed lines).

5.4 Discussion

When considering heterogeneity signatures, the velocity distributions shown in figure 5.6 are key to understanding the initial propagators in figure 5.8, similar to the pore-scale description provided in Bijeljic et al., 2013b. The higher probability of transitions faster than the mean velocity increases as the heterogeneity increases from Het. 1 to 3. This is more evident in Het. 3 that shows more displacement for $\zeta/\langle\zeta\rangle > 1$. Furthermore, the velocities at the lower end of the distribution represent longer transit-times and stagnant particles. Figure 5.17 shows the velocity distribution and the contribution of each individual region to the particle transitions at the pore-scale associated with the links in the lattice. Bijeljic et al. (2013a) showed a similar plot based on pore-scale direct numerical simulations of transport in different carbonate rock samples. As we increase the Pe number, we increase the number of links with faster velocity.

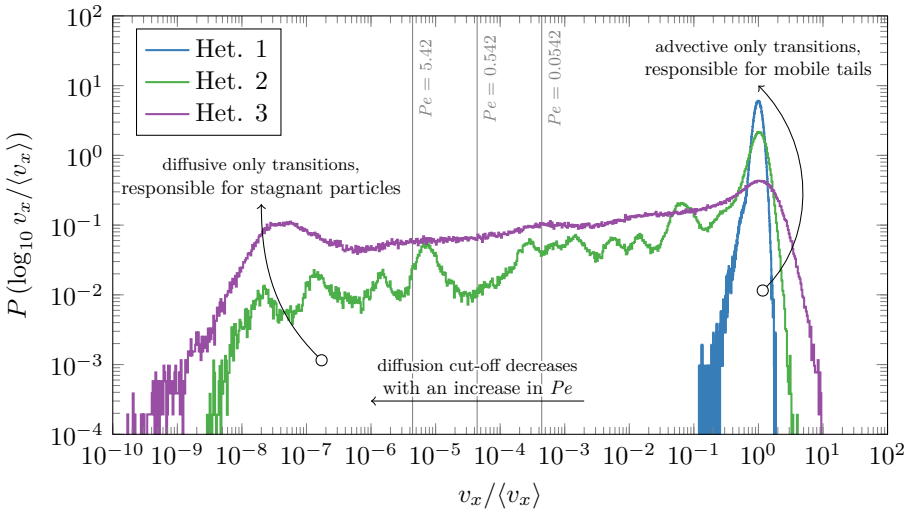


Figure 5.17: Normalized velocity distributions for the different samples. The lower velocity values contribute to the slow and diffusive only transitions. The high velocity values contribute to the advective dominated transitions, responsible for the highly mobile tails and the formation of dissolution channels.

The dissolution patterns formed for the samples using a constant transport heterogeneity parameter $\beta = 1.8$ are compared in figure 5.10 to the dissolution patterns formed when reducing the value of $\beta = 1.2$ and 0.6 respectively for Het. 2 and 3. This reduction is perceived as an increase in heterogeneity at the node and link scale; it increases the probability of a particle to experience slower time transitions. This is highlighted in figure 5.15.

The transport heterogeneity parameter β is related to the effective reaction

rate such that the lower β, the higher the maximum rate, but the faster it approaches the asymptotic behaviour $1/\sqrt{t}$ (figure 5.14). However, the asymptotic behaviour is never attained due to persistence of incomplete mixing. This behaviour is similar for different Pe numbers, but more pronounced for higher Pe.

5.5 Conclusions

We have demonstrated the impact of physical heterogeneity on the effective reaction rate during dissolution on samples of length 15 cm over time-scales up to 10×10^8 s. We constructed three samples characterised by increasing heterogeneity by uniformly distributing solid spheres of zero porosity in the domains consisting of modified packs of solid spheres. The heterogeneity is first characterized by the velocity distribution. Het. 1 has a narrow velocity distribution near $v_x/\langle v_x \rangle = 1$ reflecting the relative homogeneity of the sample, while Het. 2 and 3 have a wider distribution with a smeared-out tail towards lower velocity values. At the scale of the sample, these resemble a beadpack for Het. 1, a mildly homogeneous carbonate for Het. 2, and a highly heterogeneous carbonate for Het. 3. However, we assume that the solid dissolves with the same batch reaction rate for all three samples. At the scale of the nodes and links, to describe the local transit time distributions, Eq. 3.12, we consider $\beta = 1.8$ for Het. 1, $\beta = 1.2$ for Het. 2 and $\beta = 0.6$ for Het. 3, to better represent difference in heterogeneity in the corresponding velocity fields. Each of these samples were subjected to fluid reactant injection under different advective dominated flow regimes, from low to strongly advective dominated regimes, by choosing Peclét numbers of $Pe = 0.0542$, 0.542 and 5.42.

The different Pe numbers led to the appearance of two distinct dissolution patterns – a compact or face dissolution for $Pe = 0.0542$, and a channelized dissolution for $Pe = 0.542$ and 5.42. The emergence of preferential channels in heterogeneous media, as opposed to uniform dissolution, is consistent with experiments in carbonates (Menke et al., 2015). For all samples and advective regimes, the change in porosity is proportional to the time at early times while the effective reaction rate deviates from long-time scaling behaviour characterised by $1/\sqrt{t}$, assuming complete mixing. Instead, at late times we found a power-law scaling t^{-a} with $a > 0.5$, as a result of the persistence of incomplete mixing.

The propagator distributions showed the imprint of heterogeneity on its asymmetrical shape, as well as the contrast between slow and fast regions that increased with the dissolution process. The variation in the velocity distribution of Het. 1 is very narrow and there are almost no stagnant particles. However

for Het. 2 and 3, the variation in the velocity distribution is orders of magnitude higher and this is perceived by the amount of stagnant particles for $Pe = 0.542$ and 5.42, that experience the highest contrast between the characteristics advective time t_1 and diffusive cut-off time t_2. After the dissolution process, Het. 1 starts to recover a symmetrical shape at late times but it is still far from the initial observed state. However Het. 2 and 3 have significant amount of stagnant particles and are asymmetric in shape. Overall, dissolution increases the degree of non-Fickianity in transport.

Finally, we examined the impact of β on the average porosity evolution and effective reaction rates. The transport heterogeneity parameter β shows that irrespective of the advection regime, more heterogeneous samples had lower long-time reaction rates, as reaction was eventually confined to a small subset of the pore space in preferential channels. An increase in Pe also exacerbated the effect of channelling and incomplete mixing, although at early time the reaction rates were higher, due to a greater degree of spreading by advection.

CHAPTER 6

Coupled Flow and Chemical Heterogeneities — The Impact of Chemical Spatial Distribution on Effective Reaction Rate

In the previous chapter we studied the impact of physical heterogeneity on the effective reaction rates in porous media. We showed how the effective reaction rates depend upon the initial physical heterogeneity and the transport conditions. In this chapter we build upon our CTRW reactive transport model, and extend it to account for heterogeneous spatial distributions of different minerals. This allows us to study systems with undergoing simultaneous kinetics and equilibrium of many different species. We will show that this is essential to study dynamics of reactive transport in porous media.

We start by studying a multi-species fluid-fluid reaction only model, while later examining a multi-species fluid-solid reactive model. We show the results of the fluid-fluid reactive system consisting of sodium carbonate and calcium chloride, commonly studied in the literature (Willingham et al., 2008; De Anna et al., 2014; Oliveira et al., 2020; Puyguiraud et al., 2020), and demonstrate how physical heterogeneity increases mixing of the system and rate of production of sodium chloride and calcium carbonate. Finally we study a fluid-solid reactive

system composed of calcite and dolomite (Busenberg and Plummer, 1982; Peng et al., 2015; Peng et al., 2016; Al-Khulaifi et al., 2018), with the dissolution of randomly distributed minerals at different ratios on the effective reaction rates in the presence of HCl, and show the impact of mineral content and distribution in chemically heterogeneous systems.

6.1 Description of the Geochemical Solver

Due to its nature, modelling the coupled transport and reactions using an implicit scheme is prohibitive for our cases. Given that we model transport using discrete particles, the iterative methods are a natural choice. Among those, the Sequential Iterative Approach (SIA) or Sequential Non-Iterative Approach (SNIA) are the most traditionally used approaches (Steefel and MacQuarrie, 1996). The SNIA solves transport and reactions independently: first solves transport as if no reaction takes place, then solves the reactions using the transported concentrations. This is suitable when the characteristic reaction times are much shorter than the characteristic advective and diffusive times, as in the applications in sections 6.2 and 6.3.

To solve the chemical reactions of the fluid-fluid and fluid-solid systems, we use the geochemical solver Reaktoro (Leal, 2014; Leal et al., 2014; Leal et al., 2015). Other geochemical solvers, *e.g.* GEM-Selektor (Kulik et al., 2013) and PHREEQC (Parkhurst and Appelo, 2013), can be used instead of Reaktoro but were not considered here. Reaktoro solves multiphase chemical equilibrium and kinetics of species as in a complete mixing batch reactor. It makes use of partial equilibrium to separate reactions in either chemical kinetics or under equilibrium. The solver efficiency comes from formulating the chemical equilibrium as a Gibbs Energy Minimization (GEM), simultaneously solving both the chemical equilibrium and kinetics, and treating it as a non-linear programming problem (Leal et al., 2014).

The thermodynamic properties of the species are extracted directly from the SUPCRT98 database (revised from SUPCRT92, Johnson et al., 1992). This provides the necessary parameters for the equations of state for the aqueous (Tanger and Helgeson, 1988), the gaseous (Peng and Robinson, 1976), and mineral species (Maier and Kelley, 1932).

6.2 Fluid-Fluid Reactive System

In this section we show the multi-species fluid-fluid reaction model consisting of sodium carbonate and calcium chloride as reactants, leading to the production

of sodium chloride and calcium carbonate. We describe the fluid-fluid reactive system model in section 6.2.1. We use the same samples as before in chapter 5, Het. 1 and Het. 3 to respectively represent a relatively homogeneous beadpack and a heterogeneous carbonate. Next, in section 6.2.2, we show the effects of the physical heterogeneity in the mixing of the species and rate of formation of products for $Pe = 10$ and 100.

6.2.1 Description of the Fluid-Fluid CTRW Reactive Transport Model

Our model uses a multi-species approach, studying species transport in an inert medium; there is no dissolution or precipitation, so there is no change in porosity or permeability induced by the different reactions happening in the system. Over-saturation does not lead to precipitation, but is instead transported with the rest of the produced species. There is no gaseous phase, so any gaseous species are considered as always being dissolved in the aqueous phase.

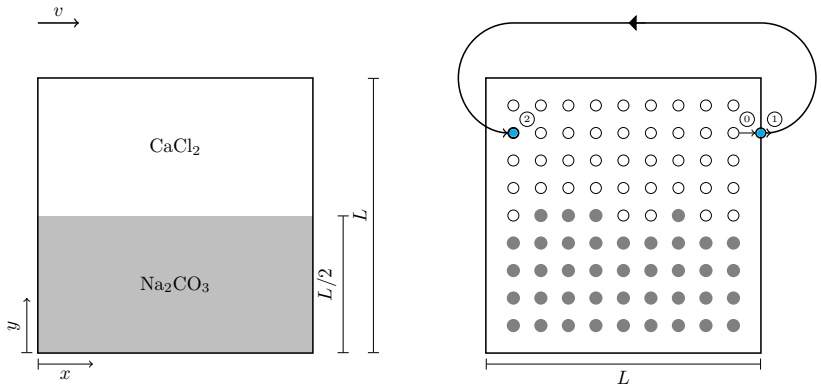
We study the parallel injection of two aqueous solutions to model fluid-fluid reactions at the interface where both solutions mix. The solutions consist of sodium carbonate Na_2CO_3 and calcium chloride $CaCl_2$, that leads to production of sodium chloride NaCl and calcium carbonate $CaCO_3$:

$$Na_2CO_3 + CaCl_2 \rightleftharpoons NaCl + CaCO_3 \tag{6.1}$$

The system described in equation (6.1) is composed of the following homogeneous reactions:

$$H_2O\,(l) \rightleftharpoons H^+ + OH^- \tag{6.2a}$$
$$CO_2(aq) + H_2O\,(l) \rightleftharpoons HCO_3{}^- + H^+ \tag{6.2b}$$
$$HCO_3{}^- \rightleftharpoons H^+ + CO_3{}^{2-} \tag{6.2c}$$
$$NaOH\,(aq) \rightleftharpoons Na^+ + OH^- \tag{6.2d}$$
$$CaCl_2(aq) \rightleftharpoons CaCl^+ + Cl^- \tag{6.2e}$$
$$CaCl^+ \rightleftharpoons Ca^{2+} + Cl^- \tag{6.2f}$$
$$CaOH^+ \rightleftharpoons Ca^{2+} + OH^- \tag{6.2g}$$
$$HCl\,(aq) \rightleftharpoons H^+ + Cl^- \tag{6.2h}$$
$$NaCl\,(aq) \rightleftharpoons Na^+ + Cl^- \tag{6.2i}$$
$$CaCO_3(aq) \rightleftharpoons Ca^{2+} + CO_3{}^{2-} \tag{6.2j}$$
$$CaHCO_3{}^+ \rightleftharpoons Ca^{2+} + HCO_3{}^- \tag{6.2k}$$

The reaction system and equilibrium calculations described by equation (6.2) takes place in the nodes of the lattice. We assume that the fluid-fluid reactions are instantaneous, or that the reactive time scale is much faster than the diffusive time scales. This makes the species production only limited by transport, $Da \to \infty$ (De Simoni et al., 2005), and rate of formation of products can vary both time and space due to physical and transport heterogeneities. Figure 6.1 illustrates the initial conditions of the problem studied.



(a) Domain geometry (b) Reinjection condition

Figure 6.1: Domain geometry and the particle representation with the reinjection condition. The domain is filled with $CaCl_2$ in the top half and with Na_2CO_3 in the bottom half, which flow in the positive $x-$direction. To conserve mass, all the produced particles when transitioning ⓪ beyond the domain ① $x > L$, are reinjected ② at $x = 0$.

Differently than in chapters 4 and 5, the particles in the fluid-fluid model are responsible for transporting several chemical species at once. The species and amounts for this case are detailed later in table 6.2. Even though the molecular diffusion coefficient is a function of the specific concentration of a given chemical species, temperature and other factors, we define the molecular diffusion coefficient constant and equal to the molecular self-diffusion of water, $D_m = 2.2 \times 10^{-9}\,\mathrm{m^2\,s^{-1}}$. This makes the ψ function in each individual link depend only on the velocity in the link.

At $t = 0\,\mathrm{s}$, the domain is divided in two halves, and it is completely saturated with $25\,\mathrm{mol\,m^{-3}}$ of Na_2CO_3 solution in the bottom half and with $25\,\mathrm{mol\,m^{-3}}$ of $CaCl_2$ solution in the top half. The injection is similarly divided in two halves with the same concentrations of Na_2CO_3 and $CaCl_2$ respectively injected into the bottom and into the top of the domain. When a given particle transitions beyond the domain, $x > L$, it is re-injected at a random location in the inlet.

Figure 6.2 illustrates the conceptual representation of the fluid-fluid reactive

system. Each node of the lattice behaves as a batch reactor, mixing and equilibrating all the particles species in it. As described in chapter 4, we require that all particles are synchronized at a common checkpoint after a time-step Δt. We choose the value of Δt as a fraction of the expected value of ψ, or $\Delta t = \alpha \, \mathrm{E}(\psi)$, for $0 < \alpha \leq 1$. For the results showed here, we selected a value of $\alpha = 0.01$. The smaller the value of α the more frequent are the equilibrium calculations, and more precise are the results. However, this is the most computationally demanding step of the algorithm, so the values of α have to be selected appropriately.

At each checkpoint we gather all the particles in the individual nodes and we collect the total amount of species from the particles in each node. We then proceed with the state equilibrium calculations for each node. The resulting species are then equally scattered among the particles in the individual nodes. After the species distribution, the particles are ready to transit again, transporting the equilibrated species to other nodes.

The steps in the algorithm are listed below:

1. Create the lattice with an initial distribution of porosity ϕ and permeability K.
2. Solve the pressure field P in the lattice, calculate the local velocities v_{ij} and local Péclet numbers Pe_{ij} in the links.
3. Calculate the local probabilities of displacement p_{ij} (eq. 3.14) and the local transit-time distribution ψ_{ij} (eq. 3.12) in the links.
4. Distribute $CaCl_2$ rich particles in the top half and Na_2CO_3 rich particles in the bottom half of the sample weighted by the porosity of the nodes.
5. Inject $CaCl_2$ rich particles in the top and Na_2CO_3 rich particles in bottom using a flow-weighted injection rule.
6. Sample a displacement direction $\Delta \mathbf{x}$ from p_{ij} and transit-time $\Delta\tau$ from ψ_{ij} for each particle.
7. Move the particle from the node i to the node j, if $\sum \Delta\tau^m \leq \Delta t$, where m labels each particle transition. This is performed individually for each particle.
8. Repeat steps 6 – 7 for all particles while $\sum \Delta\tau^m \leq \Delta t$. Each particle can undergo several transitions in one time step before the pressure field is updated.
9. Gather all the particles in the node i and collect the total amount of species in it.

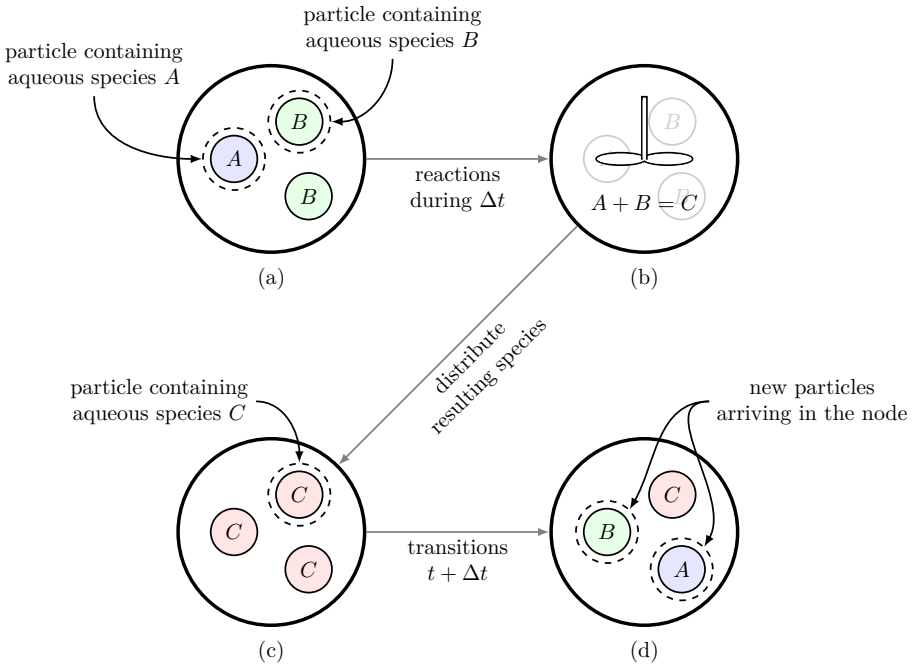


Figure 6.2: Conceptual representation of the fluid-fluid reactive system. Particles might contain any distribution of species, but for simplicity this diagram shows particles containing only theoretical species A or B, that produces species C. (a) We start with a distribution of particles with theoretical aqueous species A and B at a given node. (b) At checkpoint times Δt, each node behaves as a batch reactor, mixing and reacting all available species in it. (c) The resulting species C are then distributed among the particles contained in the node. (d) The model proceeds with the particles transitions, when particles either leave with the produced species or arrive with other species.

10. Calculate the equilibrium state for the node i.
11. Distribute the resulting species from the new state of node i back to the particles in it.
12. Repeat steps 9 – 11 for all the nodes in the lattice.
13. Repeat steps 2 – 12 until the end of the simulation.

We choose the lattice as in the samples Het. 1 and Het. 3 described in chapter 5. These are displayed in figure 6.3 and summarized in table 6.1. The lattice domain starts with randomly distributed particles weighted by the porosity of the node, such that the higher the porosity of a node, higher the number of particles in it.

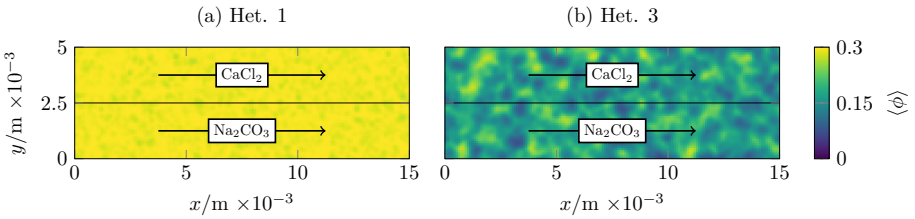


Figure 6.3: Initial porosity fields for (a) Het. 1 and (b) Het. 3. The porosity field is constructed using zero-porosity inclusions in the background porosity field of $\langle\phi\rangle = 0.3$ as shown in figure 5.2 and discussed in chapter 5.

Table 6.1: Initial sample properties. All samples are built using the same background porosity and permeability correlation factors. The molecular diffusion coefficient is considered to be the same for all species.

Parameter	S.I. Unit	Het. 1	Het. 3
$\langle\phi_{bg}\rangle$		0.30	0.30
$\sigma_{\phi\text{bg}}$		0.10	0.10
$\langle\phi\rangle$		0.29	0.17
$\langle K\rangle$	m^2	1.69×10^{-12}	4.50×10^{-15}
a	m^2	1.00×10^{-8}	1.00×10^{-8}
b		7.00	7.00
$\langle r\rangle$	m	1.50×10^{-3}	4.50×10^{-3}
σ_r		0.20	0.20
β		1.80	1.80
ρ	$\text{m}^3\,\text{kg}^{-1}$	2.70×10^3	2.70×10^3
l	m	1.00×10^{-3}	1.00×10^{-3}
D_m	$\text{m}^2\,\text{s}^{-1}$	9.00×10^{-10}	9.00×10^{-10}

Table 6.2 shows the initial composition at the inlet for the top and bottom half of the domain. As described earlier, the top half consists of Na_2CO_3 solution and the bottom half consists of a $CaCl_2$ solution. We assume a uniform and constant temperature and $T = 25\,°C$ and pressure $P = 1\,MPa$. The molecular diffusion coefficient is defined as $D_m = 2.2 \times 10^{-9}\,m^2\,s^{-1}$, irrespective of the species and species concentration. At the initial states, there are no particles sharing both $CaCl_2$ and Na_2CO_3 species, and like so no produced species resulting from this interaction: NaCl(aq), $CaCO_3$(aq) and $CaHCO_3{}^+$, are present at $t = 0\,s$. The solution has pH = 10.49 in the top half and pH = 6.43 in the bottom half.

Table 6.2: Composition of the injected fluids at $T = 25\,°C$ and $P = 1\,MPa$. The composition of the injected particles is divided between two halves: the top consisting of Na_2CO_3 solution and the bottom consisting of a $CaCl_2$ solution. At the initial states, there are no particles sharing both a $CaCl_2$ and Na_2CO_3 concentration, and like so no produced species resulting of its reaction: NaCl (aq), $CaCO_3$(aq) and $CaHCO_3{}^+$, are present at $t = 0\,s$. The solution has pH = 10.49 in the top half and pH = 6.43 in the bottom half.

Species	Top/mol m^{-3}	Bottom/mol m^{-3}
Na^+	3.33	0
$CO_3{}^{2-}$	1.40	0
$HCO_3{}^-$	2.69×10^{-1}	0
CO_2(aq)	1.16×10^{-5}	0
NaOH(aq)	5.24×10^{-3}	0
Ca^{2+}	0	1.64
Cl^-	0	3.31
$CaCl^+$	0	2.47×10^{-2}
$CaCl_2$(aq)	0	2.13×10^{-4}
$CaOH^+$	0	8.03×10^{-6}
HCl(aq)	0	1.64×10^{-7}
NaCl(aq)	0	0
$CaCO_3$(aq)	0	0
$CaHCO_3{}^+$	0	0
H^+	2.68×10^{-9}	3.09×10^{-5}
H_2O(l)	3.69×10^3	3.69×10^3
OH^-	2.64×10^{-1}	2.30×10^{-5}

6.2.2 Mixing Induced by Physical Heterogeneity

We simulate two advective regimes, characterised by Péclet numbers of Pe = 10 and 100. Table 6.3 shows the average molar concentrations of the injected species at the initial state, the expected results for the concentration of the

species for an ideal fully-mixed system, and for the advective systems with characteristic Péclet number of Pe = 10 and 100. The fully mixed system is equivalent to a perfect stirred-tank reactor, where all available species at t =0 s are perfectly mixed and the system is in steady state. The system shows how the advective dynamics contributes to the incomplete mixing of the species, reducing the expected conversion of $CaCl_2$ and Na_2CO_3 into NaCl(aq), $CaCO_3$(aq) and $Ca(HCO_3)^+$. The production of these species is nearly 10 times smaller when comparing the ideal fully-mixed case to the Pe = 10, and when comparing Pe = 10 to Pe = 100.

Table 6.3: Average molar concentrations of the injected species at the initial state, for the species at an ideal fully-mixed system, and for the advective systems with characteristic Péclet number of Pe = 10 and 100 at $t/t_1 = 1$. The system shows how the advective dynamics contributes to the incomplete mixing of the species, reducing the expected conversion of $CaCl_2$ and Na_2CO_3 into NaCl(aq), $CaCO_3$(aq) and $Ca(HCO_3)^+$.

Species/mol m^{-3}	$t = 0$ s	Fully mixed	Pe = 10	Pe = 100
Na^+	3.33	3.32	8.68×10^{-1}	1.01
$CO_3{}^{2-}$	1.40	3.11×10^{-1}	2.39×10^{-1}	4.10×10^{-1}
$HCO_3{}^-$	2.69×10^{-1}	1.91×10^{-1}	6.47×10^{-2}	8.11×10^{-2}
CO_2(aq)	1.16×10^{-5}	2.40×10^{-5}	7.26×10^{-6}	4.11×10^{-6}
NaOH(aq)	5.24×10^{-3}	1.99×10^{-3}	9.84×10^{-4}	1.55×10^{-3}
Ca^{2+}	1.64	4.86×10^{-1}	4.29×10^{-1}	4.76×10^{-1}
Cl^-	3.31	3.32	1.13	9.88×10^{-1}
$CaCl^+$	2.47×10^{-2}	4.52×10^{-3}	5.95×10^{-3}	7.11×10^{-3}
$CaCl_2$(aq)	2.13×10^{-4}	2.17×10^{-5}	4.72×10^{-5}	6.09×10^{-5}
$CaOH^+$	8.03×10^{-6}	1.16×10^{-2}	2.17×10^{-3}	2.13×10^{-4}
HCl(aq)	1.64×10^{-7}	4.15×10^{-11}	3.59×10^{-9}	4.18×10^{-8}
NaCl(aq)	0	1.24×10^{-2}	1.62×10^{-3}	1.77×10^{-4}
$CaCO_3$(aq)	0	1.16	1.31×10^{-1}	1.46×10^{-2}
$Ca(HCO_3)^+$	0	4.68×10^{-3}	9.33×10^{-4}	8.97×10^{-5}
H^+	3.09×10^{-5}	1.41×10^{-8}	6.80×10^{-7}	7.90×10^{-6}
OH^-	2.64×10^{-1}	1.82×10^{-1}	6.25×10^{-2}	7.95×10^{-2}

Figures 6.4 and 6.5 show the averaged species concentration at the nodes of the lattice of Het. 1 and 3 for Ca^{2+}, Na^+, NaCl and $CaOH^+$ in the $z-$direction for characteristic Péclet numbers of Pe = 10 and 100 at $t/t_1 = 1$. The selected species highlight the presence of Ca^+ due to the injection of a Na_2CO_3 solution at the top, and Na^+ due to the injection of a $CaCl_2$ solution at the bottom. The symmetry around the middle plane is marked by the production of NaCl (aq), only possible with the combination of both solutions injected at the top and bottom. The species $CaCO_3$(aq) and $Ca(HCO_3)^+$ are omitted as their

production and spatial distribution are similar to NaCl(aq). The production of $CaOH^+$ is controlled by the concentration of H^+, making it more available at the middle but also at the top where the H^+ concentration is lower. An increase of the Péclet number, reduces movement perpendicular to the flow direction by diffusion, reducing then the effective production of NaCl(aq).

Figure 6.6 shows the average concentration of NaCl normal to the flow direction for Pe = 10 and 100 at $t/t_1 = 1$. As the system becomes more advective, mixing becomes less efficient and the production of NaCl is reduced.

Figure 6.7 shows the change in the concentration of NaCl for Pe = 10 and 100 over normalized time and the departure from equilibrium concentration. At early times the increase in the change in concentration is nearly constant but then sharply reduces at late times. When analysing the change in concentration over the departure from equilibrium concentration, the increase in the change in concentration is weakly dependent on the concentration when far from equilibrium.

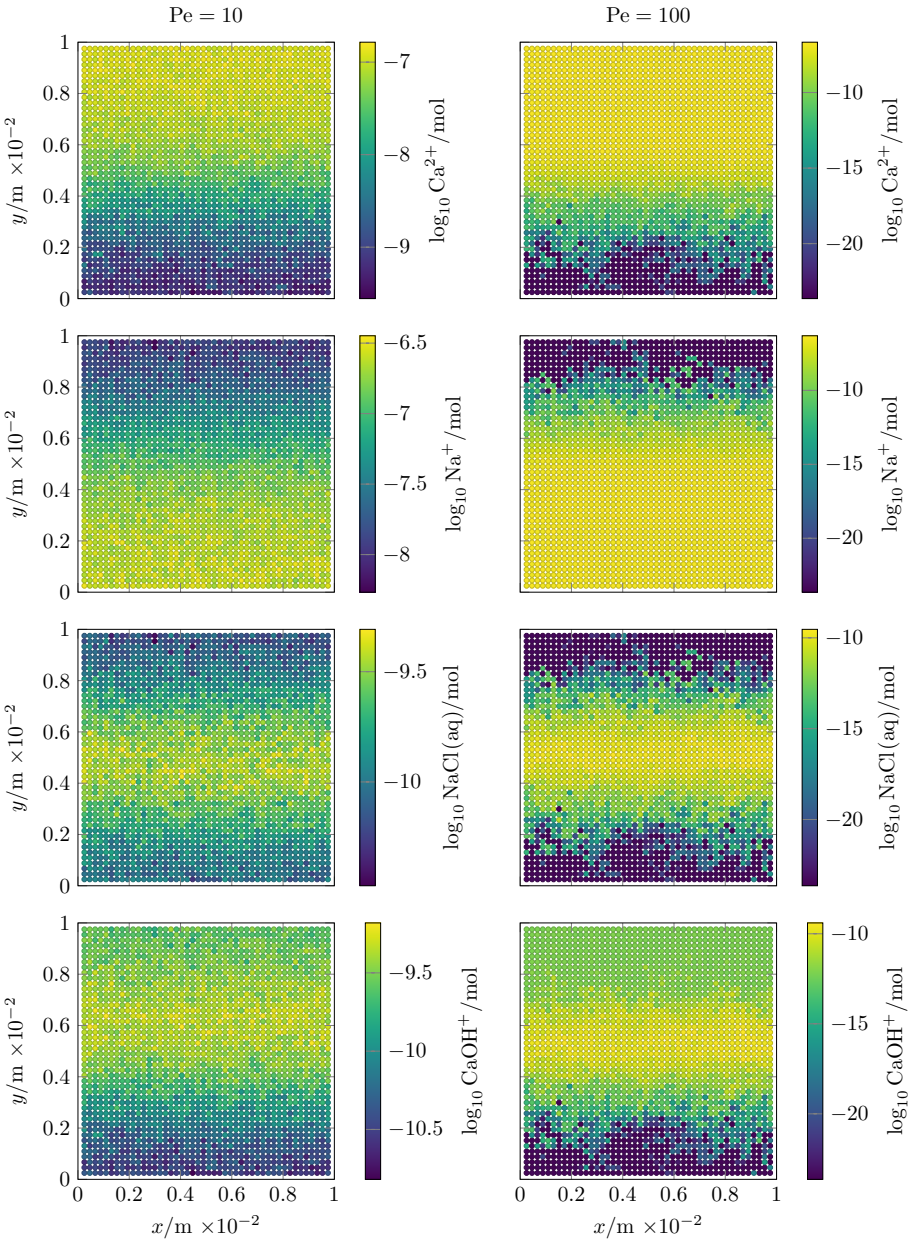


Figure 6.4: Averaged species concentration at the nodes of the lattice of Het. 1 for Ca^{2+}, Na^+, NaCl and $CaOH^+$ in $z-$direction for Pe = 10 and 100 at $t/t_1 = 1$. Flow is from left to right with the injection of Na_2CO_3 solution at the top and of $CaCl_2$ solution at the bottom.

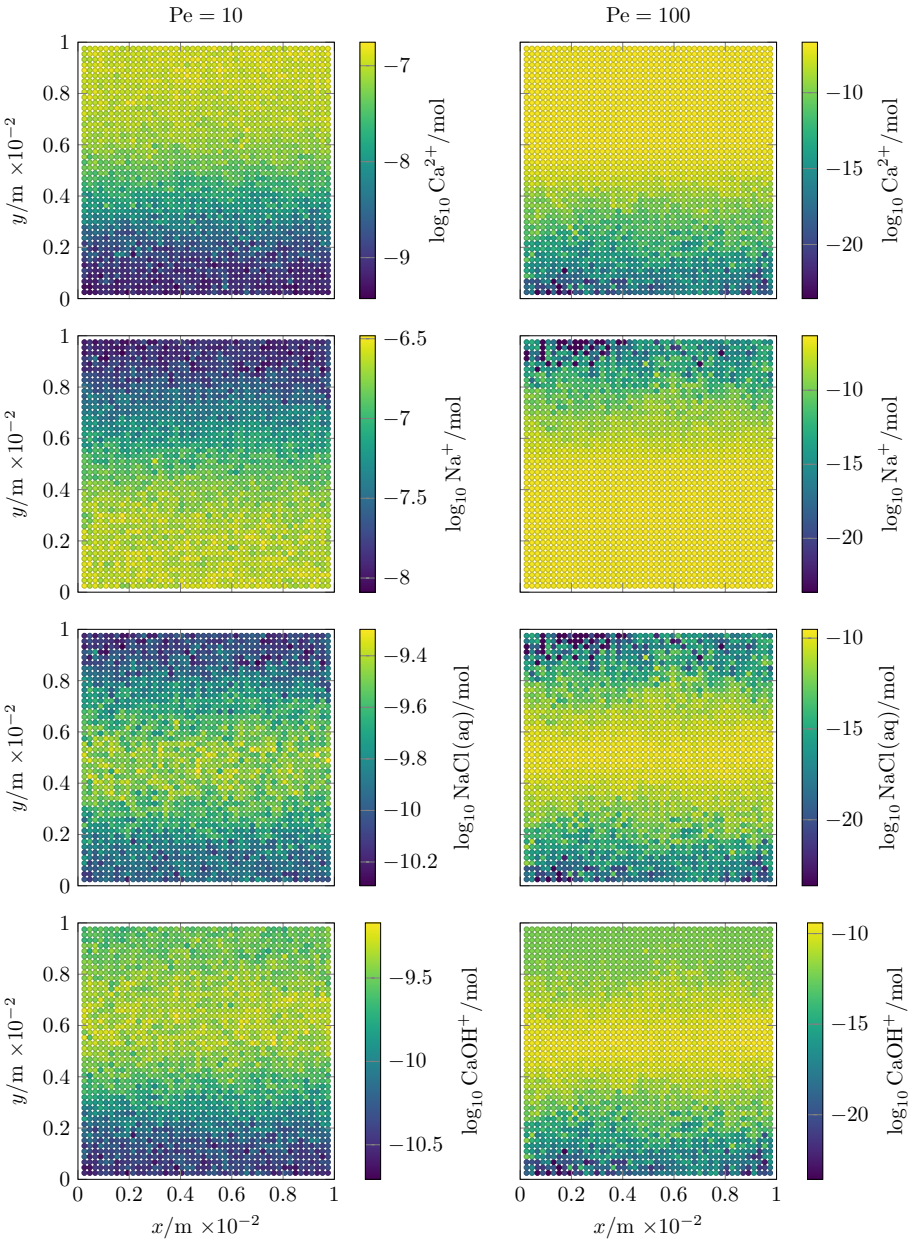


Figure 6.5: Averaged species concentration at the nodes of the lattice of Het. 3 for Ca^{2+}, Na^+, NaCl and $CaOH^+$ in $z-$direction for Pe = 10 and 100 at $t/t_1 = 1$. Flow is from left to right with the injection of Na_2CO_3 solution at the top and of $CaCl_2$ solution at the bottom.

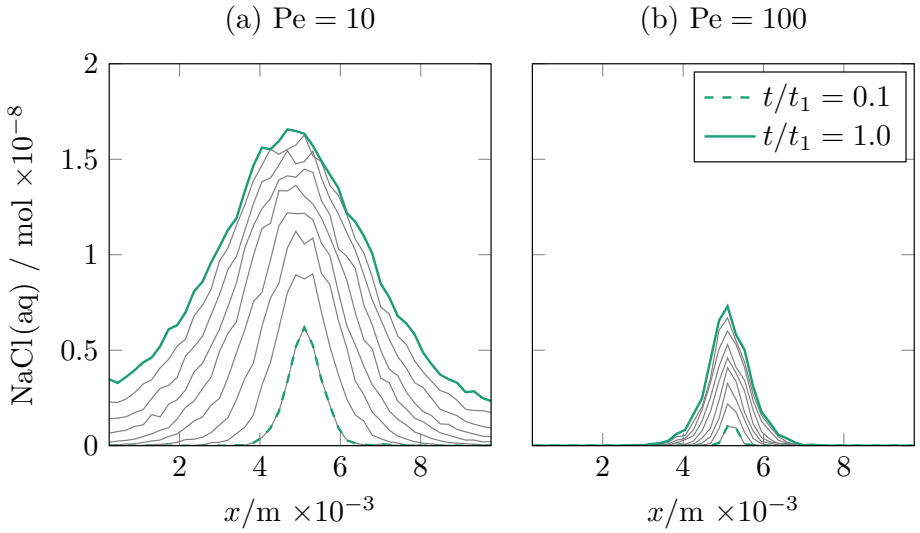


Figure 6.6: Average concentration of NaCl along the flow direction for Péclet number of (a) Pe = 10 and (b) 100 at $t/t_1 = 1$. As the system becomes more advective, mixing becomes less efficient and the production of NaCl is reduced.

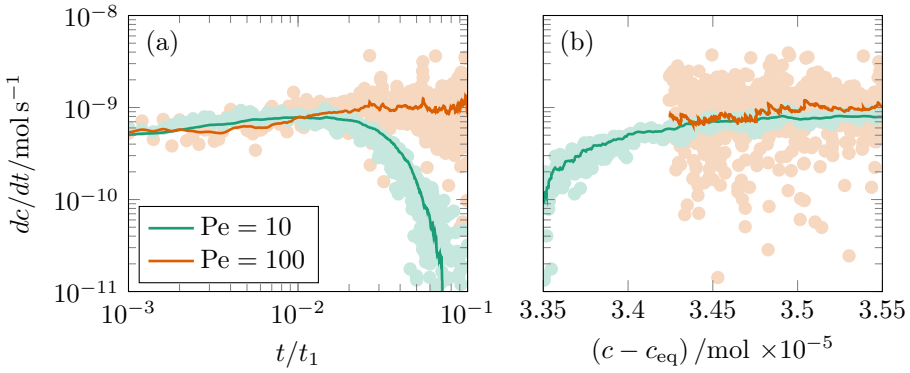


Figure 6.7: Change in the concentration of NaCl for Péclet number of Pe = 10 and 100 over (a) normalized time and the (b) departure from equilibrium concentration. At early times the increase in the change in concentration is constant but then sharply reduces. The increase in the change in concentration is weakly dependent on the concentration when far from equilibrium.

6.3 Fluid-Solid Reactive System

After showing the impact of physical heterogeneity on the mixing of different species in section 6.2, we extend the previous model and incorporate changes in porosity induced by dissolution of different minerals. The model consists of randomly distributed calcite and dolomite at different ratios upon the injection of hydrochloric acid, as described in section 6.3.1, with the sample properties listed in table 6.1 and for $Pe = 10$ only. Next we show the impact of mineral distribution in controlling the dissolution fronts in section 6.3.2.

6.3.1 Description of the Fluid-Solid CTRW Reactive Transport Model

Reaction of calcite $CaCO_3$ and dolomite $CaMg(CO_3)_2$ with a hydrochloric acid HCl involves a combination of homogeneous and heterogeneous reactions. The chemical equilibrium between hydrochloric acid and calcite leads to the production of calcium chloride $CaCl_2$ and is controlled by

$$CaCO_3 + 2\,HCl \rightleftharpoons CaCl_2 + CO_2 + H_2O, \tag{6.3}$$

and the chemical equilibrium between hydrochloric acid and dolomite leads to the production of magnesium chloride and calcium chloride, and is controlled by

$$CaMg(CO_3)_2 + HCl \rightleftharpoons MgCl_2 + CaCl_2 + CO_2 + H_2O. \tag{6.4}$$

Several intermediate chemical species are formed from the linear combination of the elements Ca, Mg, C, H and O present in the reactions in equations (6.3) and (6.4). Aqueous homogeneous reactions are generally faster than mineral reactions, so are assumed to reach equilibrium instantaneously. The mineral heterogeneous reactions are controlled by kinetics, and are much slower than the aqueous reactions. At temperature T =50 °C and pressure p =10 MPa the measured batch reaction rate for calcite is $8.1 \times 10^{-4}\,mol\,m^{-2}\,s$ and for dolomite is $5.1 \times 10^{-5}\,mol\,m^{-2}\,s$ (Peng et al., 2015; Peng et al., 2016). This makes the batch reaction rate of calcite nearly 15 times bigger than the reaction rate of dolomite.

Figure 6.8 illustrates the conceptual representation of the fluid-solid reactive system. Similarly to section 6.2, the reaction system composed of equations (6.3) and (6.4) is solved at the nodes, and the injected and produced chemical species are transported within the particles. The main difference is that the nodes of our lattice now contain two phases: a solid and a liquid phase. This difference is significant, since it takes into account the presence of a system with kinetics

and equilibrium controlled reactions. The solid species are available to react with the aqueous species, resulting in a reduction of the porosity of the node.

The total porosity change contribution of each mineral is obtained by the change in the number moles of the minerals, or

$$\Delta\phi_{\text{mineral}} = \Delta n_{\text{mineral}} \frac{M_{\text{mineral}}}{V \rho_{\text{mineral}}}, \tag{6.5}$$

and the total change in the porosity is equal to the sum of the porosity changes from the different minerals,

$$\phi_{\text{total}} = \sum_{i=0}^{N} \Delta\phi_i. \tag{6.6}$$

We have to account for the changes in porosity, and we need to update the pressure and velocity field accordingly. This is the main difference to the algorithm in section 6.2.1. The steps in the algorithm are listed below:

1. Create the lattice with an initial distribution of porosity ϕ, permeability K, calcite and dolomite fractions.
2. Solve the pressure field P in the lattice, calculate the local velocities v_{ij} and local Péclet numbers Pe_{ij} in the links.
3. Calculate the local probabilities of displacement p_{ij} (eq. 3.14) and the local transit-time distribution ψ_{ij} (eq. 3.12) in the links.
4. Sample a displacement direction $\Delta\mathbf{x}$ from p_{ij} and transit-time $\Delta\tau$ from ψ_{ij} for each particle.
5. Move the particle from the node i to the node j, if $\sum \Delta\tau^m \leq \Delta t$, where m labels each particle transition. This is performed individually for each particle.
6. Repeat steps 4 – 5 for all particles while $\sum \Delta\tau^m \leq \Delta t$. Each particle can undergo several transitions in one time step before the pressure field is updated.
7. Gather all the particles in the node i and collect the total amount of aqueous species and solid species in it.
8. Solve the kinetic path in node i for the total amount of species in the time interval $[t, t + \Delta t]$.
9. Distribute the resulting species from the new state of node i back to the particles in it.

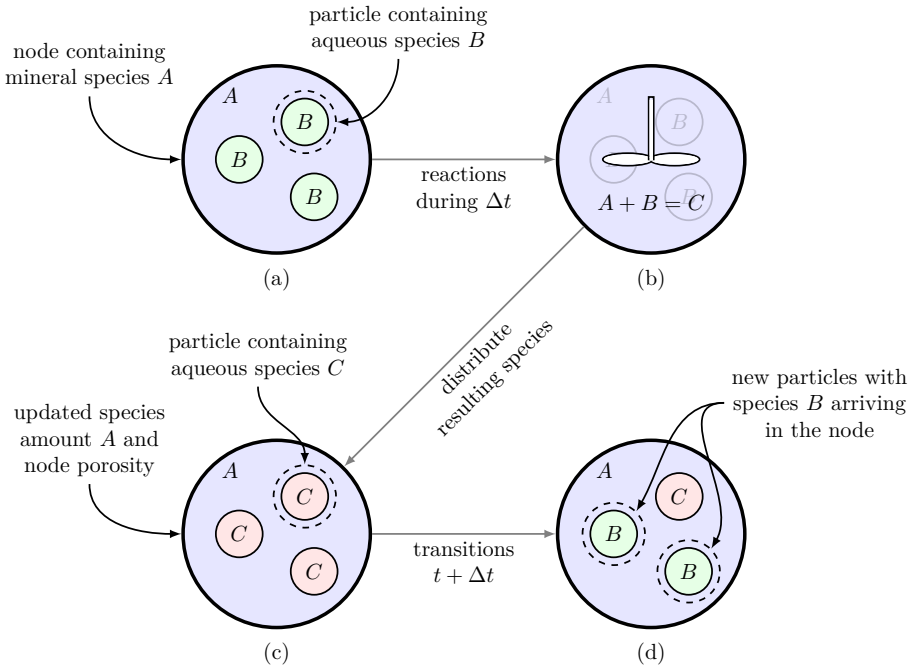


Figure 6.8: Conceptual representation of the fluid-solid reactive system. Particles might contain any distribution of species, but for simplicity this diagram shows particles containing only theoretical mineral species A and aqueous species B, that produces species C. (a) We start with a distribution of particles with theoretical aqueous species B and nodes with solid species A. (b) At checkpoint times Δt, each node behaves as a batch reactor, mixing and reacting all available species in it. (c) The total porosity in the node is then updated to reflect the dissolved species from the solid phase of the nodes to the aqueous species, and the resulting species in the aqueous phase are then distributed among the particles contained in the node. (d) The model proceeds with the particles transitions, when particles either leave with the produced species or arrive with other species.

10. Correct the porosity for the moles of the solid species lost in the solid and now in the aqueous phase.
11. Repeat steps 7 – 9 for all the nodes in the lattice.
12. Update the pressure field P if the mean porosity change is higher than a given threshold.
13. Repeat steps 2 – 12 until the end of the simulation.

At the end of each time step Δt, we calculate the domain mean porosity difference $\Delta\phi$ and if it is smaller than a given precision ϵ_ϕ we continue, otherwise the pressure field is re-calculated. We use $\epsilon_\phi = 1 \times 10^{-4}$, as in chapter 4.

6.3.2 Dissolution of Mineral Heterogeneous Systems

To evaluate the impact of a heterogeneous mineral distribution, we randomly distributed calcite and dolomite in the domain. There is no spatial correlation in this distribution, minerals are randomly distributed in the domain such that the ratio of calcite to dolomite is 3:1 and 1:3. For every node, we sample the calcite volumetric fraction from a uniform distribution function and multiply it by a volumetric fraction factor f, $c_{\text{calcite}} \sim f \times \mathcal{U}[0,1]$, and we define the dolomite volumetric fraction complementary to calcite fraction, as $c_{\text{dolomite}} = 1 - c_{\text{calcite}}$. for our cases, $f = 3/4$ or $1/4$, respectively for the 3:1 and 1:3 ratios of calcite to dolomite.

Figure 6.9 shows the average molar concentration averaged perpendicular to the flow in 3D lattice network which was the same as the most heterogeneous Het. 3 domain in chapter 5. The local fluctuation in the mineral moles reflects the local variation in porosity, that is not constant for the selected sample Het. 3.

We study a constant injection of HCl with pH = 4, where table 6.4 shows the molar concentration of the injected species. Despite some of the species initially being equal to zero, these species listed in table 6.4 are all transported in the particles, used in the solver, and might be locally available at particular nodes at particular times.

Figure 6.10 shows the dissolved surface front for the case studied. The dissolution front in the case with the higher concentration of calcite (3:1 calcite to dolomite ratio) reaches further into the domain, whereas for the case 1:3, the lower reactivity of dolomite acts as a shield to the reactive front. Moreover, in the case with the higher concentration of dolomite, the number of dissolved channels is smaller than in the case with the lower dolomite concentration.

Figure 6.11 shows the porosity, and calcite and dolomite mean volumetric fraction along the flow direction at the initial and final states. The fraction

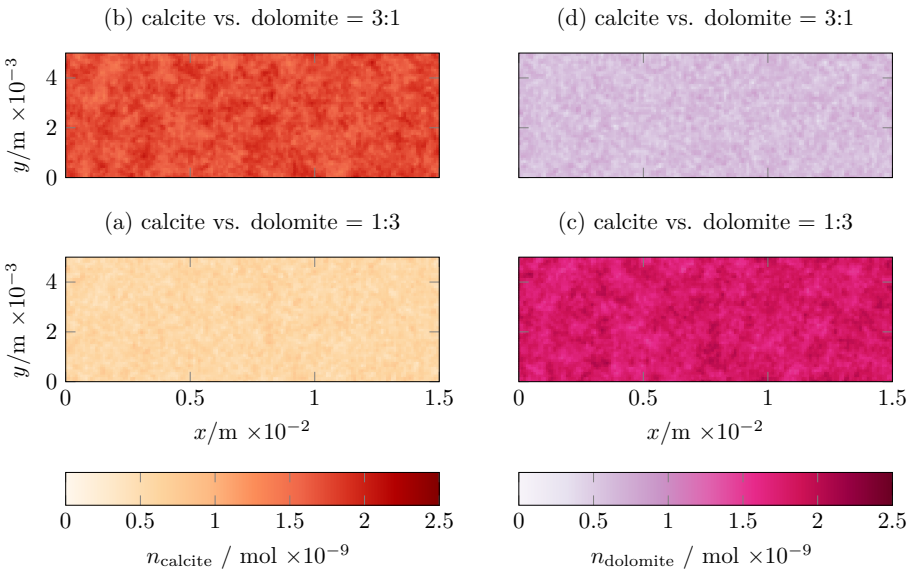


Figure 6.9: Molar concentrations of calcite and dolomite averaged perpendicular to the flow in 3D lattice network having physical heterogeneity Het. 3. The concentration of calcite and dolomite was randomly distributed over the domain following a 3:1 and 1:3 ratio.

Table 6.4: Composition of the injected fluid ($T = 25\,°\mathrm{C}$, $p = 1\,\mathrm{MPa}$) at the inlet $x = 0\,\mathrm{m}$.

Species	$\mathrm{mol\,m^{-3}}$	Species	$\mathrm{mol\,m^{-3}}$
$CO(aq)$	0.00	HCO_3^-	0.00
$CO_2(aq)$	0.00	$HCl(aq)$	2.80×10^{-1}
CO_3^{--}	0.00	$HClO(aq)$	0.00
$Ca(HCO_3)^+$	0.00	$HClO_2(aq)$	0.00
Ca^{++}	0.00	HO_2^-	0.00
$CaCO_3(aq)$	0.00	$Mg(HCO_3)^+$	0.00
$CaCl^+$	0.00	Mg^{++}	0.00
$CaCl_2(aq)$	0.00	$MgCO_3(aq)$	0.00
$CaOH^+$	0.00	$MgCl^+$	0.00
Cl^-	4.97×10^1	$MgOH^+$	0.00
ClO^-	0.00	Na^+	0.00
ClO_2^-	0.00	$NaCl(aq)$	0.00
ClO_3^-	0.00	$NaOH(aq)$	0.00
ClO_4^-	0.00	$O_2(aq)$	0.00
H^+	4.97×10^1	OH^-	3.03×10^{-9}
$H_2(aq)$	0.00	$H_2O(g)$	0.00
$H_2O(l)$	5.53×10^4	$CO_2(g)$	0.00
$H_2O_2(aq)$	0.00		

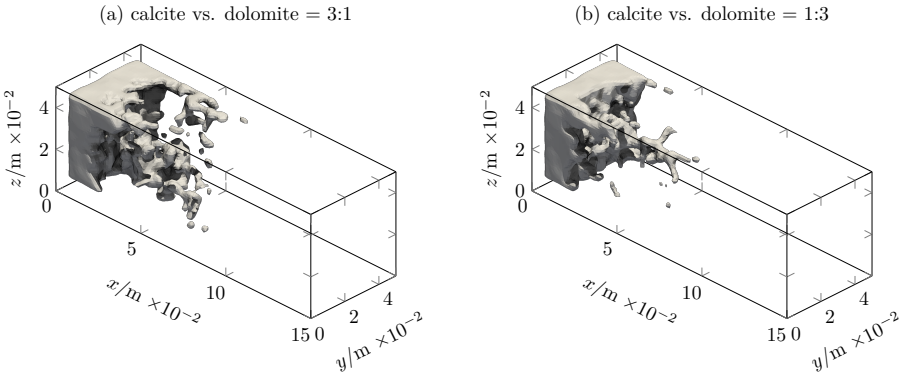


Figure 6.10: Dissolution induced fluid-solid surfaces for both cases with the ratio of the distribution of calcite to dolomite of (a) 3:1 and (b) 1:3. The dissolution front in the case with the higher concentration of calcite reaches further, since for the case (b), dolomite acts as a shield to the reactive front.

of calcite and dolomite is nearly constant along the sample, averaging at 0.60 and 0.20 respectively for the calcite vs. dolomite ratio of 3:1, and 0.20 and 0.60 respectively for the calcite vs. dolomite ratio of 1:3. For both cases, the biggest increase in porosity occurs at the inlet, and hence this is mirrored in the proportional decrease in calcite and dolomite volumetric fractions. The increase in porosity is not limited to the inlet only, but propagates inside the sample, more effectively for higher concentrations of calcite.

We assume that all different species in the solid phase are uniformly distributed in any given node and are available for reaction. The effective reaction rate is then calculated for each individual node and mineral as

$$r_{\text{eff}} = \frac{\rho_{\text{mineral}}}{M_{\text{mineral}} S} \frac{\Delta\phi_{\text{mineral}}}{\Delta t}, \tag{6.7}$$

where ρ is the mineral density, M is the molar mass of the mineral, and $S = V_t \sigma_A$ is the surface area estimated from the total volume of the simulation domain V_t and the defined specific surface area σ_A.

From equations (6.5) and (6.7), we obtain that the individual effective reaction rate for calcite and dolomite can be defined as

$$r_{\text{eff, calcite}} = \frac{\rho_{\text{calcite}}}{M_{\text{calcite}} S} \frac{\Delta\phi_{\text{calcite}}}{\Delta t}, \tag{6.8a}$$

$$r_{\text{eff, dolomite}} = \frac{\rho_{\text{dolomite}}}{M_{\text{dolomite}} S} \frac{\Delta\phi_{\text{dolomite}}}{\Delta t}. \tag{6.8b}$$

Figure 6.12 shows the dynamic change in the effective reaction rates for calcite and dolomite using equations (6.8a) and (6.8b), separately calculated according to their proximity to the fast flowing channels and the slow regions.

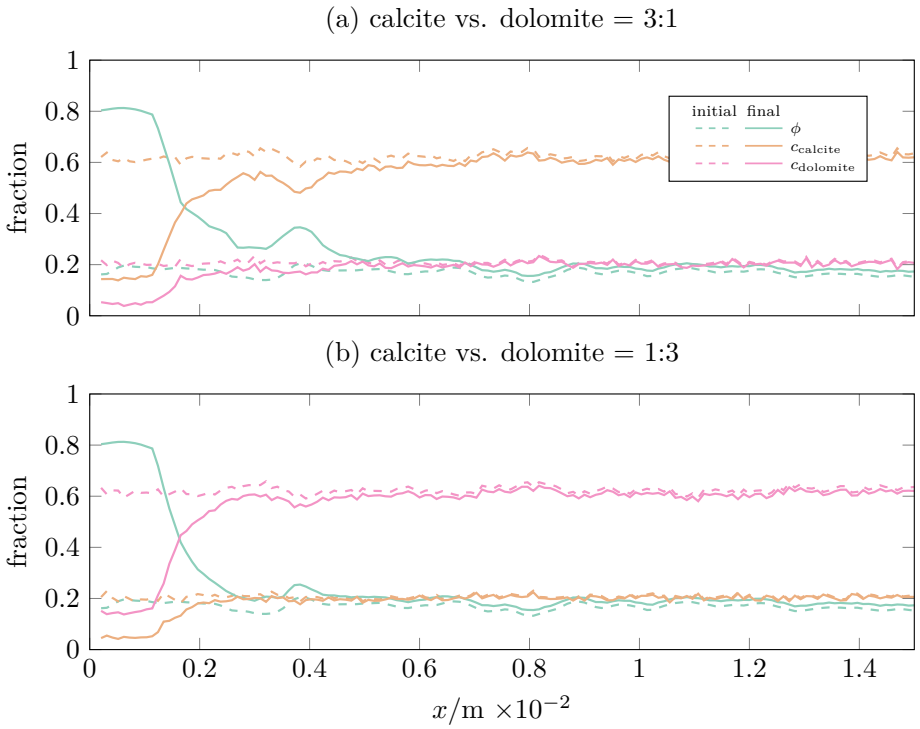


Figure 6.11: Porosity, calcite and dolomite mean volumetric fraction along the flow direction at the initial state (dashed line) and the final state (continuous line), for both cases with the ratio of the distribution of calcite to dolomite of (a) 3:1 and (b) 1:3. For both cases the majority of the sample inlet is dissolved, but more effectively in the case with the higher calcite content.

The method for separation of fast channels and slow regions is reported in appendix D. The effective reaction rates for calcite are consistently higher than for dolomite, with the exception of the case with the higher content of dolomite in the fast flowing channels. The effective reaction rates of calcite and dolomite decrease with the dissolved channel formation since the reactant is now focused in the fast regions thus decreasing calcite and dolomite exposure to reaction. In the case with a calcite to dolomite ratio of 1:3, when the dominant dissolution channel is formed the higher dolomite content in this fast flow region shields the calcite so its effective reaction rate decreases even to the extent that becomes slower than the effective rate of dolomite. This has been observed in the pore-scale brine equilibrated CO_2 dissolution of mixed mineralogy calcite/dolomite sample with the ratio of 1:7 (Al-Khulaifi et al., 2019). Our findings are the first confirmation of this phenomena at the continuum scale. These observations imply that the effective reaction rate of calcite may be overestimated if the impact of heterogeneity in the flow field and especially channel formation is not taken into account. In general, figure 6.12 shows that the decrease in the effective reaction rate for dolomite is slower than that of calcite. Furthermore, all the effective reaction rates of calcite and dolomite are lower by 1 to 2 orders of magnitude than the respective batch reaction rates for calcite and dolomite. This is due to mass transfer limitations which result in slower reactions in the porous media as compared to the ideal mixing conditions in the batch reactors as discussed in chapters 4 and 5. Power-law scaling characterizing the evolution of calcite and dolomite effective reaction rates including these in fast channels and slow regions are shown in table 6.5.

Table 6.5: Power-law scaling a (t^{-a}) for the effective reaction rate related to the total mineral volume of the sample, the fast flowing channels and slow regions, for both cases with the ratio of the distribution of calcite to dolomite of 3:1 and 1:3

	calcite vs. dolomite 3:1		calcite vs. dolomite 1:3	
	calcite	dolomite	calcite	dolomite
full sample	0.91	0.88	0.97	0.89
fast channels	0.71	0.76	0.98	0.94
slow regions	0.94	0.91	0.97	0.89

Another measure of the impact of coupled flow and mineral spatial distribution heterogeneities is the proximity of a mineral to fast flow channels and slow regions (Al-Khulaifi et al., 2019). We calculate the proximity function of links to fast flow channels by separating the links in either fast or slow and calcite or dolomite. The complete description is presented in appendix chapter D.

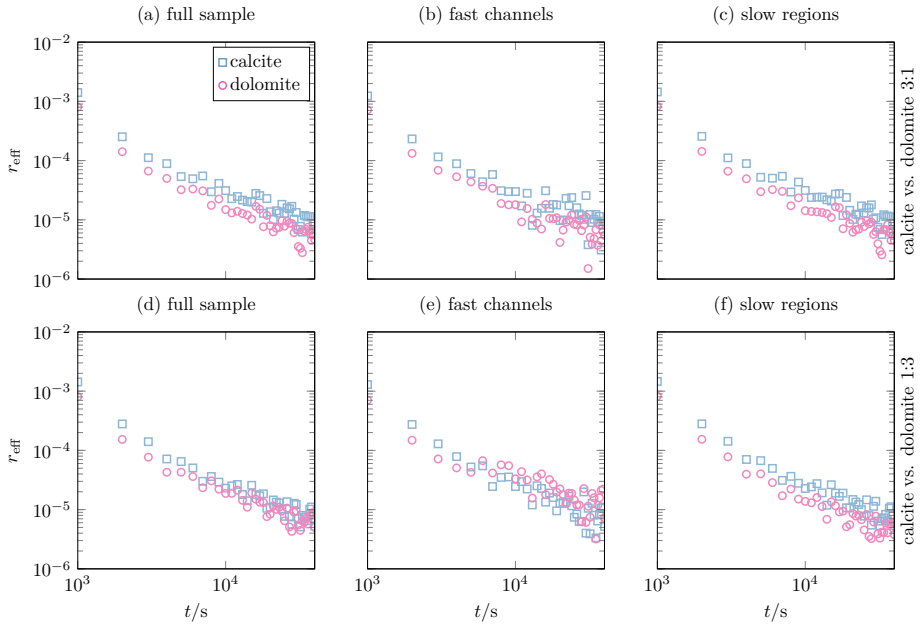


Figure 6.12: Effective reaction rates related to the total mineral volume of the sample, the fast flowing channels and slow regions, for both cases with the ratio of the distribution of calcite to dolomite of (a) to (c) 3:1 and (d) to (f) 1:3. At late times, in the case of calcite to dolomite ratio 1:3 the reaction rate of dolomite in fast flowing channels is higher than that of calcite due to dolomite shielding calcite from the reactant supply.

The mineral distance proximity to fast flowing channels and slow regions are displayed in figure 6.13. The calcite and dolomite distances from the fast flow channels and slow regions become bigger for all studied cases. This is manifested as the slowing down of the effective reaction rates of calcite and dolomite, as previously shown in figure 6.12. It is also noted that the shape of the proximity histograms are similar for calcite and dolomite – this is because of their random distributions throughout the porous domains.

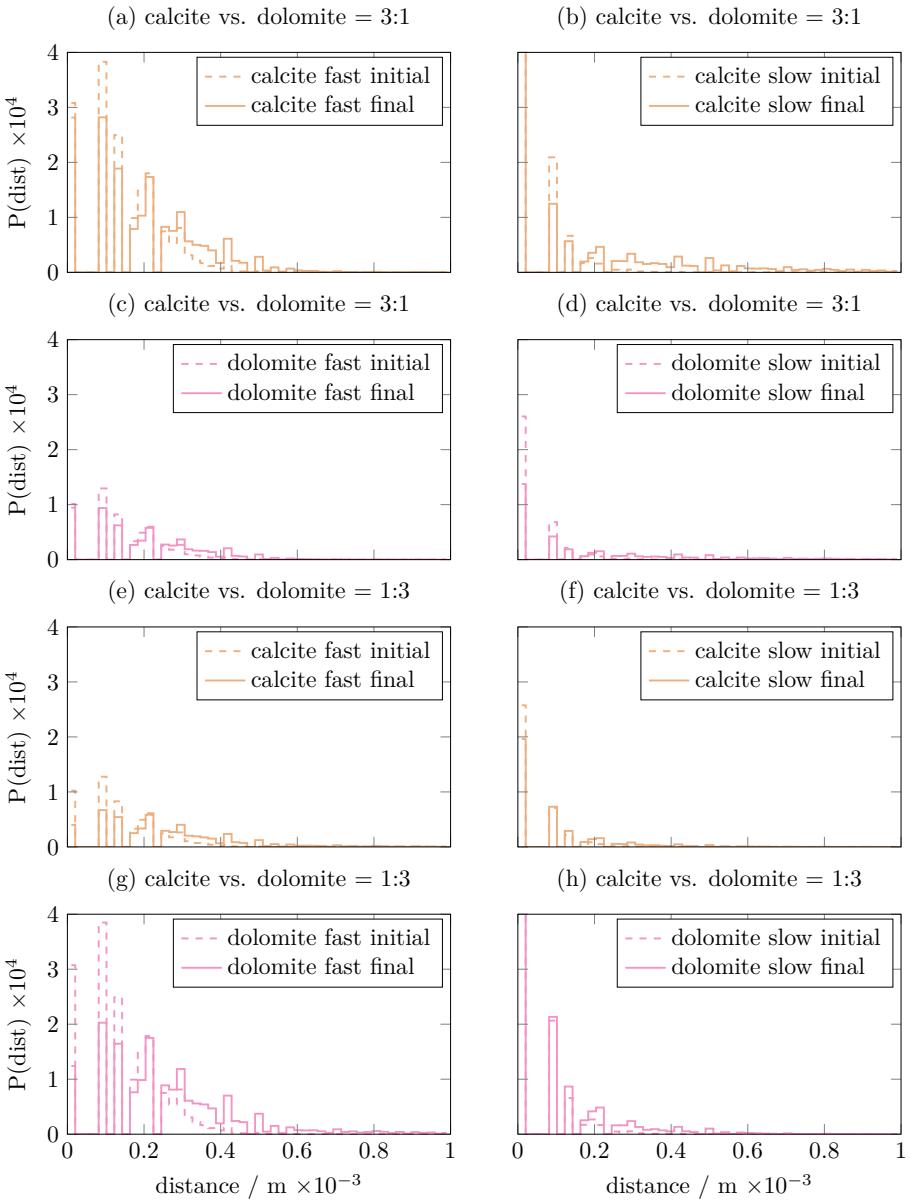


Figure 6.13: Histograms showing the initial and the final proximity to the fast flowing channels and to slow regions, for both cases with the ratio of the distribution of calcite to dolomite of (a) to (d) 3:1 and (e) to (h) 1:3.

6.4 Discussion

We previously showed in chapter 5 how flow and transport (physical) heterogeneity impacts the effective reaction rates. Analysing the batch reaction rates for calcite and dolomite, the batch reaction rate for calcite is approximately 15 times higher than the batch reaction rate of dolomite. Furthermore, all the effective reaction rates of calcite and dolomite are 1 to 2 order of magnitudes lower than the respectively batch reaction rates. This is due to mass transfer limitations in porous media compared to ideal mixing in batch reactors. The effective reaction rates for calcite and dolomite decreased with time due to the formation of a dominant dissolution channel which resulted in flow focusing of the injected reactant and its lower availability throughout the sample volume. In some cases, where dolomite is more abundant in the sample than calcite, this can lead to an effective reaction rate of calcite in the fast flow regions becoming smaller to that of dolomite. Al-Khulaifi et al. (2019) obtained a similar behaviour by experimentally studying a limestone dissolution at the pore scale albeit with difference in the ratio of calcite to dolomite (1:7). In their studies, the appearance of a main dissolution channel hindered the dissolution of calcite when compared to dolomite which acted as a shield to the calcite reaction.

6.5 Conclusions

In this chapter we showed how to use our newly developed multi-species reactive transport solver to study the impact of physical and chemical heterogeneity both in a fluid-fluid reactive system, and a fluid-solid reactive system. We achieved this by extending the reactive transport solver, presented previously in section 4.5.2 of the chapter 4 and section 5.1 of the chapter 5, to include a geochemical solver developed in (Leal, 2014; Leal et al., 2014; Leal et al., 2015).

We started by presenting the multi-species fluid-fluid reactive system formed by sodium carbonate and calcium chloride that leads to the production of sodium chloride and calcium carbonate. This model did not consider changes in porosity by dissolution or precipitation. Examining two porous media with different flow heterogeneity (Het. 1 and Het. 3 as defined in chapter 5) at Pe = 10 and 100, we showed that an increase in physical heterogeneity increases the mixing of species and therefore chemical reaction. The width of the product creation zone was narrower for the higher Pe as there was less mixing by diffusion.

Next, we studied dissolution in a multi-species fluid-solid reactive system arising from the injection of hydrochloric acid in samples with different mineralogical content of randomly distributed calcite and dolomite. We showed

how the emerging dissolution front changes with the different ratio of calcite to dolomite in the sample. The higher the content in calcite, the further the dissolution channels travels along the flow direction. Dolomite, as a slower reacting mineral, shields the propagation of the dissolution front.

Finally, we showed the effective reaction rates for different minerals in relation to flow heterogeneity, namely fast channels and slow regions. We found that flow focusing due to developed dissolution channels leads to a decrease in the effective reaction rates of calcite and dolomite with time. If the lower reacting mineral (dolomite) is more abundant than the higher reacting mineral (calcite) we observed the effect of shielding, or preventing the contact of higher reactive mineral with fluid reactant. This can lead to the effective reaction rates being lower than anticipated based purely on the mineralogical content of the sample. Hence, it is highly important to consider the evolution of both physical (fast channels and slow regions) and chemical (proximity of minerals to fast and slow regions) heterogeneity to be able to systematically characterize the dynamics of reactive transport in porous media.

CHAPTER 7

Conclusions and Future Work

7.1 Conclusions

In this thesis we have developed a novel method for modelling reactive transport in porous media using Continuous Time Random Walk (CTRW). This work comes as a natural extension of the work on modelling transport in porous media by CTRW presented by Rhodes et al. (2008) and Muljadi et al. (2018). We considered transport and reaction for samples of size 0.15 m over time-scales of 10^5 - 10^6 s.

In chapter 3 we described the CTRW model responsible for the transport component of our solver that is later used in chapters 4 to 6 for modelling and validation of dissolution in porous media. We showed how we use the flow and diffusion properties in the nodes and links of a lattice to construct transit-time distributions and probabilities of spatial transitions to calculate particle transport. The asymptotic macroscopic transport parameters obtained reproduced both sub- and super-diffusive regimes.

We then proceed to incorporate a single-species reaction system in our model in chapter 4. Each particle carries a given number of moles of chemical species and as it transits through the lattice. The particles also act to dissolve the solid and increase the porosity. We used Nuclear Magnetic Resonance (NMR) experimental data from a Ketton limestone dissolution experiment, including molecular propagators continuously obtained throughout the experiment, and 3D NMR porosity maps at the start and end of the experiment. The NMR data was obtained at the Magnetic Resonance Research Centre (MRRC) at the

University of Cambridge through a collaborative project and used to validate the CTRW reactive model, from an initial state calibrated from the experiments. The effective reaction rates from the experiment on a limestone dissolution were in a good agreement with our reactive transport model. They were up to three orders of magnitude lower than the batch reaction rate of calcite which further demonstrated the crucial role of mass transfer limitations controlling reaction rates in porous media.

Having validated the reactive transport model, we systematically demonstrate the impact of initial physical heterogeneity and transport conditions on reaction rates in chapter 5. We showed that it is possible to model unresolved physical heterogeneity with a truncated power-law function for the transit-time distribution containing a transport heterogeneity parameter β. For the three physical heterogeneities resembling a beadpack, a homogeneous carbonate and a highly heterogeneous carbonate we observed persistence of non-Fickian transport describing incomplete mixing even at late times with an anomalous t^{-a} time dependence of reaction rate with $a > 0.5$. At lower Pe the rates were controlled by the impact of mixing by diffusion. The impact of heterogeneity was also observed at early-times for high Péclet numbers due to enhanced advective mixing for the most heterogeneous media. As observed experimentally, in a highly heterogeneous medium we do not observe uniform dissolution; rather preferential channels form that lead to very restricted mixing.

Finally we extended the CTRW reactive solver to model multi-species fluid-fluid and fluid-solid reactive systems. Here the particles could contain an arbitrary composition, allowing many chemical species to be tracked. A flexible geochemical solver was applied at each node in the lattice at each time step to update the concentration of both fluid and solid species. We assumed that fluid-fluid reactions were instantaneous, but considered rate-limited dissolution. This enabled the study of heterogeneous samples with a spatial distribution of different minerals. We first showed how physical heterogeneity increases the mixing in a fluid-fluid reactive system. For fluid-solid multi-species reaction we studied the impact of coupled physical and chemical heterogeneity on HCl induced dissolution of a rock that is a mix of calcite and dolomite. Then we demonstrated how different mineral content and spatial distribution of minerals impact the dissolution front and effective reaction rates. We observed a monotonous decrease in the effective reaction rates of calcite and dolomite as a consequence of the development of a dominant dissolution channel. We then showed how the flow focusing in the dominant channel results in the decreased availability of injected reactant for reaction with minerals that become situated at a distance further from the fast flow regions. This decreased availability of minerals for the reaction is very important since it can lead to lower than an-

ticipated effective reaction rates that are estimated only from the mineralogical content. Therefore mineralogical content, spatial distribution of minerals and proximity of minerals to the fast flow regions should all be taken into account when predicting the effective reaction rates.

7.2 Suggestions for Future work

Some interesting points, observations and assumptions were made during the development of the models in this thesis, but unfortunately were not possible to be addressed fully herein. In this chapter we propose subsequent topics and steps to be considered in the future, focussing on how to improve the reactive transport model and a multi-scale model proposal.

7.2.1 Reactive Transport Modelling

Our basic assumption about the reactive transport is that we can successfully separate it from the transport component. Transport is then modelled using a practical relation that includes under-resolved heterogeneity below the scale of our model and reactions are included using kinetic rate laws. It is only natural to extend the chemical reaction model to include under-resolved heterogeneities as well. To improve the predictability of our model, it is interesting to explore other approaches to include upscaled reactive equations. Bolster et al. (2017) proposes a modification for the reaction term to include a memory function instead of the naive inclusion of the first-order reactive term. This is applied using a different approach, the time-fractional dispersion equation (Schumer et al., 2003). Aquino and Dentz (2017) suggested the use of CTRW to model the general waiting-times between reactions.

When including the multi-species chemical solver, it became the bottleneck of the simulation, in that it was the most time consuming step in the algorithm. The framework originally developed by Gillespie (1976) was later approximated to allow for larger steps with a given accuracy in Gillespie (2001), and is a perhaps a good starting point to study simplifications to the chemical solver.

The use of a particle that transports different species is an approximation that needs to be further explored. Additional attention should be given when averaging the molecular diffusion coefficient using the concentration of a species in a particle versus the drawback of having additional particles per species, and each using the correct molecular diffusion coefficient. The molecular diffusion coefficient was considered constant, but it depends on the temperature of the system, as well as the chemical species, which should be taken in account when modelling reactive systems.

Finally we limited our model to study dissolution of porous media. With the current framework, it is straight forward to include precipitation, and even adsorption, and this will be the subject of future studies.

7.2.2 Multi-scale Modelling

Obtaining a complete description from pore-scale to field-scale is a challenging task. However experimental and modelling studies at pore- and core-scales are widely available.

Rhodes et al. (2008) proposed a workflow using CTRW from pore-to-field scales that can be used as a starting point. Bijeljic et al. (2011), Bijeljic et al. (2013a), and Bijeljic et al. (2013b) showed emergent non-Fickian transport signatures at the pore-scale that can be used to describe flow and transport at larger scales. Each link conceptually consists of several different pore-scale domains like the ones shown in previous work could be included forming a different ψ distribution in the links. This concept is illustrated in figure 7.1.

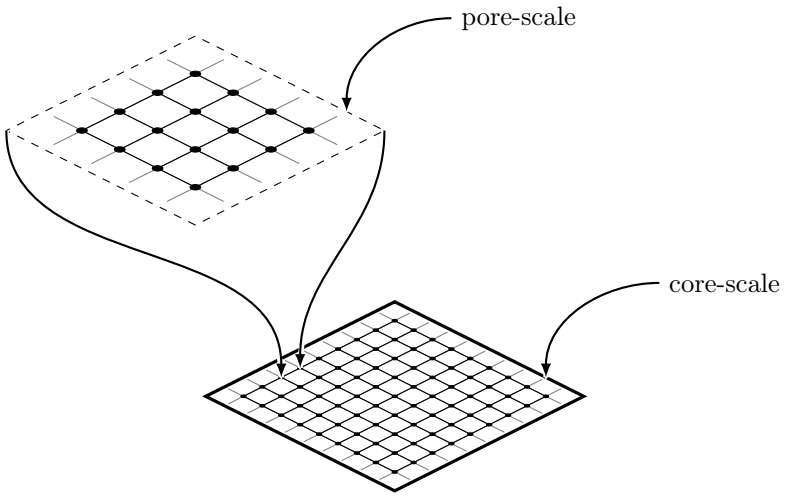


Figure 7.1: Idealized graph upscale from pore-scale to core-scale. The motivation behind this approach is to model a core-scale domain as if it is composed of several different pore-scale models, each being enough to describe the length-scale of a link in the core-scale. The naming of pore and core-scale is simply to relate to the problems described herein; the same idea can be implemented from any fine to coarser models.

Observing the breakthrough curves of a tracer at incrementally larger regions can potentially be used to characterize the sample with distinct tensors using different transit-time models. To illustrate this concept, figure 7.2 shows 2 steps of upscaling from a given original scale. At each face Γ of the subdomain Ω we can observe the breakthrough of particles and describe it accordingly. The

truncated power-law model is not necessarily needed. Other models such as the Multirate Mass Transfer (MRMT) can be employed to describe advection and diffusion in mobile-immobile regions as shown by Dentz and Berkowitz (2003) and Comolli et al. (2016) and more recently by Kurotori et al. (2019) and Kurotori et al. (2020).

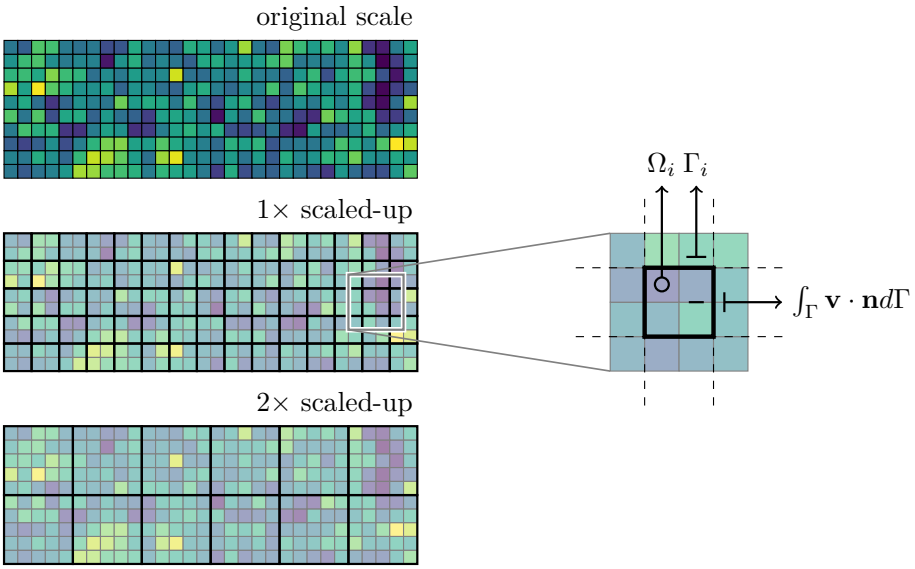
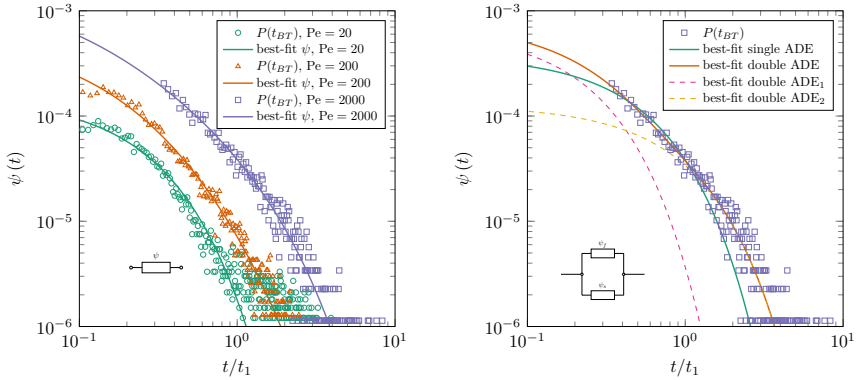


Figure 7.2: Upscaling concept from a given original scale to two upscaling steps up. At each face Γ of the subdomain Ω we can observe the breakthrough of particles and characterize it accordingly.

The use of a single β for the whole domain is an assumption of the model to account for under-resolved heterogeneities at a node and link scale. The observations of a different emergent β at a larger scale shows how dissolution impacts the domain heterogeneity. The use of a distribution of spatially varying β is of interest to account for the sample variability and the temporal variation of β for the local changes in the properties of the links. Values of $\beta > 2$ resembles Fickian transport with very few space and time transitions, so naturally an adoption of an Advective-Dispersion Equation (ADE) model is justified. Moreover, regions where permeability is extremely high or already resolved at the scale of the link could be considered another description as Brinkman or Stokes flow models.

Enriching the parameter space can be done based on the work of Bauer et al. (2012) with a dual pore network and Bultreys et al. (2015) connecting regions via under-resolved micro-porosity. This process is illustrated in figure 7.3a, by fitting a single truncated power-law function for the ψ transit-time distribution to the sample heterogeneity 3 (described in chapter 5) by simultaneously fitting

two different ADE for the ψ transit-time distribution of the same sample.



(a) Distribution of particle time to breakthrough the model and the best-fit CTRW model.

(b) Concept to generate a composite ψ function by combining two different ψ ADE functions.

Figure 7.3: Different ψ fits using a truncated power-law function for ψ and a composite ADE combining two different distributions. There is a high degree of error at larger times and the model fails to perform as well as expected, when using a single ψ function. Using of a composite ψ intends for better adjustment of the transit-time distribution, specially for the particles arriving at late times.

Overall there is an opportunity to use the concepts developed in this thesis to construct a pore-to-field reactive transport framework to account for behaviour over a wide range of temporal and spatial scales, while accounting for multi-species transport. The models could aid in the design and interpretation of many reactive transport problems.

Bibliography

Abhyankar, S., Brown, J., Constantinescu, E. M., Ghosh, D., Smith, B. F., and Zhang, H. (2018). "PETSc/TS: A Modern Scalable ODE/DAE Solver Library". In: *Numerical Analysis*. arXiv: 1806.01437. URL: https://arxiv.org/abs/1806.01437.

Abramovitz, M. and Stegun, I. A. (1974). *Handbook of Mathematical Functions with Formulas, Graphs and Mathematical Tables*. Ed. by M. Abramovitz and I. A. Stegun. Dover Publications, Inc., p. 1046. ISBN: 978-0-486-61272-0. URL: https://dl.acm.org/doi/book/10.5555/1098650.

Adams, E. E. and Gelhar, L. W. (1992). "Field study of dispersion in a heterogeneous aquifer: 2. Spatial moments analysis". In: *Water Resources Research* 28.12, pp. 3293–3307. ISSN: 19447973. DOI: 10.1029/92WR01757. URL: http://doi.wiley.com/10.1029/92WR01757.

Agertz, O., Moore, B., Stadel, J., Potter, D., Miniati, F., Read, J., Mayer, L., Gawryszczak, A., Kravtsov, A., Nordlund, Å., Pearce, F., Quilis, V., Rudd, D., Springel, V., Stone, J., Tasker, E., Teyssier, R., Wadsley, J., and Walder, R. (2007). "Fundamental differences between SPH and grid methods". In: *Monthly Notices of the Royal Astronomical Society* 380.3, pp. 963–978. ISSN: 00358711. DOI: 10.1111/j.1365-2966.2007.12183.x. URL: http://mnras.oxfordjournals.org/cgi/doi/10.1111/j.1365-2966.2007.12183.x.

Ahmed, U., Crary, S. F., and Coates, G. R. (1991). "Permeability estimation: The various sources and their interrelationships". In: *JPT, Journal of Petroleum Technology* 43.5, pp. 578–587. ISSN: 01492136. DOI: 10.2118/19604-PA.

Ahr, W. M. (2008). *Geology of Carbonate Reservoirs*. Hoboken, NJ, USA: John Wiley & Sons, Inc. ISBN: 9780470370650. DOI: 10.1002/9780470370650. URL: http://doi.wiley.com/10.1002/9780470370650.

Akanji, L. T. and Matthai, S. K. (2010). "Finite Element-Based Characterization of Pore-Scale Geometry and Its Impact on Fluid Flow". In: *Transport in Porous Media* 81.2, pp. 241–259. ISSN: 0169-3913. DOI: 10.1007/s11242-009-9400-7. URL: http://link.springer.com/10.1007/s11242-009-9400-7.

Alhashmi, Z., Blunt, M. J., and Bijeljic, B. (2016). "The Impact of Pore Structure Heterogeneity, Transport, and Reaction Conditions on FluidFluid Reaction Rate

Studied on Images of Pore Space". In: *Transport in Porous Media* 115.2, pp. 215–237. ISSN: 15731634. DOI: 10.1007/s11242-016-0758-z. URL: https://link.springer.com/article/10.1007/s11242-016-0758-z.

Andrew, M., Bijeljic, B., and Blunt, M. J. (2014). "Pore-scale contact angle measurements at reservoir conditions using X-ray microtomography". In: *Advances in Water Resources* 68, pp. 24–31. ISSN: 03091708. DOI: 10.1016/j.advwatres.2014.02.014.

Aquino, T. and Dentz, M. (2017). "Chemical Continuous Time Random Walks". In: *Physical Review Letters* 119.23, p. 230601. ISSN: 0031-9007. DOI: 10.1103/PhysRevLett.119.230601. arXiv: 1711.08373. URL: http://dx.doi.org/10.1103/PhysRevLett.119.230601.

Aris, R. (1956). "On the dispersion of a solute in a fluid flowing through a tube". In: *Proceedings of the Royal Society of London. Series A. Mathematical and Physical Sciences* 235.1200, pp. 67–77. ISSN: 0080-4630. DOI: 10.1098/rspa.1956.0065. URL: https://royalsocietypublishing.org/doi/10.1098/rspa.1956.0065.

Bachu, S. (2003). "Screening and ranking of sedimentary basins for sequestration of CO2 in geological media in response to climate change". In: *Environmental Geology* 44.3, pp. 277–289. ISSN: 09430105. DOI: 10.1007/s00254-003-0762-9. URL: http://link.springer.com/10.1007/s00254-003-0762-9.

Bandara, U. C., Tartakovsky, A. M., Oostrom, M., Palmer, B. J., Grate, J., and Zhang, C. (2013). "Smoothed particle hydrodynamics pore-scale simulations of unstable immiscible flow in porous media". In: *Advances in Water Resources* 62, pp. 356–369. ISSN: 03091708. DOI: 10.1016/j.advwatres.2013.09.014. URL: http://www.sciencedirect.com/science/article/pii/S0309170813001759.

Bauer, D., Youssef, S., Fleury, M., Bekri, S., Rosenberg, E., and Vizika, O. (2012). "Improving the Estimations of Petrophysical Transport Behavior of Carbonate Rocks Using a Dual Pore Network Approach Combined with Computed Microtomography". In: *Transport in Porous Media* 94.2, pp. 505–524. ISSN: 01693913. DOI: 10.1007/s11242-012-9941-z. URL: https://link.springer.com/article/10.1007/s11242-012-9941-z.

Bazin, B. (2001). "From Matrix Acidizing to Acid Fracturing: A Laboratory Evaluation of Acid/Rock Interactions". In: *SPE Production & Facilities* 16.1, pp. 22–29. ISSN: 1064668X. DOI: 10.2118/66566-PA. URL: http://www.onepetro.org/doi/10.2118/49491-MS.

Bear, J. (1972). *Dynamics of fluids in porous media*. New York: Dover, p. 764. ISBN: 9780486656755.

Ben-Zvi, R., Jiang, S., Scher, H., and Berkowitz, B. (2019). "Finite-Element Method Solution of Non-Fickian Transport in Porous Media: The CTRW-FEM Package".

In: *Groundwater* 57.3, pp. 479–484. ISSN: 17456584. DOI: 10.1111/gwat.12813. URL: https://onlinelibrary.wiley.com/doi/abs/10.1111/gwat.12813.

Ben-Zvi, R., Nissan, A., Scher, H., and Berkowitz, B. (2018). "A continuous time random walk (CTRW) integro-differential equation with chemical interaction". In: *European Physical Journal B* 91.1, p. 15. ISSN: 14346036. DOI: 10.1140/epjb/e2017-80417-8. URL: http://link.springer.com/10.1140/epjb/e2017-80417-8.

Berkowitz, B., Cortis, A., Dentz, M., and Scher, H. (2006). "Modeling Non-fickian transport in geological formations as a continuous time random walk". In: *Reviews of Geophysics* 44.2, RG2003. ISSN: 87551209. DOI: 10.1029/2005RG000178. URL: http://doi.wiley.com/10.1029/2005RG000178.

Berkowitz, B., Dror, I., Hansen, S. K., and Scher, H. (2016). "Measurements and models of reactive transport in geological media". In: *Reviews of Geophysics* 54.4, pp. 930–986. ISSN: 87551209. DOI: 10.1002/2016RG000524. URL: http://doi.wiley.com/10.1002/2016RG000524.

Berkowitz, B., Kosakowski, G., Margolin, G., and Scher, H. (2001). "Application of continuous time random walk theory to tracer test measurements in fractured and heterogeneous porous media". In: *Ground Water* 39.4, pp. 593–604. ISSN: 0017467X. DOI: 10.1111/j.1745-6584.2001.tb02347.x. URL: http://doi.wiley.com/10.1111/j.1745-6584.2001.tb02347.x.

Berkowitz, B. and Scher, H. (1997). "Anomalous Transport in Random Fracture Networks". In: *Physical Review Letters* 79.20, pp. 4038–4041. ISSN: 0031-9007. DOI: 10.1103/PhysRevLett.79.4038. URL: https://link.aps.org/doi/10.1103/PhysRevLett.79.4038.

— (2009). "Exploring the nature of non-Fickian transport in laboratory experiments". In: *Advances in Water Resources* 32.5, pp. 750–755. ISSN: 03091708. DOI: 10.1016/j.advwatres.2008.05.004. URL: https://www.sciencedirect.com/science/article/pii/S0309170808000900.

Berkowitz, B., Scher, H., and Silliman, S. E. (2000). "Anomalous transport in laboratory-scale, heterogeneous porous media". In: *Water Resources Research* 36.1, pp. 149–158. ISSN: 00431397. DOI: 10.1029/1999WR900295. URL: http://doi.wiley.com/10.1029/1999WR900295.

Berner, R. A. and Morse, J. W. (1974). "Dissolution kinetics of calcium carbonate in sea water; IV, Theory of calcite dissolution". In: *American Journal of Science* 274.2, pp. 108–134. ISSN: 0002-9599. DOI: 10.2475/ajs.274.2.108. URL: http://www.ajsonline.org/cgi/doi/10.2475/ajs.274.2.108.

Bijeljic, B. and Blunt, M. J. (2006). "Pore-scale modeling and continuous time random walk analysis of dispersion in porous media". In: *Water Resources Research*

42.1. ISSN: 00431397. DOI: 10.1029/2005WR004578. URL: https://agupubs.onlinelibrary.wiley.com/doi/abs/10.1029/2005WR004578.

Bijeljic, B. and Blunt, M. J. (2007). "Pore-scale modeling of transverse dispersion in porous media". In: *Water Resources Research* 43.12. ISSN: 00431397. DOI: 10.1029/2006WR005700. URL: http://doi.wiley.com/10.1029/2006WR005700.

Bijeljic, B., Mostaghimi, P., and Blunt, M. J. (2011). "Signature of non-fickian solute transport in complex heterogeneous porous media". In: *Physical Review Letters* 107.20, p. 204502. ISSN: 00319007. DOI: 10.1103/PhysRevLett.107.204502. URL: https://journals.aps.org/prl/abstract/10.1103/PhysRevLett.107.204502.

— (2013a). "Insights into non-Fickian solute transport in carbonates". In: *Water Resources Research* 49.5, pp. 2714–2728. ISSN: 00431397. DOI: 10.1002/wrcr.20238. URL: http://doi.wiley.com/10.1002/wrcr.20238.

Bijeljic, B., Muggeridge, A. H., and Blunt, M. J. (2004). "Pore-scale modeling of longitudinal dispersion". In: *Water Resources Research* 40.11. ISSN: 00431397. DOI: 10.1029/2004WR003567. URL: http://doi.wiley.com/10.1029/2004WR003567.

Bijeljic, B., Raeini, A., Mostaghimi, P., and Blunt, M. J. (2013b). "Predictions of non-Fickian solute transport in different classes of porous media using direct simulation on pore-scale images". In: *Physical Review E - Statistical, Nonlinear, and Soft Matter Physics* 87.1. ISSN: 15393755. DOI: 10.1103/PhysRevE.87.013011.

Black, J. R., Carroll, S. A., and Haese, R. R. (2015). "Rates of mineral dissolution under CO2 storage conditions". In: *Chemical Geology* 399, pp. 134–144. ISSN: 00092541. DOI: 10.1016/j.chemgeo.2014.09.020.

Blunt, M. J., Bijeljic, B., Dong, H., Gharbi, O., Iglauer, S., Mostaghimi, P., Paluszny, A., and Pentland, C. (2013). "Pore-scale imaging and modelling". In: *Advances in Water Resources* 51, pp. 197–216. ISSN: 03091708. DOI: 10.1016/j.advwatres.2012.03.003. URL: http://linkinghub.elsevier.com/retrieve/pii/S0309170812000528.

Boek, E. S. and Venturoli, M. (2010). "Lattice-Boltzmann studies of fluid flow in porous media with realistic rock geometries". In: *Computers & Mathematics with Applications* 59.7, pp. 2305–2314. ISSN: 08981221. DOI: 10.1016/j.camwa.2009.08.063. URL: https://linkinghub.elsevier.com/retrieve/pii/S0898122109006427.

Bolster, D., Benson, D. A., and Singha, K. (2017). "Upscaling chemical reactions in multicontinuum systems: When might time fractional equations work?" In: *Chaos, Solitons and Fractals* 102, pp. 414–425. ISSN: 09600779. DOI: 10.1016/j.chaos.2017.04.028.

Boon, M., Bijeljic, B., Niu, B., and Krevor, S. (2016). "Observations of 3-D transverse dispersion and dilution in natural consolidated rock by X-ray tomography". In: *Advances in Water Resources* 96, pp. 266–281. ISSN: 03091708. DOI: 10.1016/j.advwatres.2016.07.020. URL: http://linkinghub.elsevier.com/retrieve/pii/S0309170816302962.

Bos, F. C. and Burland, D. M. (1987). "Hole transport in polyvinylcarbazole: The vital importance of excitation-light intensity". In: *Physical Review Letters* 58.2, pp. 152–155. ISSN: 00319007. DOI: 10.1103/PhysRevLett.58.152. URL: https://link.aps.org/doi/10.1103/PhysRevLett.58.152.

Boyd, A., Souza, A., Carneiro, G., Machado, V., Trevizan, W., Santos, B., Netto, P., Bagueira, R., Polinski, R., and Bertolini, A. (2015). "Presalt Carbonate Evaluation for Santos Basin, Offshore Brazil". In: *Petrophysics - The SPWLA Journal of Formation Evaluation and Reservoir Description* 56.06, pp. 577–591. ISSN: 1529-9074. URL: https://onepetro.org/petrophysics/article-abstract/56/06/577/171397/Presalt-Carbonate-Evaluation-for-Santos-Basin.

BP (2008). *BP Statistical Review of World Energy 2008*. Tech. rep. BP p.l.c.

Brinkman, H. C. (1949). "A calculation of the viscous force exerted by a flowing fluid on a dense swarm of particles". In: *Applied Scientific Research* 1.1, pp. 27–34. ISSN: 03657132. DOI: 10.1007/BF02120313. URL: https://link.springer.com/article/10.1007/BF02120313.

Britton, M. M. (2011). "Porous Media Studied by MRI". In: *Encyclopedia of Magnetic Resonance*. Ed. by K. R. Harris and R. L. Wasylishen. Chichester, UK: John Wiley & Sons, Ltd. ISBN: 9780470034590. DOI: 10.1002/9780470034590.emrstm1263. URL: http://doi.wiley.com/10.1002/9780470034590.emrstm1263.

Bruker Almanac (2013). https://www.theresonance.com/wp-content/uploads/2013/02/Bruker_Almanac_Tables.pdf. (online, accessed June 12, 2020).

Bultreys, T., Van Hoorebeke, L., and Cnudde, V. (2015). "Multi-scale, micro-computed tomography-based pore network models to simulate drainage in heterogeneous rocks". In: *Advances in Water Resources* 78, pp. 36–49. ISSN: 03091708. DOI: 10.1016/j.advwatres.2015.02.003.

Busenberg, E. and Plummer, L. N. (1982). "The kinetics of dissolution of dolomite in CO2-H2O systems at 1.5 to 65oC and 0 to 1 atm PCO2." In: *American Journal of Science* 282.1, pp. 45–78. ISSN: 00029599. DOI: 10.2475/ajs.282.1.45. URL: https://pubs.er.usgs.gov/publication/70011818.

Callaghan, P. T. (1993). *Principles of nuclear magnetic resonance microscopy*. Reprinted 2011. Clarendon Press, p. 492. ISBN: 9780198539971. URL: https://www.worldcat.org/title/principles-of-nuclear-magnetic-resonance-microscopy/oclc/1004245706.

Carman, P. C. (1937). "Fluid flow through a granular bed". In: *Transactions of the Institution of Chemical Engineers* 15, pp. 150–167.

Chatzis, I. and Dullien, F. A. L. (1985). "The modeling of mercury porosimetry and the relative permeability of mercury in sandstones using percolation theory". In: *International Chemical Engineering* 25.1, pp. 47–66. ISSN: 00206318.

Chen, S., Kim, K. H., Qin, F., and Watson, A. T. (1992). "Quantitative NMR imaging of multiphase flow in porous media". In: *Magnetic Resonance Imaging* 10.5, pp. 815–826. ISSN: 0730725X. DOI: 10.1016/0730-725X(92)90417-X. URL: https://www.sciencedirect.com/science/article/pii/0730725X9290417X.

Choquette, P. W. and Pray, L. C. (1970). "Geologic nomenclature and classification of porosity in sedimentary carbonates". In: *AAPG Bulletin* 54.2, pp. 207–244. ISSN: 0149-1423.

Chou, L., Garrels, R. M., and Wollast, R. (1989). "Comparative study of the kinetics and mechanisms of dissolution of carbonate minerals". In: *Chemical Geology* 78.3-4, pp. 269–282. ISSN: 00092541. DOI: 10.1016/0009-2541(89)90063-6. URL: https://www.sciencedirect.com/science/article/abs/pii/0009254189900636.

Clerke, E. A. (2009). "Permeability, Relative Permeability, Microscopic Displacement Efficiency and Pore Geometry of M_1 Bimodal Pore Systems in Arab-D Limestone". In: *SPE Journal* 14.03, pp. 524–531. ISSN: 1086-055X. DOI: 10.2118/105259-PA. URL: http://www.onepetro.org/doi/10.2118/105259-PA.

Colbourne, A. A., Sederman, A. J., Mantle, M. D., and Gladden, L. F. (2016). "Accelerating flow propagator measurements for the investigation of reactive transport in porous media". In: *Journal of Magnetic Resonance* 272, pp. 68–72. ISSN: 10907807. DOI: 10.1016/j.jmr.2016.08.018. URL: https://www.sciencedirect.com/science/article/pii/S1090780716301604.

Comolli, A., Hidalgo, J. J., Moussey, C., and Dentz, M. (2016). "Non-Fickian Transport Under Heterogeneous Advection and Mobile-Immobile Mass Transfer". In: *Transport in Porous Media* 115.2, pp. 265–289. ISSN: 15731634. DOI: 10.1007/s11242-016-0727-6. URL: http://link.springer.com/10.1007/s11242-016-0727-6.

Compton, R. G., Pritchard, K. L., and Unwin, P. R. (1989). "The dissolution of calcite in acid waters: mass transport versus surface control". In: *Freshwater Biology* 22.2, pp. 285–288. ISSN: 0046-5070. DOI: 10.1111/j.1365-2427.1989.tb01101.x. URL: http://doi.wiley.com/10.1111/j.1365-2427.1989.tb01101.x.

Cortis, A. and Berkowitz, B. (2004). "Anomalous Transport in Classical Soil and Sand Columns". In: *Soil Science Society of America Journal* 68.5, pp. 1539–1548. ISSN: 03615995. DOI: 10.2136/sssaj2004.1539. URL: http://doi.wiley.com/10.2136/sssaj2004.1539.

Cotts, R. M., Hoch, M. J. R., Sun, T., and Markert, J. T. (1989). "Pulsed field gradient stimulated echo methods for improved NMR diffusion measurements in heterogeneous systems". In: *Journal of Magnetic Resonance (1969)* 83.2, pp. 252–266. ISSN: 00222364. DOI: 10.1016/0022-2364(89)90189-3. URL: https://linkinghub.elsevier.com/retrieve/pii/0022236489901893.

Daccord, G., Lenormand, R., and Liétard, O. (1993). "Chemical dissolution of a porous medium by a reactive fluid-I. Model for the "wormholing" phenomenon". In: *Chem-*

ical Engineering Science 48.1, pp. 169–178. ISSN: 00092509. DOI: 10.1016/0009-2509(93)80293-Y. URL: https://www.sciencedirect.com/science/article/pii/000925099380293Y.

Darcy, H. (1856). *Les fontaines publiques de la ville de Dijon*. Ed. by V. Dalmont. Paris: Victor Dalmont, p. 647. ISBN: 0047-2875. DOI: 10.1177/004728759203100107. URL: http://catalogue.bnf.fr/ark:/12148/cb30300204t.

De Anna, P., Jimenez-Martinez, J., Tabuteau, H., Turuban, R., Le Borgne, T., Derrien, M., and Méheust, Y. (2014). "Mixing and reaction kinetics in porous media: An experimental pore scale quantification". In: *Environmental Science and Technology* 48.1, pp. 508–516. ISSN: 15205851. DOI: 10.1021/es403105b. URL: https://pubs.acs.org/sharingguidelines.

De Simoni, M., Carrera, J., Sánchez-Vila, X., and Guadagnini, A. (2005). "A procedure for the solution of multicomponent reactive transport problems". In: *Water Resources Research* 41.11, pp. 1–16. ISSN: 00431397. DOI: 10.1029/2005WR004056. URL: http://doi.wiley.com/10.1029/2005WR004056.

Delgado, J. M. P. Q. (2007). "Longitudinal and transverse dispersion in porous media". In: *Chemical Engineering Research and Design* 85.9 A, pp. 1245–1252. ISSN: 02638762. DOI: 10.1205/cherd07017. URL: http://linkinghub.elsevier.com/retrieve/pii/S0263876207731635.

Dentz, M. and Berkowitz, B. (2003). "Transport behavior of a passive solute in continuous time random walks and multirate mass transfer". In: *Water Resources Research* 39.5. ISSN: 00431397. DOI: 10.1029/2001WR001163. URL: http://doi.wiley.com/10.1029/2001WR001163.

Dentz, M., Cortis, A., Scher, H., and Berkowitz, B. (2004). "Time behavior of solute transport in heterogeneous media: Transition from anomalous to normal transport". In: *Advances in Water Resources* 27.2, pp. 155–173. ISSN: 03091708. DOI: 10.1016/j.advwatres.2003.11.002. URL: http://linkinghub.elsevier.com/retrieve/pii/S0309170803001726.

Dentz, M., Le Borgne, T., Englert, A., and Bijeljic, B. (2011). "Mixing, spreading and reaction in heterogeneous media: A brief review". In: *Journal of Contaminant Hydrology* 120-121.C, pp. 1–17. ISSN: 01697722. DOI: 10.1016/j.jconhyd.2010.05.002. URL: https://www.sciencedirect.com/science/article/pii/S0169772210000495.

Dong, H. and Blunt, M. J. (2009). "Pore-network extraction from micro-computerized-tomography images". In: *Physical Review E* 80.3, p. 036307. ISSN: 1539-3755. DOI: 10.1103/PhysRevE.80.036307. URL: https://link.aps.org/doi/10.1103/PhysRevE.80.036307.

Dunham, R. J. (1962). "Classification of Carbonate Rocks According to Depositional Textures". In: *Classification of Carbonate Rocks–A Symposium*, pp. 108–121. URL:

https://pubs.geoscienceworld.org/books/book/1475/chapter/107178011/Classification-of-Carbonate-Rocks-According-to.

Edery, Y. (2021). "The Effect of varying correlation lengths on Anomalous Transport". In: *Transport in Porous Media* 0123456789. ISSN: 1573-1634. URL: https://doi.org/10.1007/s11242-021-01563-9.

Edery, Y., Dror, I., Scher, H., and Berkowitz, B. (2015). "Anomalous reactive transport in porous media: Experiments and modeling". In: *Physical Review E - Statistical, Nonlinear, and Soft Matter Physics* 91.5, p. 052130. ISSN: 15502376. DOI: 10.1103/PhysRevE.91.052130. URL: http://link.aps.org/doi/10.1103/PhysRevE.91.052130.

Edery, Y., Guadagnini, A., Scher, H., and Berkowitz, B. (2014). "Origins of anomalous transport in heterogeneous media: Structural and dynamic controls". In: *Water Resources Research* 50.2, pp. 1490–1505. ISSN: 00431397. DOI: 10.1002/2013WR015111. URL: http://doi.wiley.com/10.1002/2013WR015111.

Edery, Y., Scher, H., and Berkowitz, B. (2010). "Particle tracking model of bimolecular reactive transport in porous media". In: *Water Resources Research* 46.7. ISSN: 00431397. DOI: 10.1029/2009WR009017. URL: http://doi.wiley.com/10.1029/2009WR009017.

Egbe, D. I. O., Jahanbani Ghahfarokhi, A., Nait Amar, M., and Torsæter, O. (2021). "Application of Low-Salinity Waterflooding in Carbonate Cores: A Geochemical Modeling Study". In: *Natural Resources Research* 30.1, pp. 519–542. ISSN: 1520-7439. DOI: 10.1007/s11053-020-09712-5. URL: http://link.springer.com/10.1007/s11053-020-09712-5.

Fanchi, J. R. (1986). "BOAST-DRC: Black Oil and Condensate Reservoir Simulation on an IBM-PC". In: *Proceedings of Petroleum Industry Application of Microcomputers*. Society of Petroleum Engineers, pp. 137–144. ISBN: 9781555636081. DOI: 10.2523/15297-MS. URL: http://www.onepetro.org/doi/10.2118/15297-MS.

Fatt, I. (1956). "The Network Model of Porous Media". In: *Petroleum Transactions, AIME* 207, pp. 144–181. URL: https://www.onepetro.org/general/SPE-574-G.

Fenwick, D. H. and Blunt, M. J. (1998). "Three-dimensional modeling of three phase imbibition and drainage". In: *Advances in Water Resources* 21.2, pp. 121–143. ISSN: 03091708. DOI: 10.1016/S0309-1708(96)00037-1. URL: https://www.sciencedirect.com/science/article/pii/S0309170896000371.

Ferreira, L. d. P., Oliveira, T. D. S. de, Surmas, R., Silva, M. A. P. da, and Peçanha, R. P. (2020). "Brinkman equation in reactive flow: Contribution of each term in carbonate acidification simulations". In: *Advances in Water Resources* 144, p. 103696. ISSN: 03091708. DOI: 10.1016/j.advwatres.2020.103696.

Fick, A. (1855). "Über Diffusion". In: *Annalen der Physik und Chemie* 170.1, pp. 59–86. ISSN: 00033804. DOI: 10.1002/andp.18551700105. URL: http://doi.wiley.com/10.1002/andp.18551700105.

Fogg, G. E. and Zhang, Y. (2016). "Debates-Stochastic subsurface hydrology from theory to practice: A geologic perspective". In: *Water Resources Research* 52.12, pp. 9235–9245. ISSN: 00431397. DOI: 10.1002/2016WR019699. URL: http://doi.wiley.com/10.1002/2016WR019699.

Fogler, S. H. (1987). *Elements of chemical reaction engineering*. Vol. 42. 10, p. 2493. DOI: 10.1016/0009-2509(87)80130-6.

Folk, R. L. (1959). "Practical Petrographic Classification of Limestones". In: *AAPG Bulletin* 43.1, pp. 1–38. URL: http://archives.datapages.com/data/bulletns/1957-60/data/pg/0043/0001/0000/0001.htm.

Fordham, E. J., Kenyon, W. E., Ramakrishnan, T. S., Schwartz, L., and Wilkinson, D. J. (1999). "Forward Models For Nuclear Magnetic Resonance In Carbonate Rocks". In: *The Log Analyst* 40.04, pp. 260–270. ISSN: 0024-581X. URL: https://www.onepetro.org/journal-paper/SPWLA-1999-v40n4a1.

Fourar, M., Radilla, G., Lenormand, R., and Moyne, C. (2004). "On the non-linear behavior of a laminar single-phase flow through two and three-dimensional porous media". In: *Advances in Water Resources* 27.6, pp. 669–677. ISSN: 03091708. DOI: 10.1016/j.advwatres.2004.02.021.

Fourier, J. B. J. (1822). *Theorié analytique de la chaleur*. Chez Firmin Didot, p. 638. URL: https://www.irphe.fr/%7B~%7Dclanet/otherpaperfile/articles/Fourier/N0029061%7B%5C_%7DPDF%7B%5C_%7D1%7B%5C_%7D676.pdf.

Fredd, C. N. and Fogler, H. S. (1998). "Influence of transport and reaction on wormhole formation in porous media". In: *AIChE Journal* 44.9, pp. 1933–1949. ISSN: 00011541. DOI: 10.1002/aic.690440902. URL: http://doi.wiley.com/10.1002/aic.690440902.

Gaver, D. P. (1966). "Observing Stochastic Processes, and Approximate Transform Inversion". In: *Operations Research* 14.3, pp. 361–553. ISSN: 0030-364X. DOI: 10.1287/opre.14.3.444. URL: https://doi.org/10.1287/opre.14.3.444.

Gayon Lombardo, A., Simon, B. A., Taiwo, O., Neethling, S. J., and Brandon, N. P. (2019). "A pore network model of porous electrodes in electrochemical devices". In: *Journal of Energy Storage* 24, p. 100736. ISSN: 2352152X. DOI: 10.1016/j.est.2019.04.010.

Gillespie, D. T. (1976). "A general method for numerically simulating the stochastic time evolution of coupled chemical reactions". In: *Journal of Computational Physics* 22.4, pp. 403–434. ISSN: 10902716. DOI: 10.1016/0021-9991(76)90041-3.

Gillespie, D. T. (1977). "Exact stochastic simulation of coupled chemical reactions". In: *Journal of Physical Chemistry*. Vol. 81. 25. American Chemical Society, pp. 2340–2361. ISBN: 1749810441. DOI: 10.1021/j100540a008. arXiv: arXiv:1011.1669v3. URL: http://pubs.acs.org/doi/abs/10.1021/j100540a008.

— (2001). "Approximate accelerated stochastic simulation of chemically reacting systems". In: *Journal of Chemical Physics* 115.4, pp. 1716–1733. ISSN: 00219606. DOI: 10.1063/1.1378322. URL: http://aip.scitation.org/doi/10.1063/1.1378322.

Golfier, F., Zarcone, C., Bazin, B., Lenormand, R., Lasseux, D., and Quintard, M. (2002). "On the ability of a Darcy-scale model to capture wormhole formation during the dissolution of a porous medium". In: *Journal of Fluid Mechanics* 457, pp. 213–254. ISSN: 00221120. DOI: 10.1017/S0022112002007735. URL: http://www.journals.cambridge.org/abstract%7B%5C_%7DS0022112002007735.

Gomes, J. L. M. A., Pavlidis, D., Salinas, P., Xie, Z., Percival, J. R., Melnikova, Y., Pain, C. C., and Jackson, M. D. (2017). "A force-balanced control volume finite element method for multi-phase porous media flow modelling". In: *International Journal for Numerical Methods in Fluids* 83.5, pp. 431–445. ISSN: 10970363. DOI: 10.1002/fld.4275. URL: http://doi.wiley.com/10.1002/fld.4275.

Gostick, J. T. (2017). "Versatile and efficient pore network extraction method using marker-based watershed segmentation". In: *Physical Review E* 96.2, p. 023307. ISSN: 2470-0045. DOI: 10.1103/PhysRevE.96.023307. URL: https://link.aps.org/doi/10.1103/PhysRevE.96.023307.

Grader, A., Mu, Y., Toelke, J., Baldwin, C., Fang, Q., Carpio, G., Stenger, B. A., Al-Dayyani, T., and Kalam, M. Z. (2010). "Estimation Of Relative Permeability Using The Lattice Boltzmann Method For Fluid Flows, Thamama Formation, Abu Dhabi". In: *Abu Dhabi International Petroleum Exhibition and Conference*. Vol. 3. Society of Petroleum Engineers, pp. 2053–2060. ISBN: 9781617820434. DOI: 10.2118/138591-MS. URL: http://www.onepetro.org/doi/10.2118/138591-MS.

Gramling, C. M., Harvey, C. F., and Meigs, L. C. (2002). "Reactive Transport in Porous Media: A Comparison of Model Prediction with Laboratory Visualization". In: *Environmental Science & Technology* 36.11, pp. 2508–2514. ISSN: 0013-936X. DOI: 10.1021/es0157144. URL: https://pubs.acs.org/doi/abs/10.1021/es0157144.

Gray, F., Anabaraonye, B., Shah, S., Boek, E., and Crawshaw, J. (2018). "Chemical mechanisms of dissolution of calcite by HCl in porous media: Simulations and experiment". In: *Advances in Water Resources* 121, pp. 369–387. ISSN: 03091708. DOI: 10.1016/j.advwatres.2018.09.007. URL: https://www.sciencedirect.com/science/article/pii/S0309170818303713.

Gringarten, A. C. (2012). "Well Test Analysis in Practice". In: *The Way Ahead* 08.02, pp. 10–14. ISSN: 2224-4522. DOI: 10.2118/0212-010-TWA. URL: http://www.onepetro.org/doi/10.2118/0212-010-TWA.

Hennig, J., Nauerth, A., and Friedburg, H. (1986). "RARE imaging: A fast imaging method for clinical MR". In: *Magnetic Resonance in Medicine* 3.6, pp. 823–833. ISSN: 15222594. DOI: 10.1002/mrm.1910030602. URL: https://onlinelibrary.wiley.com/doi/full/10.1002/mrm.1910030602.

Herrera, P. A., Massabó, M., and Beckie, R. D. (2009). "A meshless method to simulate solute transport in heterogeneous porous media". In: *Advances in Water Resources* 32.3, pp. 413–429. ISSN: 03091708. DOI: 10.1016/j.advwatres.2008.12.005. URL: https://linkinghub.elsevier.com/retrieve/pii/S0309170808002273.

Hoefner, M. L. and Fogler, H. S. (1988). "Pore evolution and channel formation during flow and reaction in porous media". In: *AIChE Journal* 34.1, pp. 45–54. ISSN: 15475905. DOI: 10.1002/aic.690340107. URL: http://doi.wiley.com/10.1002/aic.690340107.

Honari, A., Bijeljic, B., Johns, M. L., and May, E. F. (2015). "Enhanced gas recovery with CO 2 sequestration: The effect of medium heterogeneity on the dispersion of supercritical CO2CH4". In: *International Journal of Greenhouse Gas Control* 39, pp. 39–50. ISSN: 17505836. DOI: 10.1016/j.ijggc.2015.04.014. URL: https://www.sciencedirect.com/science/article/pii/S1750583615001577.

Hoog, F. R. de, Knight, J. H., and Stokes, A. N. (1982). "An Improved Method for Numerical Inversion of Laplace Transforms". In: *SIAM Journal on Scientific and Statistical Computing* 3.3, pp. 357–366. ISSN: 0196-5204. DOI: 10.1137/0903022. URL: http://epubs.siam.org/doi/10.1137/0903022.

IEA (2006). *World Energy Outlook 2008*. Tech. rep. Paris: International Energy Agency. URL: https://www.iea.org/reports/world-energy-outlook-2008.

Jackson, M. D., Percival, J. R., Mostaghimi, P., Tollit, B. S., Pavlidis, D., Pain, C. C., Gomes, J. L., El-Sheikh, A. H., Salinas, P., Muggeridge, A. H., and Blunt, M. J. (2015). "Reservoir modeling for flow simulation by use of surfaces, adaptive unstructured meshes, and an overlapping-control-volume finite-element method". In: *SPE Reservoir Evaluation and Engineering*. Vol. 18. 2. Society of Petroleum Engineers, pp. 115–132. DOI: 10.2118/163633-PA.

Johnson, J. W., Oelkers, E. H., and Helgeson, H. C. (1992). "SUPCRT92: A software package for calculating the standard molal thermodynamic properties of minerals, gases, aqueous species, and reactions from 1 to 5000 bar and 0 to 1000ŕC". In: *Computers and Geosciences* 18.7, pp. 899–947. ISSN: 00983004. DOI: 10.1016/0098-3004(92)90029-Q. URL: https://linkinghub.elsevier.com/retrieve/pii/009830049290029Q.

Kandhai, D., Kandhai, D., Hlushkou, D., Hlushkou, D., Hoekstra, A. G., Sloot, P. M., Van As, H., Tallarek, U., and Tallarek, U. (2002). "Influence of stagnant zones on transient and asymptotic dispersion in macroscopically homogeneous porous media". In: *Physical Review Letters* 88.23, pp. 2345011–2345014. ISSN: 00319007.

DOI: 10.1103/PhysRevLett.88.234501. URL: https://link.aps.org/doi/10.1103/PhysRevLett.88.234501.

Kang, P. K., Dentz, M., Le Borgne, T., and Juanes, R. (2011). "Spatial Markov model of anomalous transport through random lattice networks". In: *Physical Review Letters* 107.18, p. 180602. ISSN: 00319007. DOI: 10.1103/PhysRevLett.107.180602. URL: https://link.aps.org/doi/10.1103/PhysRevLett.107.180602.

Kenkre, V. M., Montroll, E. W., and Shlesinger, M. F. (1973). "Generalized master equations for continuous-time random walks". In: *Journal of Statistical Physics* 9.1, pp. 45–50. ISSN: 00224715. DOI: 10.1007/BF01016796. URL: https://link.springer.com/article/10.1007/BF01016796.

Kenney, J. P. L., Kirby, M. E., Cuadros, J., and Weiss, D. J. (2017). "A conceptual model to predict uranium removal from aqueous solutions in waterrock systems associated with low- and intermediate-level radioactive waste disposal". In: *RSC Advances* 7.13, pp. 7876–7884. ISSN: 2046-2069. DOI: 10.1039/C6RA26773D. URL: http://xlink.rsc.org/?DOI=C6RA26773D.

Kenyon, W. E. (1997). "Petrophysical Principles of Applications of NMR Logging". In: *The Log Analyst* 38.02. ISSN: 0024-581X. URL: https://onepetro.org/petrophysics/article-abstract/170864/Petrophysical-Principles-of-Applications-of-NMR.

Kenyon, W. E., Day, P. I., Straley, C., and Willemsen, J. F. (1988). "Three-part study of NMR longitudinal relaxation properties of water-saturated sandstones". In: *SPE Formation Evaluation* 3.3, pp. 622–636. ISSN: 0885923X. DOI: 10.2118/15643-pa.

Khrapitchev, A. A. and Callaghan, P. T. (2003). "Reversible and irreversible dispersion in a porous medium". In: *Physics of Fluids* 15.9, pp. 2649–2660. ISSN: 10706631. DOI: 10.1063/1.1596914. URL: http://aip.scitation.org/doi/10.1063/1.1596914.

Al-Khulaifi, Y., Lin, Q., Blunt, M. J., and Bijeljic, B. (2017). "Reaction Rates in Chemically Heterogeneous Rock: Coupled Impact of Structure and Flow Properties Studied by X-ray Microtomography". In: *Environmental Science and Technology* 51.7, pp. 4108–4116. ISSN: 15205851. DOI: 10.1021/acs.est.6b06224. URL: http://pubs.acs.org/doi/10.1021/acs.est.6b06224.

— (2018). "Reservoir-condition pore-scale imaging of dolomite reaction with supercritical CO2 acidified brine: Effect of pore-structure on reaction rate using velocity distribution analysis". In: *International Journal of Greenhouse Gas Control* 68, pp. 99–111. ISSN: 17505836. DOI: 10.1016/j.ijggc.2017.11.011. URL: https://linkinghub.elsevier.com/retrieve/pii/S1750583617306205.

— (2019). "Pore-Scale Dissolution by CO2 Saturated Brine in a Multimineral Carbonate at Reservoir Conditions: Impact of Physical and Chemical Heterogeneity". In: *Water Resources Research* 55.4, pp. 3171–3193. ISSN: 19447973. DOI: 10.1029/

2018WR024137. URL: https://onlinelibrary.wiley.com/doi/abs/10.1029/2018WR024137.

Kitanidis, P. K. (1994). "The concept of the Dilution Index". In: *Water Resources Research* 30.7, pp. 2011–2026. ISSN: 19447973. DOI: 10.1029/94WR00762. URL: http://doi.wiley.com/10.1029/94WR00762.

Klafter, J. and Silbey, R. (1980). "Derivation of the continuous-time random-walk eEquation". In: *Physical Review Letters* 44.2, pp. 55–58. ISSN: 00319007. DOI: 10.1103/PhysRevLett.44.55. URL: https://journals.aps.org/prl/abstract/10.1103/PhysRevLett.44.55.

Klinkenberg, L. J. (1941). "The permeability of porous media to liquids and gases". In: *Drilling and Production Practice* API-41-200, pp. 200–213. ISSN: 22188622. DOI: 10.5510/OGP20120200114.

Kolmogorov, A. N. (1933). "Sulla determinazione empirica di una legge di distribuzione". In: *Giorn. Inst. Italiano Attuari* 4, pp. 83–91.

Kosakowski, G., Berkowitz, B., and Scher, H. (2001). "Analysis of field observations of tracer transport in a fractured till". In: *Journal of Contaminant Hydrology* 47.1, pp. 29–51. ISSN: 01697722. DOI: 10.1016/S0169-7722(00)00140-6.

Kozeny, J. (1927). "Über kapillare Leitung des Wassers im Boden". In: *Akad. Wiss. Wien* 136, pp. 271–306.

Kuchuk, F. and Biryukov, D. (2015). "Pressure-transient tests and flow regimes in fractured reservoirs". In: *SPE Reservoir Evaluation and Engineering* 18.2, pp. 187–204. ISSN: 10946470. DOI: 10.2118/166296-PA.

Kulik, D. A., Wagner, T., Dmytrieva, S. V., Kosakowski, G., Hingerl, F. F., Chudnenko, K. V., and Berner, U. R. (2013). "GEM-Selektor geochemical modeling package: Revised algorithm and GEMS3K numerical kernel for coupled simulation codes". In: *Computational Geosciences* 17.1, pp. 1–24. ISSN: 14200597. DOI: 10.1007/s10596-012-9310-6. URL: http://link.springer.com/10.1007/s10596-012-9310-6.

Kump, L. R. and Hine, A. C. (1986). "Ooids as sea-level indicators." In: *Sea-level research*, pp. 175–193. DOI: 10.1007/978-94-009-4215-8_7. URL: https://link.springer.com/chapter/10.1007/978-94-009-4215-8%7B%5C_%7D7.

Kurotori, T., Zahasky, C., Benson, S. M., and Pini, R. (2020). "Description of Chemical Transport in Laboratory Rock Cores Using the Continuous Random Walk Formalism". In: *Water Resources Research* 56.9. ISSN: 19447973. DOI: 10.1029/2020WR027511. URL: https://onlinelibrary.wiley.com/doi/10.1029/2020WR027511.

Kurotori, T., Zahasky, C., Hosseinzadeh Hejazi, S. A., Shah, S. M., Benson, S. M., and Pini, R. (2019). "Measuring, imaging and modelling solute transport in a microporous limestone". In: *Chemical Engineering Science* 196, pp. 366–383. ISSN:

00092509. DOI: 10.1016/j.ces.2018.11.001. URL: https://www.sciencedirect.com/science/article/pii/S0009250918307796.

Laubach, S. E., Lamarche, J., Gauthier, B. D., Dunne, W. M., and Sanderson, D. J. (2018). "Spatial arrangement of faults and opening-mode fractures". In: *Journal of Structural Geology* 108, pp. 2–15. ISSN: 01918141. DOI: 10.1016/j.jsg.2017.08.008.

Le Borgne, T. and Gouze, P. (2008). "Non-Fickian dispersion in porous media: 2. Model validation from measurements at different scales". In: *Water Resources Research* 44.6. ISSN: 00431397. DOI: 10.1029/2007WR006279. URL: http://doi.wiley.com/10.1029/2007WR006279.

Le Borgne, T., Dentz, M., Bolster, D., Carrera, J., Dreuzy, J.-R. de, and Davy, P. (2010). "Non-Fickian mixing: Temporal evolution of the scalar dissipation rate in heterogeneous porous media". In: *Advances in Water Resources* 33.12, pp. 1468–1475. ISSN: 03091708. DOI: 10.1016/j.advwatres.2010.08.006. URL: https://linkinghub.elsevier.com/retrieve/pii/S0309170810001508.

Leal, A. M. M. (2014). "Computational methods for geochemical modelling". PhD thesis. Imperial College London. DOI: 10.1007/978-3-319-56327-5_2. URL: https://spiral.imperial.ac.uk/handle/10044/1/24920.

Leal, A. M., Blunt, M. J., and LaForce, T. C. (2014). "Efficient chemical equilibrium calculations for geochemical speciation and reactive transport modelling". In: *Geochimica et Cosmochimica Acta* 131, pp. 301–322. ISSN: 00167037. DOI: 10.1016/j.gca.2014.01.038. URL: https://linkinghub.elsevier.com/retrieve/pii/S0016703714000829.

Leal, A. M., Blunt, M. J., and LaForce, T. C. (2015). "A chemical kinetics algorithm for geochemical modelling". In: *Applied Geochemistry* 55, pp. 46–61. ISSN: 18729134. DOI: 10.1016/j.apgeochem.2014.09.020.

Levy, M. and Berkowitz, B. (2003). "Measurement and analysis of non-Fickian dispersion in heterogeneous porous media". In: *Journal of Contaminant Hydrology* 64.3-4, pp. 203–226. ISSN: 01697722. DOI: 10.1016/S0169-7722(02)00204-8. URL: https://www.sciencedirect.com/science/article/pii/S0169772202002048.

Li, L., Steefel, C. I., and Yang, L. (2008). "Scale dependence of mineral dissolution rates within single pores and fractures". In: *Geochimica et Cosmochimica Acta* 72.2, pp. 360–377. ISSN: 00167037. DOI: 10.1016/j.gca.2007.10.027. URL: http://linkinghub.elsevier.com/retrieve/pii/S0016703707006035.

Lin, Q., Al-Khulaifi, Y., Blunt, M. J., and Bijeljic, B. (2016). "Quantification of sub-resolution porosity in carbonate rocks by applying high-salinity contrast brine using X-ray microtomography differential imaging". In: *Advances in Water Resources* 96, pp. 306–322. ISSN: 03091708. DOI: 10.1016/j.advwatres.2016.08.002. URL:

https://www.sciencedirect.com/science/article/pii/S0309170816303098%7B%5C#%7Dfig0004.

Liu, M. and Mostaghimi, P. (2018). "Numerical simulation of fluid-fluid-solid reactions in porous media". In: *International Journal of Heat and Mass Transfer* 120, pp. 194–201. ISSN: 00179310. DOI: 10.1016/j.ijheatmasstransfer.2017.11.141. URL: https://www.sciencedirect.com/science/article/pii/S0017931017336360.

Lucy, L. B. (1977). "A numerical approach to the testing of the fission hypothesis". In: *The Astronomical Journal* 82, p. 1013. ISSN: 00046256. DOI: 10.1086/112164. URL: http://adsabs.harvard.edu/abs/1977AJ.....82.1013L.

Lund, K., Fogler, H. S., McCune, C. C., and Ault, J. W. (1975). "Acidization-II. The dissolution of calcite in hydrochloric acid". In: *Chemical Engineering Science* 30.8, pp. 825–835. ISSN: 00092509. DOI: 10.1016/0009-2509(75)80047-9. URL: https://www.sciencedirect.com/science/article/pii/0009250975800479.

Lund, K., Fogler, H. S., and McCune, C. C. (1973). "AcidizationI. The dissolution of dolomite in hydrochloric acid". In: *Chemical Engineering Science* 28.3, 691–IN1. ISSN: 00092509. DOI: 10.1016/0009-2509(77)80003-1. URL: https://www.sciencedirect.com/science/article/pii/0009250977800031.

Luquot, L. and Gouze, P. (2009). "Experimental determination of porosity and permeability changes induced by injection of CO2 into carbonate rocks". In: *Chemical Geology* 265.1-2, pp. 148–159. ISSN: 00092541. DOI: 10.1016/j.chemgeo.2009.03.028.

MacQuarrie, K. T. and Sudicky, E. A. (1990). "Simulation of biodegradable organic contaminants in groundwater: 2. Plume behavior in uniform and random flow fields". In: *Water Resources Research* 26.2, pp. 223–239. ISSN: 19447973. DOI: 10.1029/WR026i002p00223. URL: http://doi.wiley.com/10.1029/WR026i002p00223.

Maier, C. G. and Kelley, K. K. (1932). "An equation for the representation of high-temperature heat content data". In: *Journal of the American Chemical Society* 54.8, pp. 3243–3246. ISSN: 15205126. DOI: 10.1021/ja01347a029. URL: https://pubs.acs.org/doi/abs/10.1021/ja01347a029.

Margolin, G. and Berkowitz, B. (2000). "Application of continuous time random walks to transport in porous media". In: *Journal of Physical Chemistry B* 104.16, pp. 3942–3947. ISSN: 10895647. DOI: 10.1021/jp993721x. URL: https://pubs.acs.org/doi/abs/10.1021/jp993721x.

Meakin, P. and Tartakovsky, A. M. (2009). "Modeling and simulation of pore-scale multiphase fluid flow and reactive transport in fractured and porous media". In: *Reviews of Geophysics* 47.3, RG3002. ISSN: 8755-1209. DOI: 10.1029/2008RG000263. URL: http://doi.wiley.com/10.1029/2008RG000263.

Menke, H. P., Andrew, M. G., Blunt, M. J., and Bijeljic, B. (2016). "Reservoir condition imaging of reactive transport in heterogeneous carbonates using fast synchrotron

tomography - Effect of initial pore structure and flow conditions". In: *Chemical Geology* 428, pp. 15–26. ISSN: 00092541. DOI: 10.1016/j.chemgeo.2016.02.030.

Menke, H. P. (2015). "Reservoir condition pore-scale imaging of reaction". PhD thesis. Imperial College London, p. 176. URL: https://spiral.imperial.ac.uk/handle/10044/1/33324.

Menke, H. P., Bijeljic, B., Andrew, M. G., and Blunt, M. J. (2015). "Dynamic Three-Dimensional Pore-Scale Imaging of Reaction in a Carbonate at Reservoir Conditions". In: *Environmental Science & Technology* 49.7, pp. 4407–4414. ISSN: 0013-936X. DOI: 10.1021/es505789f. URL: http://pubs.acs.org/doi/abs/10.1021/es505789f.

Menke, H. P., Reynolds, C. A., Andrew, M. G., Pereira Nunes, J. P., Bijeljic, B., and Blunt, M. J. (2018). "4D multi-scale imaging of reactive flow in carbonates: Assessing the impact of heterogeneity on dissolution regimes using streamlines at multiple length scales". In: *Chemical Geology* 481, pp. 27–37. ISSN: 00092541. DOI: 10.1016/j.chemgeo.2018.01.016. URL: https://www.sciencedirect.com/science/article/pii/S0009254118300287.

Metz, B., Davidson, O., Coninck, H. de, Loos, M., and Meyer, L. (2010). *Carbon Dioxide Capture and Storage*. Tech. rep. 35. Geneva, Switzerland: IPCC, p. 443. URL: http://www.ncbi.nlm.nih.gov/pubmed/20698658.

Mitchell, J., Sederman, A. J., Fordham, E. J., Johns, M. L., and Gladden, L. F. (2008). "A rapid measurement of flow propagators in porous rocks". In: *Journal of Magnetic Resonance* 191.2, pp. 267–272. ISSN: 10907807. DOI: 10.1016/j.jmr.2007.12.014. URL: https://www.sciencedirect.com/science/article/pii/S1090780707003825.

Molins, S., Trebotich, D., Steefel, C. I., and Shen, C. (2012). "An investigation of the effect of pore scale flow on average geochemical reaction rates using direct numerical simulation". In: *Water Resources Research* 48.3. ISSN: 00431397. DOI: 10.1029/2011WR011404. URL: http://doi.wiley.com/10.1029/2011WR011404.

Monaghan, J. J. (2005). *Frontiers of Numerical Analysis*. en. Ed. by J. F. Blowey and A. W. Craig. Universitext. Berlin/Heidelberg: Springer-Verlag. Chap. Theory and, pp. 143–194. ISBN: 3-540-23921-9. DOI: 10.1007/3-540-28884-8. URL: http://link.springer.com/chapter/10.1007/3-540-28884-8%7B%5C_%7D3.

Montroll, E. W. E. and Weiss, G. H. G. (1965). "Random walks on lattices. II". In: *Journal of Mathematical Physics* 6.2, pp. 167–181. ISSN: 00222488. DOI: 10.1063/1.1704269. URL: http://aip.scitation.org/doi/10.1063/1.1704269.

Montroll, E. W. and Scher, H. (1973). "Random walks on lattices. IV. Continuous-time walks and influence of absorbing boundaries". In: *Journal of Statistical Physics* 9.2, pp. 101–135. ISSN: 0022-4715. DOI: 10.1007/BF01016843. URL: http://link.springer.com/10.1007/BF01016843.

Muljadi, B. P., Bijeljic, B., Blunt, M. J., Colbourne, A., Sederman, A. J., Mantle, M. D., and Gladden, L. F. (2018). "Modelling and upscaling of transport in carbonates during dissolution: Validation and calibration with NMR experiments". In: *Journal of Contaminant Hydrology* 212, pp. 85–95. ISSN: 18736009. DOI: 10.1016/j.jconhyd.2017.08.008. URL: http://linkinghub.elsevier.com/retrieve/pii/S0169772217300980.

Nickolls, J., Buck, I., Garland, M., and Skadron, K. (2008). "Scalable parallel programming with CUDA". In: *Queue* 6.2, pp. 40–53. ISSN: 15427730. DOI: 10.1145/1365490.1365500. URL: http://portal.acm.org/citation.cfm?doid=1365490.1365500.

Nierode, D. E. and Williams, B. B. (1971). "Characteristics of Acid Reaction in Limestone Formations". In: *Society of Petroleum Engineers Journal* 11.4, pp. 406–418. ISSN: 0197-7520. DOI: 10.2118/3101-PA. URL: http://www.onepetro.org/doi/10.2118/3101-PA.

Noiriel, C., Luquot, L., Madé, B., Raimbault, L., Gouze, P., and Lee, J. van der (2009). "Changes in reactive surface area during limestone dissolution: An experimental and modelling study". In: *Chemical Geology* 265.1-2, pp. 160–170. ISSN: 00092541. DOI: 10.1016/j.chemgeo.2009.01.032.

Nordahl, K. and Ringrose, P. S. (2008). "Identifying the representative elementary volume for permeability in heterolithic deposits using numerical rock models". In: *Mathematical Geosciences* 40.7, pp. 753–771. ISSN: 18748961. DOI: 10.1007/s11004-008-9182-4.

Ogata, A. and Banks, R. B. (1961). "A solution of the differential equation of longitudinal dispersion in porous media: fluid movement in earth materials". In: *Geological Survey Professional Paper 411-A*, pp. 1–7. ISSN: 2330-7102. DOI: 10.3133/PP411A. URL: https://pubs.usgs.gov/pp/0411a/report.pdf.

Ohm, G. S. (1827). *Die galvanische Kette - Mathematisch bearbeitet*. Berlin: T. H. Riemman, p. 203. ISBN: 1168419514.

Oliveira, R. (2014). "Finite element method applied to flow in heterogeneous porous media". Dissertation. Pontifical Catholic University of Rio de Janeiro, p. 90. URL: http://www.dbd.puc-rio.br/pergamum/tesesabertas/1112332%7B%5C_%7D2014%7B%5C_%7Dcompleto.pdf.

Oliveira, R., Bijeljic, B., Blunt, M. J., Colbourne, A., Sederman, A. J., Mantle, M. D., and Gladden, L. F. (2021). "A continuous time random walk method to predict dissolution in porous media based on validation of experimental NMR data". In: *Advances in Water Resources* 149. ISSN: 03091708. DOI: 10.1016/j.advwatres.2021.103847. URL: https://linkinghub.elsevier.com/retrieve/pii/S0309170821000026.

Oliveira, T. D. S., Blunt, M. J., and Bijeljic, B. (2020). "Multispecies reactive transport in a microporous rock: impact of flow heterogeneity and reversibility of re-

action". In: *Water Resources Research* 56.12. ISSN: 0043-1397. DOI: 10.1029/2020wr027317. URL: https://agupubs.onlinelibrary.wiley.com/doi/full/10.1029/2020WR027317.

Oliveira, T. D., Blunt, M. J., and Bijeljic, B. (2019). "Modelling of multispecies reactive transport on pore-space images". In: *Advances in Water Resources* 127, pp. 192–208. ISSN: 03091708. DOI: 10.1016/j.advwatres.2019.03.012. URL: https://www.sciencedirect.com/science/article/pii/S0309170818306742.

Oppenheim, I., Schuler, K. E., and Weiss, G. H. (1977). *Stochastic Processes in Chemical Physics: The Master Equation*. 1st Editio. MIT Press, p. 561. ISBN: 9780262150170.

Orlob, G. T. and Radhakrishna, G. N. (1958). "The effects of entrapped gases on the hydraulic characteristics of porous media". In: *Transactions American Geophysical Union* 39.4, pp. 648–659. ISSN: 23249250. DOI: 10.1029/TR039i004p00648. URL: http://doi.wiley.com/10.1029/TR039i004p00648.

Parkhurst, D. L. and Appelo, C. A. J. (2013). *Description of input and examples for PHREEQC version 3: a computer program for speciation, batch-reaction, one-dimensional transport, and inverse geochemical calculations*. Tech. rep. Reston, VA: U.S. Geological Survey. DOI: https://doi.org/10.3133/tm6A43. URL: https://pubs.er.usgs.gov/publication/tm6A43.

Paulsen, J. L., Cho, H., Cho, G., and Song, Y. Q. (2011). "Acceleration of multi-dimensional propagator measurements with compressed sensing". In: *Journal of Magnetic Resonance* 213.1, pp. 166–170. ISSN: 10907807. DOI: 10.1016/j.jmr.2011.08.025. URL: https://www.sciencedirect.com/science/article/pii/S1090780711002953.

Peaceman, D. (1978). "Interpretation of Well-Block Pressures in Numerical Reservoir Simulation". In: *Society of Petroleum Engineers Journal* 18.03, pp. 183–194. ISSN: 0197-7520. DOI: 10.2118/6893-PA. URL: http://www.onepetro.org/doi/10.2118/6893-PA.

Peng, C., Anabaraonye, B. U., Crawshaw, J. P., Maitland, G. C., and Trusler, J. P. (2016). *Kinetics of carbonate mineral dissolution in CO2-acidified brines at storage reservoir conditions*. DOI: 10.1039/c6fd00048g. URL: https://doi.org/10.1039/C6FD00048G.

Peng, C., Crawshaw, J. P., Maitland, G. C., and Trusler, J. P. P. (2015). "Kinetics of calcite dissolution in CO2-saturated water at temperatures between (323 and 373) K and pressures up to 13.8 MPa". In: *Chemical Geology* 403, pp. 74–85. ISSN: 00092541. DOI: 10.1016/j.chemgeo.2015.03.012. URL: https://www.sciencedirect.com/science/article/pii/S0009254115001461.

Peng, D. Y. and Robinson, D. B. (1976). "A New Two-Constant Equation of State". In: *Industrial and Engineering Chemistry Fundamentals* 15.1, pp. 59–64. ISSN:

01964313. DOI: 10.1021/i160057a011. URL: https://pubs.acs.org/doi/abs/10.1021/i160057a011.

Pereira Nunes, J. P., Bijeljic, B., and Blunt, M. J. (2015). "Time-of-Flight Distributions and Breakthrough Curves in Heterogeneous Porous Media Using a Pore-Scale Streamline Tracing Algorithm". In: *Transport in Porous Media* 109.2, pp. 317–336. ISSN: 0169-3913. DOI: 10.1007/s11242-015-0520-y. URL: http://link.springer.com/10.1007/s11242-015-0520-y.

— (2016a). "Pore-space structure and average dissolution rates: A simulation study". In: *Water Resources Research* 52.9, pp. 7198–7212. ISSN: 00431397. DOI: 10.1002/2016WR019313. URL: http://doi.wiley.com/10.1002/2016WR019313.

Pereira Nunes, J. P., Blunt, M. J., and Bijeljic, B. (2016b). "Pore-scale simulation of carbonate dissolution in micro-CT images". In: *Journal of Geophysical Research: Solid Earth* 121.2, pp. 558–576. ISSN: 21699313. DOI: 10.1002/2015JB012117. URL: http://doi.wiley.com/10.1002/2015JB012117.

Pfannkuch, H. O. (1963). "Contribution a l'étude des déplacements de fluides miscibles dans un milieu poreux". In: *Rev. Inst. Fr. Pet* 18, pp. 1215–1270.

Plummer, L. N., Wigley, T. M. L., and Parkhurst, D. L. (1978). "The kinetics of calcite dissolution in CO 2 -water systems at 5 degrees to 60 degrees C and 0.0 to 1.0 atm CO 2". In: *American Journal of Science* 278.2, pp. 179–216. ISSN: 0002-9599. DOI: 10.2475/ajs.278.2.179. URL: http://www.ajsonline.org/cgi/doi/10.2475/ajs.278.2.179.

Price, D. J. (2012). "Smoothed particle hydrodynamics and magnetohydrodynamics". In: *Journal of Computational Physics* 231.3, pp. 759–794. ISSN: 00219991. DOI: 10.1016/j.jcp.2010.12.011. URL: http://linkinghub.elsevier.com/retrieve/pii/S0021999110006753.

Puyguiraud, A., Perez, L. J., Hidalgo, J. J., and Dentz, M. (2020). "Effective dispersion coefficients for the upscaling of pore-scale mixing and reaction". In: *Advances in Water Resources* 146, p. 103782. ISSN: 03091708. DOI: 10.1016/j.advwatres.2020.103782. URL: https://linkinghub.elsevier.com/retrieve/pii/S0309170820303006.

Quintard, M. and Whitaker, S. (1994). "Transport in ordered and disordered porous media II: Generalized volume averaging". In: *Transport in Porous Media* 14.2, pp. 179–206. ISSN: 01693913. DOI: 10.1007/BF00615200. URL: https://link.springer.com/article/10.1007/BF00615200.

Raeini, A. Q., Bijeljic, B., and Blunt, M. J. (2017). "Generalized network modeling: Network extraction as a coarse-scale discretization of the void space of porous media". In: *Physical Review E* 96.1, p. 013312. ISSN: 2470-0045. DOI: 10.1103/PhysRevE.96.013312. URL: http://link.aps.org/doi/10.1103/PhysRevE.96.013312.

Raeini, A. Q., Bijeljic, B., and Blunt, M. J. (2018). "Generalized network modeling of capillary-dominated two-phase flow". In: *Physical Review E* 97.2, p. 023308. ISSN: 2470-0045. DOI: 10.1103/PhysRevE.97.023308. arXiv: 1707.02788. URL: https://link.aps.org/doi/10.1103/PhysRevE.97.023308.

Rajaram, H. (2016). "Debates-Stochastic subsurface hydrology from theory to practice: Introduction". In: *Water Resources Research* 52.12, pp. 9215–9217. ISSN: 00431397. DOI: 10.1002/2016WR020066. URL: http://doi.wiley.com/10.1002/2016WR020066.

Raje, D. S. and Kapoor, V. (2000). "Experimental study of bimolecular reaction kinetics in porous media". In: *Environmental Science and Technology* 34.7, pp. 1234–1239. ISSN: 0013936X. DOI: 10.1021/es9908669. URL: https://pubs.acs.org/sharingguidelines.

Raoof, A., Nick, H. M., Hassanizadeh, S. M., and Spiers, C. J. (2013). "PoreFlow: A complex pore-network model for simulation of reactive transport in variably saturated porous media". In: *Computers and Geosciences* 61, pp. 160–174. ISSN: 00983004. DOI: 10.1016/j.cageo.2013.08.005. URL: https://www.sciencedirect.com/science/article/pii/S0098300413002264%7B%5C#%7Dbib50.

Rasmussen, A. F., Sandve, T. H., Bao, K., Lauser, A., Hove, J., Skaflestad, B., Klöfkorn, R., Blatt, M., Rustad, A. B., Sævareid, O., Lie, K.-A., and Thune, A. (2019). "The Open Porous Media Flow Reservoir Simulator". In: *Other Computer Science*. arXiv: 1910.06059. URL: http://arxiv.org/abs/1910.06059.

Rathinam, M., Petzold, L. R., Cao, Y., and Gillespie, D. T. (2003). "Stiffness in stochastic chemically reacting systems: The implicit tau-leaping method". In: *Journal of Chemical Physics* 119.24, pp. 12784–12794. ISSN: 00219606. DOI: 10.1063/1.1627296.

Rezende, M. F. and Pope, M. C. (2015). "Importance of depositional texture in pore characterization of subsalt microbialite carbonates, offshore Brazil". In: *Geological Society, London, Special Publications* 418.1, pp. 193–207. DOI: 10.1144/SP418.2. URL: http://sp.lyellcollection.org/cgi/doi/10.1144/SP418.2.

Rhodes, M. E., Bijeljic, B., and Blunt, M. J. (2008). "Pore-to-field simulation of single-phase transport using continuous time random walks". In: *Advances in Water Resources* 31.12, pp. 1527–1539. ISSN: 03091708. DOI: 10.1016/j.advwatres.2008.04.006. URL: https://www.sciencedirect.com/science/article/pii/S0309170808000584.

— (2009). "A Rigorous Pore-to-Field-Scale Simulation Method for Single-Phase Flow Based on Continuous-Time Random Walks". In: *SPE Journal* 14.01, pp. 88–94. ISSN: 1086-055X. DOI: 10.2118/106434-PA. URL: http://www.onepetro.org/doi/10.2118/106434-PA.

Rhodes, M. E. and Blunt, M. J. (2006). "An exact particle tracking algorithm for advective-dispersive transport in networks with complete mixing at nodes". In:

Water Resources Research 42.4. ISSN: 00431397. DOI: 10.1029/2005WR004504. URL: http://doi.wiley.com/10.1029/2005WR004504.

Ribeiro, A. C. F., Barros, M. C. F., Teles, A. S. N., Valente, A. J. M., Lobo, V. M. M., Sobral, A. J. F. N., and Esteso, M. A. (2008). "Diffusion coefficients and electrical conductivities for calcium chloride aqueous solutions at 298.15K and 310.15K". In: *Electrochimica Acta* 54.2, pp. 192–196. ISSN: 00134686. DOI: 10.1016/j.electacta.2008.08.011. URL: https://linkinghub.elsevier.com/retrieve/pii/S0013468608010128.

Ringrose, P. S., Martinius, A. W., and Alvestad, J. (2008). "Multiscale geological reservoir modelling in practice". In: *Geological Society, London, Special Publications* 309.1, pp. 123–134. ISSN: 0305-8719. DOI: 10.1144/SP309.9. URL: http://sp.lyellcollection.org/lookup/doi/10.1144/SP309.9.

Ringrose, P. and Bentley, M. (2015). *Reservoir Model Design*. 1st ed. Springer Netherlands, p. 249. ISBN: 978-94-007-5496-6. DOI: 10.1007/978-94-007-5497-3. URL: https://www.springer.com/gp/book/9789400754966.

Saad, Y. and Schultz, M. H. (1986). "GMRES: A Generalized Minimal Residual Algorithm for Solving Nonsymmetric Linear Systems". In: *SIAM Journal on Scientific and Statistical Computing* 7.3, pp. 856–869. ISSN: 0196-5204. DOI: 10.1137/0907058. URL: http://epubs.siam.org/doi/10.1137/0907058.

Sahimi, M. (2011). *Flow and Transport in Porous Media and Fractured Rock: From Classical Methods to Modern Approaches*. Second Edi. Weinheim, Germany: Wiley-VCH Verlag GmbH & Co. KGaA. ISBN: 9783527404858. DOI: 10.1002/9783527636693. URL: http://doi.wiley.com/10.1002/9783527636693.

Sahimi, M., Ted Davis, H., and Scriven, L. E. (1983). "Dispersion in disordered porous media". In: *Chemical Engineering Communications* 23.4-6, pp. 329–341. ISSN: 15635201. DOI: 10.1080/00986448308940483. URL: https://www.tandfonline.com/doi/full/10.1080/00986448308940483.

Salamon, P., Fernàndez-Garcia, D., and Gómez-Hernández, J. J. (2006). "A review and numerical assessment of the random walk particle tracking method". In: *Journal of Contaminant Hydrology* 87.3-4, pp. 277–305. ISSN: 01697722. DOI: 10.1016/j.jconhyd.2006.05.005. URL: https://linkinghub.elsevier.com/retrieve/pii/S0169772206000957.

Salehikhoo, F. and Li, L. (2015). "The role of magnesite spatial distribution patterns in determining dissolution rates: When do they matter?" In: *Geochimica et Cosmochimica Acta* 155, pp. 107–121. ISSN: 00167037. DOI: 10.1016/j.gca.2015.01.035.

Salles, J., Thovert, J. F., Delannay, R., Prevors, L., Auriault, J. L., and Adler, P. M. (1993). "Taylor dispersion in porous media. Determination of the dispersion tensor". In: *Physics of Fluids A: Fluid Dynamics* 5.10, pp. 2348–2376. ISSN: 0899-8213.

DOI: 10.1063/1.858751. URL: http://aip.scitation.org/doi/10.1063/1.858751.

Sanchez-Vila, X. and Fernàndez-Garcia, D. (2016). "Debates - Stochastic subsurface hydrology from theory to practice: Why stochastic modeling has not yet permeated into practitioners?" In: *Water Resources Research* 52.12, pp. 9246–9258. ISSN: 19447973. DOI: 10.1002/2016WR019302. arXiv: 2014WR016527 [10.1002]. URL: http://doi.wiley.com/10.1002/2016WR019302.

Scanziani, A., Singh, K., Blunt, M. J., and Guadagnini, A. (2017). "Automatic method for estimation of in situ effective contact angle from X-ray micro tomography images of two-phase flow in porous media". In: *Journal of Colloid and Interface Science* 496, pp. 51–59. ISSN: 10957103. DOI: 10.1016/j.jcis.2017.02.005. URL: https://linkinghub.elsevier.com/retrieve/pii/S0021979717301583.

Scheidegger, A. E. (1959). "An evaluation of the accuracy of the diffusivity equation for describing miscible displacement in porous media". In: *Theory of Fluid Flow in Porous Media Conference*, pp. 101–116.

Scher, H. and Lax, M. (1973a). "Stochastic Transport in a Disordered Solid. I. Theory". In: *Physical Review B* 7.10, pp. 4491–4502. ISSN: 0556-2805. DOI: 10.1103/PhysRevB.7.4491. URL: https://link.aps.org/doi/10.1103/PhysRevB.7.4491.

— (1973b). "Stochastic Transport in a Disordered Solid. II. Impurity Conduction". In: *Physical Review B* 7.10, pp. 4502–4519. ISSN: 0556-2805. DOI: 10.1103/PhysRevB.7.4502. URL: https://link.aps.org/doi/10.1103/PhysRevB.7.4502.

Scher, H. and Montroll, E. W. (1975). "Anomalous transit-time dispersion in amorphous solids". In: *Physical Review B* 12.6, pp. 2455–2477. ISSN: 01631829. DOI: 10.1103/PhysRevB.12.2455. URL: https://link.aps.org/doi/10.1103/PhysRevB.12.2455.

Scheven, U. M., Verganelakis, D., Harris, R., Johns, M. L., and Gladden, L. F. (2005a). "Quantitative nuclear magnetic resonance measurements of preasymptotic dispersion in flow through porous media". In: *Physics of Fluids* 17.11, p. 117107. ISSN: 1070-6631. DOI: 10.1063/1.2131871. URL: http://aip.scitation.org/doi/10.1063/1.2131871.

Scheven, U. M., Seland, J. G., and Cory, D. G. (2005b). "NMR-propagator measurements in porous media in the presence of surface relaxation and internal fields". In: *Magnetic Resonance Imaging* 23.2 SPEC. ISS. Pp. 363–365. ISSN: 0730725X. DOI: 10.1016/j.mri.2004.11.054. URL: https://www.sciencedirect.com/science/article/pii/S0730725X05000664.

Schiff, J. L. (1999). *The Laplace transform: theory and applications*. New York, NY: Springer-Verlag New York, Inc., p. 235. ISBN: 0387986987.

Schlumberger (2007a). *Carbonate Reservoirs - Meeting Unique Challenges to Maximize Recovery*. Tech. rep. Schlumberger.

Schlumberger (2007b). *Schlumberger Market Analysis*. Tech. rep. Schlumberger. URL: https://investorcenter.slb.com/static-files/9969f735-4ad4-48fc-85d5-70582c9dad4d.

Schumer, R., Benson, D. A., Meerschaert, M. M., and Baeumer, B. (2003). "Fractal mobile/immobile solute transport". In: *Water Resources Research* 39.10. ISSN: 00431397. DOI: 10.1029/2003WR002141. URL: https://agupubs.onlinelibrary.wiley.com/doi/full/10.1029/2003WR002141.

Seymour, J. D. and Callaghan, P. T. (1997). "Generalized Approach to NMR Analysis of Flow and Dispersion in Porous Media". In: *AIChE Journal* 43.8, pp. 2096–2111. ISSN: 00011541. DOI: 10.1002/aic.690430817. URL: http://doi.wiley.com/10.1002/aic.690430817.

Seymour, J. D., Gage, J. P., Codd, S. L., and Gerlach, R. (2004). "Anomalous Fluid Transport in Porous Media Induced by Biofilm Growth". In: *Physical Review Letters* 93.19, p. 198103. ISSN: 0031-9007. DOI: 10.1103/PhysRevLett.93.198103. URL: https://journals.aps.org/prl/abstract/10.1103/PhysRevLett.93.198103.

Shlesinger, M. F. (1974). "Asymptotic solutions of continuous-time random walks". In: *Journal of Statistical Physics* 10.5, pp. 421–434. ISSN: 00224715. DOI: 10.1007/BF01008803. URL: https://link.springer.com/article/10.1007/BF01008803.

— (2003). "Random Processes". In: *digital Encyclopedia of Applied Physics*. DOI: 10.1002/3527600434.eap382. URL: http://doi.wiley.com/10.1002/3527600434.eap382.

Sidle, R. C., Nilsson, B., Hansen, M., and Fredericia, J. (1998). "Spatially varying hydraulic and solute transport characteristics of a fractured till determined by field tracer tests, Funen, Denmark". In: *Water Resources Research* 34.10, pp. 2515–2527. ISSN: 00431397. DOI: 10.1029/98WR01735. URL: http://doi.wiley.com/10.1029/98WR01735.

Silliman, S. E., Konikow, L. F., and Voss, C. I. (1987). "Laboratory investigation of longitudinal dispersion in anisotropic porous media". In: *Water Resources Research* 23.11, pp. 2145–2151. ISSN: 19447973. DOI: 10.1029/WR023i011p02145. URL: http://doi.wiley.com/10.1029/WR023i011p02145.

Silliman, S. E. and Simpson, E. S. (1987). "Laboratory evidence of the scale effect in dispersion of solutes in porous media". In: *Water Resources Research* 23.8, pp. 1667–1673. ISSN: 19447973. DOI: 10.1029/WR023i008p01667. URL: https://agupubs.onlinelibrary.wiley.com/doi/full/10.1029/WR023i008p01667.

Singh, K., Anabaraonye, B. U., Blunt, M. J., and Crawshaw, J. (2018). "Partial dissolution of carbonate rock grains during reactive CO2-saturated brine injection under reservoir conditions". In: *Advances in Water Resources* 122, pp. 27–36. ISSN: 03091708. DOI: 10.1016/j.advwatres.2018.09.005. URL: https://www.sciencedirect.com/science/article/pii/S0309170818305311.

Smirnov, N. V. (1939). "Estimate of deviation between empirical distribution functions in two independent samples". In: *Bull. Moscow Univ.* 2, pp. 3–16.

Smith, M. M., Sholokhova, Y., Hao, Y., and Carroll, S. A. (2013). "CO2-induced dissolution of low permeability carbonates. Part I: Characterization and experiments". In: *Advances in Water Resources* 62, pp. 370–387. ISSN: 03091708. DOI: 10.1016/j.advwatres.2013.09.008.

Sochi, T. (2010). "Non-Newtonian flow in porous media". In: *Polymer* 51.22, pp. 5007–5023. ISSN: 0032-3861. DOI: 10.1016/J.POLYMER.2010.07.047. URL: https://www.sciencedirect.com/science/article/pii/S0032386110006750.

Steefel, C. I., Appelo, C. A., Arora, B., Jacques, D., Kalbacher, T., Kolditz, O., Lagneau, V., Lichtner, P. C., Mayer, K. U., Meeussen, J. C., Molins, S., Moulton, D., Shao, H., imnek, J., Spycher, N., Yabusaki, S. B., and Yeh, G. T. (2015). "Reactive transport codes for subsurface environmental simulation". In: *Computational Geosciences* 19.3, pp. 445–478. ISSN: 15731499. DOI: 10.1007/s10596-014-9443-x. URL: https://link.springer.com/article/10.1007/s10596-014-9443-x.

Steefel, C. I. and MacQuarrie, K. T. (1996). "Approaches to modeling of reactive transport in porous media". In: *Reactive Transport in Porous Media*. Ed. by P. C. Lichtner, C. I. Steefel, and E. H. Oelkers. Vol. 34. Washington, DC, United States: Mineralogical Society of America. Chap. 2, pp. 83–129. ISBN: 9781501509797. DOI: 10.1515/9781501509797-005. URL: https://www.degruyter.com/document/doi/10.1515/9781501509797-005/html.

Steefel, C. I. and Maher, K. (2009). "Fluid-rock interaction: A reactive transport approach". In: *Reviews in mineralogy and geochemistry* 70.1, pp. 485–532. ISSN: 1529-6466. DOI: 10.2138/rmg.2009.70.11. URL: http://rimg.geoscienceworld.org/content/70/1/485.

Stehfest, H. (1970). "Algorithm 368: Numerical inversion of Laplace transforms [D5]". In: *Communications of the ACM* 13.1, pp. 47–49. ISSN: 00010782. DOI: 10.1145/361953.361969. arXiv: 9807051 [physics]. URL: http://portal.acm.org/citation.cfm?doid=361953.361969.

Stöhr, M. (2003). "Analysis of Flow and Transport in Refractive Index Matched Porous Media[1] M. Stöhr, Analysis of Flow and Transport in Refractive Index Matched Porous Media, Heidelberg University, 2003." Dissertation. Heidelberg University, p. 197. DOI: 10.11588/heidok.00003733. URL: http://www.ub.uni-heidelberg.de/archiv/3733.

Swoboda-Colberg, N. G. and Drever, J. I. (1993). "Mineral dissolution rates in plot-scale field and laboratory experiments". In: *Chemical Geology* 105.1-3, pp. 51–69. ISSN: 00092541. DOI: 10.1016/0009-2541(93)90118-3. URL: https://www.sciencedirect.com/science/article/pii/0009254193901183.

Szymczak, P. and Ladd, A. J. (2012). "Reactive-infiltration instabilities in rocks. Fracture dissolution". In: *Journal of Fluid Mechanics* 702, pp. 239–264. ISSN: 00221120. DOI: 10.1017/jfm.2012.174. arXiv: 1204.0917. URL: https://doi.org/10.1017/jfm.2012.174.

Tanger, J. C. and Helgeson, H. C. (1988). "Calculation of the thermodynamic and transport properties of aqueous species at high pressures and temperatures; revised equations of state for the standard partial molal properties of ions and electrolytes". In: *American Journal of Science* 288.1, pp. 19–98. ISSN: 0002-9599. DOI: 10.2475/ajs.288.1.19. URL: http://www.ajsonline.org/cgi/doi/10.2475/ajs.288.1.19.

Tansey, J. and Balhoff, M. T. (2016). "Pore Network Modeling of Reactive Transport and Dissolution in Porous Media". In: *Transport in Porous Media* 113.2, pp. 303–327. ISSN: 0169-3913. DOI: 10.1007/s11242-016-0695-x. URL: http://link.springer.com/10.1007/s11242-016-0695-x.

Tartakovsky, A. M., Trask, N., Pan, K., Jones, B., Pan, W., and Williams, J. R. (2015). "Smoothed particle hydrodynamics and its applications for multiphase flow and reactive transport in porous media". In: *Computational Geosciences*. ISSN: 1420-0597. DOI: 10.1007/s10596-015-9468-9. URL: http://link.springer.com/10.1007/s10596-015-9468-9.

Terra, G. J. S., Spadini, A. R., França, A. B., Sombra, C. L., Zambonato, E. E., Juschaks, L. C. d. S., Arienti, L. M., Erthal, M. M., Blauth, M., Franco, M. P., Matsuda, N. S., Silva, N. G. C. da, Moretti, P., D'Avila, R. S. F., Souza, R. S. de, Tonietto, S., Anjos, S. M. C. dos, Campinho, V. S., and Winter, W. R. (2010). "Classificação de rochas carbonáticas aplicável às bacias sedimentares brasileiras". In: *Boletim de Geociencias - Petrobras* 18.1, pp. 9–29.

Tiedje, T. (1984). "Chapter 6 Information about Band-Tail States from Time-of-Flight Experiments". In: *Semiconductors and Semimetals*. Vol. 21. PC. Elsevier, pp. 207–238. ISBN: 0127521496. DOI: 10.1016/S0080-8784(08)63070-7. URL: https://www.sciencedirect.com/science/article/pii/S0080878408630707.

Timur, A. (1969). "Pulsed Nuclear Magnetic Resonance Studies of Porosity, Movable Fluid, and Permeability of Sandstones". In: *J Petroleum Technology* 21.6, pp. 775–786. ISSN: 0149-2136. DOI: 10.2118/2045-pa.

Tosca, N. J. and Wright, V. P. (2015). "Diagenetic pathways linked to labile Mg-clays in lacustrine carbonate reservoirs: a model for the origin of secondary porosity in the Cretaceous pre-salt Barra Velha Formation, offshore Brazil". In: *Geological Society, London, Special Publications* 435, SP435.1. DOI: 10.1144/SP435.1. URL: http://sp.lyellcollection.org/cgi/doi/10.1144/SP435.1.

Vafai, K., ed. (2015). *Handbook of Porous Media*. 3rd Editio. CRC Press, p. 959. ISBN: 9780429184345. DOI: 10.1201/b18614. URL: https://www.taylorfrancis.com/books/9781439885574.

Valvatne, P. H. and Blunt, M. J. (2004). "Predictive pore-scale modeling of two-phase flow in mixed wet media". In: *Water Resources Research* 40.7. ISSN: 00431397. DOI: 10.1029/2003WR002627. URL: http://doi.wiley.com/10.1029/2003WR002627.

Warren, J. E. and Root, P. J. (1963). "The Behavior of Naturally Fractured Reservoirs". In: *Society of Petroleum Engineers Journal* 3.03, pp. 245–255. ISSN: 0197-7520. DOI: 10.2118/426-pa.

Weishaupt, K., Joekar-Niasar, V., and Helmig, R. (2019). "An efficient coupling of free flow and porous media flow using the pore-network modeling approach". In: *Journal of Computational Physics: X* 1, p. 100011. ISSN: 25900552. DOI: 10.1016/j.jcpx.2019.100011.

Whitaker, S. (1999). *The Method of Volume Averaging*. 1st ed. Vol. 13. Theory and Applications of Transport in Porous Media. Dordrecht: Springer Netherlands, p. 210. ISBN: 978-90-481-5142-4. DOI: 10.1007/978-94-017-3389-2. URL: http://link.springer.com/10.1007/978-94-017-3389-2.

White, A. F. and Brantley, S. L. (2003). "The effect of time on the weathering of silicate minerals: Why do weathering rates differ in the laboratory and field?" In: *Chemical Geology* 202.3-4, pp. 479–506. ISSN: 00092541. DOI: 10.1016/j.chemgeo.2003.03.001.

Wildenschild, D. and Sheppard, A. P. (2013). "X-ray imaging and analysis techniques for quantifying pore-scale structure and processes in subsurface porous medium systems". In: *Advances in Water Resources* 51, pp. 217–246. ISSN: 03091708. DOI: 10.1016/j.advwatres.2012.07.018. URL: https://www.sciencedirect.com/science/article/pii/S0309170812002060.

Williams, B. B., Gidley, J. L., Guin, J. A., Schechter, R. S., Gidley, J. L., Guin, J. A., Schechter, R. S., and Williams, B. B. (1970). "Characterization of Liquid-Solid Reactions: Hydrochloric Acid-Calcium Carbonate Reaction". In: *Industrial and Engineering Chemistry Fundamentals* 9.4, pp. 589–596. ISSN: 01964313. DOI: 10.1021/i160036a011. URL: http://pubs.acs.org/doi/abs/10.1021/i160036a011.

Willingham, T. W., Werth, C. J., and Valocchi, A. J. (2008). "Evaluation of the effects of porous media structure on mixing-controlled reactions using pore-scale modeling and micromodel experiments". In: *Environmental Science and Technology* 42.9, pp. 3185–3193. ISSN: 0013936X. DOI: 10.1021/es7022835. URL: http://pubs.acs.org/doi/abs/10.1021/es7022835.

Wilson, M., Monea, M., Whittaker, S., White, D., Law, D., and Chalaturnyk, R. (2004). *IEA GHG Weyburn CO 2 Monitoring & Storage Project*. Tech. rep. Vancouver, Canada: International Energy Agency Greenhouse Gas. URL: https://www.osti.gov/etdeweb/biblio/20564154.

Wright, V. P. and Barnett, A. J. (2015). "An abiotic model for the development of textures in some South Atlantic early Cretaceous lacustrine carbonates". In: *Geological*

Society, London, Special Publications 418.1, pp. 209–219. DOI: 10.1144/SP418.3. URL: http://sp.lyellcollection.org/cgi/doi/10.1144/SP418.3.

Zhao, W. and Ioannidis, M. A. (2007). "Effect of NAPL film stability on the dissolution of residual wetting NAPL in porous media: A pore-scale modeling study". In: *Advances in Water Resources* 30.2, pp. 171–181. ISSN: 03091708. DOI: 10.1016/j.advwatres.2005.03.025. URL: https://linkinghub.elsevier.com/retrieve/pii/S0309170806000170.

APPENDIX A

CTRW Solutions Using Numerical Laplace Inversion

We demonstrate the analytical solutions for the first and second spatial moments, or the mean velocity and dispersion coefficient, of the used Continuous Time Random Walk (CTRW) model present in Dentz et al. (2004) and used in section 3.2 to estimate the particle number effect and the asymptotic behaviour of the spatial moments of the plume formed by the particles. Additionally, we show the comparison between the Laplace Transform Inversion method developed by Hoog et al. (1982), adopted in the thesis, and the method developed by Stehfest (1970), used in Cortis and Berkowitz (2004).

A.1 Centre of Mass Velocity and Dispersion Coefficients

The centre of mass velocity and the dispersion coefficients are derived from the first, $m_i^1(t)$, and second $m_{ij}^2(t)$, spatial moments of $P(\mathbf{x}, t)$.

Using the definition of memory function as

$$\tilde{M}(u) \equiv \frac{ut_1\tilde{\psi}(u)}{\left(1-\psi\tilde{(u)}\right)}, \tag{A.1}$$

with the Laplace transform of $\psi(t)$ defined as

$$\tilde{\psi}(u) = (1+\tau_2 u t_1)^{\beta} \exp t_1 u \Gamma\left(-\beta, \tau_2^{-1} + t_1 u\right) / \Gamma\left(-\beta, \tau_2^{-1}\right), \tag{A.2}$$

we can obtain the Laplace Transform of the first and second spatial moments

$$\mathscr{L}\left\{m_i^{(1)}(t)\right\} = \delta_{i1} v u^{-2} \tilde{M}(u), \tag{A.3a}$$

$$\mathscr{L}\left\{m_{ii}^{(2)}(t)\right\} = 2D_{ii} u^{-2} \tilde{M}(u) + \delta_{i1} 2v^2 u^{-3} \left(\tilde{M}(u)\right)^2 \tag{A.3b}$$

At late times, when $t \to \infty$, transport behaves as Fickian and the solute is characterized by constant centre of mass velocity and dispersion coefficients,

$$v_i^m = \delta_{i1} \frac{t_1}{\bar{t}} \tag{A.4a}$$

$$D_{ii}^m = \frac{t_1}{\bar{t}} + \delta_{i1} \frac{\bar{s_i}^2}{\bar{s_i^2}} \frac{\left(\bar{t^2} - 2\bar{t}^2\right)}{\bar{t}^3} m. \tag{A.4b}$$

A.2 Resident Concentration

Using the equation and simplification from Cortis and Berkowitz (2004),

$$\tilde{c}(u,x) = \frac{1}{u} \frac{2z \exp\left(\frac{1}{2\alpha_\psi} + \frac{z}{2}\right)}{z\left(e^z+1\right) + \alpha_\psi^{-1}\left(e^z-1\right) + \frac{2u}{\tilde{M} v_\psi}\left(e^z-1\right)} \tag{A.5}$$

where

$$z = \frac{1}{\alpha_\psi} \sqrt{1 + \frac{4u\alpha_\psi}{\tilde{M} v_\psi}}. \tag{A.6}$$

and using the approximation for large Péclet number (Pe),

$$\tilde{c}(u,x) = \frac{1}{u} \exp\left(\frac{1}{2\alpha_\psi} - \frac{z}{2}\right) \tag{A.7}$$

A.3 Numerical Laplace Transform Inversion

The Laplace Transform of a function $f(t)$ is defined as

$$\mathscr{L}\{f(t)\} = F(s) = \int_0^\infty f(t) e^{-st} \mathrm{d}t, \tag{A.8}$$

and the Laplace Transform Inversion of $F(s)$ is similarly defined as

$$\mathscr{L}^{-1}\{F(s)\} = f(t) = \int_{\gamma-i\infty}^{\gamma+i\infty} \frac{F(s)}{2\pi i} e^{st} \mathrm{d}s. \tag{A.9}$$

Appendix A. CTRW Solutions Using Numerical Laplace Inversion

The Laplace Transform or the inverse of some functions are straightforward to calculate and are generally tabulated Schiff (1999). However not all functions in the Laplace domain can be inverted back to the time domain analytically, requiring the use of numerical techniques.

The numerical Laplace Transform Inversion $\mathscr{L}^{-1}$ of a function $F(s)$ was approximated by Gaver (1966) and Stehfest (1970) using the following relation

$$f(t) \approx \frac{\ln 2}{t} \sum_{i=1}^{n} V_i F\left(i \frac{\ln 2}{t}\right), \tag{A.10}$$

where V_i is given by

$$V_i = (-1)^{i+\frac{n}{2}} \sum_{k=\frac{i+1}{2}}^{\min\left(i,\frac{n}{2}\right)} \frac{k^{\frac{n}{2}+1}(2k)!}{\left(\frac{n}{2}-k\right)!k!(k-1)!(i-k)!(2k-i)!}. \tag{A.11}$$

The values for V_i obtained by equation (A.11) and are generally calculated *a priori* and tabulated for convenience and to increase algorithms run-time efficiency. The first 18 values of V_i are displayed in table A.1 with 8 digits precision.

Table A.1: First 18 coefficients shown with 12 digits precision. The columns runs faster than the rows, such that the elements in the table read as $a_i = a_{\text{row,col}}$, *e.g.* the first and second elements are $a_1 = a_{1,1} = 4.9 \times 10^{-5}$ and $a_2 = a_{1,2} = -6.0 \times 10^{-1}$.

	a_{i0}	a_{i1}	a_{i2}
a_{0j}	$4.960\,317\,460\,317 \times 10^{-5}$	$-6.095\,734\,126\,984 \times 10^{-1}$	$2.745\,940\,476\,190 \times 10^{2}$
a_{1j}	$-2.630\,695\,674\,603 \times 10^{4}$	$9.572\,572\,013\,889 \times 10^{5}$	$-1.735\,869\,484\,583 \times 10^{7}$
a_{2j}	$1.824\,212\,226\,472 \times 10^{8}$	$-1.218\,533\,288\,309 \times 10^{9}$	$5.491\,680\,025\,283 \times 10^{9}$
a_{3j}	$-1.736\,213\,111\,521 \times 10^{10}$	$3.945\,509\,690\,353 \times 10^{10}$	$-6.526\,651\,698\,518 \times 10^{10}$
a_{4j}	$7.873\,006\,832\,822 \times 10^{10}$	$-6.855\,644\,419\,612 \times 10^{10}$	$4.198\,434\,347\,505 \times 10^{10}$
a_{5j}	$-1.716\,093\,471\,184 \times 10^{10}$	$4.204\,550\,039\,103 \times 10^{9}$	$-4.671\,722\,265\,670 \times 10^{8}$

The common intuition concludes that the accuracy of equation (A.10) increases with $n \to \infty$, however Stehfest (1970) notes that round-off errors worsen with n and suggests that an optimal value of $n = 18$ suffices for double precision arithmetic.

To illustrate the behaviour of both numerical Laplace Transform Inversion algorithms, figure A.1 shows the evolution of the error. The error of both methods evolve similarly, but Hoog et al. (1982) shows smaller error, or higher numerical precision.

Table A.2: Comparison between the numerical Laplace Transform Inversion using the algorithms developed by Stehfest (1970) and Hoog et al. (1982) for $f(t) = e^t$ and $1 \geq t \leq 10$, ϵ represents the error between the analytical function and the numerical Laplace Transform Inversion algorithms.

		Gaver (1966) and Stehfest (1970)		Hoog et al. (1982)	
t	$f(t)$	$\mathscr{L}^{-1}\{F(s)\}$	ϵ	$\mathscr{L}^{-1}\{F(s)\}$	ϵ
1.0	3.68×10^{-1}	3.68×10^{-1}	2.09×10^{-6}	3.68×10^{-1}	1.73×10^{-12}
2.0	1.35×10^{-1}	1.35×10^{-1}	1.07×10^{-6}	1.35×10^{-2}	7.69×10^{-12}
3.0	4.98×10^{-2}	4.98×10^{-2}	2.78×10^{-6}	4.98×10^{-2}	4.99×10^{-12}
4.0	1.83×10^{-2}	1.83×10^{-2}	1.09×10^{-4}	1.83×10^{-2}	3.04×10^{-11}
5.0	6.74×10^{-3}	6.73×10^{-3}	4.53×10^{-4}	6.74×10^{-3}	1.72×10^{-9}
6.0	2.48×10^{-3}	2.48×10^{-3}	2.94×10^{-4}	2.48×10^{-3}	2.51×10^{-10}
7.0	9.12×10^{-4}	9.15×10^{-4}	3.69×10^{-3}	9.12×10^{-4}	5.05×10^{-11}
8.0	3.35×10^{-4}	3.40×10^{-4}	1.43×10^{-2}	3.35×10^{-4}	1.44×10^{-9}
9.0	1.23×10^{-4}	1.29×10^{-4}	4.51×10^{-2}	1.23×10^{-4}	6.17×10^{-9}
10.0	4.54×10^{-5}	5.05×10^{-5}	1.12×10^{-1}	4.54×10^{-5}	4.43×10^{-8}

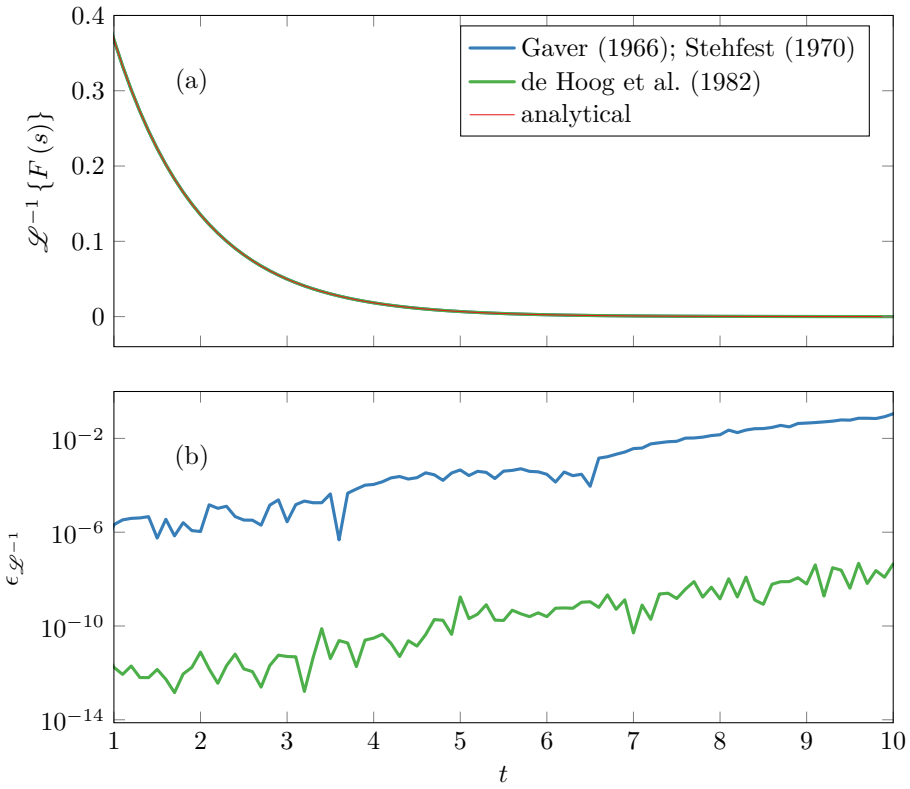


Figure A.1: Comparison between (a) the numerical Laplace Transform Inversion algorithms of Gaver (1966) and Stehfest (1970) and Hoog et al. (1982) and the analytical solution of the function $f(t) = e^t$ (b) and the error between the analytical solution and the numerical methods.

APPENDIX B

Procedure to Generate Heterogeneous Domains

The 3D samples Het. 1, 2 and 3 used in chapters 5 and 6 are constructed using a simple procedure detailed below, and illustrated using a 2D representation of the image and lattice in figure B.1.

1. Create a 3D image with $N_x = 150$ and $N_y = N_z = 50$ grid cells.
   (a) Create a normally distributed porosity field with mean $\langle \phi_{bg} \rangle = 0.3$ and standard deviation $\sigma_{\phi bg} = 0.1$.
   (b) Uniformly distribute solid spheres with centres (x_c, y_c, z_c) and with normally distributed radius with mean $\langle r_3 \rangle = 1.5 \times 10^{-3}$ m, $\langle r_2 \rangle = 3.0 \times 10^{-3}$ m and $\langle r_3 \rangle = 4.5 \times 10^{-3}$ m and standard deviation $\sigma_{r1} = \sigma_{r2} = \sigma_{r3} = 0.2$.
   (c) For all solid spheres, anywhere $(x - x_c)^2 + (y - y_c)^2 + (z - z_c)^2 < r^2$, the porosity in the grid cell of the image becomes $\phi = 0$.
2. Create a regular lattice nodes coincident with the 3D grid cell centres.
   (a) Populate the porosity of the nodes with the porosity from the 3D image.

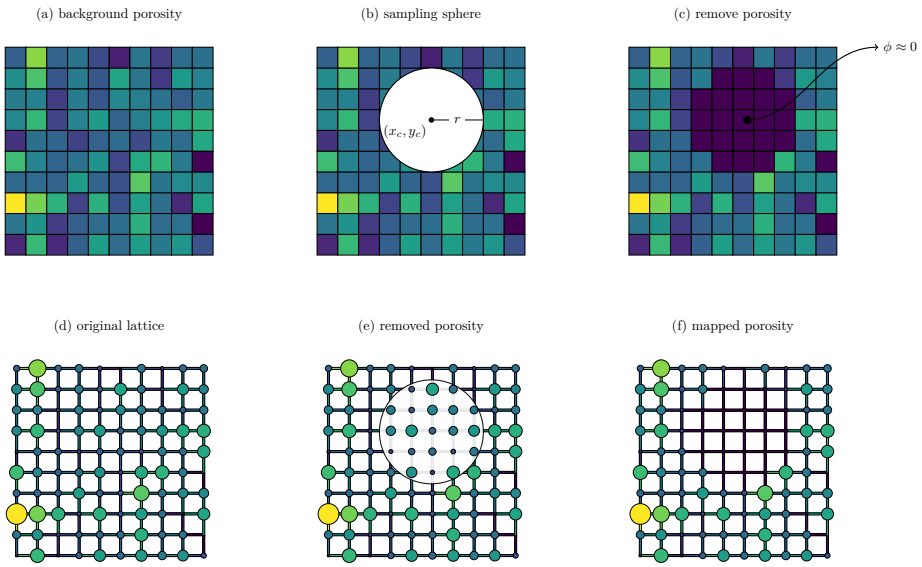


Figure B.1: Illustration of the procedure to create the samples Het. 1, 2 and 3. We start with (a) a 3D image with background porosity, (b) sample the radius and centres of several solid spheres, (c) use it to remove porosity from the background porosity image, (d) the original lattice with nodes centres coincident with the 3D image cell centres, (e) the highlighted nodes that will be modified, and finally (d) the lattice with the porosity of the nodes mapped from the 3D image with the removed porosity.

APPENDIX C

Evolution of the Dissolution Patterns

We showed the porosity dissolution of Het. 1, 2 and 3 at fixed normalized times $t/t_1 = 1$ for $Pe = 20$ and $t/t_1 = 10$ for $Pe = 200$ and 2000 in figure 5.10. In this appendix we show the detailed porosity dissolution evolution of Het. 1, 2 and 3 with a constant $\beta = 1.8$ in figures C.1 to C.3 and the comparison for Het. 2 with $\beta = 1.2$ and Het. 3 with $\beta = 0.6$ in figures C.4 to C.6. We selected the porosity dissolution snapshots at $t/t_1 = [1, 2, \ldots, 10]$ for all figures.

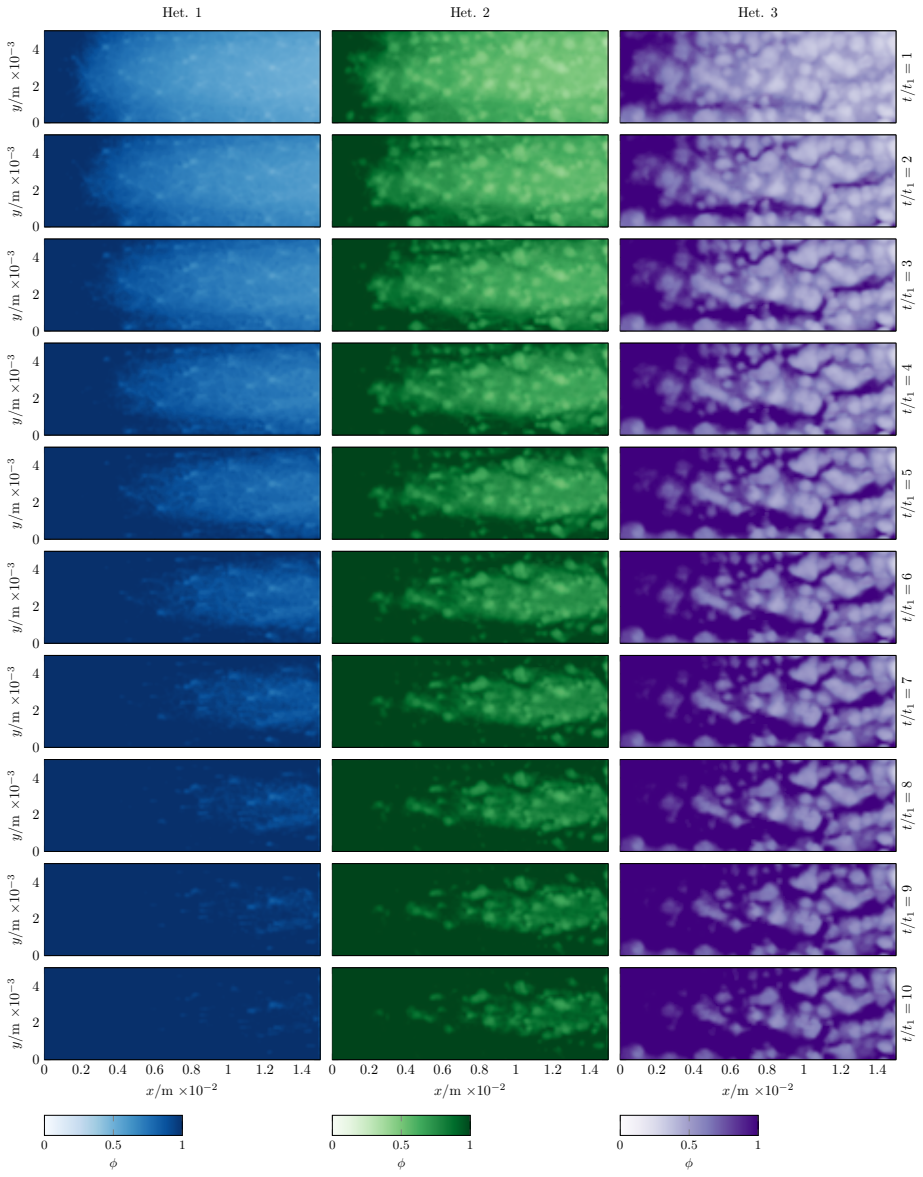


Figure C.1: Porosity dissolution of Het. 1, 2 and 3 with $\beta = 1.8$ at $t/t_1 = 1$ to 10 and Péclet number $Pe = 20$.

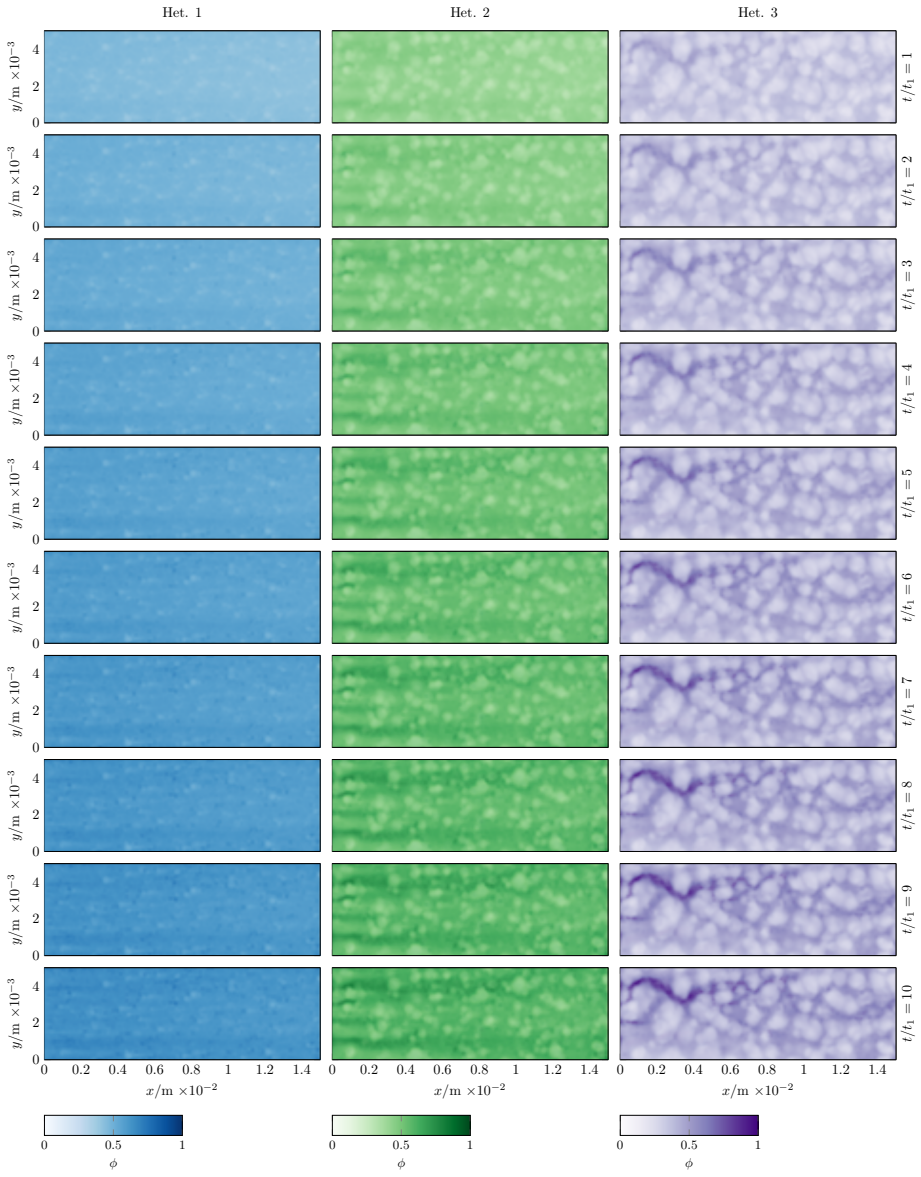


Figure C.2: Porosity dissolution of Het. 1, 2 and 3 with $\beta = 1.8$ at $t/t_1 = 1$ to 10 and Péclet number $Pe = 200$.

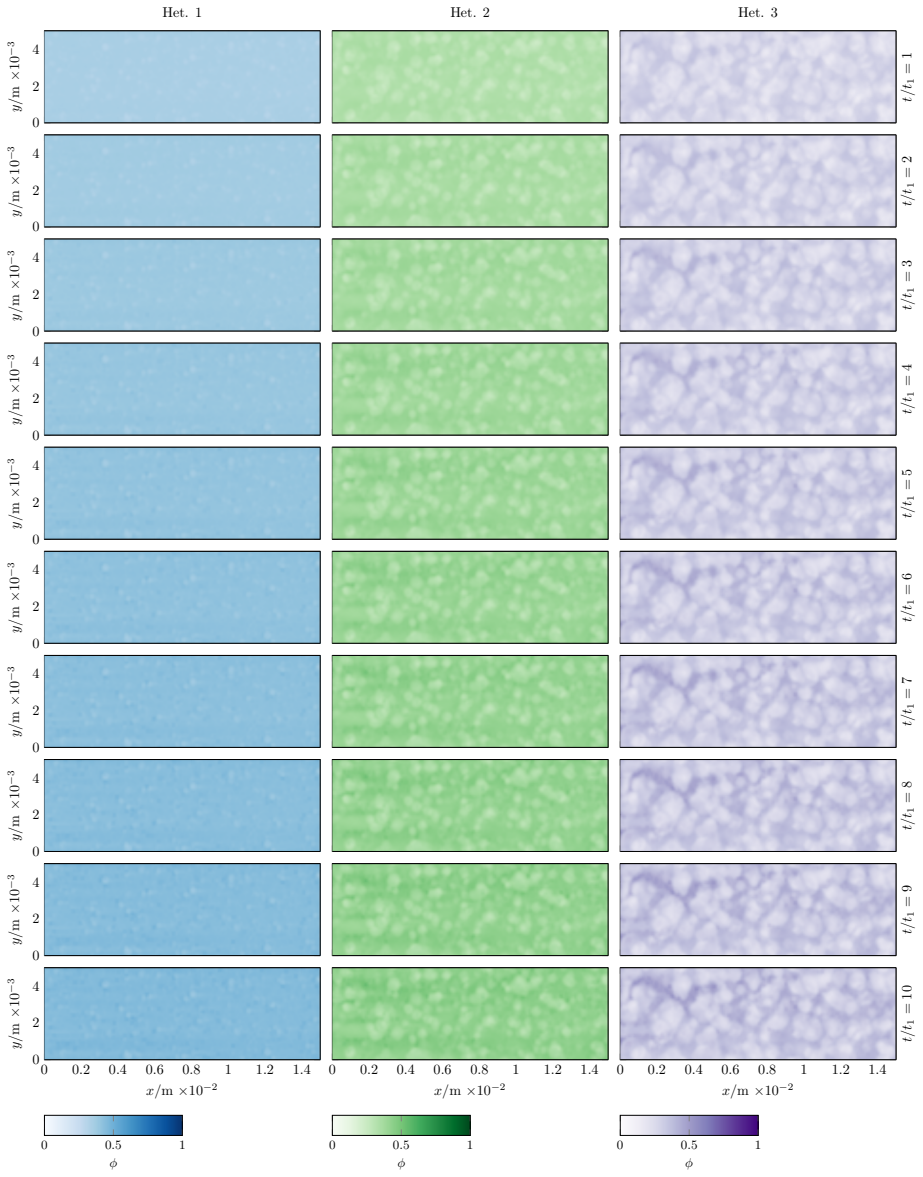


Figure C.3: Porosity dissolution of Het. 1, 2 and 3 with $\beta = 1.8$ at $t/t_1 = 1$ to 10 and Péclet number $Pe = 2000$.

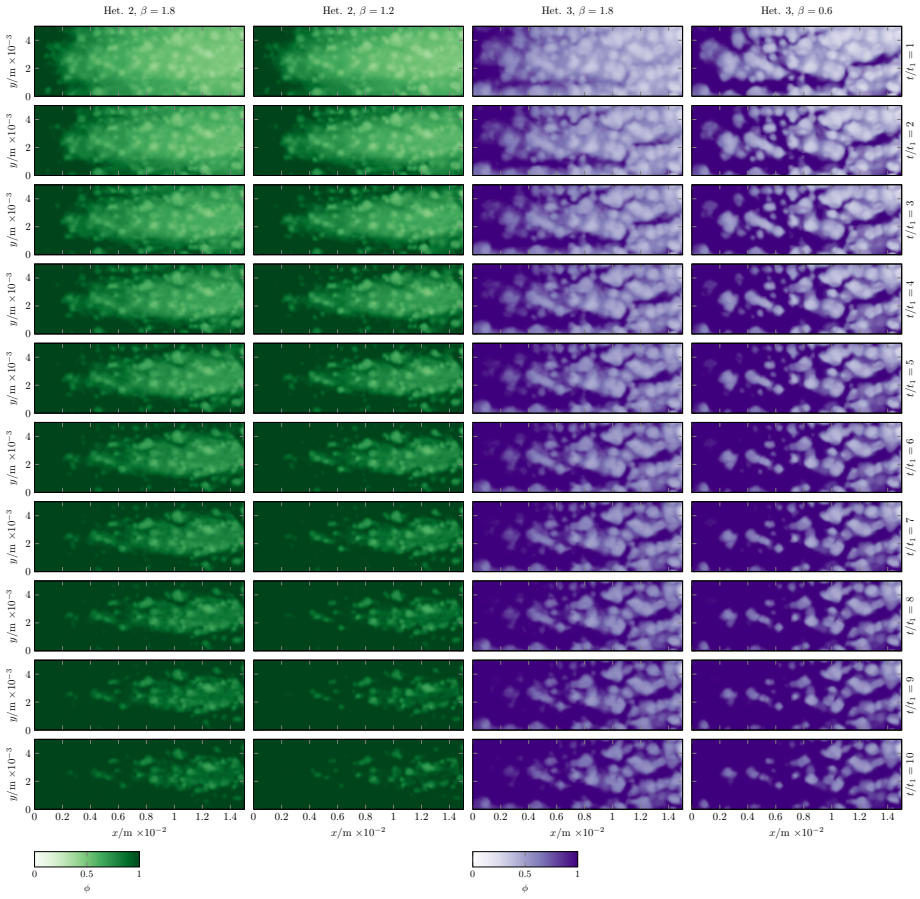


Figure C.4: Comparison of the porosity dissolution of Het. 2 with $\beta = 1.8$ and 1.2 and Het. 3 with $\beta = 1.8$ and 0.6 at $t/t_1 = 1$ to 10 and Péclet number $Pe = 20$. We omit the results of Het. 1 because there are no differences in the transport parameter β.

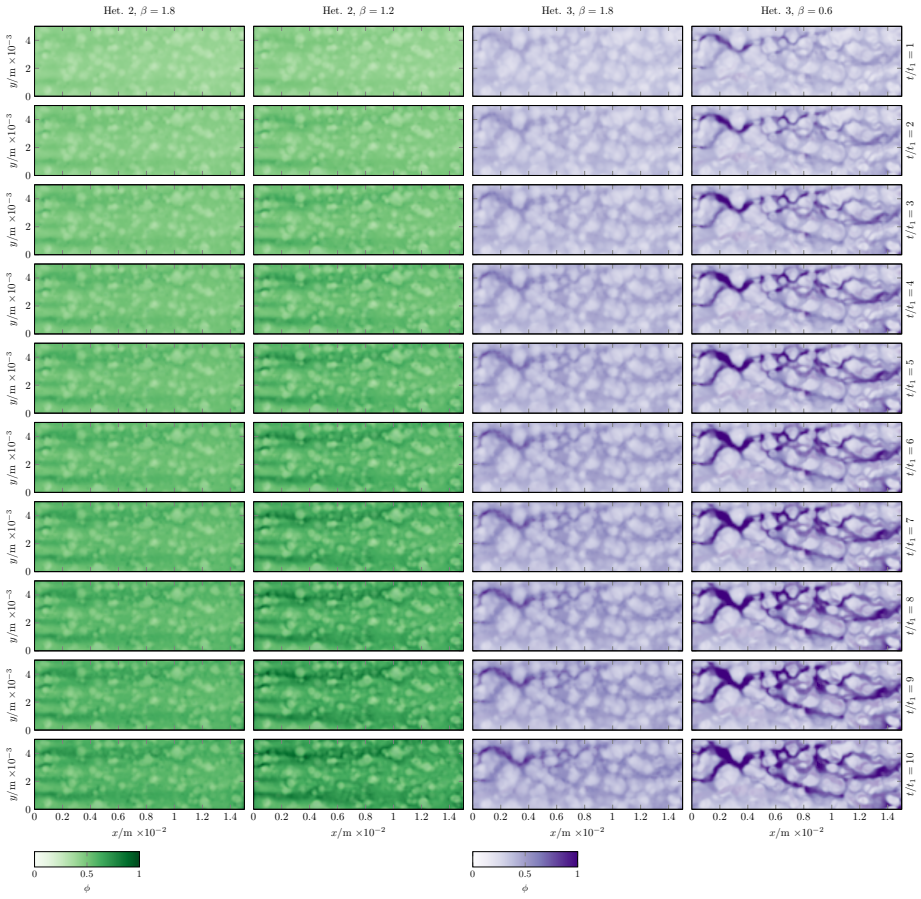


Figure C.5: Comparison of the porosity dissolution of Het. 2 with $\beta = 1.8$ and 1.2 and Het. 3 with $\beta = 1.8$ and 0.6 at $t/t_1 = 1$ to 10 and Péclet number $Pe = 200$. We omit the results of Het. 1 because there are no differences in the transport parameter β.

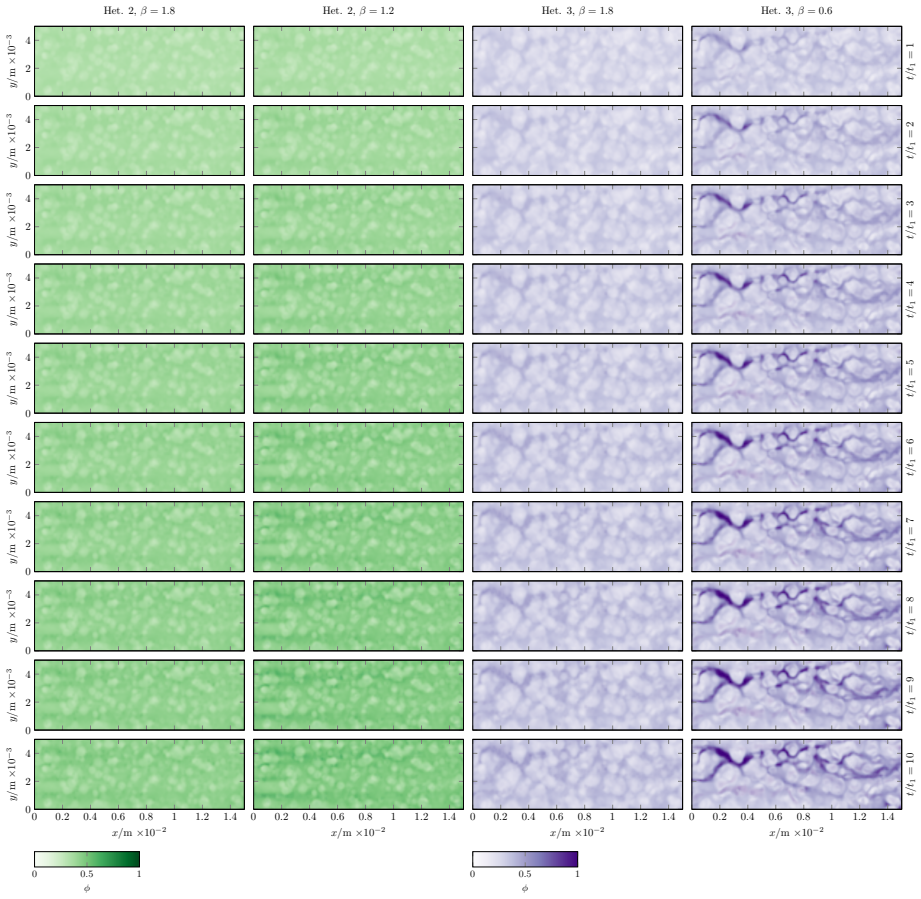


Figure C.6: Comparison of the porosity dissolution of Het. 2 with $\beta = 1.8$ and 1.2 and Het. 3 with $\beta = 1.8$ and 0.6 at $t/t_1 = 1$ to 10 and Péclet number $Pe = 2000$. We omit the results of Het. 1 because there are no differences in the transport parameter β.

APPENDIX D

Procedure to Calculate Histograms of Proximities

To construct the histogram of the proximity distances to fast flow channels and slow regions in figure 6.13 we use the procedure illustrated in figure D.1:

1. Create the PDF and CDF of the normalized velocity distribution $v_x/\langle v_x \rangle$.
2. Find the value velocity cut-off at which the CDF ≥ 0.75.
   (a) Use the velocity cut-off to separate the links in fast or slow.
   (b) Identify the closest nodes to the center-line of the fast flow channels.
   (c) Identify the closest nodes to the boundary of the fast flow channels region.

Next, we identify the links accordingly to their mineral content, such that we can separate the links in further classes:

1. Interpolate the mineral molar concentrations to the links.
2. Find the links where $c_{\text{calcite}} > 0.5$.
3. Use the calcite concentration cut-off to separate the calcite rich links from the dolomite rich links.

Finally, we calculate the Euclidean distance functions for both calcite and dolomite rich links belonging to each region differently:

1. For the links in the fast flow channels:

(a) Calculate the Euclidean distance from the links to the closest nodes in the center-line of the fast flow channel.

2. For the links outside the fast flow channels:

(a) Calculate the Euclidean distance from the links to the closest boundary of the fast flow channels.

With these two index mappings, we separate the links in either belonging to fast channels or slow regions and in either calcite or dolomite rich, and construct the histogram of proximity to fast flow channels displayed in figure 6.13.

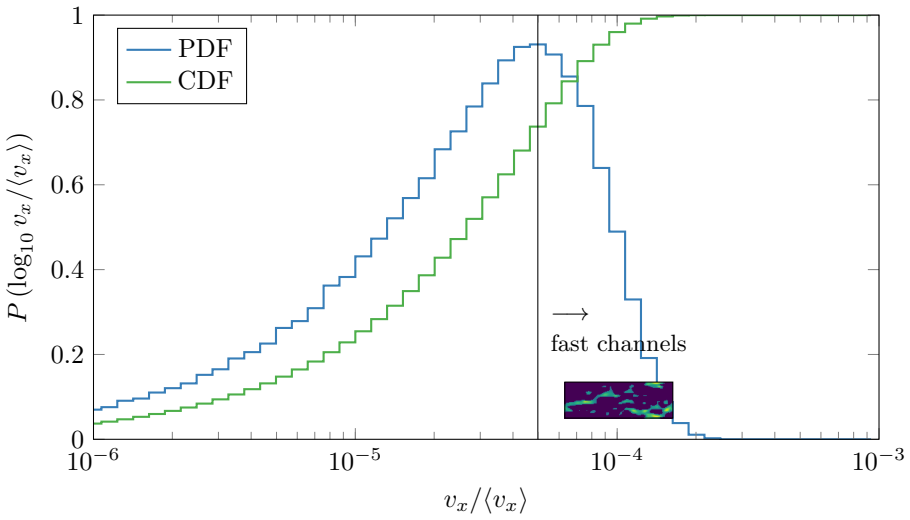


Figure D.1: Probability density function and cumulative distribution function of the velocity. The vertical line shows the cut-off at 0.75 of the CDF, and all velocities above this value are selected to locate the fast flow channels.

APPENDIX E

Permissions for Reuse of Copyrighted Materials

Table E.1: List of the used references, the published media and the copyright holders.

name	reference	media	copyright holder
figure 1.1	Schlumberger (2007a)	Schlumberger 07-OS-003	Copyright © 2007 Schlumberger
figure 1.4a	Levy and Berkowitz (2003)	Journal of Contaminant Hydrology	Copyright © 2003 Elsevier B.V.
figure 1.4b	Adams and Gelhar (1992)	Water Resources Research	Copyright © 1992 American Geophysical Union
figure 2.3	Bijeljic et al. (2004)	Water Resources Research	Copyright © 2004 American Geophysical Union
figure 2.4	Fredd and Fogler (1998)	American Institute of Chemical Engineers Journal	Copyright © 1998 American Institute of Chemical Engineers
figure 2.5	Fredd and Fogler (1998)	American Institute of Chemical Engineers Journal	Copyright © 1998 American Institute of Chemical Engineers
figure 2.6	Golfier et al. (2002)	Journal of Fluid Mechanics	Copyright © 2002 Cambridge University Press
figure 2.7	Scheven et al. (2005a)	Physics of Fluids	Copyright © 2005 American Institute of Physics
figure 2.8	Bijeljic et al. (2013a)	Water Resources Research	Copyright © 2013 American Geophysical Union
figure 2.9	Al-Khulaifi et al. (2019)	Water Resources Research	Copyright © 2019 The Authors
figure 2.13	Berkowitz et al. (2000)	Water Resources Research	Copyright © 2000 by the American Geophysical Union
figure 2.15	Cortis and Berkowitz (2004)	Soil Science Society of America Journal	Copyright © 2004 Soil Science Society of America

Modelling of Reactive Transport in Porous Media using Continuous Time Random Walks

Rodolfo Oliveira

Imperial College London
Department of Earth Science and Engineering